UNIVERSITÀ
DEGLI STUDI
DI BRESCIA

DOTTORATO DI RICERCA IN INGEGNERIA CIVILE, AMBIENTALE, DELLA COOPERAZIONE INTERNAZIONALE E DI MATEMATICA

Settore Scientifico Disciplinare ICAR/03 Ingegneria Sanitaria-Ambientale

CICLO

XXXVII

ASSESSMENT OF SUSTAINABLE RECOVERY AND RECYCLING POSSIBILITIES OF MATERIALS FROM END-OF-LIFE LI-ION BATTERIES

RELATORE
Prof. Mentore Vaccari,
Università Degli Studi di Brescia

CORRELATRICE
Prof. Denise Crocce Romano Espinosa, Universidade de São Paulo

Dilshan Sandaruwan Premathilake

I dedicate this work to "free education"

Riassunto

Nell'ambito dello sviluppo sostenibile, l'urban mining dei rifiuti elettronici, in particolare delle batterie agli ioni di litio (LiB), rappresenta una via fondamentale per soddisfare l'aumento della domanda di materie prime critiche riducendo l'impatto ambientale. Le LiB, essenziali per i veicoli elettrici e l'elettronica di consumo, hanno determinato un aumento previsto della domanda di batterie, intensificando la necessità di un riciclo efficiente per mitigare la scarsità di risorse e le conseguenze ambientali. Questa ricerca mira a risolvere le sfide e le opportunità per un riciclo sostenibile delle LiB attraverso uno studio approfondito che include la revisione della letteratura, l'ottimizzazione dei processi, valutazioni del ciclo di vita (LCA) e costi del ciclo di vita (LCC) per massimizzare il recupero delle risorse con il minimo impatto ambientale.

La prima fase dello studio prevede una revisione sistematica delle tecnologie di riciclo delle LiB esistenti, con un'attenzione particolare allo sviluppo di una linea di pretrattamento decentralizzata in grado di gestire diverse chimiche di batterie. I passaggi essenziali identificati per un'elaborazione efficiente includono frantumazione, separazione per densità, essiccazione, seconda frantumazione, riscaldamento con CaO, vibro-setacciatura, lavaggio e separazione basata su flottazione, organizzati per ottimizzare il recupero dei materiali attivi delle batterie e migliorare la compatibilità con diversi tipi di LiB.

Nella seconda fase, lo studio esamina le tecniche idrometallurgiche emergenti per il recupero sostenibile degli ossidi metallici dei catodi, in particolare cobalto, nichel e litio. Attraverso simulazioni e ottimizzazione dei processi come lisciviazione, purificazione e calcinazione, sono state raggiunte efficienze di recupero superiori all'83% per l'ossido di cobalto, al 77% per l'ossido di nichel e al 74% per l'ossido di manganese, in particolare utilizzando la lisciviazione con acidi inorganici, la purificazione basata su materiali adsorbenti e la calcinazione. I metodi sono stati valutati per la loro fattibilità ambientale ed economica, con risultati che indicano che il miglioramento dei metodi può ridurre drasticamente il fabbisogno energetico, abbattendo gli impatti complessivi di circa quattro volte. L'analisi evidenzia il potenziale di questi metodi emergenti come alternative sostenibili con una maggiore efficienza di recupero, prestazioni ambientali ed economiche.

Nella terza fase, è stata condotta un'analisi comparativa di tre metodi—processi a freddo, caldo e umido—per il recupero della grafite dagli anodi delle LiB. Il processo a freddo, che utilizza la separazione meccanica, si è rivelato il più sostenibile dal punto di vista ambientale (impatto a punteggio singolo (SSI) di -432 μpt) e il più conveniente, con un costo di recupero di $-40 per chilogrammo grazie ai benefici combinati del recupero della grafite e dell'estrazione del rame. Il processo a caldo, che incorpora CaO, ha fornito grafite con il più basso distanziamento interstrato (0,345 nm), migliorandone la qualità per applicazioni ad alta purezza con un impatto leggermente inferiore (SSI di 317 μpt). Il processo umido, sebbene produca grafite con un alto contenuto di carbonio (81%), ha mostrato un degrado ambientale significativo (SSI di 695 μpt) principalmente a causa dell'elevato consumo di reagenti e dell'uso dell'acqua.

La fase finale esplora il potenziale riutilizzo della grafite residua in applicazioni per il trattamento delle acque reflue. L'ossido di grafite (GO) e l'ossido di grafene (GrO) sintetizzati dalla grafite residua hanno dimostrato capacità di adsorbimento superiori, superando 550 mg/g per la rimozione di coloranti e raggiungendo oltre 93 mg/g per la rimozione di Ni^{2+}. Il GrO, con una superficie specifica e una porosità maggiori, ha mostrato una rimozione del 97% dei coloranti e circa il 94% dei metalli, superando i materiali disponibili in commercio. Questo studio rivela la fattibilità della grafite riciclata come sostituto della grafite naturale in applicazioni ambientali, supportando ulteriormente un modello di risorse circolare.

Questa tesi evidenzia la fattibilità del riciclo sostenibile delle LiB ottimizzando i metodi di recupero per ottenere materie prime secondarie di valore. Le metodologie sviluppate contribuiscono a un modello di economia circolare, integrando la riduzione dell'impatto ambientale con la praticità economica, fornendo soluzioni scalabili per l'urban mining sostenibile. Svolta in collaborazione con diverse università e partner industriali, questa ricerca sottolinea il ruolo cruciale del riciclo delle LiB nell'avanzamento della gestione sostenibile delle risorse.

Abstract

In the pursuit of sustainable development, urban mining of electronic waste, particularly lithium-ion batteries (LiBs), offers a vital pathway to fulfill increasing demands for critical raw materials while reducing environmental impact. LiBs, pivotal for electric vehicles and consumer electronics, have led to an anticipated rise in battery demand, intensifying the need for efficient recycling to mitigate resource scarcity and environmental consequences. This research aims to address the challenges and opportunities for sustainable LiB recycling through a comprehensive investigation that spans literature review, process optimization, life cycle assessments (LCA) and life cycle costing (LCC) to maximize resource recovery with minimal environmental footprint.

The first phase of the study involves a systematic review of existing LiB recycling technologies, with a particular focus on developing a decentralized pretreatment line to handle a variety of battery chemistries. Essential steps identified for efficient processing include crushing, density separation, drying, secondary crushing, heating with CaO, vibro-sieving, washing, and flotation-based separation, arranged to streamline the recovery of active battery materials and improve compatibility with various LiB types.

In the second phase, the study investigates emerging hydrometallurgical techniques for the sustainable recovery of cathode metal oxides, specifically cobalt, nickel, and lithium. By simulation arrangements and optimizing processes such as leaching, purification and calcination, recovery efficiencies achieved were over 83% for cobalt oxide, 77% for nickel oxide, and 74% for manganese oxide particularly for inorganic acid-based leaching, adsorbent material-based purification and calcination. Methods were evaluated for environmental and economic feasibility, with findings indicating that improving the methods can reduce the energy requirement drastically by reducing the overall impacts by roughly four folds. The assessment underscores the potential of these emerging methods to offer sustainable alternatives with enhanced recovery efficiency, environmental performance and economic benefits.

In the third phase, a comparative analysis of three methods—cold, hot, and wet processes—was conducted for the recovery of graphite from LiB anodes. The cold process, which employs mechanical separation, proved to be the most environmentally sustainable (single score impact (SSI) of -432 μpt) and cost-effective, with a recovery cost of $-40 per kilogram due to the dual benefits of graphite recovery and copper extraction. The hot process, incorporating CaO,

provided graphite with the lowest interlayer spacing (0.345 nm), enhancing its quality for high-purity applications with slightly lower impact (SSI at 317 μpt). The wet process, though yielding graphite with a high carbon content (81%), presented notable environmental degradation (SSI of 695 μpt) primarily due to high reagent consumption and water usage.

The final phase explores the potential reuse of residual graphite in wastewater treatment applications. Graphite oxide (GO) and graphene oxide (GrO) synthesized from residual graphite demonstrated superior adsorption capacities, exceeding 550 mg/g for dye removal and achieving over 93 mg/g for Ni^{2+} removal. GrO, with higher surface area and porosity, showed 97% dye removal and approximately 94% metal removal, outperforming commercially available materials. This study reveals the feasibility of recycled graphite as a substitute for natural graphite in environmental applications, further supporting a circular resource model.

This thesis highlights the feasibility of sustainable LiB recycling by optimizing recovery methods to yield valuable secondary raw materials. The developed methodologies contribute to a circular economy model by integrating environmental impact reduction with economic practicality, providing scalable solutions for sustainable urban mining. Conducted in collaboration with multiple universities and industry partners, this research underscores LiB recycling's pivotal role in advancing sustainable resource management.

Table of contents

List of Figures

Chapter 1

Chapter 2

Chapter 3

Chapter 4

Chapter 5

List of Table

Chapter 2

Chapter 3

Chapter 4

Chapter 5

Annexure 1

Annexure 3

Annexure 4

Chapter One-Introduction

1. Sustainability as a concept

The Earth, home to all humans, animals, and plants, consists of a finite number of resources. Due to this finite supply, the rapid economic growth of human civilization may eventually lead to various drawbacks, not only from an environmental perspective but also from social perspectives. This idea was first put forward by the Club of Rome in 1972 [1]. Later, the Brundtland Commission, under the guidance of the United Nations, provided a political framework for this idea in 1987, where the term "sustainable development (SD)" came into existence with its broad meaning [2]. According to the Brundtland Commission, sustainable development is:

"*Development that meets the needs of the present without compromising the ability of future generations to meet their own needs*."

The definition above explains how the actions and choices of the current generation can affect future generations. It further suggests that the overuse of resources by the current generation may impose limitations on the needs of future generations. Therefore, it is important to maintain a balance between ecological resource use and generational needs. More importantly, sustainable development implies that the advancement of a society should be determined not only by economic means but also by environmental and social perspectives.

Three dimensions have been identified to assess sustainable development: 1) environmental, 2) societal, and 3) economic (Figure 1.1). While the economy was historically considered the primary indicator of development, it is now only one part of the overall development picture. Environmental and social impacts are now given equal importance in development. Hence, any development activity requires a comprehensive assessment of its environmental, societal, and economic consequences. It is important to recognize that every technological or development activity impacts all three dimensions of sustainable development. A development activity with zero environmental, societal, or economic impact does not exist. However, with proper assessment, it is possible to limit the environmental damages of such activities. It is a balance between what society wants and what it costs. Furthermore, when considering costs, both intragenerational and intergenerational impacts must be considered.

Some authors suggest that “sustainability” is distinct from “sustainable development” because the latter addresses infinite economic progress within the limits of finite resources. On the other hand, sustainability does not emphasize economic progress but rather considers the possibility of coexistence through concepts like “degrowth” or “buen vivir” [3]. However, growing population, the spread of new diseases, and increasing food needs challenge these new concepts, as they may not adequately address these inevitable issues. Instead, concepts like the circular economy and green economy are more practical and useful [4]. These concepts emphasize the importance of circular resource use rather than linear models. In a circular economy, resources are circulated within the economy without being discarded as waste. Recycling waste reduces the need for new material extraction, which can help minimize environmental damage while meeting intergenerational societal needs. Moreover, due to the reduced resource use, it also aligns with intragenerational needs.

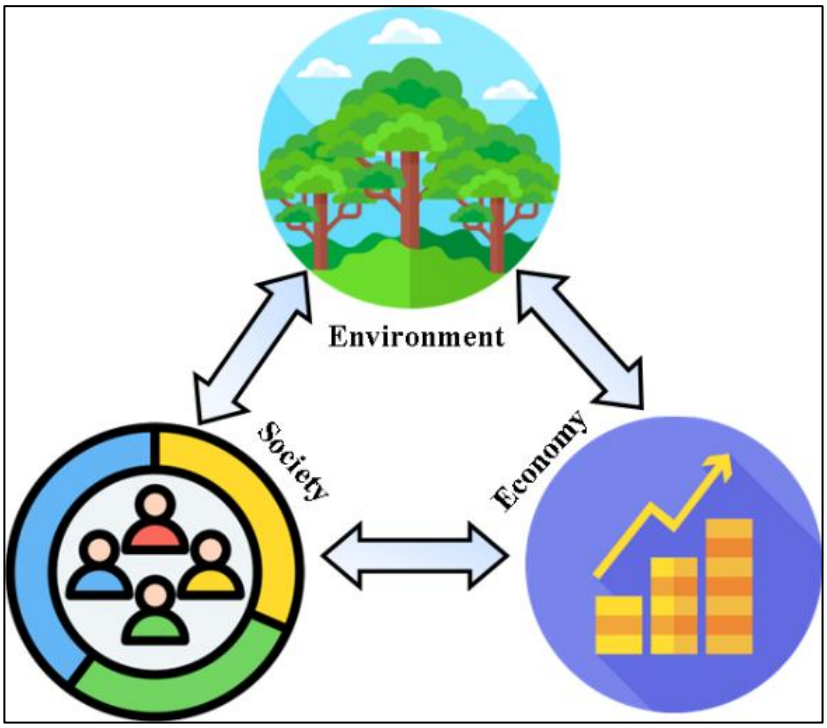

Figure 1.1 Representation of dimensions in sustainable development

Taking these concepts into account, any resource use activity can be converted into a sustainable resource use system. This can be achieved by applying the following three criteria to the resource use activity in question [5].

1) Efficiency

Efficiency reflects the percentage of useful material conversion in producing the output from the total input material. Consequently, high efficiency in material usage tends to minimize

overall material or resource consumption, which supports sustainability. On the other hand, lower efficiency is often associated with reduced sustainability due to increased resource waste. This relationship can also be linked to production costs. High-efficiency systems can reduce production costs, as they require fewer materials. Additionally, lower material requirements result in reduced mining activities and decreased energy consumption across the entire supply chain, which offers significant environmental advantages.

2) Consistency

Consistency on the other hand, allow materials to use infinitely on a loop which much more correlate with circular economy concepts. Though consistency is not playing a big role in renewable resources (sunlight, wind energy, sea currents), infrastructure building to synthesis of energy requires to use finite resources available. However, when the infrastructure needs to demolish and modify, the materials that used before should be reused to build the new infrastructures as well. At least, in a similar application where the materials are efficiently reuse. It is important to note that, under 100% consistency the material will be subjected into reuse infinite times without ever transforming it to an unusable state.

3) Sufficiency

Sufficiency approaches sustainability from a societal perspective, emphasizing a shift from a utilitarian mindset to a minimalist one. Lower consumption patterns in society will ultimately reduce product manufacturing and, consequently, resource extraction. However, the concept of sufficiency relates to Kothari's degrowth concept, which may negatively affect economic development. Nonetheless, if properly adopted, sufficiency can help achieve sustainability more quickly.

2. Urban mining: A focus-on E-waste

Urban mining directly relates to most of the criteria discussed above in the path of sustainable development (SD). It adopts the concept of a circular economy by recirculating waste products as new valuable materials and is governed by the concept of consistency. Urban mining is defined as the recovery of valuable materials, material coordination, or enabling the recovery of materials through various means (such as information gathering or services) from industrial and urban wastes. Since these wastes are derived from human activities, they are often referred to as man-made ores [6]. Utilizing these waste types for valuable material recovery can help

reduce collected waste, decrease new material extraction from natural ores, lower environmental damages, and contribute to sustainable growth.

Among the categories of urban waste, e-waste and construction and demolition waste (CDW) make up the largest fractions [7,8]. Notably, the construction sector generates the highest waste volumes, with a large portion of this waste ending up in landfills. Meanwhile, the rate of e-waste generation is increasing at a pace three times faster than other types of waste, with an annual growth rate currently estimated at 5%. In 2019, e-waste generation reached approximately 53.6 million metric tons globally [9]. Figure 1.2 shows the countries generating the most e-waste in 2022.

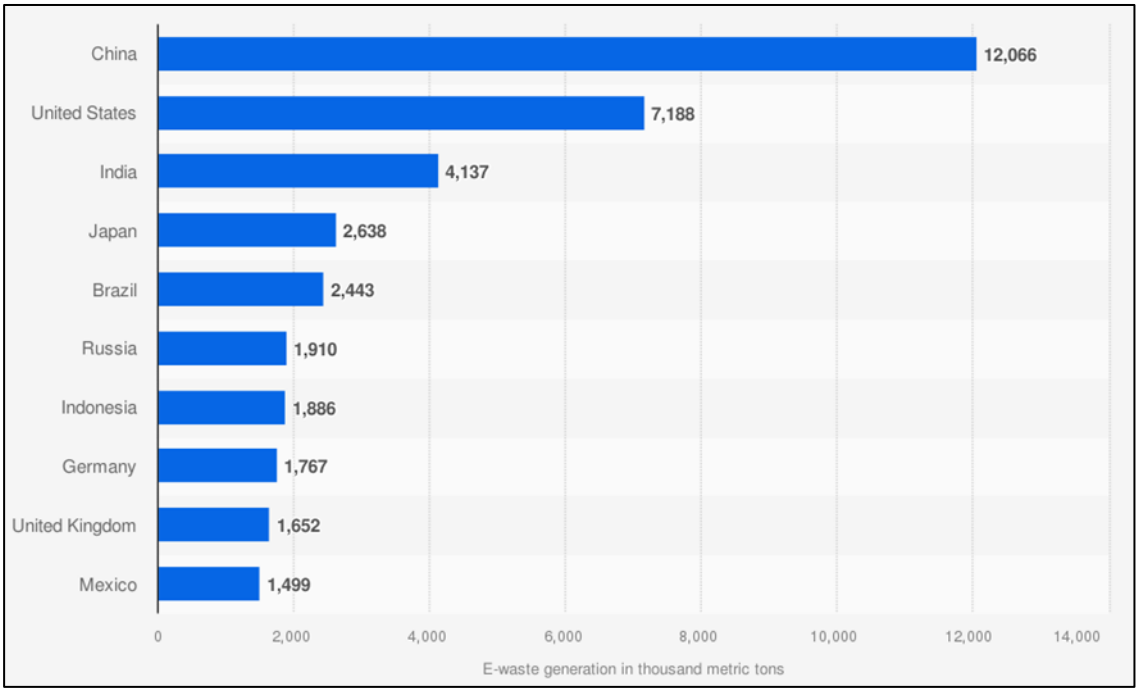

Figure 1.2 Leading countries based on electronic waste generation worldwide in 2022 (in 1000 metric tons) [10].

As shown in Figure 1.2, China is the leading generator of e-waste, followed by the USA and India. China currently leads many electronic manufacturing industries; hence, higher waste generation can be expected. For instance, lithium-ion battery (LiB) manufacturing is predominantly conducted by Chinese companies, which also dominate raw material supply for battery production [11]. The LiB industry stands out due to its high utilization in the electric vehicle (EV) sector, which is considered a transformative force in the transport sector, significantly reducing long-term emissions. Consequently, many countries have already implemented policies to promote EV use (discussed in detail in Chapter 2). As a result, demand for materials required for LiB manufacturing is rising rapidly, while the market for recycling

spent batteries (e-waste) is also expanding. Figure 1.3 (a) and (b) illustrate the projected growth in metal demand for battery production by 2028 and the anticipated growth in the global battery recycling market value.

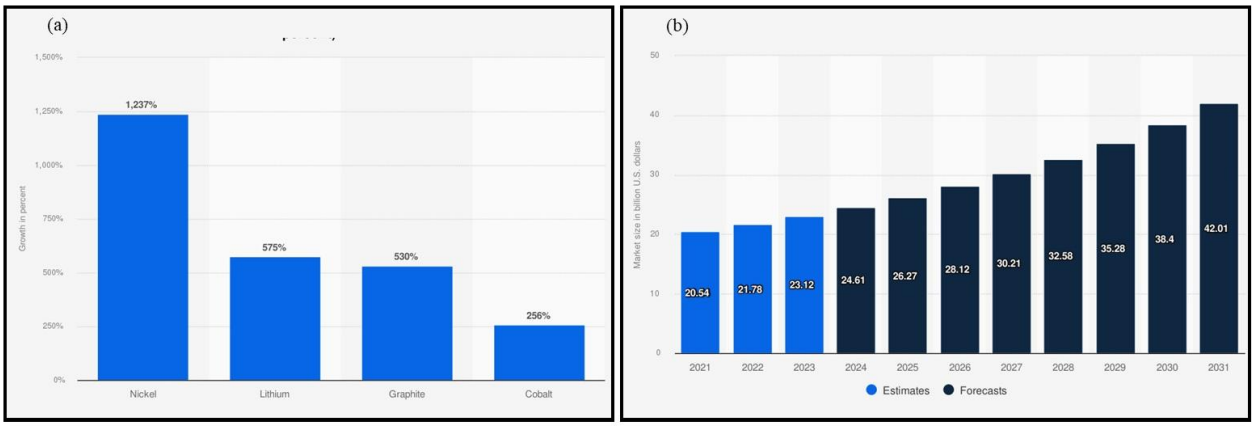

Figure 1.3 (a) Projected metal demand growth for battery production worldwide by 2028 (b) Global battery recycling market value forecasting [11,12].

It is evident that demand for primary battery active materials is projected to increase by 256% for cobalt (the minimum growth) and 1237% for nickel (the highest). Due to this high demand, the battery recycling industry is rapidly expanding, as material extraction from natural ores is no longer sufficient to meet these requirements. Additionally, most of these raw material ores are controlled by Chinese companies, where much of the battery manufacturing currently takes place, making the supply chain potentially vulnerable to interruptions [13]. Furthermore, almost all the materials in LiBs are categorized as critical raw materials (CRM) or strategic materials for Europe [14]. This fact further highlights the importance of recovering materials from spent LiBs under the urban mining concept.

These factors motivate the establishment of the current research project on sustainable CRM recovery from end-of-life (EoL) LiBs. This research study aims to answer the question, “Are the current recovery and recycling methods for spent LiBs sustainable?” Additionally, the project seeks to explore ways to improve these methods, either by recovering higher-quality materials or by reducing the environmental impact. Opportunities for value addition will also be evaluated where applicable. The economic impacts of the existing and newly introduced methods will be assessed. Sustainability assessments will involve life cycle assessments (LCA) and life cycle costing (LCC) analyses. Social criteria of sustainability will not be considered, as the research work is carried out at the laboratory level. The research will focus specifically on pretreatment, cathode material treatment, and anode material treatment segments, focusing on the availability of valuable materials.

Finally, this research project is an outcome of the 3-year project "Sustainable Mining: Recovery of Critical Raw Materials from Batteries Using Environmentally Friendly Technologies," co-funded by the Italian Ministry of Foreign Affairs and International Cooperation and the São Paulo Research Foundation. The University of Brescia (Italy), the Polytechnic University of São Paulo (Brazil), and the Federal University of Rio de Janeiro (Brazil) participated as members of the research group. Furthermore, the research was supported by RMB SpA, Polpenazze (BS, Italy), and the University of Pavia (Italy), by providing laboratory facilities and analytical supports.

3. Structure of the thesis

The research thesis will take the following structure,

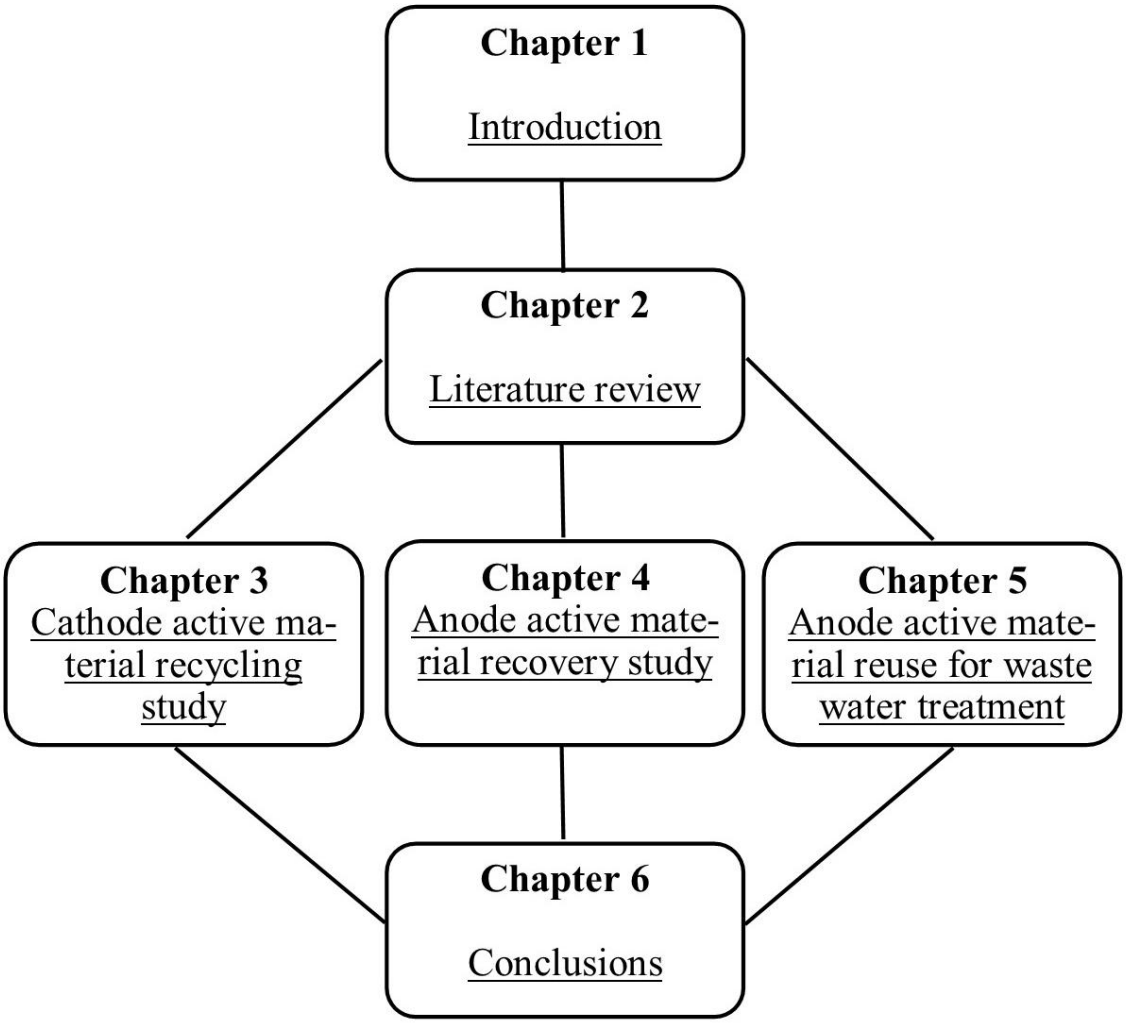

Figure 1.4 Schematic representation of the thesis structure.

In Chapter 1, an introduction to the thesis is provided, outlining the motivation, research questions, and objectives to be achieved. Chapter 2 presents a bibliographic review, addressing common problems and the current status of battery-related policies, lithium-ion battery (LiB) waste collection, discharging processes, and active material separation techniques from battery components. The review also proposes a potential mechanism for the pre-treatment of battery materials to facilitate the separate recovery of active materials.

Chapter 3 explores emerging methods for cathode active material treatment to recover metal oxides from spent batteries using hydrometallurgical techniques. Technologies are evaluated based on their efficiency, environmental impact, and economic implications across different extraction routes. In Chapter 4, the focus shifts to anode material recovery, with a detailed discussion of novel methods for graphite recycling, route optimization, and characterization. Sustainable approaches for graphite recovery will be assessed by examining their environmental and economic performance.

Chapter 5 explores the potential reuse of recycled graphite from spent LiBs, with a focus on graphite modification methods and possible applications in dye and metal-contaminated wastewater treatment. Finally, in Chapter 6, the research synthesizes treatment mechanisms for each segment (pre-treatment, active material recovery, and recycling), identifying pathways to generate valuable secondary raw materials and concluding the research project.

References

[1] D. H. Meadows, D. L. Meadows, J. • Rgen, R. William, and W. Behrens Ill, “The Limits to Growth. A report for the Club of Rome’s project on the predicament of mankind.,” 1971.

[2] Brundtland Commission, “Our Common Future,” Oct. 1987.

[3] A. Kothari, F. Demaria, and A. Acosta, “Buen Vivir, Degrowth and Ecological Swaraj: Alternatives to sustainable development and the Green Economy,” Development, vol. 57, no. 3–4, pp. 362–375, Dec. 2014, doi: 10.1057/dev.2015.24.

[4] C. A. Ruggerio, “Sustainability and sustainable development: A review of principles and definitions,” Science of The Total Environment, vol. 786, p. 147481, Sep. 2021, doi: 10.1016/j.scitotenv.2021.147481.

[5] M. Fischer et al., “The Concept of Sustainable Development,” 2023, pp. 17–27. doi: 10.1007/978-3-031-25397-3_2.

[6] A. B. Botelho Junior, F. P. Martins, L. O. Cezarino, L. B. Liboni, J. A. S. Tenório, and D. C. R. Espinosa, “The sustainable development goals, urban mining, and the circular economy,” Extr Ind Soc, vol. 16, p. 101367, Dec. 2023, doi: 10.1016/j.exis.2023.101367.

[7] N. H. Hoang, T. Ishigaki, R. Kubota, M. Yamada, and K. Kawamoto, “A review of construction and demolition waste management in Southeast Asia,” J Mater Cycles Waste Manag, vol. 22, no. 2, pp. 315–325, Mar. 2020, doi: 10.1007/s10163-019-00914-5.

[8] C. Zhang et al., “Upgrading construction and demolition waste management from downcycling to recycling in the Netherlands,” J Clean Prod, vol. 266, p. 121718, Sep. 2020, doi: 10.1016/j.jclepro.2020.121718.

[9] Vanessa Forti, Cornelis Peter Baldé, Ruediger Kuehr, and Garam Bel, “The Global E-waste Monitor 2020,” 2020. Accessed: Oct. 29, 2024. [Online]. Available: https://www.greene.gov.in/wp-content/uploads/2020/12/2020120929.pdf

[10] Statista, “Leading countries based on electronic waste generation worldwide in 2022 (in 1,000 metric tons),” 2024. Accessed: Oct. 29, 2024. [Online]. Available: https://www.statista.com/statistics/499952/ewaste-generation-worldwide-by-major-country/

[11] Madhumitha Jaganmohan, “Global projected growth in metal demand for battery production 2028,” Apr. 2024. Accessed: Jun. 11, 2024. [Online]. Available: https://www.statista.com/statistics/665038/projected-growth-in-metal-demand-for-battery-production-worldwide/

[12] Statista, “Projected metal demand growth for battery production worldwide by 2028 (in percent),” 2024. Accessed: Oct. 29, 2024. [Online]. Available: https://www.statista.com/statistics/665038/projected-growth-in-metal-demand-for-battery-production-worldwide/

Chapter Two-Bibliographic Review

Designing of a Decentralized Pretreatment Line for EOL-LIBs Based on Recent Literature of LIB Recycling for Black Mass

This paper has been published in the journal *metals* (https://doi.org/10.3390/met13020374). The author contributed in writing the original draft, editing and reviewing, conceptualization, methodology and formal analysis.

1. Background

Humans' dependence on energy will never cease but will continue to grow along with population growth, technological advances, and societal needs. As an example, it is predicted that the world energy requirement will be increased by 50% by 2050, which will be responsible for 911 trillion BTU [1]. To supply the demand, dependencies on different energy sources are to be expected. However, it is a fact that conventional energy sources such as fossil fuels carry a huge environmental burden. In fact, CO_2 emission along with limited availability makes fossil fuel unreliable and disputed as an energy source. Accordingly, many developed economies have made it a top priority to switch to reliable and renewable energy sources which cause less or no environmental deterioration. For instance, the European Union (EU) has imposed a number of rules that instruct its member countries to increase the EU's renewable energy share up to 32% by 2030 [2].

Nevertheless, many international and local communities have made sustainable energy plans and policies a number one priority. In addition, several energy companies' statistical analyses elaborated that due to the continued growth of renewable energy productions, the global energy usage growth was limited to 1.3% in 2019, which is a considerable drop when compared to the growth rate of 2.8% in 2018 [3].

Nonrenewable energy sources such as fossil fuels (stored chemical energy) have their own advantages over the renewable energy sources. One such advantage is the ease of storage which also made it popular as the main energy source of transportation mediums. Renewable energies, on the other hand, are not readily available like fossil fuel; they need to be harvested (transformed from other energy sources) using different methods and this makes renewable energy subject to fluctuations when supplying energy. In addition, fluctuations in energy supply highlight the importance of surplus energy storage to keep a smooth supply. Li-ion battery (LIB) is one of the best and prominent technologies available for the purpose of energy storage.

LIBs are well renowned for their enhanced energy density, ability to undergo many recharging and discharging cycles, ability to provide high voltage, least charge lost and least self-discharge. Moreover, LIBs can be considered a good transitioning technology, as they intensify the energy efficiency of the systems. Due to all the reasons listed, LIBs are currently used in a range of applications from domestic electrical items to hybrid and pure electric vehicles (EV), and many industrial applications [4–7]. Among the many applications of LIBs, researchers expect that LIB applications in EV will rise significantly during the near future [8]. The power output of total used LIBs will rise from around 400 GWh to 1300 GWh within 5 years starting from 2035 in the transport sector only [9,10]. Such achievements will contribute to lower CO_2 emissions drastically, hence supporting the achievement of the targets of the Paris climate goals.

Though LIBs aid the creation of a green energy supply, manufacturing of LIBs will elevate environmental impacts in resource extraction as it requires importation of many critical raw materials (CRM) to Europe, such as lithium (Li), cobalt (Co) and graphite [11]. Co, for instance, is considered critical in the EU and in the USA, and a strategic raw material in Brazil since most of its global production is from one country—Democratic Republic of Congo [12–15].

Moreover, LIBs require other types of metallic and non-metallic resources like Al, Cu, plastic, electrolytic salts and other organic binder making chemicals. As reported by Trading Economics, the price of Co has increased by 0.71% since the beginning of 2022 and the price was recorded as USD 71,000 per metric ton as of 2022 February. The commercial value of Co is rising as a function of its limited availability and significance in applications. Currently, 25 million tons of terrestrial Co resources are available in several countries and DR Congo is responsible for around 70% of total production, followed by Russia [14]. China is identified as the largest consumer of Co so far, and from its total consumption, 80% is used for LIB productions [15]. Co is identified as an element that has many other applications as well [14,16,17].

In contrast, the largest productive Li reserve worldwide was analyzed to be around 18 million metric tons by 2020 [18]. On the other hand, Li is identified as a tactical element important in many industrial and commercial applications, such as stoneware and glass manufacturing, metallurgy, medical uses and polymer manufacturing. Li production has experienced a more than 100% increase from 2016 to 2019 due to its high demand for LIB manufacturing.

However, this rise includes a slight decrease from 2018 because of the subsidy policy introduced during this period as EVs required a considerable amount of high-quality Li production [15,19,20].

Though available Li resources are sufficient for LIB manufacturing for several years, alternatives must be taken into consideration in the long term. Sodium ion batteries are one such alternative [21]. As per the current research studies, these batteries cannot meet market demands due to their low electrochemical properties in comparison to LIBs [22,23]. Accordingly, it is not yet likely that further research and development on these alternatives will lower the demand for high grade Li minerals in the near future. In contrast, Nassar et al., in 2020, concluded that graphite is one of the elements with highest supply risk to the USA based on disruption potential, trade exposure and economic vulnerability [24]. Further, graphite is a critical material and industries such as rechargeable battery and body armor are highly vulnerable because of this [25]. Currently, Turkey has the largest graphite reserves at around 90 million metric tons, followed by China and Brazil, with 73 and 70 million metric tons, respectively. In 2020 alone, worldwide graphite production was 1.1 million metric tons, including the largest share from China (650,000 metric tons), followed by Brazil (95,000 metric tons). Moreover, graphite's market value is expected to increase further from USD 18 billion in 2018 to higher than USD 27 billion by 2025 due to its vast applications and identical properties [26]. It is a clear fact that the demand for these materials will not cease but will rather increase. Rising demand will further make the material supply more critical for industries which rely on high-grade pure material, such as the LIB industry.

In addition to extraction of resources, End of Life (EoL) disposal of LIBs will also add more toxic substances to the environment along with huge amounts of waste in resource elements if not managed properly. It has been identified that electrolyte content in LIB can react with water and air to create secondary pollutants. Li, being a highly reactive element upon contact with natural substances, can cause explosive reactions releasing many harmful substances such as phosphorus, nitrogen-rich contaminants, halogenic gases, or heavy metal leachate to the environment. Organic solvents can provide a medium for other chemical reactions to take place such as disintegration reactions, ignitions or decaying. These reactions can form many organic compounds with carbonyl bonds. It is a known fact that these substances can dissolve in natural waters easily and create serious issues for human sanitation. So, improper disposal of LIB electrolytes can create both environmental and human sanitation problems [27].

In addition, landfilling used LIBs can remove useful resource elements from the loop. This resource elimination must be refilled along with extra resource capacities for the rising demand using new virgin materials from primary resources. Extraction of new virgin materials creates huge energy requirements and a huge environmental burden on both sides (extraction of resources and disposal of LIBs). Hence, high priority must be given to innovative research on recycling of LIBs and recovered metals [10].

Another point to be concerned about is the rising market for EVs. It is expected that the global EV market will rise four-fold from its 2021 status by 2026 (Figure 2.1) [28]. In addition, major countries including EU, China and USA who have EV initiatives, noted a rapid increase in new EV registrations as a result of their policy implementations [29]. Further increase is to be expected with new procedures adopted by several countries. For instance, the USA has implemented the EV30@30 campaign through its Clean Energy Ministry to increase EV usage by 30% by the end of this decade. Many other nations such as Canada, China, India, France, Finland, and Mexico are also supporting this initiative [30]. As another example, the Chinese government's "13th five-year plan (2016–2020)" can be considered. It has proposed to enhance and increase EV and LIB power usage. Accordingly, by the end of 2020, it was reported that the total number of EVs hit five million, and new registrations in 2020 hit 1.25 million [31]. There is no doubt that these demands will increase further in the future and the growing EV market will contribute to an increase in LIB battery production as well. If proper recycling and material recovery methods from spent LIBs are not implemented, higher extraction of metals is expected in future to supply the demand.

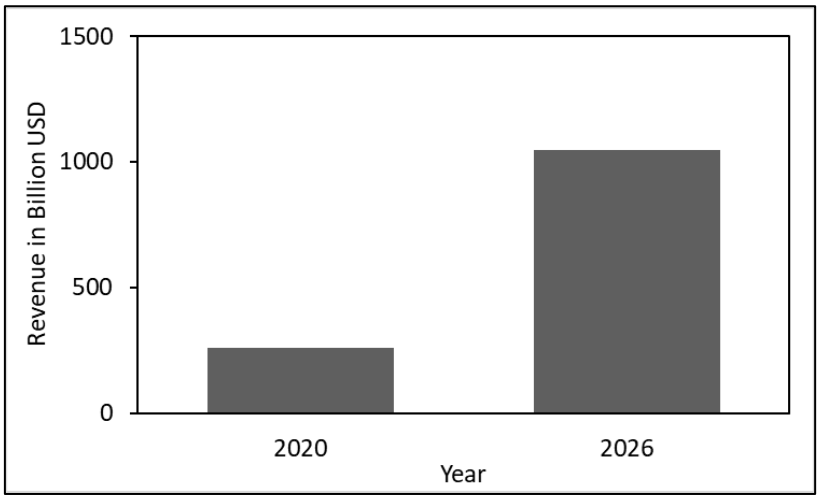

Figure 2.1. Size of the global market for EVs in 2020 and 2026 (in billions USD) Data source: [28]

Larcher and Tarascon reported that it is possible to recover 1 ton of Li through 28 tons of used LIBs. Extraction of the same amount of virgin Li would require 250 tons of ore materials or

750 tons of brine material with approximately 2–7% weight ratio of Li [32]. So, it is evident that recovering minerals through recycling is worth more than adding enormous pressure to the natural ore supply, because processing a smaller amount of mineral-rich waste electrical and electronic equipment (WEEE) would be easier than extracting virgin minerals from a large amount of ore materials. Further, it can lessen the environmental impacts through avoided virgin products. Moreover, it can also reduce the pressure on natural ore materials as most of the recovered resources would still be in use. It is estimated that, by the end of 2030, WEEE generation will total 74.7 million tons/year which includes a significant weight share of spent LIBs from different sources (EVs, laptops, mobile phones, etc.) [33]. Therefore, it is worth noting that there is a huge unexploited research gap to be addressed in the near future to turn this waste into resources in an efficient and economically feasible manner [34].

Many directives from different nations have come into play to make the battery recycling process more stringent and sustainable. In the EU's Circular Economy action plan in 2020 [12], directives on battery and accumulators [13], and a policy on battery passport [35] play an important role in establishing guidelines for LIB recycling. In contrast, support from the USA for such initiatives seems to be lower. The Battery Act in 1996 and Universal Waste Rule under Resource conservation and Recovery Act in 1995 are the only directives that provide guidelines to the whole USA in battery recycling and disposal [36,37]. However, some states have adopted their own policies on battery recycling, newly based on the mentioned acts. Accordingly, 25 states impose laws on banning landfilling and open burning of lead-acid batteries (LAB). Nevertheless, the Rechargeable battery act launched by the state of California in 2006 is another decree that deals with handling and recycling of batteries [38–42]. China, on the other hand, implemented measures in 2016 (law on pollution prevention techniques of waste batteries) and in 2018 (transitional measures) providing a broad spectrum of guidelines for the handling and recycling of rechargeable batteries [43].

1. **Novelty and Scope of Study**

Current literature reviews in the field denote methods such as hydrometallurgy, pyrometallurgy (or both), and other mechanical methods as possible for material recovery from battery parts [44–49]. Moreover, in recent studies, investigators clarified that most established industrial lines need further insights to make them sustainable [50]. All the existing reviews and studies emphasize the importance of focusing on each of the life cycle segments from cradle to grave, and possibly, value chains. As an example, Mossali et al. (2020) concluded that

product design plays a huge role when it comes to recycling. This point deals with designing an LIB with easy dismantling abilities, hence the importance of considering the design phase [51]. Nevertheless, Doose et al. (2021) have shown how changing cell chemistries affect recycling efficiency through different approaches [45].

Due to these facts, most of the recycling routes are planned to focus on a single type of cathode material [52,53]. Moreover, the complexity of collecting, sorting and separating for particular battery types, limits recycling of the same [44]. In spite of that, if the recycling route for LIBs is decentralized, the pretreatment can be done in one single type of plant and can recover widely available metal types easily. Therefore, the materials in electrodes can be recovered at later stages in different plants where they can focus on one precious material available in it. This can enhance the efficiency of the process and decrease CO_2 emissions in transportation and the energy intensity of the processes, improving total sustainability. In addition, this will address the research gap of the lack of automated, total recycling lines for LIBs [54].

Decentralized recycling of LIBs can aid in planning a fully automated pretreatment plant to recover widely available metals in casings and current collectors. Since the electrode materials can be forwarded, sorted or unsorted to secondary recycling units, where they can focus on one specific element recovery, the total recycling route for LIBs can also be achieved through this. The total recycling line for LIBs, hence, will be segmented and decentralized accordingly.

Existing review articles ignore the most commonly available metals such as Cu and Al which are easy to recover. Further, these articles have given less priority to the pretreatment process. In particular, a well-defined sustainable pretreatment process is not yet described to be used industrially. Focusing on these research gaps and highlighting the importance of decentralizing the recycling of LIBs, this review article examines the recent research studies, lab experiments and pilot projects carried out to recover materials from LIBs to evaluate the different pretreatment strategies used. In addition, the conclusions of the article will suggest potential environmentally friendly and cost-efficient technologies that can be utilized for a universal automated pretreatment line for LIBs. The novelty of the article can also be seen in the methods of discussing existing technologies, using illustrated summaries at the end of each section, and prioritizing pretreatment strategies to develop segments to include in a universal pretreatment line for waste LIBs of EVs. The work will be useful for industries involved in metal recovery to start new lines to recover higher amounts of widely available metals from LIBs, and battery recycling companies to develop secondary treatment lines only for electrode materials.

Moreover, policy makers and environmentalists can also use this resource to suggest methods to reduce energy consumption for recovery steps using decentralized plants. Finally, researchers on the topic will be able identify existing research gaps that need further evaluation in the topic area.

2. LIB Classification, Collection, and Sorting

3.1 Battery Characterization

As one of the major determinants of the recycling steps, understanding the chemistry of the battery is vital. In any LIB battery, it is possible to identify cells, modules, and packs as the main parts of it. Further, each cell contains a cathode, anode, organic electrolyte and a separator covered by a housing (or case). The separator is wetted by electrolyte salts. The cells are connected in series or in parallel to make up the module according to the usage of the battery. A combination of two arrays may be also possible for some batteries. A module will be contained in a house made from insulating material for battery safety. A pack of batteries can contain several modules interconnected [55]. It seems that the size, shape and content of the battery are highly dependent on the application of the battery. However, categorizing the LIBs based on their cathode material is more useful to make a good judgment.

Lithium cobalt oxide ($LiCoO_2$) (LCO) cathode batteries can be identified as the first LIBs that use a liquid electrolyte [44,56,57]. However, applications of LCO batteries are limited to small electronic devices such as mobile phones or laptops. While $LiCoO_2$ acts as the cathode material in LCO batteries, graphite acts as the anode material with a conductive polymer as the electrolyte [56,57]. Though graphite as the anode material has not changed much in the past years since its first introduction, cathode material has undergone various changes. LCO cathode material is easy to produce and has a stable discharging which makes it a favorable material for the cathode. However, having high Li and Co proportions make it undesirable due to extensive environmental burden, less economic viability and human health concern occurring during the extraction period of Li and Co. In addition, the performance of the battery is average compared to the other available LIB battery types. This makes it urgent to further modify the cathode materials in future LIBs [56,58].

Accordingly, it is possible to identify LIBs with lower Co content with enhanced performance. Lithium manganese oxide ($LiMn_2O_4$) (LMO) cathode is a material used as an LIB cathode with no Co involved. It is also the reason for the low cost of the same. LMO batteries have better

performance than LCO batteries. For example, LMO has a higher charge rate and higher voltage than LCO batteries which makes it applicable in portable devices other than smaller electronic equipment. LMO batteries are also seen combined with other battery types to use for EVs [59]. However, as some authors elaborate, LMO has a short lifetime along with a medium energy density, which makes it unfavorable in some ways [27]. Due to these factors, LMO batteries have a low market share.

Lithium iron phosphate (LiFePO4) (LFP) is another alternative that uses no Co in its cathode material. Further, the structure of the LFP cathode gives it an additional stability which enhances its total lifetime. Low environmental degradation caused during the extraction period is another plus point for these cathode materials. However, low energy density and relatively low potential make it undesirable in many high-end applications like EVs. However, the demand for LFP batteries has risen due to its low cost and extended lifetime involved [56,58].

Commonly, LCO, LMO and LFP cathode battery types are involved with low to medium energy densities in relation to the other battery types found in the market. In contrast, lithium nickel cobalt manganese oxide ($LiNi_xCo_yMn_zO_2$) (NCM) cathode materials and lithium nickel cobalt aluminum oxide ($LiNi_xCo_yAl_zO_2$) (NCA) have been identified for their high specific capacities and high energy densities due to the availability of Ni in the structure [60,61]. Since both NCM and NCA types use Co, they are implicated in relatively high environmental degradation and human safety issues. However, a lower Co ratio makes the impact relatively lower than LCO battery types. It seems that high energy density is the main source that made these batteries the dominant battery types in the market. Nevertheless, the same criterion made them applicable in EVs. One notable difference among these two battery types is the expected life span. According to current studies, NCM batteries have a higher lifetime than NCA batteries, which makes NCM batteries have a higher market share than NCA batteries [27].

Doose et al. (2021) suggests that the trend of LIBs goes towards NCM cathode types due to low Co content. NCM 811 has a molar ratio of Ni:Co:Mn as 8:1:1, which makes it better in environmental performance due to less Co content, whereas NCM 622 has a molar ratio of 6:2:2 and NMC 111 has the ratio of 1:1:1 [45]. However, some authors show that higher content of Ni reduces the performance of the battery drastically in many aspects. For instance, reduced lifetime, reduced heat resistance and a few other technical problems (voltage decay, low initial coulombic efficiency, capacity loss, termination of transitional metals) can be listed [57,62,63]. So, NCM 622 can be identified as a relatively better performer in both environmental and

technical aspects. A comprehensive summary of cathode types is discussed in Table 2.1. It shows the chemical formula, possible voltage ranges, energy densities and applications.

Table 2.1 Comprehensive summary of different LIB battery types based on cathode material. Data source: [64,65].

Battery type (Based on Cathode material)	**LCO**	**LMO**	**LFP**	**NCA**	**NCM**
Chemical Formula	$LiCoO_2$	$LiMn_2O_4$	$LiFePO_4$	$LiNi_xCo_yAl_zO_2$	$LiNi_xCo_yMn_zO_2$
Operating Voltage (V / Cell)	3.0 – 4.2	3.0 - 4.2	2.0 – 3.65	3.0 – 4.2	3.6 – 4.0
Energy Density (Wh/ kg)	150 - 200	100 - 150	90 - 160	200 -260	160 - 230
Applications	Small devices (Laptops, mobile phones)	Small devices, EVs with combination of NCM	Smaller portable devices, Limited applications in EVs.	EVs (Tesla vehicles)	EVs (Many manufacturers), Small appliances, Power station applications
Remarks	Low safety, high cost and medium performance	Medium safety, medium performance, low lifetime	Low cost, medium performance, high thermal resistance	Medium safety and cost, High performance	Medium safety and cost, High performance

However, more materials are being investigated to be used as cathode materials of LIBs. $LiMnO_2$ is a material which has the structure of LCO cell types (layered oxide). Other than that, $LiMnPO_4$ or metal sulfides and cathode materials made from sulfur-carbon composites are also under investigation and have the potential of entering the market in near future [65,66].

Graphite or composite carbon being the anode material of the LIBs has not significantly changed over the past years. However, there are other materials used in the anode other than the graphite or composite carbon, which will be discussed soon under this section. Graphite or carbon-based composite in the anode material is very popular due to the properties of these materials and structures. Mainly, their safety for humans when not contaminated, structural and chemical stability under different temperatures, and economical quality are some reasons for their repeated application as the anode material. Other than that, low working potential and high theoretical capacities (~0.15 V vs. Li^+/Li and 372 mAh g^{-1}, respectively) of these materials are also reasons to become popular for this aspect [66–68].

In contrast, the lithium titanium oxide (LTO) battery type uses LTO as the anode material instead of carbon [69,70]. The use of LTO has some advantages over graphite, such as

generating a higher power with a low energy loss and durability [69–71]. However, the high cost in manufacturing such batteries makes it unfavorable for commercial use. Other than this, new materials for anode materials are being investigated. Among them, graphene, silicon composite or silicon-based nanomaterials, and Li metal are available. These new research studies will address the problems involved with current anode materials such as heat generation in LMO and LFP cathodes or rupture generation occurring due to repeated charge cycles [72]. Titanium niobium oxide (TNO) has been studied for application as an anode material [71]. For instance, TNO/NMC batteries have up to 14,000 cycles at 80% capacity retention, which is considered as another option with LTO/NMC batteries [72].

Other than the cathode and anode materials, in a spent LIB battery, some hazardous waste can also be found. This can be easily understood by understanding the cross-sectional structure of a spent LIB. Figure 2.2 shows the structure of the spent LIB.

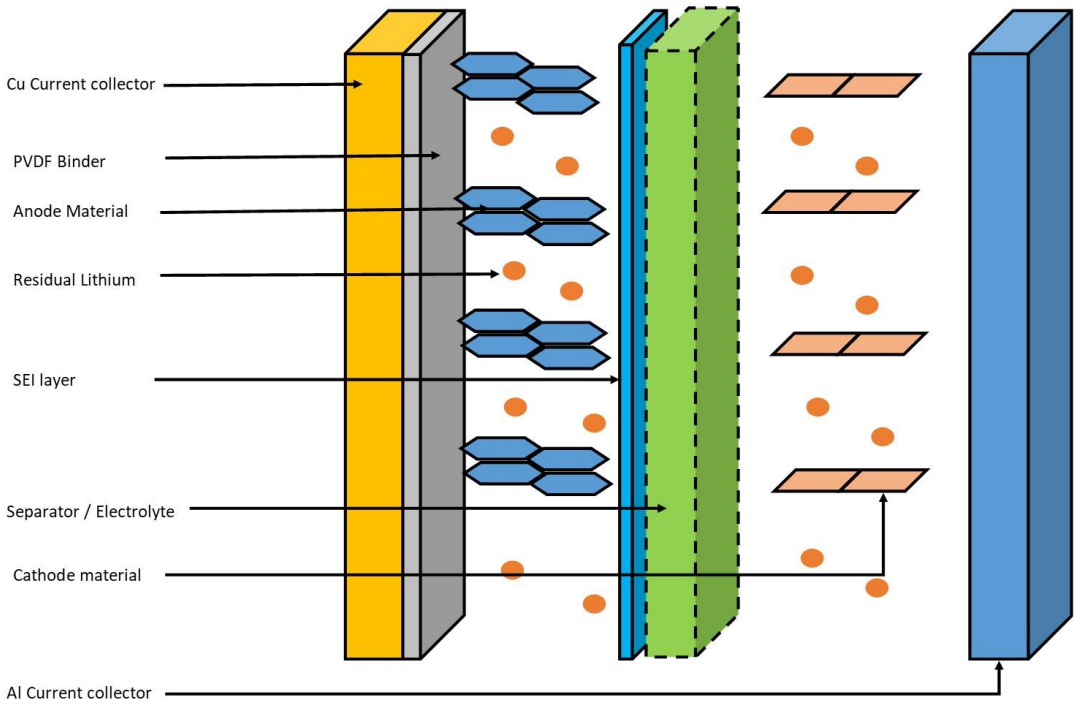

Figure 2.2 Schematic model of the spent LIB developed based on: [70–72].

For instance, graphite is attached to the Cu current collector through polyvinylidene fluoride (PVDF) layer in LIB. Additionally, between the surface of the graphite and the electrolyte, the solid electrolyte interface (SEI) is built through a reaction between the graphite surface and the Li from electrolyte during the recharge and discharge cycles. Usually, electrolytes are made up

of Li salts such as LiPF6 or LiClO4 dissolved in organic solvents. As an organic solvent, ethylene or ethylene carbonate is used [72,73]. Authors suggest that, at the EoL of the LIB, the spent anode material can contain residuals from all these electrolytes and binders, as well as Cu foil with a higher degree of degradation to the anode material [74–76].

According to the chemistry of the battery, improper disposal of these materials can have a significant impact on the environment and human health. Of course, the soil and natural water body contamination are the first steps of a series of chemical reactions that are waiting to follow. In particular, metallic Li can have explosive reactions with natural waters. Other metals included can affect the biodiversity of the contaminated sites. Moreover, organic materials, electrolyte, and waste graphite, upon disposal into the environment, can have a series of reactions and can lead to the release of toxic substances into the environment according to the following reaction series.

$$LiPF_6 \rightarrow PF_5 + LiF \text{----------(1)}$$

$$LiPF_6 + H_2O \rightarrow 2HF + OPF_3 + LiF \text{----------(2)}$$

$$(C_2H_5O)2CO + H_2O \rightarrow CO_2 + 2C_2H_5OH \text{---(3)}$$

$$(CH_3O)2CO + H_2O \rightarrow CO_2 + 2CH_3OH \text{------(4)}$$

Importantly, these substances are highly water soluble and can cause health impact on humans and on other living beings as well. Due to these factors, proper disposal, or more importantly, material recovery from spent LIBs is necessary to implement circular economic concepts in battery manufacturing. However, designing a common recycling process for all the LIBs seems to be an impossible task given the varieties of battery chemistries. Nevertheless, current research studies suggest common frameworks that can be used as prototypes when designing an LIB recycling process. Based on this, current battery recycling companies have adopted their recycling facilities considering only one battery chemistry type. This is mainly since mixing different chemistries for recycling can imply a negative effect on the outcome. However, separate recycling is costly and reduces the overall recycling rate.

3.2 Material Collection

An efficient waste collection system is always the key to a successful recycling route. Accordingly, establishing an effective and efficient collection system for spent LIBs will aid in

maximizing the recycling capacity and economic benefits. Further, decisions on environmental and economic aspects can be easily taken upon knowing the collection capacities.

Availability of a range of LIB products in the market is one major problem for collection. Nevertheless, LIBs have a variety of applications, due to their design, size, content, shapes, and capacities which are also changing. These factors make waste collection more difficult and complex for LIBs [77–79]. It is possible to distinguish three market segments for LIBs, such as small-scale electrical equipment (SSEE) (household scale), stationary energy storage (SES) and EVs. SSEE markets and SES markets are well established, and as discussed previously, an increase can be expected in EV markets, and hence an increase in spent EV LIBs. Given the differences in the three market types, the types of LIBs in a market segment are significantly different from others. As a matter of fact, different collection routes need to be established for each of these market types. SSEE, or simply household electrical equipment batteries, can be collected at locations established by the manufacturers or at retailers/supermarkets. However, large-scale LIBs (SES and EVs) need the attention of expert/trained personnel for dissembling from the equipment prior to collection [80,81]. The availability of the LIBs for collection at the end of their lifetime is vital. As per literature, the largest proportion are available in domestic-scale equipment (SSEE). Usually, LIBs from SSEE last for 3–10 years before coming to the waste stream [81]. However, this is far more than the usual lifetime of the equipment. Most domestic scale electric equipment passes a hibernation period (inactive stage) after its service period before being added to the waste stream, extending their true lifetime. The lifetime of the EVs depends on many factors such as the annual mileage, charging frequency and condition, and the type of battery; manufacturers usually expect the battery to last for 8–10 years. In running distance, this is around 160,000 km for most of the EV types (Toyota, Nissan, BMW, etc.) [82,83]. Further, Yang et al. (2018) have predicted that EV lifetime can be varied in the range of 5–13 years in different USA cities, considering average driving conditions using predictive tools. Additionally, this can be elevated by another 10–12 years by giving them a second lifetime in SES applications (also depending on the application) [82].

According to these long-life EV batteries and the infancy stage of the EV sector, near- term priority is worth giving to mature, small-scale electric equipment batteries. However, designing recycling processes, collection mechanisms and applications for the upcoming huge waste stream of EV batteries is also important to manage these hazardous wastes from now on [84,85]. Presently, only a small fraction of electronic waste is being collected and recycled

properly. Hence, a larger amount is being neglected and ends up in landfills, adding more toxic substances to natural soils and waters [86]. In 2020, Europe collected and recycled the highest fraction of e-waste (42.5%). In contrast, Asia has the second-highest waste recycling with 11.4%. America and Oceania stayed at 9.4% and 8.8%, respectively. The least recycling is recorded in Africa, which is 0.9%. So, as an average, only 17.4% of total e-waste is subjected to collection and recycling on the global scale [86]. Moreover, the generation is the highest in Asia, responsible for 24.9 Mt followed by 12 Mt from Europe and 7.7 Mt from North America [86]. For this reason, it is a clear fact that the waste generation to waste collection rate is not balanced, which leads to a lot of e-waste ending up in landfills. Due to this, it is vital to plan effective collection routes for such waste streams and use the available resources for this cause. Moreover, designing, installing and establishing structures to recycle EV batteries and SES batteries is also important at early stages to face the rapidly growing markets of the same.

As a solution to this problem of collection, proper labeling can be identified. Providing information about the battery content, applications, or secondary applications on a label or in a source that can be easily accessible will be useful. Training personnel at dismantling facilities to identify batteries using labels or brands can also be an alternative.

3.3 Material Sorting

Sorting of spent LIBs to forward them to pretreatment is as complex as collection due to large mix of materials (different NMC-cathode batteries, LCO, NCA, LFP . . .). However, sorting is mandatory for LIBs before undertaking any further steps due to the same factor. According to the majority of authors, the most suitable sorting method for spent LIBs is categorizing them according to the battery chemistry [87,88]. Differentiated sorting of LIBs at the household level is a bit ambiguous and it is difficult to achieve a high collection rate. It would also require an additional workload from the consumer end which is highly unlikely to be obtained in this case. Alternatively, sorting of spent batteries can be done at the recycling facilities in the reverse logistic process. Yet, this would increase the transportation costs for sorted batteries as most battery recycling facilities are not designed to receive all types of waste batteries. As an answer for this, establishment of consolidated treatment facilities with different recycling routes for a range of battery types can be put forward. The cost for such plants would be high and not economically feasible to achieve through the private sector. In contrast, scattered or partitioned recycling facilities are ideal to overcome the complexity of the material mix. For instance, separated pretreatment plants can handle the preliminary steps of the recycling routes for all

types of batteries. Sorting of the batteries, separating of the casing, discharging the batteries and separation of battery modules can be some of the steps involved in a pretreatment facility. Afterwards, sorted and partially treated battery types can be forwarded to other facilities for further treatment and recycling. This can reduce the high cost involved in a single treatment plant and can enhance the total efficiency of the recycling process [84,87].

While sorting is an essential part of the pretreatment process, identifying the battery chemistry can only be done through a laboratory analysis. So, appropriate labeling for the battery from the manufacturer can be useful in sorting. The labeling can contain the essential details of the battery such as battery chemistry, date of manufacture, name and location of the manufacturer and application area of the battery, for instance. Through these details, the sorting process can be performed effectively, safely and reliably. Moreover, it can save resources involved in laboratory analysis [84].

Current battery labeling practices in the EU and in the USA only instruct how to handle and dispose batteries. For example, it provides instructions to not dispose of the spent battery with household waste. Moreover, availability of metals such as Hg, Cd and Pb will also be noted in the labeling [89].

A new set of labeling requirements was published by the EU commission in 2020 with repealing directive 2006/66/EC and amending Regulation (EU) No 2019/1020, also known as the EU battery passport and electronic information exchange system. Though the directive came into effect in January 2022, a set of deadlines have been implemented for adaptation of different objectives. Accordingly, by 1st of January 2026, all the batteries that enter the EU market will register in an online electronic exchange system where the public can access and refer to all the information about the battery. Moreover, there will be engraved or printed QR code which will indicate information about battery lifetime, charge capacity and presence of hazardous metals. The QR code will be linked with the battery passport where online traceability and management of the battery can be implemented. Through the identifier, the online digital file of the battery will be frequently updated by the economic operators of the battery throughout its lifetime. In addition, it will include information about the status of the battery, repairs or repurposing done. Moreover, the QR code labeling will also be linked with carbon footprint declaration of the battery entering into force on 1 July 2024 and carbon footprint performance, starting from no later than 1 January 2026 for industrial or EV batteries with a capacity above 2 kWh. In addition, effective from 1 January 2027, the percentage of

availability of recovered Li, Co, Pb and Ni in the battery with the set guidelines must also be provided along with other active minerals in the battery [35,90].

Compared to the EU, the USA has no dedicated rules applied to labeling of LIBs for the purpose of sorting. Instead, rules and regulations for normal battery labeling will take effect on LIBs as well. Accordingly, batteries must contain information about the battery type (Ni-Cd or Pb-acid) which will be helpful in disposing and recycling. Further, recycling symbols must be shown on the battery. However, specifically LIBs in the USA should contain an additional label for transportation safety purposes. This label will be useful in obtaining certificates for safety tests and provide information on packaging and transport volume limitations [36,37].

China, on the other hand, has imposed labeling guidelines for LIBs with the Interim Provisions on the Traceability Management of Power Battery Recovery and Utilization of New Energy Vehicles in 2018. According to this measure, a platform should be maintained to trace the entire lifecycle stages of the LIBs that enter the market. The platform will provide information about production, use, disposal, recycling or repurposing of the LIB in question [43,91]. This interim measure will act like the battery passport decree in the EU.

In summary, an effective collection of spent LIBs is mandatory for better recycling outcomes. Optimum use of resources and new technologies for collection of EOL LIBs is ideal to match the rising demand of EV market. At the same time, decentralized pretreatment plants for waste LIBs could be beneficial in enhancing sorting, discharging and dismantling. Therefore, sorted, pretreated LIBs or battery parts can be forwarded to dedicated recycling and recovery facilities. Policies play a vital role as a motivational factor for recycling of LIBs. Proper establishment of policies can considerably increase the efficiency of recycling and recovering capacities.

3. Pretreatment

LIBs have a complex structure and chemistry to facilitate Li ions to move from anode to cathode and from cathode to anode in their discharging and charging cycles, respectively [92]. Pretreatment is responsible for dismantling this complex structure so that recovery steps will be easy to apply. Hence, discharging and case removal must be taken care of as the preliminary steps. Then, safe dismantling of the modules to active materials, elimination of organic adhesive and removing the impurities must be applied to facilitate the recovery later.

4.1 Discharging and Dismantling

Spent LIBs for recycling can have a minor amount of charge left. This can cause sparks during the dismantling process and can ignite because of short circuiting as well as free radical oxidation [92–94]. Furthermore, in manual dissembling of the battery, which can take place in laboratory studies, explosions can take place as the free Li can oxidize by the atmospheric air [95–97]. Accordingly, the remaining charge must be drained before the battery moves into any other recycling steps. This can be done mainly in three methods, electrolytic discharge (using a salt solution), ohmic discharge (using an external circuit) and cryogenic discharge (using liquid nitrogen or in vacuum atmosphere).

Firstly, in laboratory experiments, electrolytic discharge is common, and the use of different salts can be seen with a variety of pros and cons [98]. One study has incorporated different salts of sodium (Na^+), potassium (K^+) and ammonium (NH_4^+) cations to evaluate methodological feasibility and the quality of the outcome in discharging LIBs. The study shows that using halide salts (Cl^-, Br^- and I^-) for discharge can cause severe damage and corrosion and can permeate water into the battery, which can lead to safety issues. However, according to the same study, the use of alkali metal salts (PO_4^{-3}, CO_3^{-2} or SO_4^{-2}) does not cause corrosion and is safe for industrial use [98]. In contrast, in another study, it was concluded that Na_2SO_4 cannot provide significant discharge (26.1% in 20 h) for LIB while NaCl gives the best discharge capacity (100% in 24 h) with the shortest time span [99]. Nevertheless, using salt solutions for discharging is much more appropriate for lower voltage batteries according to Li et al. (2016) [100]. Further, discharging the batteries with salt solutions can cause contamination with internal battery material and make it complicated for further recoveries, or at least reduce recoverable material content or the value of it.

Secondly, the use of ohmic discharge is also a popular method in laboratory scale. Nan et al. (2005) used ohmic discharge to drain a spent LIB. The study incorporated a stainless-steel container with a mechanical stirrer along with water and electrolytic iron powder inside. The spent battery was immersed in water and stirred for 30 min to achieve a full discharge [101]. The same method was adapted by Gratz et al. (2014) to achieve a comparably similar discharge rate [102]. Thirdly, in some studies, cryogenic discharge has been used to drain the remaining charge of the LIB. The studies used liquid nitrogen or a vacuum atmosphere to carry out the process. However, this method is unpopular due to unsafe work conditions and high costs

involved in establishing as well as maintaining very low temperatures compared to conventional discharge methods [97,103,104].

Due to difficulty in applying salt base discharge industrially, uncertainty (no optimization) involved in ohmic discharge and high cost in cryogenic discharge, mostly industrial-scale recycling follows shredding of the spent battery under a protected environment. This can reduce the cost of the recycling process as well as the complexity of the process. For an instant, Retrieve Technologies (Toxco) undertook the dismantling of the battery along with a water spray or nitrogen gas spray (or both) [105]. Another possibility is using CO_2 atmosphere for shredding, which can be seen in Batrec Stores [106]. Using an inert gas (argon or nitrogen) atmosphere is also possible for shredding to prevent oxidizing of Li while shredding [107]. In addition, methods like Umicore's UHT furnace do not need discharge of the battery as they skip dangerous steps such as shredding [108]. These technologies are discussed broadly under the dismantling section.

In a practical approach, as aqueous salt affects the quality and the quantity of the recoveries, less corrosive or non-corrosive salt would be ideal for discharging the LIB as well as receiving stable products. In contrast, using corrosive salts can even lead to the production of HF after the contamination of trace amounts of water with electrolyte material [100,102]. In addition, discharge of LIB using ohmic discharging needs further optimization to determine its discharging rates and economic performances. As shown by previous studies, excess discharging of the battery can adversely affect the material recovery from spent LIBs [103,109]. In addition, applying ohmic discharging at industrial levels can cause extra economic difficulties such as investments and maintenance issues. However, as the bright side of the ohmic discharge, it will be a benefit if one can utilize the electricity discharged from the battery in another application (energy recovery). Lastly, cryogenic discharge has limited application in the field and needs higher capital to apply industrially. A summary of discussed discharged methods along with their pros and cons is shown in Table 2.2.

Table 2.2 A summary of discharging methods for LIBs.

Discharge methods	Condition	Effects	Advantages	Disadvantages	Ref.
Salt solution-based discharge	10wt% NaCl	15% for 1 hr. 71.96% for 6 hr. 100% for 24 hr	Cheaper, simple, and efficient	Can corrode, safety issues (Cl_2 emission).	[98-100]

	5 wt% NaCl	9% for 1 hr. 88% for 24 hr.	No corrosion, simple	Time consuming	[99]
	Na_2SO_4 saturated solution with Fe	100% for 24 hr	No corrosion and emission of Cl_2	Time consuming	[98]
	10 wt% Na_2SO_4 with stirrer	26.31% for 20 hr.	-	Time consuming	[98]
	10 wt% $FeSO_4$ with stirrer	75% for 8 hr.	Relatively efficient	Impossible without a stirrer	[98]
	20 wt% $Zn_2(SO_4)_3$ with stirrer	37.5% for 20 hr.	-	Time consuming	[98]
	10wt% Na_2SO_4	1.16% for 24 hr	-	No significant discharge	[99]
	2g/L ascorbic acid and 0.8 mol/L $MnSO_4$	0.54 V for 8 hr.	Gentle discharge	Costly	[110]
	0.8 mol/L $FeSO_4$	1V for 2 hr.	Eco friendly, efficient discharge	Costly	[111,112]
Ohmic discharge	Water and electric Fe powder used in stainless steel container with a stirrer	100% for 0.5 hr.	No corrosion, highly efficient	Complex method	[101]
	Water and Fe scraps used in stainless steel container with a stirrer	Below 2 V after 4 hr.	Efficient	Complex method	[102]
Cryogenic discharge	Dipped in Liquid nitrogen (-196 °C) for 5 min.	100% for 5 min.	Efficient discharge, No corrosion, safe	High cost, cannot apply in industrial scale	[103]

Most of the laboratory-scale studies use manual dismantling using screwdrivers, pliers, bolt cutters, saws and pneumatic torque wrenches with sufficient protective measures [99]. However, not many publications can be found about the manual methods adopted [113,114]. Manual dismantling can cause several safety issues and environmental impacts. Some studies reveal that releasing volatile organic compounds is possible throughout the dismantling process [100]. Dimethyl carbonate and tert-amylbenzene have been identified as two major gasses that emit from dismantled batteries. Manual dismantling can be done under a fume hood or using a ventilating pump to reduce the environmental impact. However, it still poses a threat to human safety. To overcome these issues, semi-automated dismantling methods can also be seen. These studies have used manual methods to remove the housing prior to the discharge and mechanical

methods to dismantle the battery cells [114]. In fact, industrial-scale applications cannot use manual methods for many reasons such as inefficiency, safety issues, intense use of human labor and existence of different battery designs. So, mechanical methods are much preferable over the manual methods.

4.2 Mechanical Treatment

Mechanical treatment involves different aspects of LIB pretreatment. The method acts as a dismantling method, surface modification method, separation method or a combination of two or all those mentioned.

Li et al. (2019) proposed an automated comminution mechanism for pouch type LIBs which is known as Z-folded electrode separator (Figure 2.3a). The method proposed does not use destructive forces; instead, it uses a specialized tool set to unwind the z-folded separators and feed it. The tools will then scrape off the electrode materials on both sides of the separator [115]. However, most of the mechanical dismantling uses heavy destructive forces such as crushing or grinding to dismantle the battery as briefly discussed under discharge. This dismantling is often useful for further treatment processes such as hydrometallurgical extractions. For instance, the BATENUS process which is identified as the first hydrometallurgy process to be used in a large-scale battery recycling facility, uses shredding of a mixture of batteries in a gas-tight unit [116].

Pinegar et al. (2019) reported that the Recupyl process for waste battery treatment uses crushing of waste batteries in two steps. In the first step, the process used a low- speed rotary mill, and in the second step it used a high-speed impact mill to crush the materials [117]. The Li-Cycle process, which came into action in 2021, also uses a two-step process to recover valuable metals from LIBs [118]. The process uses a “spoke shred” to crush the waste batteries without discharging and obtain the black mass. Then, the recovered black mass will be refined using the step called “hub refine” (hydrometallurgical method). Another experimental recycling process for treatment of a mixture of Ni metal hydride, Li-ion and primary Li containing batteries adopted a two-blade rotor crusher and hammer crushing for crushing purposes. In this process, the two-blade rotor crusher was fed first without a sieve and the hammer mill crusher was fed secondly, using a 5 mm sieve. In comparison, the same study used only two-blade rotor crushers for double crushing of the same material. The study concluded that the highest amount of electrode powder was received when using two-blade rotor crushers followed by the hammer mill crusher [119].

Zhang et al. (2013) compared performance of wet crushing (Figure 2.3b) and dry crushing (Figure 2.3c) using an LCO cathode LIB. In wet crushing, a blade crusher was used while introducing water into the crushing area. The watery medium carried the crushed particles through the sieve as a slurry. In contrast, the dry crushing used two stages, firstly with a shear crusher and secondly with an impact crusher. Products from the wet crushing appear to be finer due to the friction caused by rubbing off broken pieces while moving in a slurry. Further, finer particles are hard to recover and might be lost with the flow. However, dry crushing resulted in releasing electrode material from Cu and Al foils without crushing the current collectors into finer particles [120]. The same authors also used this dry crushing method to characterize the spent LIB active materials and to introduce effective mechanical methods in recycling spent batteries [121]. It was identified that shear crushing is responsible for breaking the metal cover of the module and impact crushing is responsible for selective crushing of electrode materials after sieving out Cu and Al parts.

A planetary ball mill is another dismantling technique that was used by several scientists to enhance the leaching efficiency in hydrometallurgical recycling routes [122–124]. Guan et al. (2017) proposed a novel mechanochemical process to enhance the leaching efficiency of Co using a ball mill. To understand the mechanochemical process clearly and due to the interference, that could occur from other impurities, first they used pure LCO powder for the extraction of Li and Co. The use of planetary ball mill is responsible for making the powdered form of the cathode material (LCO) with the help of Fe powder, while HNO3 was used for the dissolution process. It was established that mass of Fe available, rotational speed and milling time promoted the recovery of Co, and reduction of particle size, increase in surface area and changes in crystal structure promoted the recovery of Li [125].

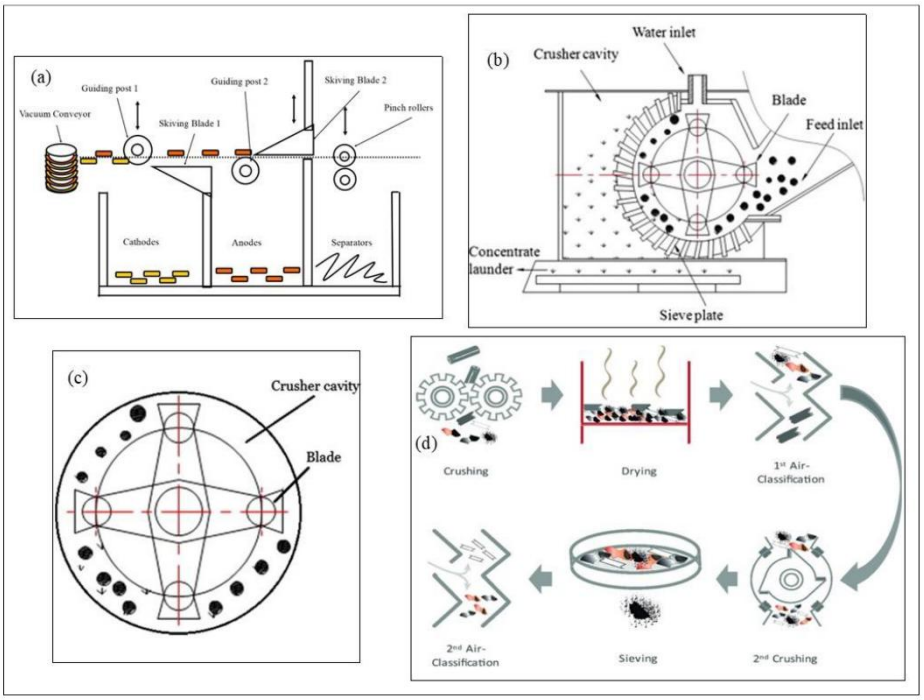

Figure 2.3 Summary of dismantling methods (a) Schematic Z-folded electrode separator [115], (b) Sketch of wet impact crusher [120], (c) Sketch of the dry impact crusher [121], (d) Process steps of the investigated recycling process with varied 2nd crushing [94].

Some studies were undertaken to study how mechanical dismantling and sorting can be affected on a mixture of four different LIB types. LCO, LFP, LMO and NMC battery types were used in studies with a commercial granulator for shredding (7.5 mm pieces) and a sieve set for sieving. The authors claim that the pretreatment process proposed is not energy-intensive and needs low capital to establish [126,127]. Barik et al. (2017) designed a single-shaft shredder with a shear-type cutting to reduce the size of dismantled pieces below 10 mm. The authors in this study focused mainly on wet crushing of Co and Mn-containing cathode LIBs at 30 ◦C. Then, the crushed materials follow flotation and sieving stages. Water in the process acts as a scouring agent as well as a cooling agent. Flotation separates the plastics from the remaining materials and the sieving separates the Cu and Al current collectors from the electrode materials [128].

Diekmann et al. (2017) studied how the second crushing step (Figure 2.3d) affects the yield of black mass (graphite electrode material) in the LithoRec process. The LithoRec process was designed to reduce the environmental impact of the battery recycling process while achieving high efficiency in material recovery from NMC type batteries in EVs and hybrid vehicles [129]. The LithoRec process uses a six-disk-rotor in a converted mill to crush the incoming material.

In Diekmann et al.'s (2017) study, a second mild-crushing step was added using a cutting mill with a 10 mm screen. It was established that old batteries tend to emit higher gas mass (electrolyte solvents and CO2) than recently disposed batteries during the first crushing step. Additionally, employing the second crushing step increased the yield of the black mass by 15% without adding any impurities from current collectors [94,129].

Grinding flotation is another method proposed by authors for dismantling and separation of LIBs. He et al. (2017) used this method to sort LCO cathode material and anode material from a mixture. Authors separated the ground electrode mixture by flotation assisted by Fenton reaction (Figure 2.4a). The result suggests that optimum conditions for successful separation are Fe2+/H2O2 ratio at 1:120, and the liquid to solid ratio at 75:1. Investigation concluded that modification of electrode material by Fenton reagent helped it to regain the original wettability of LCO cathode material and graphite [130]. Yu et al. (2018) also used a grinding flotation method to separate LCO-type cathode material and graphite of LIB (Figure 2.4b). An impact crusher was used to lower the particle size of the cathode and anode materials down to 0.075 mm. The obtained electrode mixture was then ground using a hand Groover for a range of times for optimizing. The result of the study suggests that 5 min of grinding can produce a higher grade, concentrated LCO (sinks) and graphite (floats) separation with yields of 97.13% and 73.56%, respectively. Further analysis on morphology, elemental chemical states and elemental distribution suggests that grinding eliminates the lamellar structure of graphite enhancing its hydrophobic surface and fric- tion removes organic coating of LCO, enhancing its hydrophilic structure. This makes a significant difference in the surface wettability, leading to the separation of electrode materials [131].

Cryogenic grinding of dismantled LIB was also studied to recover cathode active material (Figure 2.4d). The study was carried out with analysis and revealed that yield strength, tensile strength and impact strength of current collector significantly increased at low temperatures. The study also identified that the glass transition temperature of the PVDF binder is at around 235 K. Due to these properties, at very low temperatures, the current collector strengthens up and the organic binder fails, giving a chance for the selective grinding of cathode material and peeling off electrode materials. The study concluded that peeling efficiency of the electrode material can be enhanced by 62.26% with 5 min low temperature pretreatment and 30 s cryogenic grinding [132]. In extension, suggestions were given to integrate cryogenic grinding with flotation to separate cathode and anode material by Liu et al. (2020) [133].

Wuschke et al. (2019) studied the safety issues in mechanical crushing of LIBs. Further, correlation between the material composition of the battery and the specific energy needed for dismantling the battery was also investigated during the study. Low speed axial-gap rotary shear was used as the primary crusher to crush the LIB cells (coarser parts) and radial-gap rotary shear was used as the secondary crusher to crush the resulting parts (finer parts) for the experiment. Outlet grid size in the secondary crusher and the residence time of the materials in the crushing chamber were used as variables to adjust the mechanical energy. An infrared camera was used to detect the thermal energy released during and after the crushing of LIB in the chamber with thermographic imaging (Figure 2.4c). The batteries used in the experiment had a defined state of charge (SoC). The investigation reported that the SoC has a linear correlation with temperature difference as per the results; a 75 ◦C temperature difference was recorded with 10% SoC and 27 ◦C was recorded with 2% SoC. Hence, a higher residual charge can increase the risk of explosions or ignitions and create safety issues. Moreover, the study also evaluated the specific energy requirement for crushing the battery cells and their parts based on the composition of it. The results suggest that the least energy was consumed for crushing the electrode materials of anodes and cathodes and highest energy was used to crush down the elastic–plastic housing of the battery and the viscous–plastic separator foils. The study concludes that separation of housing materials prior to the crushing can lower the energy usage for crushing [134].

Widijatmoko et al. (2020) integrated “attrition scrubbing” (AS) to liberate the cathode active material from LCO type LIBs. Attrition scrubbing is a method designed to promote collisions and shearing action between particles to increase the friction on the surface and make fine particles. For the investigation, a 1000 rpm constant speed AS was used, and silica sand was incorporated as the abrasive material. The study compared cathode material liberated from the single stage crushing using a cutting mill to a multistage cathode material liberation using AS after the cutting mill. The study concludes that employing AS in cathode active material liberation can increase the yield significantly compared to the poor liberation of the same when used only in the cutting mill. The results show 80 wt% LCO particles liberation in the size fraction of <38 mm with 7.0 wt% of Al and 6.1 wt% of Cu [135].

Wet agitation of composite cathode material that was liberated from Al current collector was investigated. The study was carried out to assess the possibility of de- agglomeration of cathode electrode material from the composite. The wet agitation was done in a blender that produces industrial scale shear force. The cathode material was successfully de-agglomerated due to the loosening of PVDF binders from the cathode composites (Figure 2.4e) [136].

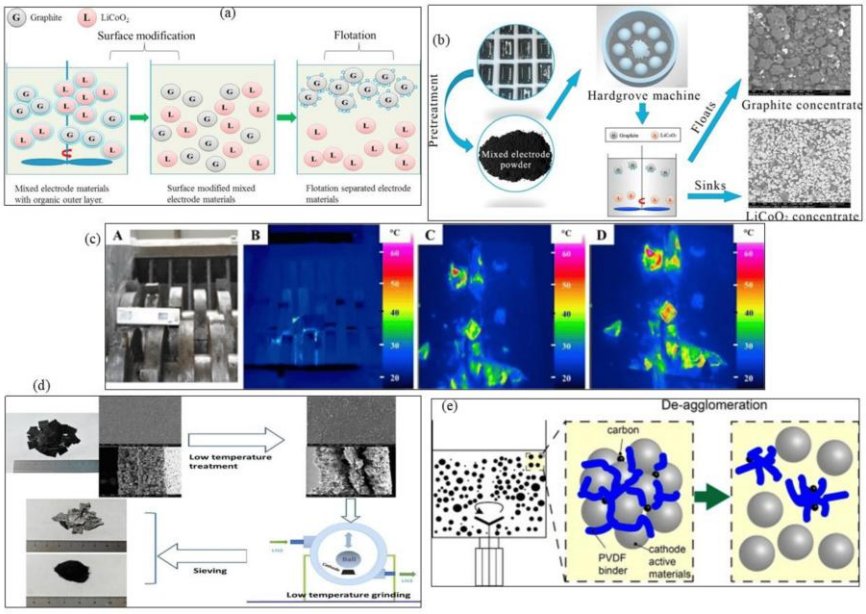

Figure 2.4 Summary of dismantling methods (a) Schematic diagram for graphite and LCO separation by Fenton reagent-assisted flotation [130], (b) Flow chart of grinding flotation to recycle LiCoO2 and graphite [131], (c) Usage of infrared camera to detect the thermal energy released during and after the crushing of LIB in the chamber with thermographic imaging [134], (d) Flow chart of cryogenic grinding and recovery of cathode action material [132], (e) de-agglomeration of cathode composites using wet agitation [136].

4.3 Sieving

Sieving has been used as a method for classification after a comminution or mechanical dismantling step since the first use of battery recycling. In LIB recycling, sieving is an important industrial step. In one of the studies undertaken by Shin et al. (2005), it was found that crushed particles from LCO LIB type can be classified into two groups using 106, 200 and 850 µm, with the finer fraction received from 850 µm being LCO particles and graphite, and the coarse fraction being plastic wrappers, metal casing materials, Al and Cu current collector materials and separators [137]. In another study, LCO-based LIB was ground to powder and sieved using 2, 1, 0.5, 0.2, 0.25 and 0.125 mm vibration-aided sieve set. The finer fraction resulting from the 1 mm sieve accumulated higher fractions of cathode metals and the coarse fraction mainly accumulated Al and Cu current collectors with 67% and 79% percentages,

respectively. Cathode metals contained in the finer fraction showed to be Li with 82%, Co with 81%, Mn with 88% and 62% of Ni [138]. Guimarães et al. (2022) have concentrated the NMC cathode after knife milling and sieving due to the removal of case and plastic separator. Despite the material losses (less than 2%), the concentration of valuable metals increased to less than 2 mm [93].

Li et al. in 2009 carried out an investigation to study the effect of the screen size of the sieve on the resulting recoveries from LCO-type LIBs. The study concluded that a 12 mm screen size would be much more appropriate than 2, 4 or 8 mm sieve sizes for the classification of the pulverized material from LCO. The results showed that 28.5% of Co could be found in the d < 12 mm with fewer impurities than the other sieve sizes [139]. Alternatively, particle size distribution in two different crushing methods (dry and wet) was studied using 2 and 0.25 mm opening sizes. The study used LCO-type LIBs, and the result suggested that d > 2 mm of wet crushing was given a 27.57% mass ratio, whereas dry crushing was given only 21.28%. However, 2 mm > d > 0.25 mm of wet crushing gave a lower fraction of materials (16.21%) compared to dry crushing (30.46%). The finest fraction of wet crushing was at 56.22%, whereas dry crushing had given about 48.26%. Accordingly, wet crushing has given a higher amount of finer and coarse particles and dry crushing contains normally distributed particle size arrangement [120]. Due to this reason, the authors studied dry crushing particle arrangement in a later study again using 2, 1, 0.5, 0.25, 0.1, 0.075 and 0.045 mm sieve sizes making eight distinctive groups. The study concluded that 0.25 mm gives 94.14% Al and Cu material in the coarse fraction, and the finer fraction gives a higher concentration of Co and graphite with 94.39% [121]. The same group experimented with how impact crushes affect the particle size distribution in LCO-type LIBs in a similar way using 1.4, 0.71, 0.5 and 0.2 mm aperture sizes. The findings suggested that electrode material mainly concentrated below 0.2 mm and a higher concentration of Al and Cu collector materials can be found above 1.4 mm aperture size [140].

Zhang et al. (2018) carried out sieving tests for LIB materials after pyrolyzing them up to different temperatures to study particle size distribution of the same. The tests were carried out for LCO-type batteries accompanied by a grinding step after pyrolyzing. A 2 mm sieve was able to keep a higher fraction of large metal casing pieces and pieces of separators on it while 0.25 mm sieve retained a higher fraction of Cu and Al particles from the current collectors with a fiber-like shape deformation. Below 0.2 mm fraction, scientists found the highest amount of electrode materials. Further, 500 ◦C was identified as the optimum pyrolyzing temperature, as

they gathered the highest amount of cathode electrode materials below 0.2 mm aperture. Concluding the study, the investigators showed that pyrolyzing aided the classification step by preventing electrode materials from making agglomerates and making it easier for particles to free from PVDF binders. A similar study that was carried out in 2021 using the same cathode type with less fraction of Ni and Mn confirmed that the highest liberation and accumulation of electrode materials can be achieved at 500 ◦C under a 0.2 mm sieve size [141,142].

Viececli et al. (2018) optimized the particle size for hydrometallurgical extraction of precious metals in electrode material. A grab shredder with a 6 mm bottom discharge sieve was used to shred the components. The d > 6 mm parts were mainly composed of plastic separator parts, Fe materials, and minor amounts of Al and Cu particles. Al and Cu materials in the coarse fraction were separated from the rest using magnetic and density base separation while the d < 6 mm part was introduced to another cutting mill with an aperture size of 2 mm discharge. The rest of the Al and Cu materials were separated as the coarse fraction and the minor fraction went for hydrometallurgical extraction. Three distinctive groups were identified: the coarse part where d > 6 mm, with 65% of Fe as it is harder to crush down; fraction 2 mm < d < 6 mm, mostly with Al and Cu materials (70%) from the anode and cathode and 22–28% of electrode materials; the finest fraction was d < 2 mm with an average of 70% electrode materials [143]. In a similar study, the leaching efficiency of Li and Co was studied under five distinctive particle size groups. The study incorporated 2 mm > d > 1 mm, 1 mm > d > 0.5 mm, 0.5 mm > d > 0.25 mm, 0.25 mm > d > 0.125 mm and d < 0.125 size fractions, where LIB materials underwent two step crushing, magnetic separation and vibro-sifting. The coarser fraction where d > 2 mm was not used for leaching as it mainly contained Al and Cu foil particles [144].

A novel approach was proposed by Yu et al. (2020) to separate impurities such as Al and Cu from electrode materials. Traditional methods include fine sieving of crushed materials or alkali leaching of the same, whereas the new method replaces these with a combination of sieving and reducing. Precisely, the method involved mild sieving of materials using a 4 mm opening size followed by alkali reducing of the material using Al and Cu as reductants. The authors further mentioned that a mild strainer (4 mm) resulted in 6.30 wt% of Cu and 9.98 wt% of Al in the corresponding finer fraction where a higher fraction of electrode materials lies below the 0.5 mm strainer [145].

A wet agitation process was applied for recycling of used LIBs. Investigators used a blender to wet agitate the LIB cathode material, hence performing the liberation of cathode active

elements. Agitated material was then subjected to wet screening using 105, 74 and 37 μm aperture sizes. Particle liberation from the Al current collector was then assessed by froth flotation as the method provides a better judgment on the surface hydrophobicity. Above 85% recovery rate of cathode active materials was achieved with below 0.3% impurities while using repeated agitation [136].

Widijatmoko et al. (2020) carried out a series of experiments to study the material recovery efficiency of LCO-type LIBs. In one of the investigations, the effect of adding an additional attrition scrubbing step after the cutting mill to recover Al, Cu and Co was studied. The experiment also incorporated wet sieving of comminution particles under 212 and 38 μm screen sizes. Moreover, the investigators screened coarser particles ($d > 212$ μm) using dry sieving under 4750, 2360 and 850 μm again. Finally, the yield of three metal types was analyzed in each group received. Results suggested that Al and Cu distribution was not much affected by the additional attrition scrubbing step. However, the yield of Co was significantly enhanced from 11.4 wt% to 80 wt% in the finest fraction ($d < 38$ μm) with a lower concentration of Al and Cu (7.0 wt% and 6.1 wt%, respectively) [146]. The same group of scientists studied how dry milling aids the release of electrode materials from the current collectors using the same type of LIBs. In addition, the group made a comparison between old and new batteries to assess how the aging of LIBs affected the efficiency of the release of electrode materials. The study was able to identify four different categories based on how the electrode materials attached to the current collectors (Figure 2.5e Cat. 1 or 2) or released from the current collectors but attached to PVDF binders making agglomerates (Figure 2.5e Cat. 3 or 4). The four categories and the results are provided in the summary at the end of this section. However, the results are similar to most of the other studies that are listed above, providing more efficient liberation of electrode materials from the fine particles ($d < 38$ μm) in old LIBs. In contrast, new LIBs show much resistance to liberating electrode materials and are highly attached to current collectors and accumulated in coarser parts (Figure 2.5e Cat. 1 and 2) [135].

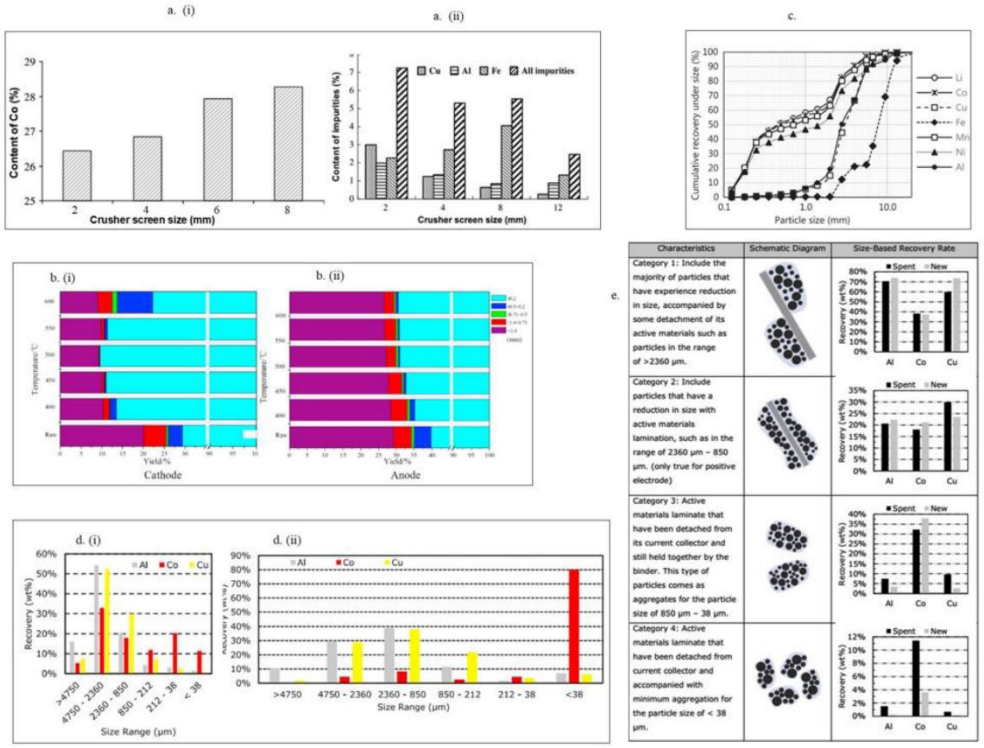

Figure 2.5 Summary of dismantling methods (a). The effect of the sieve size on (a(i)) Co and (a(ii)) the impurity content in the underflow products [139], (b). The particle size distribution of the crushed products at different pyrolysis temperatures: (b(i)) cathode and (b(ii)) anode [141], (c). Cumulative recovery of undersized particle of different elements [143], (d). Percentage recovery of different elements based on particle sizes: (d(i)) after crushing and (d(ii)) after an additional attrition scrubbing [146], (e). Characterization of liberated particles based on their sizes and age of the LIBs [135].

4.4 Dissolution

Dissolution can be used to dissolve or decompose PVDF binder that still exists in electrode materials after freeing from the current collectors. The summary of dissolution results reported in the literature is presented in Table 2.3. One solvent that is used widely in the literature for the dissolution process is N-methylpyrrolidone (NMP), which has solvent ability up to 200 g kg^{-1} and has a boiling point of 200 °C. Contestabile et al. (2001) used NMP to extract electrode materials (LCO and graphite) from the current collectors by dissolution for 1 h at 100 °C. The result suggested that Cu and Al recovered without any contaminants under said conditions by filtration of NMP solution [72]. Liu et al. (2006) experimented on N,N-dimethylacetamide (DMAC) to extract electrode materials from current collectors of LCO-type LIBs. DMAC has a solubility around 100 g kg^{-1}, a boiling point of 165 °C and is less expensive than NMC. The authors concluded that LCO electrode material can be separated from Al while keeping the

solid to liquid ratio between 1:4 and 1:5 [147]. N,N-Dimethylformamide (DMF) is another solvent that has a comparably low boiling point (153 °C) and it can be completely evaporated by heating it up to 120 °C for 12 h. As a result, Song et al. tried to extract cathode active materials from NMC and LCO-type LIBs using a combination of DMF and ethanol and heating it up to 70 °C [148–150].

In some of the literature, NMP and a range of other solvents have been used to extract cathode active materials from cathode current collectors utilizing ultrasonication [151–153]. Conclusions are made about the dissolution rate in different solvents. NMP showed a 99% dissolution rate while other solvents (water, acetone, dichloromethane, and carbon tetra-chloride) achieved lower than 18%. Further, increasing the time of ultrasonication and temperature does not affect the dissolution rate of these solvents [151]. It is worth noting that using NMP accompanied by ultrasonication for a short time is more environmentally beneficial than the method proposed by Contestabile et al. in 2001. However, the authors recommended an additional stage of calcination at 750 °C for complete removal of PVDF binder from Al foil. He et al. (2015) studied solvents such as DMAC, DMF and N, N- dimethyl sulfoxide (DMSO) and ethanol accompanied with mild ultrasonication for the dissolution of PVDF from cathode material. The liberation efficiency (E) of cathode active material was evaluated against ultrasonication time, temperature, and power. The results showed that with 1:10 solid to liquid ratio and 60 °C, along with 30 min reaction time, the liberation efficiency was less than 10% when ultrasonication was not used. In spite of this, the liberation efficiency increased by approximately six times when ultrasonication was used with the same conditions. Further, peel-off efficiency increased according to the order of ethanol < DMSO < DMF < DMAC < NMP. The highest liberation efficiency of 99% was achieved by NMP when optimized conditions (70 °C, 240 W and 90 min) were used. The authors elaborated that the highest liberation was caused by rapid dissolution of PVDF aided by ultrasonication [152].

Nayaka et al. (2018), performed an experiment with a mixture of mild organic acids (citric acid, tartaric, and ascorbic acid) to recover LCO cathode powders. The study reported that 100% of Li and 90% of Co were dissolved with a 6 h reaction time at 80 °C. The experiment also showed that Co (II) can be recovered as Co (II)-Oxalate with selective recovery [153].

He et al. (2020) suggested a method for selective liberation of LFP cathode active material from a combination of LMO, LCO, $LiNi_xCo_yAl_zO_2$ (NCA) and NMC LIB cathode types. The methodology uses a method which involves reaction of the mixture of sulfide. Since sulfide

reacts with Fe in LFP cathode active material, the crystal structure of the same will be pulverized, making it liberate from the rest. Liberated material can be categorized using a sieving step. Moreover, the article explains that the remaining PVDF binder from the Al foil will be destroyed by the micro-explosions forced from hydrogen available in water. It is mentioned that the liberation efficiency of LFP cathode active material was 100%, while others showed only 0.08% [154].

AlCl3-NaCl molten salt was used to peel off cathode active materials from Al foil by a group of investigators. The PVDF binder can be decomposed by AlCl3-NaCl molten salt when changing its phase from solid to liquid at around 153 °C. The phase change absorbs heat from the system heavily and that melts down the PVDF binder. The result shows that maximum liberation efficiency was achieved at 160 °C with 1:10 g mL^{-1} solid to liquid ratio and 20 min [155]. Zhang et al. (2014) used a strong carboxylic acid (trifluoroacetic acid (TFA)) with a relatively low boiling point (71.8 °C) to decompose polytetrafluoroethylene (PTFE) binders in NMC type LIBs. The best peeling-off efficiency was recorded with 1:8 g mL^{-1} solid to liquid ratio prepared using 15 vol% TFA solution. Further, the mixture was agitated for 180 min at 40 ◦C to obtain the optimum efficiency [121,155]. He et al. (2019) proposed a method to extract cathode active material from LFP and NMC type LIBs in the form of flakes without using acid or alkali solutions. The team was able to manufacture a special solution based on Na salts named Aquas Exfoliating and Extraction Solution (AEES) which can liberate both cathode and anode active materials with 100% efficiency. Al and Cu recovery efficiency were at 95.6% and 99%, respectively. The solution was able to weaken the mechanical interlocking force and coulomb force between the active materials and the foil for effective liberation [156]. Several results reported in the literature have demonstrated theoretically and experimentally that by removing around a 63.2 nm layer of Al foil from the cathode current collector, it is possible to weaken the forces that keep electrode materials together. So, electrode materials may be recovered with 100% efficiency and Al foil with 99% efficiency. A group of scientists used an alkaline solution to dissolve Al in LCO-type LIBs [101,102,157].

Table 2.3 Summary of dissolution methods.

Solvent type	Condition	Results	Remarks	Ref.
NMP	1 hour reaction at 100^0C	100% recovery of Al and Cu	LCO type LIBs, economically inefficient	[73]

DMAC	1:4 to 1:5 S:L ratio	Less recovery than NMP at optimum conditions	LCO type LIBs, Cheap and convenient	[147]
DMF + Ethanol	dissolution at 70^{0}C	Less recovery compared to NMP	NMC and LCO type LIBs, Cheap and convenient	[146]
NMP	3 min. ultrasonication at room temperature	99% recovery for cathode material		
Water Acetone Dichloromethane Carbon tetrachloride	3 min. ultrasonication at room temperature	less than 18%recovery	NMC type LIBs	[151]
DMAC DMF DMSO Ethanol NMP	dissolving with mild sonication 1:10 S:L ratio at 60^{0}C for 30 min.	Increased by 6 times when sonication was used than when it's not used according to; ethanol<DMSO<DMF<DMAC	Common LIB types	[152]
NMP	90 min. reaction time at 70^{0}C with 240 W sonication	99% recovery of cathode materials	Common LIB types	[152]
Sulfide Dissolved in water	at room temperature	100% selective liberation of LFP cathode materials	Beneficial when extracting LFP active materials from combination of LIBs available	[154]
$AlCl_3$-NaCl molten salts	20 min. reaction time at 160^{0}C with 1:10 S:L ratio	99.8 wt% liberation efficiency	Inexpensive and convenient method	[155]
15 vol% TFA	180 min. optimal agitation at 40^{0}C with 1:8 S:L ratio	High quality material recovery	NMC type LIBs with PTFE binders	[155]
AEES	Na based salt at room temperature	Active material 100% Cu 99% Al 95.6%	For LFP and NMC type LIBs	[156]
Alkaline solution (NaOH)	removing of 63.2 nm layer from Al foil	Cathode active material 100% Al 99%	LCO type LIBs	[101,102,157]

4.5 Thermal Pretreatment

Organic binders and electrode materials were often separated from the Al or Cu current collectors using heat treatment. Fouad et al. (2007) investigated the possibility of making γ-$LiAlO_2$ nanocrystals by heat treatment of LIB current collectors. According to the authors, the availability of nanocrystallite γ-$LiAlO_2$ along with Co_3O_2 and CoO on the surface of Al foil was observed through XRD and SEM analysis when heated to 800–900 °C for 2 h. However, the liberation efficiency of active material was not evaluated herein [158]. A comparative study conducted by Sun and Qui (2011) confirmed 100% liberation efficiency of LCO cathode material when the uncrushed LIB material was heated in a vacuum oven. Optimum experiment values were given as 600 °C temperature, with 30 min vacuum evaporation and 1 kPa gas pressure. Furthermore, the authors showed that when the temperature rises from 500 °C, the peeling-off efficiency increases. However, temperatures above 600 °C are not suitable for pyrolyzing experiments as Al foil becomes shredded into powders and this makes it harder to recover the active materials [159]. The peeling efficiency obtained by Sun and Qui (2011) was confirmed by Lu et al. (2013) in a similar study. They were able to resynthesize LCO-type electrode material by heating the discharged batteries up to 600 °C for 3 h in vacuum conditions.

In a closed loop recycling study, Kim and Shin (2013) reported the chemical perfor- mances of the recovered materials from LFP batteries with different pyrolyzing temper- atures. The study incorporated three different temperatures such as 400, 500 and 600 °C for comparison under a nitrogen atmosphere. The results show that the resynthesized materials have good cycling performance and capacity. Moreover, the cathode material treated at 500 °C showed a higher capacity than the rest. Authors confirmed that all the three temperatures were able to decompose the binders (containing sodium carboxymethyl cellulose and butadiene—CMC/SBR) fully, hence maximum recovery of cathode active materials [160]. In a similar investigation, a range of temperatures was used to liberate active materials by decomposing PVDF binders in scrapped LFP-type LIBs. The conclusions show that maximum recovery was achieved at 600 °C pyrolyzing for 1 h. Investigators confirmed complete decomposition of binders and conversion of Fe^{+2} to Fe^{+3} [161]. Sintering and solvent extraction methods were accompanied to recover electrode materials from NMC-type LIBs. The recovered materials were used to regenerate the cathode and their performances were investigated. In sintering, the cathode was scraped into 4 cm^2 pieces and heated for 2 h at different temperatures and was

then treated with a fast-stirring mixture and sieved with 400 mm aperture size. The results suggested that the maximum liberation of active mate- rials was recorded at 450 °C. However, solvent extraction was preferred to the sintering method as the sintering process added impurities (LiF) to the recovered materials [148]. Yang et al. (2016) studied a two-step process to recover materials from spent NMC-type cathode materials. The two steps involved heat treatment followed by acid leaching. As done by Song et al. (2013), authors cut the cathode active materials into 4 cm^2 pieces and heated the material under a nitrogen atmosphere. Thermogravimetric spectroscopy was analyzed to determine the thermal behavior of the materials. Results suggested that PVDF decomposition occurred around 475 to 500 °C. Furthermore, investigators showed that high leaching efficiency of Ni (98%), Mn (84%) and Co (99%) was achieved after the heat treatment as the elements are partially reduced [162].

In situ recovery of Li_2CO_3 was studied by incorporating three types of LIBs (LMO, LCO and NMC) by a group of scientists under vacuum conditions. A recovery rate of 81.9% was observed with the optimum conditions: 973 K roasting for 30 min with solid to liquid ratio of 25 g L^{-1}. The purity of Li_2CO_3 recovered was at a high level (99.7%) [163]. The same group of authors carried out another experiment to study in situ treatment of bulk LMO type batteries to recover precious materials. Firstly, electrode materials (cathode and anode active materials with binders) were mechanically separated from the bulk LIBs. Secondly, roasting treatment was carried out without the availability of oxygen. The authors identified that in situ conversion of MnO and Li_2CO_3 from electrode materials was possible at 1073 K roasting for 45 min under oxygen free atmosphere. Furthermore, it was identified that binder decomposition occurred at 573 K and conversion of electrode materials occurred at 1073 K [164].

The effect of pyrolysis temperature on ultrasonic-assisted flotation for the separation of electrode materials was studied by Zhang et al. (2018). The study was carried out on LCO-type batteries to recover graphite and $LiCoO_2$. Results showed that 500 °C pyrolysis for 30 min with N_2 atmosphere effectively decomposes the organic binders and higher liberation. Further, ultrasonication cleans the impurities attached to the electrode materials, hence increasing flotation. It was concluded that the new method can increase the separation of $LiCoO_2$ from around 75% up to more than 96% with a high purity (93.89%) [165].

The effect of mechanical crushing and pyrolysis for flotation separation of graphite and cathode active materials of LCO batteries was studied by the same group of scientists. The authors mentioned that poor flotation of electrode materials was caused by the binders and electrolyte

materials, and that at 150 °C all the electrolyte evaporates, and 15 min of pyrolyzing at 550 °C can effectively decompose the organic binders without causing any changes to the mineral structure of $LiCoO_2$. Hence, through the process, over 83.75% recovery with about 94.72% purity of the materials can be achieved. The purity of the material can be further enhanced (up to 98%) by two-stage pyrolyzing [166].

Wang et al. (2018) studied how the roasting temperature and roasting time affect the surface wettability of the electrode materials to recover through flotation treatment. Flotation of the electrode materials may be limited because of the organic layers around the crushed materials. The results showed that organic binders started to decompose into CO_2 starting from 355 °C and continued to give the highest decomposition rate at 490 °C. Further analysis concluded that the organic outer layer can be mostly decomposed at 450 °C roasting for 15 min without burning the graphite available. The authors confirmed that the original wettability of the materials was gained at this optimized value, giving the highest recovery through flotation. It is worth noting that the particle size was controlled at <0.25 mm throughout the whole process [167].

Microwave-assisted pyrolysis was studied to recover Ni, Co and Al from NCM-type LIBs as a comparison to conventional pyrolyzing at 600 °C. The authors established that microwave-assisted heating is 20 times faster than the conventional pyrolyzing methods. Moreover, the new method adds an extra degradation step to the traditional method which results in H_2 and CO. This step is aided by steam and dry reforming reactions assisted by the availability of Ni and Al. Further, high heating rates also contribute to this reaction. However, high heating can adversely affect the process as Al foil can melt by giving sparks, making it difficult to recover the intended materials. The study concluded that 360 °C is the optimum temperature for microwave-assisted pyrolysis, considering the evolving of toxic gasses, Al mass loss, heavy and light molecule production and active mass ratio yield [168]. Wang et al. (2019) achieved a much lower temperature to decompose PVDF binders assisted by CaO. The thermal decomposition of PVDF with and without CaO was studied using thermogravimetric analysis. It was found that organic binder decomposed around 400–500 °C when CaO was not used. However, PVDF could decompose at 300 °C when heated with CaO. The authors optimized the ratio of cathode materials to CaO amount to be 1:8, the optimum temperature to be 300 °C and the reaction time to be 10 min. With the optimized values, authors reached 97.1 wt% of cathode material recovery. Further, the investigators elaborated that the method proposed was

beneficial economically and environmentally [169]. A similar process was examined by Zhong et al. in 2022. This group of scientists used DMF to heat with Al foil that contained cathode active materials. The authors established that the use of DMF decreased the pyrolysis temperature from 550 °C to 450 °C, with an increase in active material yield from 61.53% to 98.93% with 2 h reaction time. According to the authors, higher recovery resulted from the microbubbles generated by DMF and enhanced decomposing of PVDF due to DMF availability [170].

Pyrolysis followed by physical separation was used to recover materials from LFP-type batteries. The method also recovered 99.91% of organic electrolyte with low- temperature evaporation. The authors tried to recover materials from pyrolytic slag using physical methods such as color sorting, flotation and high-pressure water cleaning. The highest peeling-off efficiency was recorded at 550 °C pyrolyzing for 2 h under N_2 atmosphere. The pyrolytic products received from the optimum conditions were found to contain aromatic long chain alkenes and light alcohols while the gaseous part contained light alkenes. The results showed that the investigators were able to recover 99.34% of Al, 96.25% of Cu and 49.67% cathode active materials through the proposed method [171]. Lombardo et al. (2020) tried to incinerate NMC-type LIBs under oxygenated conditions to decompose organic binders and electrolytes to recover precious materials. The authors tried to vary the heating temperature from 400–700 °C with different time intervals (30 min–90 min). Scientists were able to identify that 600 °C incineration for 90 min with air flow conditions can decompose the organic materials effectively resulting in gases and organic oil by-products [172]. Figure 2.6 shows the summary of thermogravimetric studies undertaken.

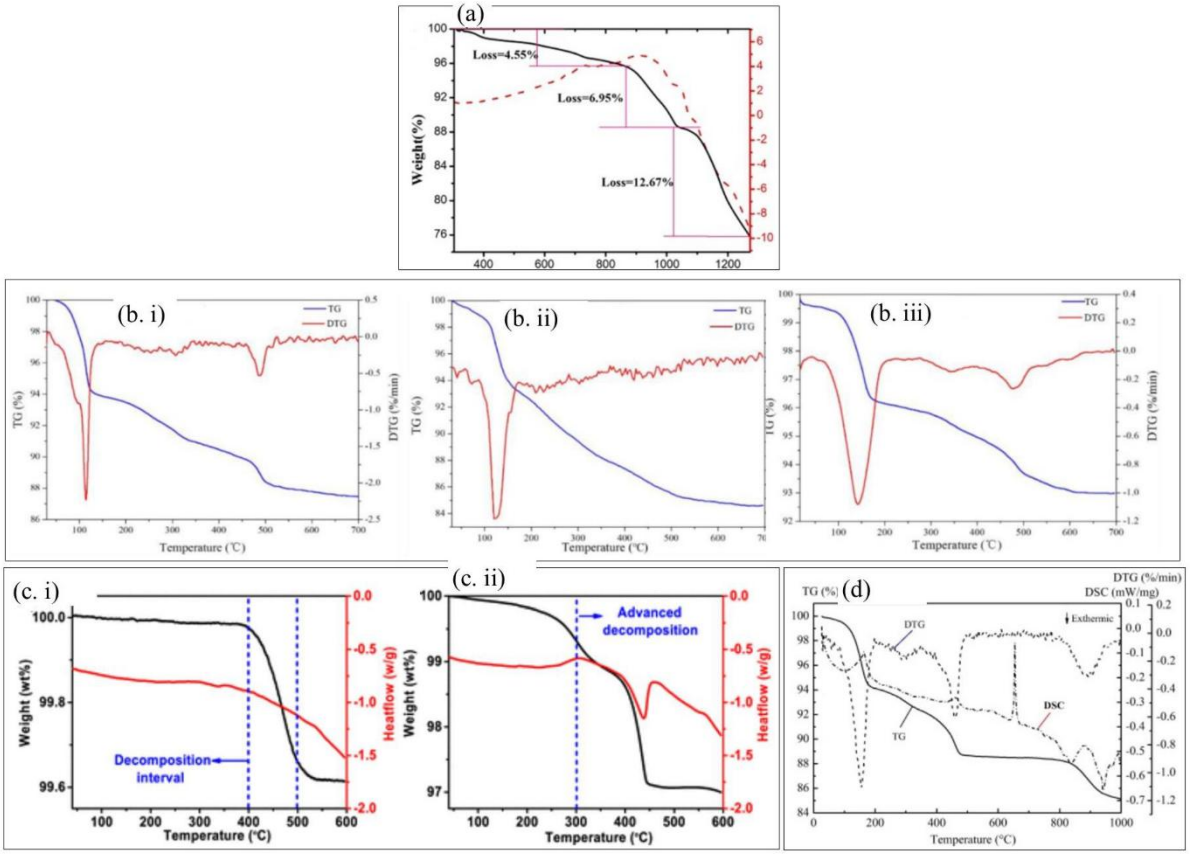

Figure 2.6 (a) TG-DSC analysis of LMO-type cathode material under N_2 flow [164]; (b) TG-DTG curve of LFP-type LIBs under air flow (b(i)) LCO with PVDF (b(ii)) graphite with SBR ((b(iii)) graphite with PVDF [166]; (c) TG-DSC curves of NCM type batteries under O_2 atmosphere (c(i)) Cathode electrode without CaO (c(ii)) Cathode electrode with CaO [169]; (d) TG-DSC curves of LFP type cathode materials under N_2 atmosphere [171].

4. Discussions and Conclusions

LIBs are one of the best technologies for energy storage and for providing a smooth voltage, which also makes it widely available in EVs as their energy storage device. The continuous growth of the EV industry with upcoming stringent environmental policies will continue to grow the demand for LIBs in the long term [28–31]. Manufacturing of LIBs requires huge amounts of virgin materials to be extracted from natural ores, which puts enormous stress on the environment directly and indirectly. Moreover, disposing of waste LIBs is also equally challenging as well. Further, improper disposal of LIBs will waste already extracted materials as it contains a lot of precious metals and non-metals. This is not only a waste of resources but also a threat to human sanitation and to ecological systems. So, there is no doubt that priorities must be given to extracting resource materials from spent LIBs.

LIBs can vary largely in their cathode electrode metal content, and slightly in anode electrode content. This imposes the biggest challenge in recycling LIBs in one single line [77–79]. However, their current collectors, casing materials and binding materials are mostly the same in different LIBs. This makes it possible to recover these common materials in one single pretreatment line. Pretreatment involves separating electrode materials from the rest of the battery components so the secondary treatment can recover the precious materials available in the electrodes.

Collection of LIBs is also challenging because most LIBs pass a hibernation period after their service as discussed under collection. This happens mostly with domestic electronic equipment. However, EV batteries are mostly given a second life after first use. Collection is further limited due to collection and sorting parameters such as type of battery, cathode material and manufacturer. Collection and sorting can be increased using proper labeling or using the QR code labeling proposed by the EU commission [91]. This will inform the collectors or handlers how to correctly sort the waste LIBs; however, it still depends on consumers' willingness to do so for most household equipment. For EVs, on the other hand, this method can elevate the collection and sorting efficiency, so high-quality secondary raw materials can be recovered in future. Though, since this decree comes into existence from 2026, these batteries will be added to the waste lines until 2046. Meanwhile, large amounts of waste batteries are expected to pile up soon after 2030 according to the discussed literature. Despite that, a decentralized pretreatment plan is a better alternative to overcome collection and sorting challenges. Since the sorting is not required for the common pretreatment line proposed, waste EV LIBs can be easily collected at car dismantling premises. This will ease the recycling process and a higher recycling rate can also be expected. However, this will be a trade-off between the quality of the recovered materials and the quantity of recovered materials.

A recent literature study conducted by Kim et al. [173] has given recommendations on the pretreatment steps to be involved in a pretreatment line. The article suggests that giving solutions for manual dismantling techniques is a must and that so far, it has not been addressed properly. Moreover, the article shows the importance of involving several mechanical dismantling steps in the line. Further, it suggests using dissolution or thermal treatments to decompose PVDF binders effectively. When designing the pretreatment line in this study, the recommendations of Kim et al. (2022) were also taken into consideration. Discharging EOL LIBs prior to dismantling is a widely accepted route [92]. However, most industrial lines skip

this step and use direct shredding or crushing [105–108,173]. Salt-base discharging is not possible to use in large industrial lines as it produces huge amounts of wastewater with toxic substances in it which make it difficult to dispose of after. Recovering energy from the batteries prior to dismantling is beneficial, but industrially, it is still difficult to apply. So, the most appropriate step would be to dismantle the LIBs without a discharging step under a safe environment. In this article, according to the literature review, we propose dismantling the spent battery in the presence of water spray and N_2 gas spray in the dismantling chamber which will be economical and easy to handle as per the current studies. Rate of N_2 and water spray should be decided upon the load of the line. In a common pretreatment line, a specialized unwinding and scraping-off tools as Li et al. (2019) suggested cannot be used, as this addresses only one type of LIB. However, two-step mechanical dismantling would be more ideal than using only one dismantling step as experimented by Diekmann et al., 2017, and suggested by Kim et al., 2022 [94,129,135,173]. The first dismantling can use a low-speed shear crusher or a granulator as a cheap and efficient dismantling step [126,129]. The first step crushing needs to dismantle the particles to be less than 10 mm in size according to the references used [126,127]. The very next step after the first crusher should be removing the plastic housing parts and separator foils. A flotation-based separation can be used to remove these light denser parts easily from the metal fraction. Given the efficiency and the ease of the method, flotation-based separation would be ideal although it produces a quantity of wastewater. However, since the water amount can be used for a longer period, the process would still be economical and environmentally friendly. An alternative method to separate the plastic fractions and separator foils is sieving or air separation [93], as these materials would not become fine particles during the first crush. Flotation separation efficiency for plastics is higher than the sieving as per the current literature [128]. The main reason for this is that plastic materials can be sieved using above 6 mm aperture size and the optimum particle size for first step crushing is below 10 mm [143]. Despite this, air separation can still replace density separation with closer efficiency.

The wet materials can be dried for several hours (3–5 h) with a slightly high temperature (around 60 °C) to reduce the moisture content before the next crushing step. However, using an air separator instead of a density separator can cut off the energy requirement for the drying step. The object of the second crushing step is to retrieve current collectors (Cu and Al) from electrode materials. Impact crushing, planetary ball milling and rotary shearing are the best options for secondary grinding as per the analyzed literature [129–131,134,135]. The output particle size of the secondary crushing needs to be much finer than the first crushing step,

approximately, below 2 mm according to the current literature examined [120,121,139]. Planetary ball milling is not very ideal in this case; it results in much finer particles as it uses Fe powder. In addition, this will add impurities for the next steps [122,124]. However, impact crushing seems to be a good candidate for this stage as suggested by many investigators through their studies [134]. The crushing time can be set to 20–30 s with 2000–3000 rpm [121]. Further, dry crushing is preferred over wet crushing given the disadvantages of wet crushing steps discussed by the previous literature [120]. Grinding is also a better alternative that can be accommodated in this step. However, the resulting material from grinding can be much finer, hence, the expected particle range would be different, and this can make complications in the next steps (sepa- ration) [130,131]. Accommodating another crushing step can result in materials that still contain electrode materials attached to current collectors through binders as per the latest studies [135]. Hence, removal of the same is important before the separation of current collectors from the electrode materials. Separation of said material after decomposing of binders will elevate the amount of electrode materials and the quality of the Al and Cu recovered at the next step.

For PVDF decomposition, two methods are at our disposal, mainly dissolution or heat treatment. Dissolution process either becomes expensive when NMP is used or results in poor dissolution if other materials (DMAC, DMF etc.) are used [73,147,149–152]. Heating also makes the process a bit expensive and can cause deterioration of Al if higher temperatures are used [159]. Due to these reasons, utilization of higher temperatures or dissolution is not ideal though Kim et al. 2022 considered them to be the best options. However, lower temperature cannot cause the decomposition of PVDF binders as the organic binders are thermally stable up to 450–500 °C [159,164]. So, the best option would be to use CaO to heat with the ground materials as suggested by Wang et al. (2019). Accordingly, the next step would be to heat the ground material with CaO under atmospheric air flow up to 300 °C for 30 min as per the optimized values by the same author. This step will further reduce the toxic emissions to the environment along with requiring less energy use. This will ensure the decomposition of available organic binders before going to the next stage. This step can be considered as an optional step if poor quality material separation is preferred. Then, simply sieved metallic parts can be refined using a flotation-based trial. However, this would produce low-quality output material and high-energy intensive steps may have to be employed in secondary treatments. Furthermore, resulting Cu and Al may contain higher fraction of PVDF binders and can emit toxic gases (e.g., HF) when purifying further. Heated material can be sieved to separate the

current collectors from the rest of the electrode materials. The highest separation efficiency for Al and Cu can be achieved using a 0.25 mm size aperture size with slightly inclined surface that is set for 30–45 s retention time of sieving [121,141,142]. Further, this sieving step can accommodate vibration-supported sieving to maximize the electrode material separation efficiency. Recovered Al and Cu can be forwarded to corresponding treatment plants to make metal ingots as EoW. Electrode materials need to be forwarded to a washing step to remove the remaining CaO and CaF_2 from the previous steps [169]. Electrode materials received from this process can be separated into the cathode active material and anode active material using a flotation chamber. Since the surface of the recovered material is mostly enhanced during the previous steps, flotation should be able to be carried out only with bubbles or with small quantities of modifiers and frothers [131]. Since grinding can enhance the hydrophobic nature of graphite in electrode materials and decomposition of organic layers enhances the hydrophilic nature of cathode active materials, the flotation would give better efficiency in separating the electrode materials [131]. Finally, the recovered material can be dried at 60 °C for several hours (3–5 h) and can be sent to secondary treatment facilities to recover precious metals available in it. As per the reviewed past works, the outcome will recover above 98% of electrode

materials and current collector materials. The summary of the proposed method is given in Figure 2.7.

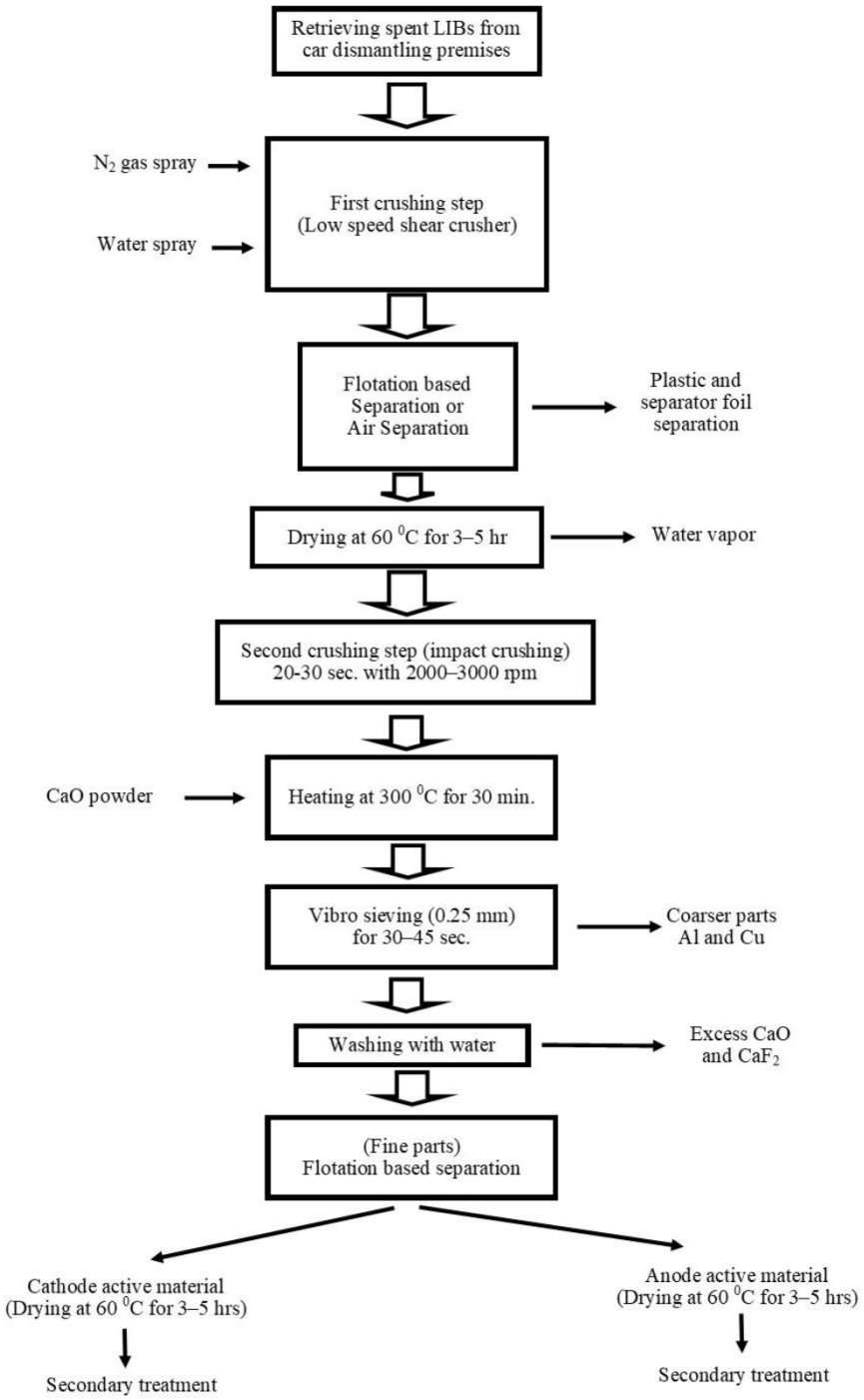

Figure 2.7 Proposed pretreatment line for LIBs.

References

[1] IEA. World Energy Outlook 2020. Available online: https://www.iea.org/reports/world-energy-outlook-2020 (accessed on3 January 2023).

[2] European Commision. Directive (eu) 2018/2001 of the European Parliament and of the Council. 2018. Available online: https://eur-lex.europa.eu/legal-

content/EN/TXT/?uri=uriserv:OJ.L_.2018.328.01.0082.01.ENG (accessed on 3 January 2023).

[3] BP. BP Statistical Review of World Energy 2020. Available online: https://www.bp.com/en/global/corporate/news-and- insights/press-releases/bp-statistical-review-of-world-energy-2020-published.html (accessed on 3 January 2023).

[4] Schmuch, R.; Wagner, R.; Hörpel, G.; Placke, T.; Winter, M. Performance and Cost of Materials for Lithium-Based Rechargeable Automotive Batteries. *Nat. Energy* **2018**, *3*, 267. http://doi.org/10.1038/s41560-018-0107-2

[5] Placke, T.; Kloepsch, R.; Dühnen, S.; Winter, M. Lithium Ion, Lithium Metal, and Alternative Rechargeable Battery Technologies: The Odyssey for High Energy Density. *J. Solid State Electrochem.* **2017**, *21*, 1939–1964. http://doi.org/10.1007/s10008-017-3610-7

[6] Armand, M.; Axmann, P.; Bresser, D.; Copley, M.; Edström, K.; Ekberg, C.; Guyomard, D.; Lestriez, B.; Novák, P.; Petranikova, M.; et al. Lithium-Ion Batteries—Current State of the Art and Anticipated Developments. *J. Power Sources* **2020**, *479*, 228708. http://doi.org/10.1016/j.jpowsour.2020.228708

[7] Qiao, H.; Wei, Q. 10-Functional Nanofibers in Lithium-Ion Batteries. In *Functional Nanofibers and Their Applications*; Wei, Q., Ed.; Woodhead Publishing: Sawston, UK, 2012; pp. 197–208, ISBN 9780857090690.

[8] Baars, J.; Domenech, T.; Bleischwitz, R.; Melin, H.E.; Heidrich, O. Circular Economy Strategies for Electric Vehicle Batteries Reduce Reliance on Raw Materials. *Nat. Sustain.* **2020**, *4*, 71–79. http://doi.org/10.1038/s41893-020-00607-0

[9] IEA. The Role of Critical Minerals in Clean Energy Transitions. 2021. Available online: https://www.iea.org/reports/the-role-of- critical-minerals-in-clean-energy-transitions (accessed on 5 January 2023).

[10] Castelvecchi, D. Electric Cars: The Battery Challenge. *Nature* **2021**, *596*, 336–339. http://doi.org/10.1038/d41586-021-02222-1

[11] European Commission. Critical Raw Materials Resilience: Charting a Path towards Greater Security and Sustainability. 2020. Available online: https://eur-lex.europa.eu/legal-content/EN/TXT/?uri=CELEX:52020DC0474 (accessed on 5 January 2023).

[12] European Commision. New Circular Economy Action Plan for a Cleaner and More Competitive Europe. 2020. Available online: https://eur-lex.europa.eu/legal-content/EN/TXT/?qid=1583933814386&uri=COM:2020:98:FIN (accessed on 5 January 2023).

[13] European Parliament. Council of the European Union Directive 2006/66/EC of the European Parliament and of the Council of 6 September 2006 on Batteries and Accumulators and Waste Batteries and Accumulators and Repealing Directive 91/157/EEC 2006. 2006. Available online: https://eur-lex.europa.eu/legal-content/EN/ALL/?uri=CELEX%3A32006L0066 (accessed on 6 January 2023).

[14] Trading Economics. Cobalt. 2023. Available online: https://tradingeconomics.com/commodity/cobalt (accessed on 6 January 2023).

[15] U.S. Geological Survey. Mineral Commodity Summaries 2020. Available online: https://pubs.usgs.gov/periodicals/mcs2020/ mcs2020.pdf (accessed on 6 January 2023).

[16] Jiang, Y.; Deng, Y.-P.; Fu, J.; Lee, D.U.; Liang, R.; Cano, Z.P.; Liu, Y.; Bai, Z.; Hwang, S.; Yang, L.; et al. Interpenetrating Triphase Cobalt-Based Nanocomposites as Efficient Bifunctional Oxygen Electrocatalysts for Long-Lasting Rechargeable Zn-Air Batteries. *Adv.*

Energy Mater. **2018**, *8*, 1702900. http://doi.org/10.1002/aenm.201702900

[17] Korstanje, T.J.; van der Vlugt, J.I.; Elsevier, C.J.; de Bruin, B. Hydrogenation of Carboxylic Acids with a Homogeneous Cobalt Catalyst. *Science* **2015**, *350*, 298–302. http://doi.org/10.1126/science.aaa8938

[18] Statista, Countries with the Largest Lithium Reserves Worldwide. 2021. Available online: https://www.statista.com/statistics/ 268790/countries-with-the-largest-lithium-reserves-worldwide/ (accessed on 7 January 2022).

[19] Thomas, C.L. Mineral Commodity Summaries 2018, U.S. Geological Survey Mineral Commodity Summaries 2019. *Miner. Commod. Summ.* **2019**, 20–200. http://doi.org/10.3133/70202434

[20] U.S. Geological Survey. Mineral Commodity Summaries 2023. Available online: https://doi.org/10.3133/mcs2023 (accessed on 6 January 2023).

[21] Pan, H.; Hu, Y.-S.; Chen, L. Room-Temperature Stationary Sodium-Ion Batteries for Large-Scale Electric Energy Storage. *Energy Environ. Sci.* **2013**, *6*, 2338–2360. http://doi.org/10.1039/c3ee40847g

[22] Hou, W.; Guo, X.; Shen, X.; Amine, K.; Yu, H.; Lu, J. Solid Electrolytes and Interfaces in All-Solid-State Sodium Batteries: Progress and Perspective. *Nano Energy* **2018**, *52*, 279–291. http://doi.org/10.1016/j.nanoen.2018.07.036

[23] Saeki, S.; Lee, J.; Zhang, Q.; Saito, F. Co-Grinding LiCoO2 with PVC and Water Leaching of Metal Chlorides Formed in Ground Product. *Int. J. Miner. Process*. **2004**, *74*, S373–S378. http://doi.org/10.1016/j.minpro.2004.08.002

[24] Nassar, N.T.; Brainard, J.; Gulley, A.; Manley, R.; Matos, G.; Lederer, G.; Bird, L.R.; Pineault, D.; Alonso, E.; Gambogi, J.; et al. Evaluating the Mineral Commodity Supply Risk of the U.S. Manufacturing Sector. *Sci Adv.* **2020**, *6*, eaay8647. http://doi.org/10.1126/sciadv.aay8647

[25] U.S. Geological Survey. Mineral Commodity Summaries 2022. Available online: https://pubs.usgs.gov/periodicals/mcs2022/ mcs2022.pdf (accessed on 6 January 2023).

[26] Statista. Reserves of Graphite Worldwide in 2021, by Country. 2021. Available online: https://www.statista.com/statistics/2673 67/reserves-of-graphite-by-country/#:~:text=In%202020%2C%20the%20total%20worldwide,650%2C000%20metric%20tons% 20of%20graphite (accessed on 6 January 2023).

[27] Jin, S.; Mu, D.; Lu, Z.; Li, R.; Liu, Z.; Wang, Y.; Tian, S.; Dai, C. A Comprehensive Review on the Recycling of Spent Lithium-Ion Batteries: Urgent Status and Technology Advances. *J. Clean. Prod.* **2022**, *340*, 130535. http://doi.org/10.1016/j.jclepro.2022.130535

[28] Statista. Worldwide Revenue from Electric Vehicles since 2010. 2023. Available online: https://www.statista.com/statistics/2715 37/worldwide-revenue-from-electric-vehicles-since-2010/ (accessed on 6 January 2023).

[29] IEA. Global EV Outlook 2019. License: CC BY 4.0. Available online: https://www.iea.org/reports/global-ev-outlook-2019 (accessed on 6 January 2023).

[30] IEA. New CEM Campaign Aims for Goal of 30% New Electric Vehicle Sales by 2030. 2017. Available online: https://www.iea. org/news/new-cem-campaign-aims-for-goal-of-30-new-electric-vehicle-sales-by-2030 (accessed on 6 January 2023).

[31] Koleski, K. The 13th Five-Year Plan (2016–2020), U.S.-China Economic and Security Review Commission. 2017. Available online:

https://www.uscc.gov/sites/default/files/Research/The%2013th%20Five-Year%20Plan_Final_2.14.17_Updated%20 (002).pdf (accessed on 6 January 2023).

[32] Larcher, D.; Tarascon, J.-M. Towards Greener and More Sustainable Batteries for Electrical Energy Storage. *Nat. Chem.* **2014**, *7*,19–29. http://doi.org/10.1038/nchem.2085

[33] Forti, V.; Baldé, C.P.; Kuehr, R.; Bel, G.; The Global E-Waste. Monitor 2020-Quantities, Flows, and the Circular Economy Potential. 2020. Available online: https://ewastemonitor.info/wp-content/uploads/2020/11/GEM_2020_def_july1_low.pdf (accessed on 6 January 2023).

[34] Fahimi, A.; Ducoli, S.; Federici, S.; Ye, G.; Mousa, E.; Frontera, P.; Bontempi, E. Evaluation of the Sustainability of Technologies to Recycle Spent Lithium-Ion Batteries, Based on Embodied Energy and Carbon Footprint. *J. Clean. Prod.* **2022**, *338*, 130493. http://doi.org/10.1016/j.jclepro.2022.130493

[35] European Commission. Regulation of the European Parliament and the Council Concerning Batteries and Waste Batteries, Repealing Directive 2006/66/EC and Amending Regulation (EU) No2019/1020. 2020. Available online: https://eur-lex.europa. eu/legal-content/EN/TXT/?uri=CELEX:52020PC0798 (accessed on 6 January 2023).

[36] The Federal Universal Waste Regulations, in Title 40 of the Code of Federal Regulations (CFR) in Part 273 1995. Available online: https://www.ecfr.gov/current/title-40/part-261/subpart-D (accessed on 6 January 2023).

[37] Bureau of National Affairs (Arlington, V.). *Environment Reporter: Cases*; Bureau of National Affairs: Virginia, NV, USA, 1996.

[38] Wu, J.; Zheng, M.; Liu, T.; Wang, Y.; Liu, Y.; Nai, J.; Zhang, L.; Zhang, S.; Tao, X. Direct recovery: A sustainable recycling technology for spent lithium-ion battery. *Energy Storage Mater.* **2023**, *54*, 120–134. http://doi.org/10.1016/j.ensm.2022.09.029

[39] State of California, California Rechargeable Battery Recycling Act of 2006. 2005. Available online: https://dtsc.ca.gov/fs-ab1125/ (accessed on 6 January 2023).

[40] State of Puerto Rico. Puerto Rico Electronics Recycling and Disposal Promotion Act. 2012. Available online: https://casetext.com/statute/laws-of-puerto-rico/title-twelve-conservation/subtitle-8-environment-ii/chapter-507-puerto-rico- electronics-recycling-and-disposal-promotion-act (accessed on 6 January 2023).

[41] New York State. Laws of New York Chapter 562-2010. Available online: https://www.call2recycle.org/wp-content/uploads/ Chaptered-New-York-State-Law.pdf (accessed on 6 January 2023).

[42] State of Minnesota. 2022 Minnesota Statutes. 2022. Available online: https://www.revisor.mn.gov/statutes/cite/325E.125 (accessed on 7 July 2022).

[43] Sun, S.; Jin, C.; He, W.; Li, G.; Zhu, H.; Huang, J. Management Status of Waste Lithium-Ion Batteries in China and a Complete Closed-Circuit Recycling Process. *Sci. Total Environ.* **2021**, *776*, 145913. http://doi.org/10.1016/j.scitotenv.2021.145913

[44] Brückner, L.; Frank, J.; Elwert, T. Industrial Recycling of Lithium-Ion Batteries—A Critical Review of Metallurgical Process Routes. *Metals* **2020**, *10*, 1107. http://doi.org/10.3390/met10081107

[45] Doose, S.; Mayer, J.K.; Michalowski, P.; Kwade, A. Challenges in Ecofriendly Battery Recycling and Closed Material Cycles: A Perspective on Future Lithium Battery Generations. *Metals* **2021**, *11*, 291. http://doi.org/10.3390/met11020291

[46] He, K.; Zhang, Z.-Y.; Zhang, F.-S. Synthesis of Graphene and Recovery of Lithium from

Lithiated Graphite of Spent Li-Ion Battery. *Waste Manag.* **2021**, *124*, 283–292. http://doi.org/10.1016/j.wasman.2021.01.017

[47] Liu, C.; Lin, J.; Cao, H.; Zhang, Y.; Sun, Z. Recycling of Spent Lithium-Ion Batteries in View of Lithium Recovery: A Critical Review. *J. Clean. Prod.* **2019**, *228*, 801–813. http://doi.org/10.1016/j.jclepro.2019.04.304

[48] Lv, W.; Wang, Z.; Cao, H.; Sun, Y.; Zhang, Y.; Sun, Z. A Critical Review and Analysis on the Recycling of Spent Lithium-Ion Batteries. *ACS Sustain. Chem. Eng.* **2018**, *6*, 1504–1521. http://doi.org/10.1021/acssuschemeng.7b03811

[49] Velázquez-Martínez, O.; Valio, J.; Santasalo-Aarnio, A.; Reuter, M.; Serna-Guerrero, R. A Critical Review of Lithium-Ion Battery Recycling Processes from a Circular Economy Perspective. *Batteries* **2019**, *5*, 68. http://doi.org/10.3390/batteries5040068

[50] Windisch-Kern, S.; Gerold, E.; Nigl, T.; Jandric, A.; Altendorfer, M.; Rutrecht, B.; Scherhaufer, S.; Raupenstrauch, H.; Pomberger, R.; Antrekowitsch, H.; et al. Recycling Chains for Lithium-Ion Batteries: A Critical Examination of Current Challenges, Opportunities and Process Dependencies. *Waste Manag.* **2022**, *138*, 125–139. http://doi.org/10.1016/j.wasman.2021.11.038

[51] Winslow, K.M.; Laux, S.J.; Townsend, T.G. A Review on the Growing Concern and Potential Management Strategies of Waste Lithium-Ion Batteries. *Resour. Conserv. Recycl.* **2018**, *129*, 263–277. http://doi.org/10.1016/j.resconrec.2017.11.001

[52] Ali, H.; Khan, H.A.; Pecht, M. Preprocessing of Spent Lithium-Ion Batteries for Recycling: Need, Methods, and Trends. *Renew. Sustain. Energy Rev.* **2022**, *168*, 112809. http://doi.org/10.1016/j.rser.2022.112809

[53] Botelho Junior, A.B.; Stopic, S.; Friedrich, B.; Tenório, J.A.S.; Espinosa, D.C.R. Cobalt Recovery from Li-Ion Battery Recycling: A Critical Review. *Metals* **2021**, *11*, 1999. http://doi.org/10.3390/met11121999

[54] Mossali, E.; Picone, N.; Gentilini, L.; Rodrìguez, O.; Pérez, J.M.; Colledani, M. Lithium-Ion Batteries towards Circular Economy: A Literature Review of Opportunities and Issues of Recycling Treatments. *J. Environ. Manag.* **2020**, *264*, 110500. http://doi.org/10.1016/j.jenvman.2020.110500

[55] Yun, L.; Linh, D.; Shui, L.; Peng, X.; Garg, A.; Le, M.L.P.; Asghari, S.; Sandoval, J. Metallurgical and Mechanical Methods for Recycling of Lithium-Ion Battery Pack for Electric Vehicles. *Resour. Conserv. Recycl.* **2018**, *136*, 198–208. http://doi.org/10.1016/j.resconrec.2018.04.025

[56] Warner, J. 7-Lithium-Ion Battery Packs for EVs. In *Lithium-Ion Batteries*; Pistoia, G., Ed.; Elsevier: Amsterdam, The Netherlands, 2014; pp. 127–150, ISBN 9780444595133.

[57] El Mofid, W.; Ivanov, S.; Konkin, A.; Bund, A. A High-Performance Layered Transition Metal Oxide Cathode Material Obtained by Simultaneous Aluminum and Iron Cationic Substitution. *J. Power Sources* **2014**, *268*, 414–422. http://doi.org/10.1016/j.jpowsour.2014.06.048

[58] Zhao, S.; Guo, Z.; Yan, K.; Wan, S.; He, F.; Sun, B.; Wang, G. Towards High-Energy-Density Lithium-Ion Batteries: Strategies for Developing High-Capacity Lithium-Rich Cathode Materials. *Energy Storage Mater.* **2021**, *34*, 716–734. http://doi.org/10.1016/j.ensm.2020.11.008

[59] Bharathraj, S.; Adiga, S.P.; Mayya, K.S.; Song, T.; Kim, J.; Sung, Y. Degradation-Guided Optimization of Charging Protocol for Cycle Life Enhancement of Li-Ion Batteries with Lithium Manganese Oxide-Based Cathodes. *J. Power Sources* **2020**, *474*, 228659.

http://doi.org/10.1016/j.jpowsour.2020.228659

[60] Chen, Y.; Wang, G.X.; Konstantinov, K.; Liu, H.K.; Dou, S.X. Synthesis ~~and~~ Characterization of LiCoxMnyNi1 x yO2 as a Cathode Material for Secondary Lithium Batteries. *J. Power Sources* **2003**, *119–121*, 184–188. http://doi.org/10.1016/S0378-7753(03)00176-9

[61] Li, Y.-C.; Xiang, W.; Wu, Z.-G.; Xu, C.-L.; Xu, Y.-D.; Xiao, Y.; Yang, Z.-G.; Wu, C.-J.; Lv, G.-P.; Guo, X.-D. Construction of Homogeneously Al^{3+} Doped Ni Rich Ni-Co-Mn Cathode with High Stable Cycling Performance and Storage Stability via Scalable Continuous Precipitation. *Electrochim. Acta* **2018**, *291*, 84–94. http://doi.org/10.1016/j.electacta.2018.08.124

[62] Wang, Z.; Liu, E.; He, C.; Shi, C.; Li, J.; Zhao, N. Effect of Amorphous FePO4 Coating on Structure and Electrochemical Performance of Li1.2Ni0.13Co0.13Mn0.54O2 as Cathode Material for Li-Ion Batteries. *J. Power Sources* **2013**, *236*, 25–32. http://doi.org/10.1016/j.jpowsour.2013.02.022

[63] Xiang, W.; Zhu, C.-Q.; Zhang, J.; Shi, H.; Liang, Y.-T.; Yu, M.-H.; Zhu, X.-M.; He, F.-R.; Lv, G.-P.; Guo, X.-D. Synergistic Coupling Effect of Sodium and Fluorine Co-Substitution on Enhancing Rate Capability and Cycling Performance of Ni-Rich Cathode for Lithium Ion Battery. *J. Alloys Compd.* **2019**, *786*, 56–64. http://doi.org/10.1016/j.jallcom.2019.01.264

[64] Mekonnen, Y.; Sundararajan, A.; Sarwat, A.I. A Review of Cathode and Anode Materials for Lithium-Ion Batteries. In *SoutheastCon 2016*; IEEE: Norfolk, VA, USA, 2016.

[65] Daniel, C.; Mohanty, D.; Li, J.; Wood, D.L. Cathode Materials Review. *AIP Conf. Proc.* **2014**, *1597*, 26–43. http://doi.org/10.1063/1.4878478

[66] Wild, M.; O'Neill, L.; Zhang, T.; Purkayastha, R.; Minton, G.; Marinescu, M.; Offer, G.J. Lithium Sulfur Batteries, a Mechanistic Review. *Energy Environ. Sci.* **2015**, *8*, 3477–3494. http://doi.org/10.1039/C5EE01388G

[67] Lahiri, I.; Choi, W. Carbon Nanostructures in Lithium Ion Batteries: Past, Present, and Future. *Crit. Rev. Solid State Mater. Sci.* **2013**, *38*, 128–166. http://doi.org/10.1080/10408436.2012.729765

[68] Winter, M.; Besenhard, J.O.; Spahr, M.E.; Novák, P. Insertion Electrode Materials for Rechargeable Lithium Batteries. *Adv. Mater.* **1998**, *10*, 725–763.

[69] Nitta, N.; Wu, F.; Lee, J.T.; Yushin, G. Li-Ion Battery Materials: Present and Future. *Mater. Today* **2015**, *18*, 252–264. http://doi.org/10.1016/j.mattod.2014.10.040

[70] Nemeth, T.; Schröer, P.; Kuipers, M.; Sauer, D.U. Lithium Titanate Oxide Battery Cells for High-Power Automotive Applications—Electro-Thermal Properties, Aging Behavior and Cost Considerations. *J. Energy Storage* **2020**, *31*, 101656. http://doi.org/10.1016/j.est.2020.101656

[71] Meng, X. Recent Progress of Graphene as Cathode Materials in Lithium Ion Batteries. *IOP Conf. Ser.: Earth Environ. Sci.* **2019**, *300*, 042039. http://doi.org/10.1088/1755-1315/300/4/042039

[72] Martins, L.S.; Guimarães, L.F.; Botelho Junior, A.B.; Tenório, J.A.S.; Espinosa, D.C.R. Electric Car Battery: An Overview on Global Demand, Recycling and Future Approaches towards Sustainability. *J. Environ. Manag.* **2021**, *295*, 113091. http://doi.org/10.1016/j.jenvman.2021.113091

[73] Contestabile, M.; Panero, S.; Scrosati, B. A Laboratory-Scale Lithium-Ion Battery

Recycling Process. *J. Power Sources* **2001**, *92*, 65–69. http://doi.org/10.1016/S0378-7753(00)00523-1

[74] Xu, J.; Thomas, H.R.; Francis, R.W.; Lum, K.R.; Wang, J.; Liang, B. A Review of Processes and Technologies for the Recycling of Lithium-Ion Secondary Batteries. *J. Power Sources* **2008**, *177*, 512–527. http://doi.org/10.1016/j.jpowsour.2007.11.074

[75] Yu, J.; Lin, M.; Tan, Q.; Li, J. High-Value Utilization of Graphite Electrodes in Spent Lithium-Ion Batteries: From 3D Waste Graphite to 2D Graphene Oxide. *J. Hazard. Mater.* **2021**, *401*, 123715. http://doi.org/10.1016/j.jhazmat.2020.123715

[76] Rothermel, S.; Evertz, M.; Kasnatscheew, J.; Qi, X.; Grützke, M.; Winter, M.; Nowak, S. Graphite Recycling from Spent Lithium-Ion Batteries. *ChemSusChem* **2016**, *9*, 3473–3484. http://doi.org/10.1002/cssc.201601062

[77] Badawy, S.M. Synthesis of High-Quality Graphene Oxide from Spent Mobile Phone Batteries. *Environ. Prog. Sustain. Energy* **2016**, *35*, 1485–1491. http://doi.org/10.1002/ep.12362

[78] Blomgren, G.E. The Development and Future of Lithium Ion Batteries. *J. Electrochem. Soc.* **2016**, *164*, A5019. http://doi.org/10.1149/2.0251701jes

[79] Sun, X.; Hao, H.; Zhao, F.; Liu, Z. Tracing Global Lithium Flow: A Trade-Linked Material Flow Analysis. *Resour. Conserv. Recycl.* **2017**, *124*, 50–61. http://doi.org/10.1016/j.resconrec.2017.04.012

[80] Zubi, G.; Dufo-López, R.; Carvalho, M.; Pasaoglu, G. The Lithium-Ion Battery: State of the Art and Future Perspectives. *Renew. Sustain. Energy Rev.* **2018**, *89*, 292–308. http://doi.org/10.1016/j.rser.2018.03.002

[81] Rallo, H.; Benveniste, G.; Gestoso, I.; Amante, B. Economic Analysis of the Disassembling Activities to the Reuse of Electric Vehicles Li-Ion Batteries. *Resour. Conserv. Recycl.* **2020**, *159*, 104785. http://doi.org/10.1016/j.resconrec.2020.104785

[82] Glöser-Chahoud, S.; Pfaff, M.; Walz, R.; Schultmann, F. Simulating the Service Lifetimes and Storage Phases of Consumer Electronics in Europe with a Cascade Stock and Flow Model. *J. Clean. Prod.* **2019**, *213*, 1313–1321. http://doi.org/10.1016/j.jclepro.2018.12.244

[83] Yang, F.; Xie, Y.; Deng, Y.; Yuan, C. Predictive Modeling of Battery Degradation and Greenhouse Gas Emissions from U.S. State-Level Electric Vehicle Operation. *Nat. Commun.* **2018**, *9*, 2429. http://doi.org/10.1038/s41467-018-04826-0

[84] Casals, L.C.; Amante García, B.; Canal, C. Second Life Batteries Lifespan: Rest of Useful Life and Environmental Analysis. *J. Environ. Manag.* **2019**, *232*, 354–363. http://doi.org/10.1016/j.jenvman.2018.11.046

[85] Gaines, L.; Richa, K.; Spangenberger, J. Key Issues for Li-Ion Battery Recycling. *MRS Energy Sustain.* **2018**, *5*, E14. http://doi.org/10.1557/mre.2018.13

[86] IEA. Global EV Outlook 2020. Available online: https://www.iea.org/reports/global-ev-outlook-2020 (accessed on 3 June 2022).

[87] Forti, V.; Balde, C.P.; Kuehr, R.; Bel, G. *The Global E-Waste Monitor 2020: Quantities, Flows and the Circular Economy Potential*; United Nations University: Bonn, Germany; United Nations Institute for Training and Research: Geneva, Switzerland; International Telecommunication Union: Geneva, Switzerland; International Solid Waste Association: Rotterdam, The Netherlands, 2020; ISBN 9789280891140.

[88] Wang, X.; Gaustad, G.; Babbitt, C.W.; Richa, K. Economies of Scale for Future Lithium-Ion

Battery Recycling Infrastructure. *Resour. Conserv. Recycl.* **2014**, *83*, 53–62. http://doi.org/10.1016/j.resconrec.2013.11.009

[89] Chen, M.; Ma, X.; Chen, B.; Arsenault, R.; Karlson, P.; Simon, N.; Wang, Y. Recycling End-of-Life Electric Vehicle Lithium-Ion Batteries. *Joule* **2019**, *3*, 2622–2646. http://doi.org/10.1016/j.joule.2019.09.014

[90] European Parliament. Directive 2008/98/ec of the European Parliament and of the Council EUR-Lex. 2008. Available online: https://eur-lex.europa.eu/legal-content/EN/TXT/?uri=CELEX%3A32008L0098 (accessed on 3 June 2022).

[91] Li, W.; Yang, M.; Long, R.; Mamaril, K.; Chi, Y. Treatment of Electric Vehicle Battery Waste in China: A Review of Existing Policies. *J. Environ. Eng. Landsc. Manag.* **2021**, *29*, 111–122. http://doi.org/10.3846/jeelm.2021.14220

[92] Alper, J. Batteries. The Battery: Not yet a Terminal Case. *Science* **2002**, *296*, 1224–1226. http://doi.org/10.1126/science.296.5571.1224

[93] Guimarães, L.F.; Botelho Junior, A.B.; Espinosa, D.C.R. Sulfuric Acid Leaching of Metals from Waste Li-Ion Batteries without Using Reducing Agent. *Miner. Eng.* **2022**, *183*, 107597. http://doi.org/10.1016/j.mineng.2022.107597

[94] Harper, G.; Sommerville, R.; Kendrick, E.; Driscoll, L.; Slater, P.; Stolkin, R.; Walton, A.; Christensen, P.; Heidrich, O.; Lambert, S.; et al. Recycling Lithium-Ion Batteries from Electric Vehicles. *Nature* **2019**, *575*, 75–86. http://doi.org/10.1038/s41586-019-1682-5

[95] Diekmann, J.; Hanisch, C.; Froböse, L.; Schälicke, G.; Loellhoeffel, T.; Fölster, A.-S.; Kwade, A. Ecological Recycling of Lithium-Ion Batteries from Electric Vehicles with Focus on Mechanical Processes. *J. Electrochem. Soc.* **2016**, *164*, A6184. http://doi.org/10.1149/2.0271701jes

[96] Lee, C.K.; Rhee, K.-I. Preparation of LiCoO2 from Spent Lithium-Ion Batteries. *J. Power Sources* **2002**, *109*, 17–21. http://doi.org/10.1016/S0378-7753(02)00037-X

[97] Jafari, M.; Torabian, M.M.; Bazargan, A. A Facile Chemical-Free Cathode Powder Separation Method for Lithium Ion Battery Resource Recovery. *J. Energy Storage* **2020**, *31*, 101564. http://doi.org/10.1016/j.est.2020.101564

[98] Ojanen, S.; Lundström, M.; Santasalo-Aarnio, A.; Serna-Guerrero, R. Challenging the Concept of Electrochemical Discharge Using Salt Solutions for Lithium-Ion Batteries Recycling. *Waste Manag.* **2018**, *76*, 242–249. http://doi.org/10.1016/j.wasman.2018.03.045

[99] Castro, F.D.; Mehner, E.; Cutaia, L.; Vaccari, M. Life Cycle Assessment of an Innovative Lithium-Ion Battery Recycling Route: A Feasibility Study. *J. Clean. Prod.* **2022**, *368*, 133130. http://doi.org/10.1016/j.jclepro.2022.133130

[100] Li, J.; Wang, G.; Xu, Z. Generation and Detection of Metal Ions and Volatile Organic Compounds (VOCs) Emissions from the Pretreatment Processes for Recycling Spent Lithium-Ion Batteries. *Waste Manag.* **2016**, *52*, 221–227. http://doi.org/10.1016/j.wasman.2016.03.011

[101] Nan, J.; Han, D.; Zuo, X. Recovery of Metal Values from Spent Lithium-Ion Batteries with Chemical Deposition and Solvent Extraction. *J. Power Sources* **2005**, *152*, 278–284. http://doi.org/10.1016/j.jpowsour.2005.03.134

[102] Gratz, E.; Sa, Q.; Apelian, D.; Wang, Y. A Closed Loop Process for Recycling Spent Lithium Ion Batteries. *J. Power Sources* **2014**, *262*, 255–262. http://doi.org/10.1016/j.jpowsour.2014.03.126

[103] Grandjean, T.R.B.; Groenewald, J.; Marco, J. The Experimental Evaluation of Lithium Ion Batteries after Flash Cryogenic Freezing. *J. Energy Storage* **2019**, *21*, 202–215. http://doi.org/10.1016/j.est.2018.11.027

[104] Torabian, M.M.; Jafari, M.; Bazargan, A. Discharge of Lithium-Ion Batteries in Salt Solutions for Safer Storage, Transport, and Resource Recovery. *Waste Manag. Res.* **2022**, *40*, 402–409. http://doi.org/10.1177/0734242X211022658

[105] Smith, N.W.; Swoffer, S. Process for Recovering and Regenerating Lithium Cathode Material from Lithium-Ion Batteries. U.S. Patent No.: US 8882007B1, 11 November 2014.

[106] Batrec, A.G. Batrec.ch. 2021. Available online: https://batrec.ch/en/battery-recycling/ (accessed on 3 January 2023).

[107] Tedjar, F.; Foudraz, J.-C. Method for the Mixed Recycling of Lithium-Based Anode Batteries and Cells. U.S. Patent 10/593,332, 27 August 2007.

[108] Cheret, D.; Santen, S. Battery Recycling. U.S. Patent 7,169,206 B2, 30 January 2007.

[109] Guo, R.; Lu, L.; Ouyang, M.; Feng, X. Mechanism of the Entire Overdischarg Process and Overdischarge-Induced Internal Short Circuit in Lithium-Ion Batteries. *Sci. Rep.* **2016**, *6*, 30248. http://doi.org/10.1038/srep30248

[110] Nie, H.; Xu, L.; Song, D.; Song, J.; Shi, X.; Wang, X.; Zhang, L.; Yuan, Z. $LiCoO_2$: Recycling from Spent Batteries and Regeneration with Solid State Synthesis. *Green Chem.* **2015**, *17*, 1276–1280. http://doi.org/10.1039/C4GC01951B

[111] Song, X.; Dai, S.; Xu, Y.; Xie, Y. Experimental Study on the Discharge of the Waste Lithium Ion Battery. *Appl. Chem. Ind.* **2015**, *4*, 594–597.

[112] Yao, L.P.; Zeng, Q.; Qi, T.; Li, J. An Environmentally Friendly Discharge Technology to Pretreat Spent Lithium-Ion Batteries. *J. Clean. Prod.* **2020**, *245*, 118820. http://doi.org/10.1016/j.jclepro.2019.118820

[113] Li, H.; Dai, J.; Wang, A.; Zhao, S.; Ye, H.; Zhang, J. Recycling and Treatment of Waste Batteries. *IOP Conf. Ser. Mater. Sci. Eng.* **2019**, *612*, 052020. http://doi.org/10.1088/1757-899X/612/5/052020

[114] Zhang, X.; Li, L.; Fan, E.; Xue, Q.; Bian, Y.; Wu, F.; Chen, R. Toward Sustainable and Systematic Recycling of Spent Rechargeable Batteries. *Chem. Soc. Rev.* **2018**, *47*, 7239–7302. http://doi.org/10.1039/C8CS00297E

[115] Li, L.; Zheng, P.; Yang, T.; Sturges, R.; Ellis, M.W.; Li, Z. Disassembly Automation for Recycling End-of-Life Lithium-Ion Pouch Cells. *JOM-J. Miner. Met. Mater. Soc.* **2019**, *71*, 4457–4464. http://doi.org/10.1007/s11837-019-03778-0

[116] Fröhlich, S.; Sewing, D. The BATENUS Process for Recycling Mixed Battery Waste. *J. Power Sources* **1995**, *57*, 27–30. http://doi.org/10.1016/0378-7753(95)02234-1

[117] Pinegar, H.; Smith, Y.R. Recycling of End-of-Life Lithium Ion Batteries, Part I: Commercial Processes. *J. Sustain. Met.* **2019**, *5*, 402–416. http://doi.org/10.1007/s40831-019-00235-9

[118] Rosova, K. Li-Cycle: Sustainable Lithium-Ion Battery Recycling Technology. 2022. Available online: https://www. innovationnewsnetwork.com/li-cycle-sustainable-lithium-ion-battery-recycling-technology/21097/ (accessed on 6 January 2023).

[119] Granata, G.; Pagnanelli, F.; Moscardini, E.; Takacova, Z.; Havlik, T.; Toro, L. Simultaneous Recycling of Nickel Metal Hydride, Lithium Ion and Primary Lithium Batteries: Accomplishment of European Guidelines by Optimizing Mechanical Pre-

Treatment and Solvent Extraction Operations. *J. Power Sources* **2012**, *212*, 205–211. http://doi.org/10.1016/j.jpowsour.2012.04.016

[120] Zhang, T.; He, Y.; Ge, L.; Fu, R.; Zhang, X.; Huang, Y. Characteristics of Wet and Dry Crushing Methods in the Recycling Process of Spent Lithium-Ion Batteries. *J. Power Sources* **2013**, *240*, 766–771. http://doi.org/10.1016/j.jpowsour.2013.05.009

[121] Zhang, T.; He, Y.; Wang, F.; Ge, L.; Zhu, X.; Li, H. Chemical and Process Mineralogical Characterizations of Spent Lithium-Ion Batteries: An Approach by Multi-Analytical Techniques. *Waste Manag.* **2014**, *34*, 1051–1058. http://doi.org/10.1016/j.wasman.2014.01.002

[122] Li, L.; Ge, J.; Chen, R.; Wu, F.; Chen, S.; Zhang, X. Environmental Friendly Leaching Reagent for Cobalt and Lithium Recovery from Spent Lithium-Ion Batteries. *Waste Manag.* **2010**, *30*, 2615–2621. http://doi.org/10.1016/j.wasman.2010.08.008

[123] Li, L.; Ge, J.; Wu, F.; Chen, R.; Chen, S.; Wu, B. Recovery of Cobalt and Lithium from Spent Lithium Ion Batteries Using Organic Citric Acid as Leachant. *J. Hazard. Mater.* **2010**, *176*, 288–293. http://doi.org/10.1016/j.jhazmat.2009.11.026

[124] Li, L.; Dunn, J.B.; Zhang, X.X.; Gaines, L.; Chen, R.J.; Wu, F.; Amine, K. Recovery of Metals from Spent Lithium-Ion Batteries with Organic Acids as Leaching Reagents and Environmental Assessment. *J. Power Sources* **2013**, *233*, 180–189. http://doi.org/10.1016/j.jpowsour.2012.12.089

[125] Guan, J.; Li, Y.; Guo, Y.; Su, R.; Gao, G.; Song, H.; Yuan, H.; Liang, B.; Guo, Z. Mechanochemical Process Enhanced Cobalt and Lithium Recycling from Wasted Lithium-Ion Batteries. *ACS Sustain. Chem. Eng.* **2017**, *5*, 1026–1032. http://doi.org/10.1021/acssuschemeng.6b02337

[126] Pagnanelli, F.; Moscardini, E.; Altimari, P.; Abo Atia, T.; Toro, L. Cobalt Products from Real Waste Fractions of End of Life Lithium Ion Batteries. *Waste Manag.* **2016**, *51*, 214–221. http://doi.org/10.1016/j.wasman.2015.11.003

[127] Wang, X.; Gaustad, G.; Babbitt, C.W. Targeting High Value Metals in Lithium-Ion Battery Recycling via Shredding and Size-Based Separation. *Waste Manag.* **2016**, *51*, 204–213. http://doi.org/10.1016/j.wasman.2015.10.026

[128] Barik, S.P.; Prabaharan, G.; Kumar, L. Leaching and Separation of Co and Mn from Electrode Materials of Spent Lithium-Ion Batteries Using Hydrochloric Acid: Laboratory and Pilot Scale Study. *J. Clean. Prod.* **2017**, *147*, 37–43. http://doi.org/10.1016/j.jclepro.2017.01.095

[129] Diekmann, K.A.A. *Recycling of Lithium-Ion Batteries [Electronic Resource]: The LithoRec Way*; Arno Kwade, J.D., Ed.; Springer International Publishing: Cham, Switzerland, 2018; Volume 1, ISBN 9783319705729.

[130] He, Y.; Zhang, T.; Wang, F.; Zhang, G.; Zhang, W.; Wang, J. Recovery of $LiCoO_2$ and Graphite from Spent Lithium-Ion Batteries by Fenton Reagent-Assisted Flotation. *J. Clean. Prod.* **2017**, *143*, 319–325. http://doi.org/10.1016/j.jclepro.2016.12.106

[131] Yu, J.; He, Y.; Ge, Z.; Li, H.; Xie, W.; Wang, S. A Promising Physical Method for Recovery of LiCoO2 and Graphite from Spent Lithium-Ion Batteries: Grinding Flotation. *Sep. Purif. Technol.* **2018**, *190*, 45–52. http://doi.org/10.1016/j.seppur.2017.08.049

[132] Wang, H.; Liu, J.; Bai, X.; Wang, S.; Yang, D.; Fu, Y.; He, Y. Separation of the Cathode Materials from the Al Foil in Spent Lithium-Ion Batteries by Cryogenic Grinding. *Waste Manag.* **2019**, *91*, 89–98. http://doi.org/10.1016/j.wasman.2019.04.058

[133] Liu, J.; Wang, H.; Hu, T.; Bai, X.; He, Y. Recovery of LiCoO2 and Graphite from Spent Lithium-Ion Batteries by Cryogenic Grinding and Froth Flotation. *Miner. Eng.* **2020**, *148*, 106223. http://doi.org/10.1016/j.mineng.2020.106223

[134] Wuschke, L.; Jäckel, H.-G.; Leißner, T.; Peuker, U.A. Crushing of Large Li-Ion Battery Cells. *Waste Manag.* **2019**, *85*, 317–326. http://doi.org/10.1016/j.wasman.2018.12.042

[135] Widijatmoko, S.D.; Gu, F.; Wang, Z.; Hall, P. Selective Liberation in Dry Milled Spent Lithium-Ion Batteries. *Sustain. Mater. Technol.* **2020**, *23*, e00134. http://doi.org/10.1016/j.susmat.2019.e00134

[136] Zhan, R.; Payne, T.; Leftwich, T.; Perrine, K.; Pan, L. De-Agglomeration of Cathode Composites for Direct Recycling of Li-Ion Batteries. *Waste Manag.* **2020**, *105*, 39–48. http://doi.org/10.1016/j.wasman.2020.01.035

[137] Shin, S.M.; Kim, N.H.; Sohn, J.S.; Yang, D.H.; Kim, Y.H. Development of a Metal Recovery from Li-Ion Battery Wastes. *Hydrometal- lurgy* **2005**, *3–4*, 172–181. http://doi.org/10.1016/j.hydromet.2005.06.004

[138] Granata, G.; Moscardini, E.; Pagnanelli, F.; Trabucco, F.; Toro, L. Product Recovery from Li-Ion Battery Wastes Coming from an Industrial Pre-Treatment Plant: Lab Scale Tests and Process Simulations. *J. Power Sources* **2012**, *206*, 393–401. http://doi.org/10.1016/j.jpowsour.2012.01.115

[139] Li, J.; Shi, P.; Wang, Z.; Chen, Y.; Chang, C.-C. A Combined Recovery Process of Metals in Spent Lithium-Ion Batteries. *Chemosphere* **2009**, *77*, 1132–1136. http://doi.org/10.1016/j.chemosphere.2009.08.040

[140] Zhang, G.; Du, Z.; He, Y.; Wang, H.; Xie, W.; Zhang, T. A Sustainable Process for the Recovery of Anode and Cathode Materials Derived from Spent Lithium-Ion Batteries. *Sustain. Sci. Pract. Policy* **2019**, *11*, 2363. http://doi.org/10.3390/su11082363

[141] Zhang, G.; He, Y.; Feng, Y.; Wang, H. Enhancement in Liberation of Electrode Materials Derived from Spent Lithium-Ion Battery by Pyrolysis. *J. Clean. Prod.* **2018**, *199*, 62–68. http://doi.org/10.1016/j.jclepro.2018.07.143

[142] Zhang, G.; He, Y.; Wang, H.; Feng, Y.; Xie, W.; Zhu, X. Removal of Organics by Pyrolysis for Enhancing Liberation and Flotation Behavior of Electrode Materials Derived from Spent Lithium-Ion Batteries. *ACS Sustain. Chem. Eng.* **2020**, *8*, 2205–2214. http://doi.org/10.1021/acssuschemeng.9b05896

[143] Vieceli, N.; Nogueira, C.A.; Guimarães, C.; Pereira, M.F.C.; Durão, F.O.; Margarido, F. Hydrometallurgical Recycling of Lithium- Ion Batteries by Reductive Leaching with Sodium Metabisulphite. *Waste Manag.* **2018**, *71*, 350–361. http://doi.org/10.1016/j.wasman.2017.09.032

[144] Peng, C.; Liu, F.; Aji, A.T.; Wilson, B.P.; Lundström, M. Extraction of Li and Co from Industrially Produced Li-Ion Battery Waste—Using the Reductive Power of Waste Itself. *Waste Manag.* **2019**, *95*, 604–611. http://doi.org/10.1016/j.wasman.2019.06.048

[145] Yu, J.; Tan, Q.; Li, J. Exploring a Green Route for Recycling Spent Lithium-Ion Batteries: Revealing and Solving Deep Screening Problem. *J. Clean. Prod.* **2020**, *255*, 120269. http://doi.org/10.1016/j.jclepro.2020.120269

[146] Widijatmoko, S.D.; Gu, F.; Wang, Z.; Hall, P. Recovering Lithium Cobalt Oxide, Aluminium, and Copper from Spent Lithium-Ion Battery via Attrition Scrubbing. *J. Clean. Prod.* **2020**, *260*, 120869. http://doi.org/10.1016/j.jclepro.2020.120869

[147] Liu, Y.; Hu, Q.; Li, X.; Wang, Z.; Guo, H. Recycle and Synthesis of LiCoO2 from

Incisors Bound of Li-Ion Batteries. *Trans. Nonferrous Met. Soc. China* **2006**, *16*, 956–959. http://doi.org/10.1016/S1003-6326(06)60359-2

[148] Song, D.; Wang, X.; Zhou, E.; Hou, P.; Zhang, L. Recovery and Heat Treatment of the Li(Ni1/3Co1/3Mn1/3)O2 Cathode Scrap Material for Lithium Ion Battery. *J. Power Sources* **2013**, *232*, 348–352. http://doi.org/10.1016/j.jpowsour.2012.10.072

[149] Song, D.; Wang, X.; Nie, H.; Shi, H.; Wang, D.; Guo, F.; Shi, X.; Zhang, L. Heat Treatment of LiCoO2 Recovered from Cathode Scraps with Solvent Method. *J. Power Sources* **2014**, *249*, 137–141. http://doi.org/10.1016/j.jpowsour.2013.10.062

[150] Xu, Y.; Song, D.; Li, L.; An, C.; Wang, Y.; Jiao, L.; Yuan, H. A Simple Solvent Method for the Recovery of LixCoO2 and Its Applications in Alkaline Rechargeable Batteries. *J. Power Sources* **2014**, *252*, 286–291. http://doi.org/10.1016/j.jpowsour.2013.11.052

[151] Yang, L.; Xi, G.; Xi, Y. Recovery of Co, Mn, Ni, and Li from Spent Lithium Ion Batteries for the Preparation of LiNi Co Mn O2 Cathode Materials. *Ceram. Int.* **2015**, *41*, 11498–11503. http://doi.org/10.1016/j.ceramint.2015.05.115

[152] He, L.-P.; Sun, S.-Y.; Song, X.-F.; Yu, J.-G. Recovery of Cathode Materials and Al from Spent Lithium-Ion Batteries by Utrasonic Cleaning. *Waste Manag.* **2015**, *46*, 523–528. http://doi.org/10.1016/j.wasman.2015.08.035

[153] Nayaka, G.P.; Zhang, Y.; Dong, P.; Wang, D.; Pai, K.V.; Manjanna, J.; Santhosh, G.; Duan, J.; Zhou, Z.; Xiao, J. Effective and Environmentally Friendly Recycling Process Designed for LiCoO2 Cathode Powders of Spent Li-Ion Batteries Using Mixture of Mild Organic Acids. *Waste Manag.* **2018**, *78*, 51–57. http://doi.org/10.1016/j.wasman.2018.05.030

[154] He, K.; Zhang, Z.-Y.; Zhang, F.-S. Selectively Peeling of Spent LiFePO4 Cathode by Destruction of Crystal Structure and Binder Matrix for Efficient Recycling of Spent Battery Materials. *J. Hazard. Mater.* **2020**, *386*, 121633. http://doi.org/10.1016/j.jhazmat.2019.121633

[155] Wang, M.; Tan, Q.; Liu, L.; Li, J. Efficient Separation of Aluminum Foil and Cathode Materials from Spent Lithium-Ion Batteries Using a Low-Temperature Molten Salt. *ACS Sustain. Chem. Eng.* **2019**, *7*, 8287–8294. http://doi.org/10.1021/acssuschemeng.8b06694

[156] He, K.; Zhang, Z.-Y.; Alai, L.; Zhang, F.-S. A Green Process for Exfoliating Electrode Materials and Simultaneously Extracting Electrolyte from Spent Lithium-Ion Batteries. *J. Hazard. Mater.* **2019**, *375*, 43–51. http://doi.org/10.1016/j.jhazmat.2019.03.120

[157] Nayaka, G.P.; Zhang, Y.; Dong, P.; Wang, D.; Zhou, Z.; Duan, J.; Li, X.; Lin, Y.; Meng, Q.; Pai, K.V.; et al. An Environmental Friendly Attempt to Recycle the Spent Li-Ion Battery Cathode through Organic Acid Leaching. *J. Environ. Chem. Eng.* **2019**, *7*, 102854. http://doi.org/10.1016/j.jece.2018.102854

[158] Fouad, O.A.; Farghaly, F.I.; Bahgat, M. A Novel Approach for Synthesis of Nanocrystalline γ-LiAlO2 from Spent Lithium-Ion Batteries. *J. Anal. Appl. Pyrolysis* **2007**, *78*, 65–69. http://doi.org/10.1016/j.jaap.2006.04.002

[159] Sun, L.; Qiu, K. Vacuum Pyrolysis and Hydrometallurgical Process for the Recovery of Valuable Metals from Spent Lithium-Ion Batteries. *J. Hazard. Mater.* **2011**, *194*, 378–384. http://doi.org/10.1016/j.jhazmat.2011.07.114

[160] Kim, H.S.; Shin, E.J. Re-Synthesis and Electrochemical Characteristics of LiFePO4 Cathode Materials Recycled from Scrap Electrodes. *Bull. Korean Chem. Soc.* **2013**, *34*, 851–855. http://doi.org/10.5012/bkcs.2013.34.3.851

[161] Zheng, R.; Zhao, L.; Wang, W.; Liu, Y.; Ma, Q.; Mu, D.; Li, R.; Dai, C. Optimized Li and Fe Recovery from Spent Lithium-Ion Batteries via a Solution-Precipitation Method. *RSC Adv.* **2016**, *6*, 43613–43625. http://doi.org/10.1039/C6RA05477C

[162] Yang, Y.; Huang, G.; Xu, S.; He, Y.; Liu, X. Thermal Treatment Process for the Recovery of Valuable Metals from Spent Lithium-Ion Batteries. *Hydrometallurgy* **2016**, *165*, 390–396. http://doi.org/10.1016/j.hydromet.2015.09.025

[163] Xiao, J.; Li, J.; Xu, Z. Novel Approach for in Situ Recovery of Lithium Carbonate from Spent Lithium Ion Batteries Using Vacuum Metallurgy. *Environ. Sci. Technol.* **2017**, *51*, 11960–11966. http://doi.org/10.1021/acs.est.7b02561

[164] Xiao, J.; Li, J.; Xu, Z. Recycling Metals from Lithium Ion Battery by Mechanical Separation and Vacuum Metallurgy. *J. Hazard. Mater.* **2017**, *338*, 124–131. http://doi.org/10.1016/j.jhazmat.2017.05.024

[165] Zhang, G.; He, Y.; Feng, Y.; Wang, H.; Zhu, X. Pyrolysis-Ultrasonic-Assisted Flotation Technology for Recovering Graphite and LiCoO2 from Spent Lithium-Ion Batteries. *ACS Sustain. Chem. Eng.* **2018**, *6*, 10896–10904. http://doi.org/10.1021/acssuschemeng.8b02186

[166] Zhang, G.; He, Y.; Wang, H.; Feng, Y.; Xie, W.; Zhu, X. Application of Mechanical Crushing Combined with Pyrolysis-Enhanced Flotation Technology to Recover Graphite and LiCoO2 from Spent Lithium-Ion Batteries. *J. Clean. Prod.* **2019**, *231*, 1418–1427. http://doi.org/10.1016/j.jclepro.2019.04.279

[167] Wang, F.; Zhang, T.; He, Y.; Zhao, Y.; Wang, S.; Zhang, G.; Zhang, Y.; Feng, Y. Recovery of Valuable Materials from Spent Lithium-Ion Batteries by Mechanical Separation and Thermal Treatment. *J. Clean. Prod.* **2018**, *185*, 646–652. http://doi.org/10.1016/j.jclepro.2018.03.069

[168] Diaz, F.; Wang, Y.; Moorthy, T.; Friedrich, B. Degradation Mechanism of Nickel-Cobalt-Aluminum (NCA) Cathode Material from Spent Lithium-Ion Batteries in Microwave-Assisted Pyrolysis. *Metals* **2018**, *8*, 565. http://doi.org/10.3390/met8080565

[169] Wang, M.; Tan, Q.; Liu, L.; Li, J. A Facile, Environmentally Friendly, and Low-Temperature Approach for Decomposition of Polyvinylidene Fluoride from the Cathode Electrode of Spent Lithium-Ion Batteries. *ACS Sustain. Chem. Eng.* **2019**, *7*, 12799–12806. http://doi.org/10.1021/acssuschemeng.9b01546

[170] Zhong, X.; Han, J.; Mao, X.; Chen, L.; Chen, M.; Zhu, H.; Zeng, H.; Qin, W. Innovative Methodology for Green Recycling of Spent Lithium-Ion Batteries: Effective Pyrolysis with DMF. *J. Clean. Prod.* **2022**, *377*, 134503. http://doi.org/10.1016/j.jclepro.2022.134503

[171] Zhong, X.; Liu, W.; Han, J.; Jiao, F.; Qin, W.; Liu, T.; Zhao, C. Pyrolysis and Physical Separation for the Recovery of Spent LiFePO4 Batteries. *Waste Manag.* **2019**, *89*, 83–93. http://doi.org/10.1016/j.wasman.2019.03.068

[172] Lombardo, G.; Ebin, B.; Foreman, M.R.S.J.; Steenari, B.-M.; Petranikova, M. Incineration of EV Lithium-Ion Batteries as a Pretreat- ment for Recycling—Determination of the Potential Formation of Hazardous by-Products and Effects on Metal Compounds.*J. Hazard. Mater.* **2020**, *393*, 122372. http://doi.org/10.1016/j.jhazmat.2020.122372

[173] Kim, S.; Bang, J.; Yoo, J.; Shin, Y.; Bae, J.; Jeong, J.; Kim, K.; Dong, P.; Kwon, K. A Comprehensive Review on the Pretreatment Process in Lithium-Ion Battery Recycling. *J. Clean. Prod.* **2021**, *294*, 126329. http://doi.org/10.1016/j.jclepro.2021.126329

Chapter Three-Cathode Active Material Treatment

Comparative Environmental and Economic Assessment of Emerging Hydrometallurgical Recycling Technologies for Li-Ion Battery Cathodes.

This paper has been published in the journal *Sustainable Production and Consumption* (https://doi.org/10.1016/j.spc.2024.09.015), Author contributed in writing the original draft, editing and reviewing, conceptualization, methodology, software and formal analysis.

1. Introduction

The development of electric vehicles (EVs) aims to reduce CO_2 emissions and fossil fuel consumption in the transport sector, primarily using lithium-ion batteries. The transition to a wireless era is causing a surge in battery demand across sectors, with projections showing a surge in Li-ion battery (LiB) power requirements from 700 GWh in 2022 to 4.7 TWh in 2030 [1]. Policy adaptations, such as incentives and reduced battery prices, and countries planning to impose restrictions on fossil fuel-governed vehicles also influence this trend [2]. For instance, China aims to sell 20% of zero-emission vehicles by 2025, while the European Union has implemented measures to reduce transportation carbon footprint, leading to increased EV usage. California's policies, for instance, have decreased state-wise CO_2 emissions in many US states, influencing worldwide demand for LiBs and increasing battery waste over time [3].

Currently, 57% of total worldwide LiB production is carried out by Asia-Pacific regions. Moreover, more than half of this production is coming from China. America and Europe are only responsible for approximately 22% and 21% of production as Statista reports [4]. In addition, this distribution will last until 2030, and total manufacturing capacities will be increased from 1.57 TWh (in 2022) to 6.79 TWh (in 2030) [5]. This increase in the production facilities is expected to boost the demand for raw materials. For instance, the demand for Cobalt, Nickel, graphite and Lithium is expected to increase by 256%, 1237%, 530% and 575% respectively. In the case of mining of these materials, around 76% of total Co mining is carried out by DR Congo followed by Indonesia (8%). Graphite is largely mined by China which is responsible for the production of 77% of the world requirement, being Madagascar and Mozambique the second largest suppliers at 6% production each. Nickel is mainly mined by Indonesia which produce around 50% of world Ni consumption [6]. Since most of these countries follow less stringent environmental laws for mining, increasing demand can produce an enormous quantity of emissions in future. Perhaps, moving towards urban mining of spent

batteries can lower this pressure exerted on mining industry, lowering the overall emissions. Moreover, it is a solution for the handling of high battery waste generation expected.

However, implementing new laboratory-identified technologies on a pilot or industrial scale presents challenges owing to uncertainties in recycling methods. Prior knowledge of the tested technologies from environmental and economic perspectives is advantageous. Decision-making of the core of the recycling process is crucial as it determines the quality of the material recovered and can also lower the overall environmental and economic pressure significantly. However, studies undertaken specifically to address this issue are not to be found.

To overcome this research gap, the current study employed a novel approach by simulating and arranging different emerging hydrometallurgical treatment steps into alternative conceptual treatment sequences that had already been tested at laboratory or pilot scales. The study aimed to evaluate the environmental and economic performance of trending and emerging technologies used to recycle $LiNi_{0.33}Mn_{0.33}Co_{0.33}O_2$-cathode (NMC 111) material from waste LiBs through these simulations. The technologies were assessed based on recent applications at the laboratory/pilot level that showed promising recovery levels suitable for industrial application.

Life Cycle Assessment (LCA) and Life Cycle Costing (LCC) were used to assess the environmental and economic performance, focusing exclusively on the hydrometallurgical treatment for extracting the critical raw materials (CRM) present in the cathode. The study also examined and compared various hydrometallurgical steps, such as leaching, purification/separation, and calcination, which extract Co-, Mn-, and Ni-based oxides from cathode active materials. Although Li was not considered for extraction as an oxide, it was accumulating in the solution for later production. The refining of metals in each study focused on Co, Ni, and Mn, and material flow was determined with an emphasis on these three metals.

The study also included recent inorganic acid (H_2SO_4)-based leaching experiments performed at the laboratory level for comparison. A novel aspect of this leaching method involved reducing the amount of oxidant (H_2O_2) used. It is from the knowledge of the authors that H_2O_2 it is not mandatory for the recycling [7], [8] but it was considered based on literature of the novel technologies evaluated

The study focuses on the target audience of battery manufacturers, recyclers, researchers, and policymakers to enhance their future recycling routes and amendments to existing routes.

2. Literature review

Since the introduction of more efficient Ni-Mn-Co (NMC)-type cathodic LiBs in 2010, LCO ($LiCoO_2$ cathode) production has led to a decrease [9]. Though the new cathode material has lower fraction of Cobalt than LCO cathode types the overall material contribution for NMC type cathodes are higher [10]. However, currently the highest market share (79% of total LiB battery market) is occupied by NMC type LiBs due to their high performance. It is expected that after 10 more years the market share of NMC type cathode would be 100% [11]. This suggests that future LiB waste generation would highly contain NMC type cathode active materials as researchers should be more focused on recycling of NMC type cathode active materials. Nevertheless, among the NMC type cathodes the NMC-111 battery type had the highest material contribution than the rest and it is the first introduced NMC type cathode material [10]. Hence, much attention should be given to recycling of NMC 111-type batteries. Moreover, given the similar chemistries in all NMC type cathodes, researchers on NMC 111 cathode materials can be easily applied on other NMC type cathodes as well.

He et al. (2024) conducted a comparative review of new hydrometallurgical and direct LiB recycling methods, discussing advancements and future commercialization pathways. However, numerical comparison is unavailable, hindering the adaptation of the best technologies for future applications [12]. Kallitsis et al. (2022) discuss the environmental impact of different recycling routes in another LCA study for NMC-type LiB recycling. This study focused on the total battery life cycle and compared hydrometallurgical and pyrometallurgical treatment options. The experiment concluded that hydrometallurgy has less environmental impact than alternative methods [13]. Therefore, hydrometallurgical recycling is gaining popularity owing to the efficient recovery of high-purity metals while reducing gas emissions and energy consumption. However, there is a lack of environmental and economic evaluation and comparison of the various hydrometallurgical recycling methods, leading to a lack of definitive determination of the most efficient approach [14].

LCA and LCC are practical tools that can compare technologies from environmental and economic perspectives. Castro et al. (2022) employed these methods to assess the potential enhancement of the entire treatment route developed. However, the higher impacts generated by the pretreatment steps used in the study hindered the impacts embedded in the hydrometallurgical steps. Fahimi et al. (2022) and Wu et al. (2022) have also conducted a study and compared the performance of various treatment routes used in treating LCO-type batteries. They performed a comparative analysis using the ESCAPE (embodied energy and carbon

footprint) approaches for the total treatment processes, which impedes the identification of more effective leaching or purification methods [15]. This is mainly because pretreatment is typically responsible for most emissions and energy utilization [16]. Wu et al. (2022) discussed and compared various hydrometallurgical and purification methods using an LCA based approach. However, as the study focused on LCO-type batteries, the applicability of these technologies in NMC-type batteries is problematic[17].

Rinne et al (2021) carried out a study to evaluate the possibilities of synergistic recovery of cathode metals from NMC-LiBs and nickel metal hydride (NiMH) batteries. However, the study discusses only one hydrometallurgical route with and without using NiMH battery materials and suggests that synergistic recycling is environmentally beneficial. Nevertheless, the study fails to compare other viable hydrometallurgical options that can be utilized to enhance the benefits. Moreover, economic evaluation is not done [18]. The study carried out by Du et al (2022) compares the use of virgin and recycled NMC cathode metals to produce power batteries in China through LCA approach. The study reveals that using recycled NMC lowers the environmental impacts than using virgin materials. However, this study also used only one hydrometallurgical route hindering the possibility of comparing various technologies applicable for the same [19]. Finally, Zhou et al (2021) elaborated comparative LCA of LiB recycling methods through merging different treatment segments such as pretreatment, pyrometallurgy, hydrometallurgy etc. Consideration of different cathode chemistries of LiBs and focusing on the total recycling line in the study hinders the importance of the hydrometallurgical refining part. This is mainly due to the higher environmental impact given by the pretreatment or pyrometallurgy method utilized. Other than that, hydrometallurgical material consumption varies largely on the cathode chemistries and using of a single hydrometallurgy route for various cathode materials can provide misleading information [20].

3. Methodology

3.1. Technology Identification

This investigation utilized the Scopus database to identify NMC cathode recycling technologies based on laboratory studies published between 2015 and 2024. The keywords "cathode", “NMC”, “recycling”, “black mass”, “hydrometallurgy", and "metal extraction" were employed with the Boolean operator "or" between terms. Articles were subsequently ranked based on their citation frequency. Initially, 250 articles were considered for the preliminary assessment, and manual filtering was conducted based on novelty and data

availability. Ultimately, nine distinct emerging technologies were identified from 20 articles. Further surveys were conducted to identify studies that converted the end products to Ni, Co and Mn oxides while Li being left in the final solution. References older than 2015 were used only if more details were required to confirm the corresponding technology. Pretreatment steps were not considered in this study, as they are well-established technologies [21]. The identified technologies are briefly summarized in Section 4.1 to provide a prior idea of the technology assessed in the next stage (Section 4.2). Among the identified technologies, three different purification technologies were incorporated for the analysis. Namely, oxalic acid-based purification, adsorbent (ion-exchange resin) based purification and solvent extraction-based purification. In order to provide a broader clarity, the flow diagrams for each purification technology were given under annexure 1, Figures S3.1, S3.2 and S3.3.

3.2. Life cycle assessment: goal and scope definition

The goal of the LCA study is to provide an extensive comparison between the emerging technologies used and those identified in Section 3.1. The technologies used in this study are all on laboratory scales with potential usage at industrial level. The possibility of using the technology on a larger scale was determined through the assessment of future recommendations of the studies referred. Recovery efficiencies, simplicity in adapting the technology, scalability and cost of materials were also considered to determine the applicability of the technology at the industrial level. As the technologies used in the study have a higher potential to be used soon, a critical analysis of their pros and cons is compulsory. Hence, the LCA and LCC based approach, and hotspot and scenario analyses were used as tools for this investigation. The LCA study will be an attributional ex-ante analysis to predict industrial level material requirement and emissions.

A treatment/extraction sequence based on NMC 111 type cathode material was used for LCA/LCC analysis to keep the consistency. Adjustments were made where necessary with assumptions to calculate the raw material requirements and products. The study was conducted according to ISO 14040 and 14044 standards. Sima Pro 9.5.0.1 software and Eco-invent 3.91V database were used to develop the model to evaluate the impacts of each theoretical route. All calculations were performed using the ReCIPe 2016 v1.1 midpoint (H) calculation method.

In the current study all the 18 impact categories: Global warming, Ozone formation (Terrestrial ecosystems), Terrestrial acidification, Freshwater eutrophication, Terrestrial ecotoxicity, Mineral resource scarcity, Fossil resource scarcity, Water consumption, Land use, Human non-

carcinogenic toxicity, Human carcinogenic toxicity, Marine ecotoxicity, Freshwater ecotoxicity, Marine eutrophication, Fine particulate matter formation, Ozone formation (Human health), Ionizing radiation, Stratospheric ozone depletion were used. Special attention was given to global warming potential impact category as it will be used for the benchmark analysis and for comparison with literature values as it represents the process emission effect. Nevertheless, freshwater eutrophication, marine eutrophication and stratospheric ozone depletion impact categories were not shown in results tables as these categories mostly showed damages less than 10^{-3} in corresponding units. However, they were shown in the damage assessment graphs in percentages for better clarity.

3.2.1. Functional unit

The functional unit of the study was selected as the treatment of 1 kg of NMC 111 cathode active material (where the oxide amounts of Co≈0.33 kg, Ni≈0.33 kg, and Mn≈0.33 kg is assumed based on the formula of the cathode material $LiNi_{0.33}Mn_{0.33}Co_{0.33}O_2$). The recovery of Co_3O_4, NiO, and MnO throughout the treatment process was considered as the final product. The total Li available in the cathode is assumed to be passed through each step and accumulate in the final solution where further refining can be done, and it was not used for mass balance calculations mainly due to the lack of focus on Li in most of the studies utilized and inconsistencies of the final form of Li. We identified each treatment route's emissions, recycling efficiencies, and outputs based on 1 kg of cathode active material input. In addition, 1 kg of NMC 111 input makes it easy to compare different routes and treatment segments.

3.2.2. System boundary

This study focuses solely on the specific hydrometallurgical treatment steps for the cathode materials of EoL LiBs. Therefore, we disregarded the steps such as production, transportation, and use that do not affect the treatment/ recovery of materials (Figure 3.1). For the LCA study, leaching, purification, and calcination (treatment for active materials) were only investigated since the study is focusing on the recovery of CRM from used LiBs cathodes. Also, unaffected treatment segments such as LiB collection of spent batteries, pretreatment, and final use of recovered materials were not considered, as they could be considered same for all the routes [16].

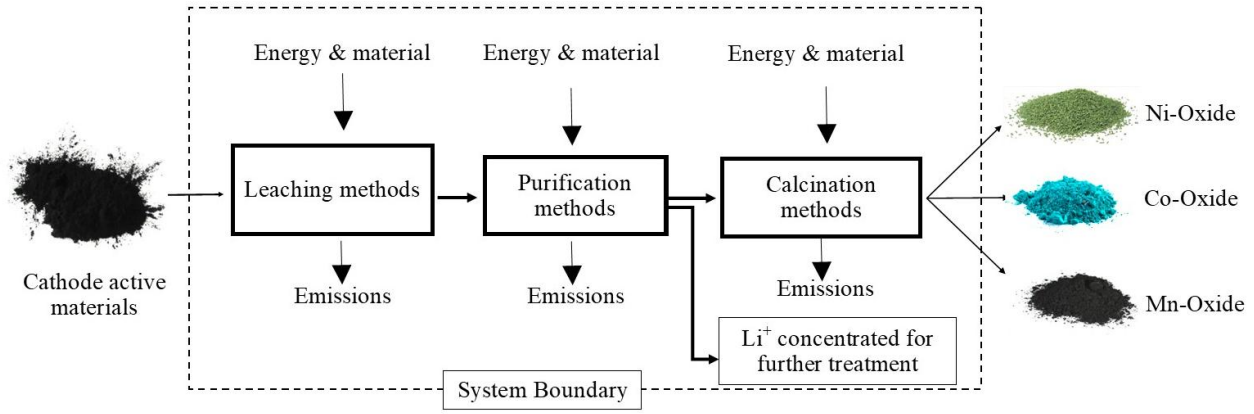

Figure 3.1 Depiction of the system boundary based on one treatment sequence.

3.2.3 Life cycle assessment: inventory and modelling

Inventories for four different leaching mechanisms (Deep eutectic solvent (DES) based leaching, Inorganic acid based leaching, Supercritical fluid (SCF) based leaching and Electrowinning (EC) based leaching), three different purification/separation mechanisms (Ion exchanged (IE) based separation, Solvent extraction (SE) based purification, Oxalate based (OP) precipitate separation), and two different calcination mechanisms (Hydroxide based calcination (HC), Oxalate based calcination (OC)) were extracted from the secondary sources. Organic acid-based leaching was not included in the study as an emerging technology as the DES based leaching is an advancement of the same where DES is made out of the combination of organic acids. At least two or more studies were used for each technology to calculate the chemical consumption, energy requirements, and emissions. Whenever no more than one study was found for a particular technology, other studies on NMC (811, 622, etc.) or LCO cathodes-based studies were utilized with necessary approximations. Stoichiometric calculations were performed to identify the products produced in each treatment step. However, the product quantity identified from stoichiometry was multiplied by the recovery efficiency at each step according to the literature. The ratio between the input and output metal oxides was used to calculate the efficiency of each treatment sequence. Since all the technologies evaluated were at the laboratory level, inventory analysis was performed for ~1 g of NMC 111 cathode active material treatment. LCA analysis was done for the 1 kg (default) NMC 111 treatments.

Chemical and energy usage and emissions identified were modelled in Sima Pro 9.5.0.1 using the Eco-invent 3.91V database (allocation cut-off, unit). The global average (GLO) eco-invent processes were selected for modelling. Whenever GLO processes were unavailable in the database, rest-of-world (RoW) processes were chosen for standardization. The unavailable process in the Eco-invent database was modelled separately using literature values. For

example, DES chemicals (oxalic acid and choline chloride) were not found in the database; hence, they were modelled using the process described by Zaib & Vahibi and Zhao and collaborators [22], [23]. The process for oxalic acid production was not available in the Eco-invent database; instead, acetic acid production was used because both acids have similar production procedure as depicted by Vahidi and Zhao (2017).

The energy consumption for each step was determined by assuming an average power consumption of the laboratory instruments for the corresponding steps. The total capacity of the instrument was used for pre-heating, and 30% working potential was used for the rest of the working period. The average instrumental power consumption is shown in the complete inventory analysis under the annexure 1. However, for EC-based leaching, the energy requirement was calculated using data from the corresponding articles [24], [25]. Consequently, equation 1 was utilized to calculate the electricity consumption of the process.

$$P = IV \text{----------(1)}$$

Where, P; power, I; current used and V; voltage applied. The energy consumptions were identified first for the total NMC 111 active materials utilized in the study. Later, the energy consumption for 1 g of the NMC 111 cathode material was calculated by dividing the total energy consumption by the amount of cathode materials treated. Nevertheless, under result and discussion section (section 4) energy consumptions were given as the Simapro-network diagram calculates for the treatment of 1 kg of cathode active materials. In addition, materials that can be used more than once, such as resins, their shelf life was used according to their data sheets to calculate the amount required for the treatment of 1 g of NMC 111. However, 20 usage cycles (standard scenario-without improvements) were assumed for the electrodes used in the EC leaching study as per the lack of data.

Finally, in addition to the eco-invent and modelled processes, dummy variables were used to link the technologies to arrange the treatment sequences. With nine technologies identified, seven treatment sequences that could be utilized to treat NMC 111 cathode active materials were elaborated.

3.2.4 Technology Comparison

Each technology under different treatment steps was discussed as per the output given by the LCA studies. Accordingly, comparison of the impacts of leaching technologies, purification steps and calcination possibilities were done based on the chemical usage, energy requirements,

and emissions for treating 1 kg of NMC 111 cathode active materials. Moreover, through the analysis, hotspots were identified for each technology where high impacts are generated.

3.2.5 Standard Scenario Comparison

The treatment sequences were simulated using technologies identified for each treatment segment, such as leaching, purification, and calcination. Only the possible sequences were considered (further elaborated under section 4.3). For example, the leaching solutions resulting from DES-based leaching contain oxalates; hence, using adsorbent materials or organic extractants is incompatible [26]. Therefore, purification based on precipitation (oxalates) was used for DES-based leaching followed by calcination. Moreover, the ion exchange resin-based purification or solvent extraction-based purification might be not compatible when oxalate anions are present in the leaching solution as it may produce flocs of precipitates and can block or reduce dissolving. Hence, these two technologies were not connected after the DES based leaching, instead oxalate-based precipitation and oxalate-based calcination was used. The identified treatment sequences are provided in the Results and Discussion section (section 4.3). The impact of each treatment sequence was analyzed based on the recovery efficiency of critical metals. Thus, the best treatment sequences for recovery efficiency and low environmental impact can be distinguished according to the standard scenario. The LCA inventory utilized for standard scenario analysis is given under annexure 2, section 1 along with methods, assumptions, process and data sources. A sensitivity analysis using a Monte Carlo simulation with 1,000 runs was also conducted to understand the uncertainty of the impact assessment. Results of the sensitivity analysis carried out for standard scenario are provided in annexure 1, Figure S3.4.

3.2.6 Improved scenario comparison

Improved scenarios for each treatment sequence (route) were established by improving the standard scenarios. For improvement, the factors identified during hotspot analysis were incorporated. Accordingly, an improved energy mix and low-voltage electricity generation by photovoltaic panels (Switzerland Energy Mix for Low Voltage) was used. The recycling rates were increased from 50% to 80% under improved scenarios for the organic acids/solvents used (e.g., DES, D2EHPA, or Cyanex 272), as suggested in the literature [22], [23]. In SCF-based leaching, the CO_2 recycling rate was assumed to be 80% in the improved version to prevent underestimation, although the literature shows that 100% recycling is possible in industrial lines [27]. Furthermore, the electrodes used in EC-based leaching were assumed to be used 50

times instead of 20 times. The organic solvents (DMSO) used in the DES-based leaching were reduced by 30%, assuming higher recycling at industry level [26].

Moreover, according to the findings of Guimaraes et al. (2022), the reducing agent usage was reduced by 50% for conventional inorganic acid leaching, although the authors mentioned leaching without reducing agents [7], [28]. The adsorbent materials (ion-exchange resin) used in adsorbent-based purification are determined to have a shelf life of 10 years instead of the 8 years used in the standard scenario [29]. The hazardous waste resulting from each purification step was reduced by 10%, assuming an industrial-level treatment [16]. Annexure 2, section 2 presents the complete LCA inventory of the improved scenario. The life-cycle impact of each treatment sequence was assessed with these improvements to approximate the industrial-level impact assessment. A sensitivity analysis is conducted to understand the uncertainties involved in the improved scenarios. Figure S3.5 in the annexure 1 provides the result obtained for the sensitivity analysis for improved scenario.

3.3 Life cycle costing study

As Villares et al. (2017) reported, material and energy efficiencies in industrial scale is significantly higher than laboratory scale estimations. Hence, Economic analyses were performed using the material consumption at improved scenario of the LCA study [30]. Using the improved scenario, it is reasonable to assume industrial-scale consumption.

The chemical consumption and waste generation for each route were calculated using the “process contribution” using the Sima-Pro software. The Ali-Baba trading, chem world and Intratec websites were consulted regarding the industrial level chemical prices [31], [32], [33]. World average electricity prices were taken from “Thunder said energy” research website [34]. Further, the costs for hazardous waste incineration and treatment of used ion exchange resin were taken from the “Boulder County” website [35]. The disposal costs for scrap metals were taken from Castro et al, 2022 [16]. The complete inventory set for the LCC analysis is given under each route in annexure 2, section S3, accordingly, the maximum and minimum values of the prices of various raw materials required for the specific treatment routes. Since the cost of materials is hidden trading information, receiving multiple values to work out the standard deviations was not possible. Hence, the highest and lowest prices given by websites had to be used for the calculation of standard deviations and variance. The following equation was utilized for the standard deviation under the assumption of uniform distribution of prices [36].

$$Stadnard\ deviation = \frac{(Maximum\ price - Minimum\ price)}{\sqrt{12}} \text{ ----------(2)}$$

Additionally, when the valuable spent products were received during the process, those were indicated with a negative price to show a potential income during the economic evaluation. As the literature proposed, this step was conducted only for organic products (DES solution and spent solvent mixtures) that could be recycled.

4. Results and discussion

4.1 Technology Analysis

Three emerging technologies were identified through recent secondary sources with promising scale-up potential. Moreover, inorganic acid-based leaching was also considered as an emerging technology as per the recent advancement achieved by many researchers in the field. Sulfuric acid-based leaching is well-reported in literature for LiBs recycling, and advancements can be observed in the reduced usage of hydrogen peroxide as a reducing agent and the reduced usage of acids [7], [28]. Different concentrations, leaching times, temperature and solid to liquid ratios are reported depending on various active materials studied.

DES-based leaching is a recent technology that has emerged for cathode material leaching. DES was made from hydrogen bond acceptors, and donors to dissolve the metal oxides available in the cathode (HBA-HBD type). This is because such solutions provide the required properties for leaching, such as low pH range, reducibility, and the ability to coordinate. According to the literature, the use of DES has environmental benefits, but recyclability is still a challenge [26]. Once the DES is made, the leaching is carried out like the inorganic acid based leaching mechanisms optimizing temperature, pH level, solid-liquid ratio and leaching time. Most recent studies show longer leaching hours for the DES based leaching as the acidic media is not corrosive as the inorganic acids [26], [37].

Supercritical fluids (SCF) are also used to leach metals from cathode active materials. In this emerging technology, the cathode active material will react with inorganic acid inside a pressurized reactor with the availability of CO_2. CO_2 will be inserted into the pressurized reactor via a high-pressure dosing pump in the liquid form. Due to the pressure and the heat inside the reactor the CO_2 will achieve its supercritical state by enhancing the speed of metal leaching. This method is highly effective because of its extremely high solubility and high stability provided by CO_2 and inorganic acid [38], [39]. The method is also seemingly

convenient for low energy use due to reduced reaction time and fast kinetics. It is reported that the leaching time can be reduced to 5-30 minutes using SCF based leaching [40].

Electrochemical (EC)-assisted leaching is an innovative technology recently used to leach NMC cathode active materials. The method is also reported as a green approach because it produces fewer toxic products and has lower energy use, with a comparably higher yield of recovered metals [24]. In this method the leaching will be carried out in a dual chamber electrochemical cell which is separated by a bi-polar membrane. For the anode, a foam made of nickel will be used while the cathode will be a stainless-steel electrode. The cathode compartment will contain the cathodic powder along with H_2SO_4 and $FeSO_4$, while the anode compartment uses KOH. As the current is passing through the cell, the metals will be leached to the solution [24], [25].

As the first purification technology, oxalate-based precipitation of metals considered as discussed by Chang et al (2022). Accordingly, when DES based leaching is used additional oxalic acid addition is not required to obtain the precipitates as the DES already contain oxalates. Hence, this method was only compatible when DES based leaching is done. Once the leachate is received, it will undergo dilution step with addition of dimethyl sulfoxide (DMSO) as the leachate has very low water dissolvability. After, leachate will be subjected to centrifugation at 10000 rpm for 5 minutes. This will separate Ni-oxalate dehydrate from the rest of the cations. The supernatant will be then diluted with DI water and heated up to 70 °C for 3 hours. Once filtered, the residue will contain Co-oxalate dehydrate while the filtrate will contain Mn metal ions. Then the pH of the filtrate will be adjusted to 12 using NaOH and the solution will be filtered for the second time. Here the residue will be Mn-Oxalate dehydrates [26], [41]. A flow diagram for the steps is given under Figure S3.1 in annexure 1.

Adsorbent material (ion-exchange resin)-based separation/purification is also an emerging technology that widely used in recent studies and most commercial chelating resins focus on Ni, Co, Mn, and Fe as iminodiacetate (Lewatit TP 207 and Amberlite IRC748), aminophosphonic acid (Purolite S950, Amberlite IRC-747, and Lewatit TP 260), and bis-picolylamine groups (Dowex M4195 and Lewatit TP 220) [25], [42]. Technology is applied once the metal ions are leached into the solution. The solution will be forced into a vessel that contains the target ion exchange resin. The flow rates must be adjusted to increase the efficiency of the metal ion exchangeability. Often, the pH of the carrier solution will be adjusted, and the carrier media will be fine-tuned to give out only the targeted metal ion to

maximize efficiency. For instance, low pH carrier solution will give out Ni^{2+} ions to the resin while, addition of ammonium acetate and diluted ammonium hydroxide will make Co^{2+} to be attached to the cation exchange resin. Later, Mn can be separated from the Li using solvent extraction method. Further, the solution might be required to pass through the ion exchange resin multiple times depending on the concentration of metal ions. Once the ion exchange resins are rich with targeted metal ions, the media will be backwashed with diluted inorganic acids (H_2SO_4) to release the metal ions back into a solution separately. Finally, the pH of the solutions will be increased up to 11 using NaOH to precipitate the metal ions as their hydroxides [25]. The Figure S3.2 in annexure 1 shows the flow diagram of the precipitation steps.

Organic solvent-based extraction is the third purification method identified. Technology uses the leached solution resulted from the leaching step. Firstly, liquid-liquid extraction can be utilized to extract Co from the leached solution towards Mn by 0.4 M Alamine 336 organic extractant which is combined with kerosene at the organic to aqueous (O/A) ratio of 0.5. The extracted Co may be contaminated with minor amounts of Mn (around 5.4%). This can be further purified by extracting Co from the Mn using D2EHPA extractant. The resulting Co rich solution can be used to precipitate Co in its hydroxide form at pH around 10 by adding NaOH. The Co depleted solution after the first extractant can be utilized to extract Ni by enriching the organic fraction with 0.7M Alamine 336 diluted with kerosene at O/A 2. This can effectively extract Ni which can be precipitated with addition of NaOH at pH of 8. This will also result in effluent rich with Li ions that may be extracted using an organic solvent of Cyanex 936. However, for the easiness of the study and for the standardization with other purification technologies, Li-ion is assumed to be left in the solution state. Mn in the organic fraction will be taken to aqueous fraction using inorganic acid (HCl) with 0.1 M concentration which can be then precipitated as $Mn(OH)_2$ with the addition of NaOH at pH 8 [43], [44]. The extraction steps are represented in the flow diagram given in annexure 1, Figure S3.3.

In addition to the three separation/purification methods, two calcination methods (hydroxide calcination and oxalate calcination) were used to convert the purified product into metal oxides. Accordingly, the precipitated metal hydroxides or metal oxalates will be heated to higher temperatures (~500-800 °C) in a vacuum furnace to eliminate water vapor or gases derived from thermal decompositions of hydroxide or oxalates. As per the studies found in secondary sources, both methods use longer calcination times (~24 hours) [45], [46]. These seven technologies, categorized into three main parts, as shown in Table 3.1, will be evaluated

regarding environmental and economic impacts using LCA and LCC studies in the next sections.

Table 3.1. Summary of technologies used in the study*.

Process	Technology	References used
Leaching technologies	Conventional leaching	[28], [47], [48]
	Deep eutectic solvent-based leaching	[26], [49], [50]
	Supercritical fluid-based leaching	[38], [51]
	Electrolysis based leaching	[24], [25]
Purification/separation technologies	Oxalate based purification	[26]
	Absorbent material-based purification	[25], [52]
	Organic solvent extractant based purification	[43], [44], [53]
Calcination technologies	Oxalate calcination	[46], [54], [55], [56]
	Hydroxide calcination	[45], [57], [58], [59]

4.2 Technology Comparison

The technologies identified in section 3.1 were compared according to their usage. For instance, the four identified leaching methods were compared with each other based on their environmental impacts. For comparison, the inputs and outputs required to treat 1 kg of NMC 111 cathode materials were considered. Similarly, the three purification methods and two calcination methods were compared. Through the comparison, hotspots for each treatment step were also identified.

4.2.1 Leaching methods

Table 3.2 shows the impacts received under significant impact categories for leaching technologies assessed. To compare the different leaching mechanisms studied, “leaching of 1 kg of NMC 111 cathode active material” was chosen as the functional unit. Results show that the highest contribution comes from electricity usage for inorganic and DES based leaching mechanisms. However, SCF and EC have very little impact from energy consumption. Highest

environmental degradation had occurred through DES based leaching and the lowest environmental impacts were reported by EC based leaching. The complete list of impacts under all 18 impact categories was given under annexure 1, Table S3.1.

Tabel 3.2 Impacts of leaching technologies under significant impact categories differentiated into contributed materials

1

		Inorganic leaching			
Impact category	Unit	Total	Sulfuric acid	Hydrogen peroxide	Electricity
Global warming	kg CO_2 eq	21.36	0.53	2.22	18.62
Ionizing radiation	kBq Co-60 eq	2.35	0.03	0.08	2.24
Ozone formation, Human health	kg NO_x eq	0.05	0.00	0.00	0.04
Fine particulate matter formation	kg PM2.5 eq	0.05	0.01	0.00	0.04
Ozone formation, Terrestrial ecosystems	kg NO_x eq	0.05	0.00	0.00	0.04
Terrestrial acidification	kg SO_2 eq	0.10	0.02	0.01	0.06
Terrestrial ecotoxicity	kg 1,4-DCB	53.00	14.01	9.30	29.69
Freshwater ecotoxicity	kg 1,4-DCB	1.58	0.27	0.16	1.16
Marine ecotoxicity	kg 1,4-DCB	2.01	0.35	0.20	1.46
Human carcinogenic toxicity	kg 1,4-DCB	1.08	0.06	0.25	0.77

Human non-carcinogenic toxicity	kg 1,4-DCB	25.39	5.18	3.04	17.17
Land use	m^2a crop eq	0.33	0.03	0.03	0.27
Mineral resource scarcity	kg Cu eq	0.15	0.12	0.01	0.02
Fossil resource scarcity	kg oil eq	5.63	0.33	0.66	4.64
Water consumption	m^3	0.32	0.07	0.11	0.14

1

		Supercritical fluid-based leaching						
Impact category	Unit	Total	Sulfuric acid	Hydrogen peroxide	Carbon dioxide	Sodium hydroxide	Water	Electricity
Global warming	kg CO_2 eq	13.42	0.30	0.93	3.53	8.63	0.00	0.03
Ionizing radiation	kBq Co-60 eq	1.12	0.02	0.03	0.12	0.95	0.00	0.00
Ozone formation, Human health	kg NO_x eq	0.03	0.00	0.00	0.00	0.02	0.00	0.00
Fine particulate matter formation	kg PM2.5 eq	0.03	0.00	0.00	0.00	0.02	0.00	0.00
Ozone formation, Terrestrial ecosystems	kg NO_x eq	0.03	0.00	0.00	0.00	0.02	0.00	0.00
Terrestrial acidification	kg SO_2 eq	0.06	0.01	0.00	0.01	0.03	0.00	0.00

Terrestrial ecotoxicity	kg 1,4-DCB	72.97	7.94	3.90	25.71	35.37	0.00	0.04
Freshwater ecotoxicity	kg 1,4-DCB	1.04	0.15	0.07	0.22	0.61	0.00	0.00
Marine ecotoxicity	kg 1,4-DCB	1.35	0.20	0.09	0.28	0.79	0.00	0.00
Human carcinogenic toxicity	kg 1,4-DCB	0.65	0.03	0.10	0.10	0.41	0.00	0.00
Human non-carcinogenic toxicity	kg 1,4-DCB	19.39	2.94	1.27	3.48	11.67	0.00	0.02
Land use	m^2a crop eq	0.28	0.02	0.01	0.05	0.20	0.00	0.00
Mineral resource scarcity	kg Cu eq	0.12	0.07	0.00	0.01	0.04	0.00	0.00
Fossil resource scarcity	kg oil eq	3.21	0.19	0.28	0.60	2.14	0.00	0.01
Water consumption	m^3	0.33	0.04	0.04	0.02	0.22	0.00	0.00

1

Deep eutectic solvent-based leaching				
Impact category	Unit	Total	Deep eutectic solvent	Electricity
Global warming	kg CO_2 eq	280.27	60.98	219.29
Ionizing radiation	kBq Co-60 eq	28.76	2.34	26.42
Ozone formation, Human health	kg NO_x eq	0.60	0.12	0.48

Fine particulate matter formation	kg PM2.5 eq	0.57	0.09	0.49
Ozone formation, Terrestrial ecosystems	kg NO_x eq	0.61	0.13	0.48
Terrestrial acidification	kg SO_2 eq	0.94	0.18	0.76
Terrestrial ecotoxicity	kg 1,4-DCB	491.82	142.07	349.74
Freshwater ecotoxicity	kg 1,4-DCB	15.97	2.36	13.61
Marine ecotoxicity	kg 1,4-DCB	20.26	3.07	17.18
Human carcinogenic toxicity	kg 1,4-DCB	10.79	1.69	9.10
Human non-carcinogenic toxicity	kg 1,4-DCB	246.76	44.51	202.25
Land use	m^2a crop eq	3.83	0.64	3.19
Mineral resource scarcity	kg Cu eq	0.37	0.15	0.22
Fossil resource scarcity	kg oil eq	87.85	33.18	54.67

		Electrolysis based leaching							
Impact category	Unit	Total	Sulfuric acid	Iron sulfate	Electrolyte, KOH	Steel	Nickel	Electricity	Scrap steel
Global warming	kg CO_2 eq	0.11	0.00	5.43	0.53	0.32	0.00	0.00	0.11

Ionizing radiation	kBq Co-60 eq	0.01	0.00	0.54	0.02	0.02	0.00	0.00	0.01
Ozone formation, Human health	kg NO_x eq	0.00	0.00	0.01	0.00	0.00	0.00	0.00	0.00
Fine particulate matter formation	kg PM2.5 eq	0.00	0.00	0.01	0.00	0.02	0.00	0.00	0.00
Ozone formation, Terrestrial ecosystems	kg NO_x eq	0.00	0.00	0.02	0.00	0.00	0.00	0.00	0.00
Terrestrial acidification	kg SO_2 eq	0.01	0.00	0.02	0.00	0.06	0.00	0.00	0.01
Terrestrial ecotoxicity	kg 1,4-DCB	2.92	0.00	22.90	17.07	14.86	0.00	0.02	2.92
Freshwater ecotoxicity	kg 1,4-DCB	0.06	0.00	0.37	0.04	0.30	0.00	0.32	0.06
Marine ecotoxicity	kg 1,4-DCB	0.07	0.00	0.48	0.06	0.39	0.00	0.39	0.07
Human carcinogenic toxicity	kg 1,4-DCB	0.01	0.00	0.30	0.20	0.05	0.00	0.01	0.01
Human non-carcinogenic toxicity	kg 1,4-DCB	1.08	0.00	7.63	0.79	4.49	0.00	0.27	1.08
Land use	m^2a crop eq	0.01	0.00	0.15	0.02	0.01	0.00	0.00	0.01
Mineral resource scarcity	kg Cu eq	0.03	0.00	0.37	0.06	0.09	0.00	0.00	0.03
Fossil resource scarcity	kg oil eq	0.07	0.00	1.34	0.12	0.08	0.00	0.00	0.07

1

A comparison of the percentage impact of each leaching method under different impact categories is shown in Figure 3.2.

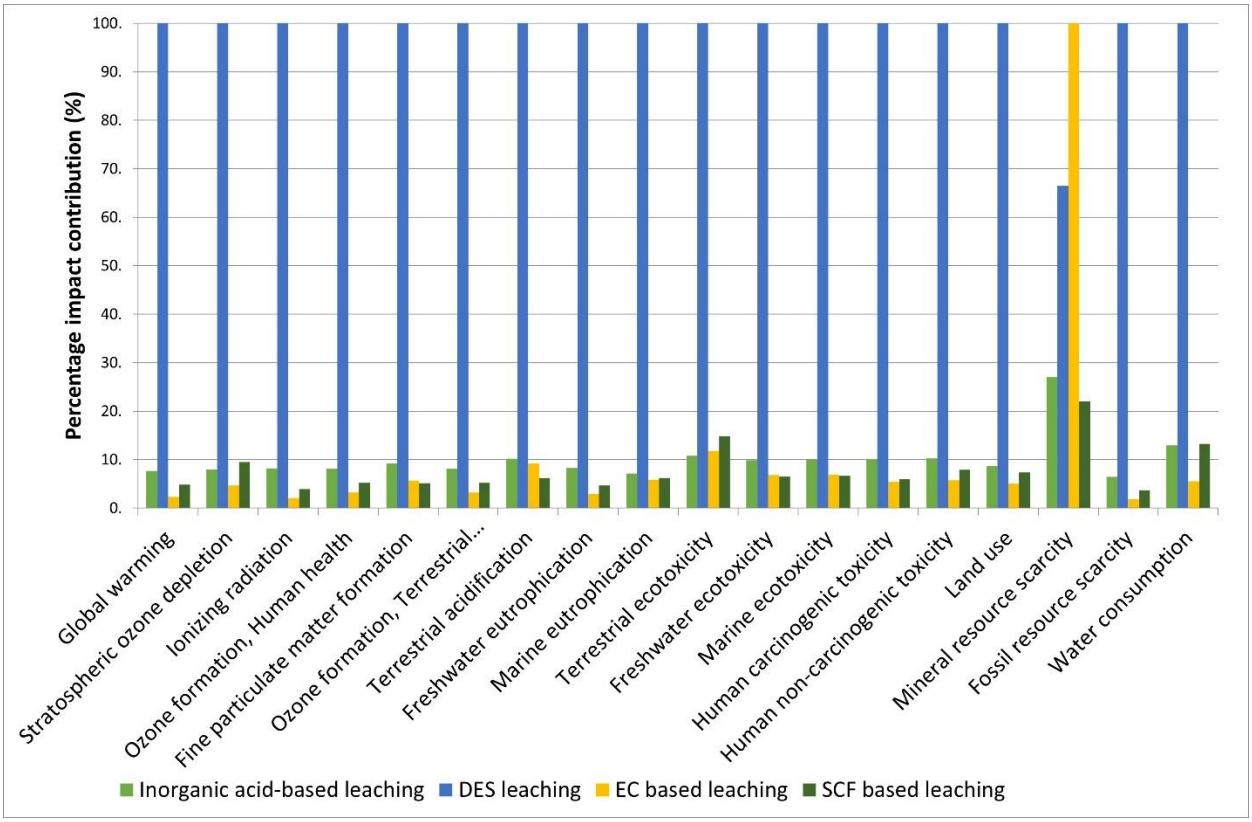

Figure 3.2 Percentage impacts of each leaching method under different impact categories (DES= Deep eutectic solvent, EC= Electrolysis, SCF= Supercritical fluid).

DES-based leaching causes more impacts under different impact categories studied, mainly due to electricity use. The total process emission effect (PEE) of DES-based leaching is 2.80×10^2 kg CO_2 eq. per 1kg of NMC 111 cathode material. The technique requires prolonged leaching hours, forcing the method to use more electricity in stirring and heating. The leaching of 1 kg of NMC 111 cathode active material requires approximately 1.04×10^3 MJ of electricity which caused approximately 78% of the impact of DES-based leaching. The rest (~22%) of the impacts were due to DES production. It seems that the use of choline chloride (ChCl) in DES has a great impact due to the high amount of ethylene oxide used in ChCl production. Despite that, most recovery mechanisms studied with DES-based leaching have repeatedly used ChCl as DES's hydrogen bond donor (HBD) [26], [37], [49]. It has been identified that the leaching of metal oxide strongly depends on the HBD of the DES, and ChCl is a good candidate for this purpose [60]. Hence, the substitutability of ChCl with a chemical with less impact is not convenient, and many authors

mentioned higher recyclability rates for DES, although we used 50% recyclability for the LCA analysis. Nevertheless, if very high recycling rates and considerable cut-off of electricity are used in the process, the impacts related may decrease, which will be analyzed under the improved scenario (Section 3.4).

The conventional leaching (inorganic) mechanism reported the second highest emission at 2.14 $\times 10^1$ kg CO_2 eq. among the techniques evaluated, considering 1 kg of cathode active material input. 87% of the reported impacts of conventional leaching by H_2SO_4 are also due to the high energy usage for heating, and the total electricity was 88.2 MJ. Moreover, 10% of the impact was generated through the production of H_2O_2. However, Guimarães et al. reported that it is possible to carry out the metal leaching process using inorganic acids such as H_2SO_4 without a reducing agent (H_2O_2), which can reduce the impact of the overall leaching process [7], [28]. The expected reaction with NMC 111 is given under equation 3.

$$6\,LiNiO_{0.33}CoO_{0.33}MnO_{0.33}O_2 + 8H_2SO_4 \rightarrow Ni_2SO_4 + 2CoSO_4 + 2MnSO_4 + 3Li_2SO_4 + 8H_2O + 5O_2 \quad (3)$$

The third highest emission was reported by SCF-based leaching, which amounted to 1.34 $\times 10^1$ kg CO_2 eq. per 1 kg of the active cathode material. The major part (~64.3%) of the reported impacts were from the use of NaOH for the treatment of CO_2 derived from the process. Electricity does not play a major role in SCF treatment because of the lower energy requirement for the reduced leaching time (approximately 5 min.) at slightly lower temperatures than those of conventional or DES-based leaching. This is a key energy-saving step in the technology considered.

Moreover, 26.3% of the total impact of the process was due to CO_2 usage. Although it is required to release CO_2 under laboratory conditions after treatment, in industrial supercritical extractions, CO_2 can be recirculated in higher percentages [27]. Hence, these emissions can be drastically lowered in actual SCF-based treatment lines. This can be further analyzed under the improved scenario.

The lowest impact was demonstrated by EC-based leaching at 6.39 $\times 10^0$ kg CO_2 eq. per 1 kg of cathode materials because of the lowest energy requirement for the electrolysis and the reusability of the electrodes. Impacts due to the energy usage is minimum as the electricity consumption is very low in the technique. So, a major part (~85%) of the impact is derived from using electrolyte

materials for electrolysis. The process uses approximately 2.5 kg of KOH electrolyte to treat 1 kg of the active materials. Approximately 9% of the impacts were derived from steel usage for the electrodes.

Additionally, EC-based leaching had the highest impact under the mineral resource scarcity impact category because steel and Ni-based minerals used for electrode manufacturing. DES-based leaching is the second highest under the same impact category because of the higher chemical and energy requirements for leaching. For the SCF and Conventional leaching methods, relatively lower amounts of mineral resources were used to prepare inorganic acids (e.g. H_2SO_4).

4.2.2 Purification/separation methods

Three different separation and purification methods were compared based on the environmental impact of each method. Moreover, for standardization, the functional unit of this part was adopted as the “purification/separation of 1 kg of NMC 111 leached metal ions”. Table 3.3 represents the impacts resulted by various purification methods under significant impact categories. In addition, Table S3.2 in annexure 1 contains the complete list of impacts of each technology analyzed under different impact categories.

1

2 Table 3.3 Impacts under significant impact categories for purification methods differentiated into contributed materials

Ion exchange-based purification									
Impact category	Unit	Total	ion-exchange resin	Sulfuric acid	Water	Hazardous waste	Ammonium hydroxide	Ammonium acetate	Electricity
Global warming	kg CO_2 eq	19.86	14.25	0.07	0.01	4.71	0.28	0.50	0.03
Ionizing radiation	kBq Co-60 eq	0.47	0.38	0.00	0.00	0.06	0.00	0.02	0.00
Ozone formation, Human health	kg NO_x eq	0.03	0.02	0.00	0.00	0.00	0.00	0.00	0.00
Fine particulate matter formation	kg PM2.5 eq	0.02	0.02	0.00	0.00	0.00	0.00	0.00	0.00
Ozone formation, Terrestrial ecosystems	kg NO_x eq	0.03	0.02	0.00	0.00	0.00	0.00	0.00	0.00
Terrestrial acidification	kg SO_2 eq	0.05	0.03	0.00	0.00	0.01	0.00	0.00	0.00
Terrestrial ecotoxicity	kg 1,4-DCB	46.26	35.79	1.85	0.03	4.55	1.58	2.40	0.04
Freshwater ecotoxicity	kg 1,4-DCB	0.72	0.55	0.04	0.00	0.10	0.01	0.02	0.00
Marine ecotoxicity	kg 1,4-DCB	0.94	0.72	0.05	0.00	0.13	0.01	0.03	0.00

Human carcinogenic toxicity	kg 1,4-DCB	1.12	0.60	0.01	0.00	0.49	0.00	0.01	0.00
Human non-carcinogenic toxicity	kg 1,4-DCB	16.20	12.28	0.69	0.01	2.71	0.13	0.37	0.02
Land use	m^2a crop eq	0.20	0.13	0.00	0.00	0.05	0.00	0.01	0.00
Mineral resource scarcity	kg Cu eq	0.06	0.04	0.02	0.00	0.00	0.00	0.00	0.00
Fossil resource scarcity	kg oil eq	5.64	4.84	0.04	0.00	0.40	0.11	0.24	0.01
Global warming	kg CO_2 eq	0.20	0.14	0.01	0.01	0.02	0.01	0.01	0.00

Oxalate based purification							
Impact category	Unit	Total	Dimethyl sulfoxide	Water	Sodium hydroxide	Electricity	Spent solvent mixture
Global warming	kg CO_2 eq	74.95	33.42	0.01	0.01	0.02	41.50
Ionizing radiation	kBq Co-60 eq	2.00	1.83	0.00	0.00	0.00	0.17
Ozone formation, Human health	kg NO_x eq	0.10	0.08	0.00	0.00	0.00	0.02
Fine particulate matter formation	kg PM2.5 eq	0.09	0.08	0.00	0.00	0.00	0.01

Ozone formation, Terrestrial ecosystems	kg NO_x eq	0.10	0.08	0.00	0.00	0.00	0.02
Terrestrial acidification	kg SO_2 eq	0.24	0.22	0.00	0.00	0.00	0.03
Terrestrial ecotoxicity	kg 1,4-DCB	154.77	140.50	0.03	0.03	0.03	14.18
Freshwater ecotoxicity	kg 1,4-DCB	2.76	2.58	0.00	0.00	0.00	0.18
Marine ecotoxicity	kg 1,4-DCB	3.57	3.32	0.00	0.00	0.00	0.24
Human carcinogenic toxicity	kg 1,4-DCB	1.33	1.07	0.00	0.00	0.00	0.26
Human non-carcinogenic toxicity	kg 1,4-DCB	44.60	39.20	0.01	0.01	0.02	5.37
Land use	m^2a crop eq	0.70	0.55	0.00	0.00	0.00	0.15
Mineral resource scarcity	kg Cu eq	0.19	0.17	0.00	0.00	0.00	0.02
Fossil resource scarcity	kg oil eq	26.64	25.39	0.00	0.00	0.00	1.23
Global warming	kg CO_2 eq	0.67	0.61	0.01	0.00	0.00	0.05

Solvent extraction-based purification

Impact category	Unit	Total	Hydrochloric acid	Extractant Solvent	Sodium hydroxide	Water	Electricity	Hazardous waste	Spent solvent mixture
Global warming	kg CO_2 eq	217.73	22.37	68.33	4.40	0.17	2.79	62.30	57.37
Ionizing radiation	kBq Co-60 eq	7.14	1.59	3.70	0.48	0.01	0.34	0.79	0.23
Ozone formation, Human health	kg NO_x eq	0.52	0.06	0.37	0.01	0.00	0.01	0.05	0.03
Fine particulate matter formation	kg PM2.5 eq	0.29	0.06	0.15	0.01	0.00	0.01	0.04	0.01
Ozone formation, Terrestrial ecosystems	kg NO_x eq	0.61	0.06	0.46	0.01	0.00	0.01	0.05	0.03
Terrestrial acidification	kg SO_2 eq	0.71	0.11	0.43	0.02	0.00	0.01	0.10	0.03
Terrestrial ecotoxicity	kg 1,4-DCB	593.22	129.47	360.58	18.04	0.84	4.45	60.23	19.60
Freshwater ecotoxicity	kg 1,4-DCB	9.28	2.37	4.86	0.31	0.02	0.17	1.29	0.25
Marine ecotoxicity	kg 1,4-DCB	12.21	3.06	6.42	0.40	0.02	0.22	1.75	0.33
Human carcinogenic toxicity	kg 1,4-DCB	10.62	1.14	2.31	0.21	0.01	0.12	6.48	0.36
Human non-carcinogenic toxicity	kg 1,4-DCB	173.67	41.31	80.31	5.95	0.29	2.58	35.82	7.42

Land use	m^2a crop eq	3.39	0.57	1.82	0.10	0.00	0.04	0.65	0.21
Mineral resource scarcity	kg Cu eq	0.73	0.27	0.36	0.02	0.00	0.00	0.06	0.03
Fossil resource scarcity	kg oil eq	118.12	6.05	103.30	1.09	0.04	0.70	5.24	1.71
Global warming	kg CO_2 eq	2.30	0.51	1.01	0.11	0.36	0.02	0.21	0.08
Ionizing radiation	kBq Co-60 eq	217.73	22.37	68.33	4.40	0.17	2.79	62.30	57.37

1

2

As per the results, the highest impact contribution is given by solvent extraction-based purification and the lowest is reported by ion-exchange resin-based purification. Unlike in leaching technologies, in purification process the highest contribution is given by the material usages rather than the energy usage. To compare the impact contribution by various mechanisms used for purification, Figure 3.3 illustrates the percentage of each technology's impact across various categories.

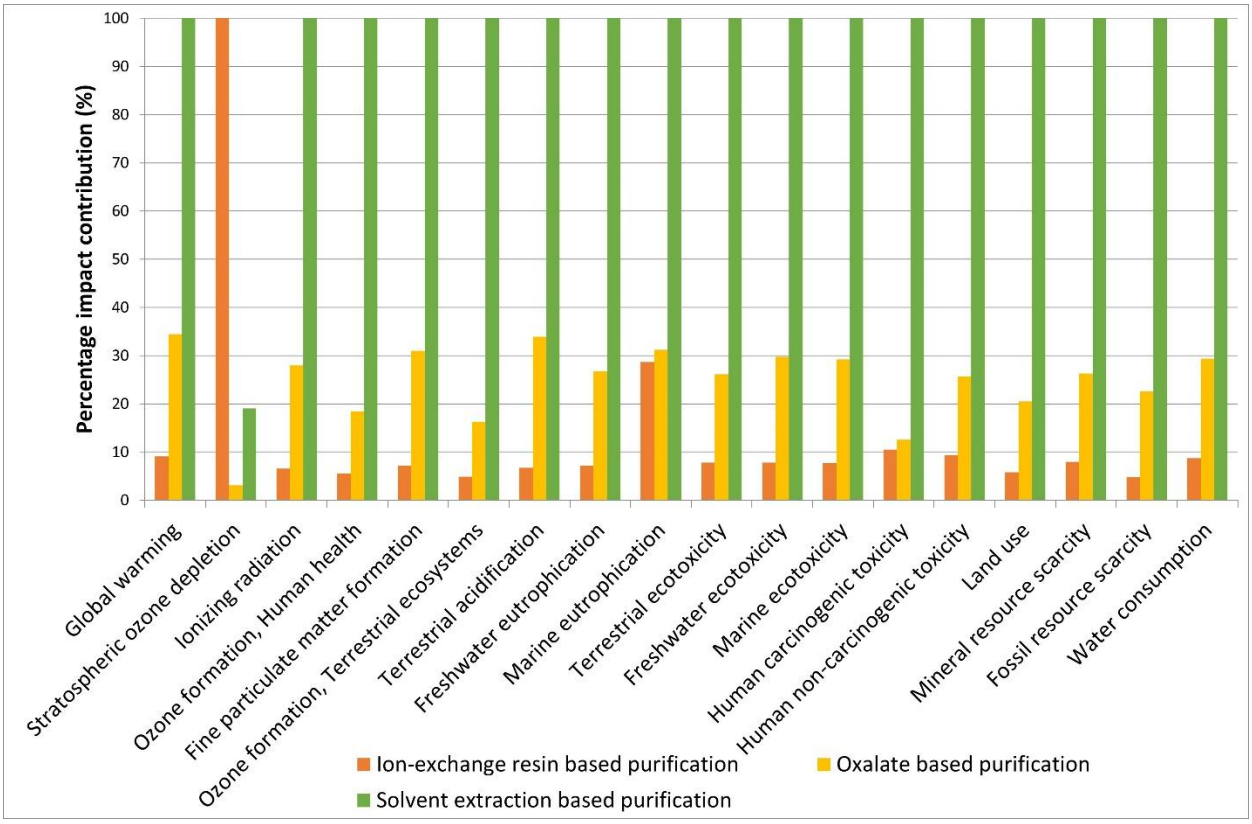

Figure 3.3 Percentage impact of each separation or purification method under different impact categories.

The solvent extraction has a high impact across many impact categories, except for stratospheric ozone depletion. The total PEE of the solvent extraction of leached metals is 2.18×10^2 kg CO_2 eq. per 1 kg of leached metal. The main contributor to the impacts generated in this category was the high use of organic solvents. It was observed that approximately 31.4% of the PEE was due to the use of organic solvents. Increasing the recyclability of organic solvents can reduce this impact.

However, it is important to note that, in this analysis, we used a recycling rate of 50% for organic solvents, which suggests that a recycling rate higher than 50% is required to lower the impact of organic solvents. Another 10% impact was attributed to the HCl used in the aqueous part when extracting metals from the organic fraction. The waste and by-products produced in the process also contribute to PEE significantly. For instance, hazardous waste from solvent extraction contributes approximately 28.6% of the overall emissions and 26.4% of the impact in the PEE caused by the heat used to treat these wastes and by-products. However, increasing the recycling rate can also reduce hazardous waste resulting from this method, thereby enhancing the overall environmental friendliness of technology. Energy use is not playing a major role in this procedure. In summary, the total sustainability of solvent-based extraction depends heavily on the recycling rate. Using organic solvents for extraction has a greater impact than inorganic solutions. However, under stratospheric ozone depletion, solvent extraction showed the lowest impact compared to the other mechanisms. The main reason for this could be the use of organic materials for the treatment. Organic solvents do not contain halogens, whereas inorganic acids or solvents are composed of halogens that can be easily released during the reaction, further impacting stratospheric ozone depletion.

Oxalate-based purification methods were designed to purify the metals derived from the DES-based leaching process as the metals leached would not be used in solvent-based or adsorbent material-based extraction as explained under section 3.2.3. Moreover, to keep the metals in the suspension until further separation, DMSO is needed due to the addition of DES, which made the solutions less soluble in water. When oxalate-based purification was used, adding DMSO had the largest effect (approximately 99%) on the total emissions (7.50×10^1 kg CO_2 eq. per 1 kg of leached metal). This impact was divided into two categories: 1) direct DMSO (44.6%) and 2) spent solvent mixture (55.4%). However, there is a higher possibility of recycling these solvents back into the process, lowering the overall impact. In the current study, we used 50% recycling, which is not sufficient to lower the overall impact generated by the solvents used. Compared with other contributors, the impact of electricity was negligible for oxalate-based purification.

Metal extraction based on adsorbent materials has the lowest impact on separation and purification treatment methods. The total emission of this mechanism is reported to be 1.99×10^1 kg CO_2 eq. per 1 kg of leached metal. The primary contributor was ion-exchange resin usage, which accounted

for approximately 71.7% of the PEE. The production and transportation of ion-exchange resins directly contribute to this impact. Moreover, the incineration of hazardous waste and the disposal of spent ion-exchange resin and waste chemicals accounted for 23.8% of the generated impact. Additionally, the adsorbent material-based purification showed the highest impact under stratospheric ozone depletion. The "ion-exchange resin usage" primarily generates 99% of the impact on this category. This originates from the use of trichloromethane to produce ion-exchange resins. Energy usage is again negligible for this process.

4.2.3 Precipitate calcination methods

Because the purification and separation methods provide different precipitates, a calcination step was used to convert the precipitates to oxides of the corresponding metals. In this study, we analyzed two calcination methods: hydroxide and oxalate calcination. The functional unit used for the analysis was 1 kg of metal oxide (Co, Mn, and Ni oxides) produced via calcination. The initial literature analysis shows that both methods used longer calcination times. However, gaseous emissions depend on the anion (-hydroxide or -oxalate) present in the precipitate. Table 3.4 shows the results of impact contribution from components for significant impact categories. Annexure 1 (Table S3.3) also provides the complete environmental impact reported for the two calcination methods for different impact categories.

Table 3.4 Impact contribution for significant impact categories from main components of calcination methods

Oxalate calcination			
Impact category	Unit	Total	Electricity
Global warming	kg CO_2 eq	94.71	93.74
Ionizing radiation	kBq Co-60 eq	11.29	11.29
Ozone formation, Human health	kg NO_x eq	0.20	0.20
Fine particulate matter formation	kg PM2.5 eq	0.21	0.21
Ozone formation, Terrestrial ecosystems	kg NO_x eq	0.21	0.21
Terrestrial acidification	kg SO_2 eq	0.32	0.32

Terrestrial ecotoxicity	kg 1,4-DCB	149.50	149.50
Freshwater ecotoxicity	kg 1,4-DCB	5.82	5.82
Marine ecotoxicity	kg 1,4-DCB	7.35	7.35
Human carcinogenic toxicity	kg 1,4-DCB	3.89	3.89
Human non-carcinogenic toxicity	kg 1,4-DCB	86.45	86.45
Land use	m^2a crop eq	1.36	1.36
Mineral resource scarcity	kg Cu eq	0.09	0.09
Fossil resource scarcity	kg oil eq	23.37	23.37

Hydroxide calcination			
Impact category	Unit	Total	Electricity
Global warming	kg CO_2 eq	60.60	60.60
Ionizing radiation	kBq Co-60 eq	7.30	7.30
Ozone formation, Human health	kg NO_x eq	0.13	0.13
Fine particulate matter formation	kg PM2.5 eq	0.13	0.13
Ozone formation, Terrestrial ecosystems	kg NO_x eq	0.13	0.13
Terrestrial acidification	kg SO_2 eq	0.21	0.21
Terrestrial ecotoxicity	kg 1,4-DCB	96.65	96.65
Freshwater ecotoxicity	kg 1,4-DCB	3.76	3.76
Marine ecotoxicity	kg 1,4-DCB	4.75	4.75
Human carcinogenic toxicity	kg 1,4-DCB	2.51	2.51
Human non-carcinogenic toxicity	kg 1,4-DCB	55.89	55.89
Land use	m^2a crop eq	0.88	0.88

Mineral resource scarcity	kg Cu eq	0.06	0.06
Fossil resource scarcity	kg oil eq	15.11	15.11
Global warming	kg CO_2 eq	0.45	0.45

Results suggest that electricity usage is the main component for the impact generation. Hydroxide based calcination has lower impact than oxalate-based calcination under different impact categories.

Figure 3.4 compares the impacts generated by the calcination of each anion-based precipitate.

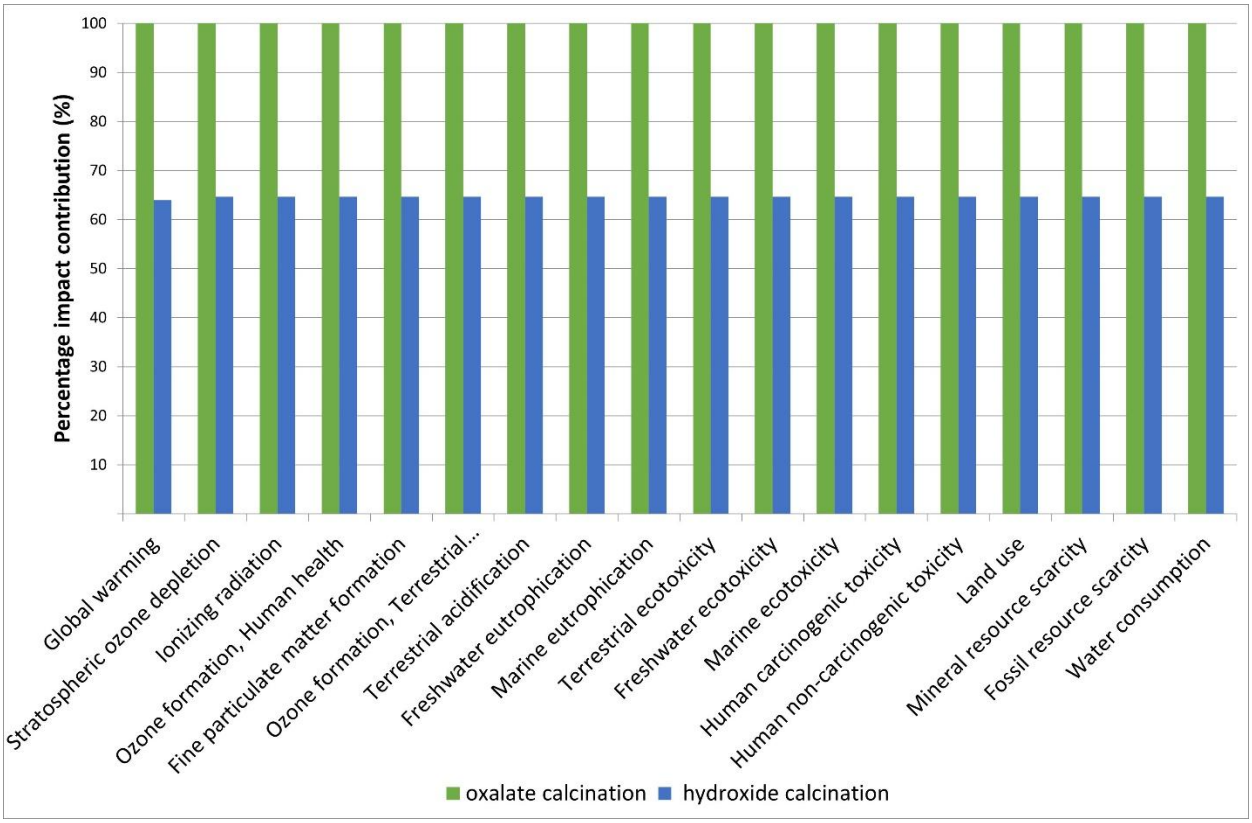

Figure 3.4 Percentage impact of the two calcination methods under different impact categories.

According to the analysis, oxalate-based calcination has a greater environmental impact than hydroxide-based calcination because it requires more oxalate salts and requires more energy than hydroxides to produce 1 kg of metal oxide. According to stoichiometry, to produce 1 kg of mixed metal oxides it would require 1.935 kg of mixed metal oxalates (eq.4). However, the same amount of metal oxides can be made by using only 1.215 kg of mixed metal hydroxides (eq.5). Moreover,

about 444 MJ of electricity is required to produce 1 kg of metal oxide through oxalate calcination. However, GHG emissions have a minimal impact compared to the energy requirement for the calcination process. In contrast, hydroxide-based calcination is environmentally friendly and requires less energy (287 MJ) to produce 1 kg of metal oxide. In both calcination methods, the impact was almost completely generated by electricity consumption because calcination processes lasting longer than 28 hours. Hence, Figure 3.4 shows a similar pattern of impact under different impact categories.

$$3CoC_2O_4 \rightarrow Co_3O_4 + 6CO_2 \text{----------(2)}$$

$$6Co(OH)_2 + O_2 \rightarrow 2Co_3O_4 + 6H_2O \text{----------(3)}$$

Furthermore, the thermal breakdown of cobalt oxalate produces GHG emissions, whereas cobalt hydroxide produces only water vapor. This also reduced the total impact generated by hydroxide calcination.

4.3 Standard scenario comparison

Standard scenarios were established using alternative possibilities of leaching, purification, and calcination technologies. Seven routes were designed using different combinations of the identified technologies and the compatibility of the resulting solutions in each step with the next combined technology was considered. For example, DES-based leaching is incompatible with adsorbent materials and solvent extraction-based purification because of the availability of oxalate [26]. Furthermore, oxalate-based precipitation and hydroxide-based calcination are incompatible methods. Only sulfate-based leaching solutions were compatible with solvent or adsorbent material extraction [25], [44]. And hydroxide-based precipitation or extraction is only compatible with hydroxide-based calcination. This also applies to oxalate-based precipitation. Therefore, these technologies have led to the design of a limited number of routes. Figure 3.5 shows each route with the corresponding hydrometallurgical steps involved.

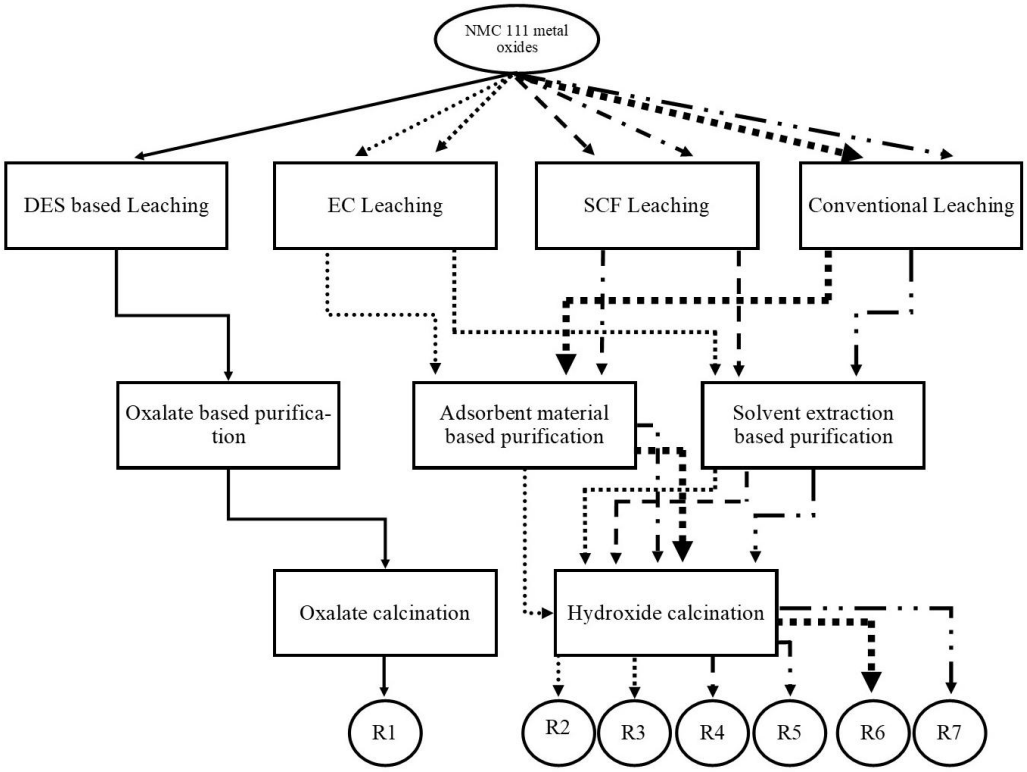

Figure 3.5 The flow chart of technologies used for each recovery route (DES= Deep eutectic solvent, EC= Electrolysis, SCF= Supercritical fluid).

The CRM mass transfer from the active material to the leaching solution was calculated considering the leaching efficiency reported in the literature. The mass of CRM in the purified solution or semi-precipitate was calculated by multiplying the mass of CRM in the leachate by the average recovery efficiency of the purification or separation method. Similarly, the calcined oxide mass for each metal was calculated by multiplying the CRM mass in the precipitates by the recovery efficiency of the calcination method. Stoichiometric calculations were also incorporated when the metal oxide changed to metal ions, metal oxalate/hydroxide, and finally to oxide again. Table 3.5 provides these mass transfer values based on 1 g of the cathode active material.

Table 3.5 Mass transfer of elected critical raw materials in each conceptual route with the final recovery efficiency*.

NMC 111 oxide	After leaching	After purification	After calcination	Total

Metal oxide	Mass (g)	Metal ion	Mass (g)	Metal oxalate/hydroxide	Mass (g)	Metal oxide	Mass (g)	**Recovery efficiency (%)**
Route 1	NMC 111 → DES leaching → Oxalate purification → Oxalate calcination → Metal oxide							
Co oxide	0.33	Co^{2+}	0.19	CoC_2O_4	0.43	Co_3O_4	0.23	70%
Ni oxide	0.33	Ni^{2+}	0.20	NiC_2O_4	0.49	NiO	0.25	76%
Mn oxide	0.33	Mn^{2+}	0.18	MnC_2O_4	0.47	MnO	0.23	71%
Route 2	NMC 111 → EC leaching → Adsorbent mat. purification → Hydroxide calcination → Metal oxide							
Co oxide	0.33	Co^{2+}	0.19	$Co(OH)_2$	0.31	Co_3O_4	0.26	80%
Ni oxide	0.33	Ni^{2+}	0.19	$Ni(OH)_2$	0.30	NiO	0.25	74%
Mn oxide	0.33	Mn^{2+}	0.18	$Mn(OH)_2$	0.29	MnO	0.23	71%
Route 3	NMC 111 → EC leaching → Solvent extr. purification → Hydroxide calcination → Metal oxide							
Co oxide	0.33	Co^{2+}	0.19	$Co(OH)_2$	0.29	Co_3O_4	0.25	76%
Ni oxide	0.33	Ni^{2+}	0.19	$Ni(OH)_2$	0.30	NiO	0.24	73%
Mn oxide	0.33	Mn^{2+}	0.18	$Mn(OH)_2$	0.26	MnO	0.20	62%
Route 4	NMC 111 → SCF leaching → Solvent extr. purification → Hydroxide calcination → Metal oxide							
Co oxide	0.33	Co^{2+}	0.15	$Co(OH)_2$	0.23	Co_3O_4	0.19	59%
Ni oxide	0.33	Ni^{2+}	0.15	$Ni(OH)_2$	0.23	NiO	0.19	57%
Mn oxide	0.33	Mn^{2+}	0.14	$Mn(OH)_2$	0.21	MnO	0.16	50%
Route 5	NMC 111 → SCF leaching → Adsorbent mat. purification → Hydroxide calcination → Metal oxide							
Co oxide	0.33	Co^{2+}	0.15	$Co(OH)_2$	0.24	Co_3O_4	0.21	62%
Ni oxide	0.33	Ni^{2+}	0.15	$Ni(OH)_2$	0.23	NiO	0.19	57%

Mn oxide	0.33	Mn^{2+}	0.14	$Mn(OH)_2$	0.23	MnO	0.19	57%
Route 6	NMC 111 → conventional leaching → Adsorbent mat. purification → Hydroxide calcination → Metal oxide							
Co oxide	0.33	Co^{2+}	0.20	$Co(OH)_2$	0.32	Co_3O_4	0.27	83%
Ni oxide	0.33	Ni^{2+}	0.20	$Ni(OH)_2$	0.32	NiO	0.26	77%
Mn oxide	0.33	Mn^{2+}	0.19	$Mn(OH)_2$	0.30	MnO	0.24	74%
Route 7	NMC 111 → conventional leaching → Solvent extr. purification → Hydroxide calcination → Metal oxide							
Co oxide	0.33	Co^{2+}	0.20	$Co(OH)_2$	0.30	Co_3O_4	0.26	79%
Ni oxide	0.33	Ni^{2+}	0.20	$Ni(OH)_2$	0.31	NiO	0.25	77%
Mn oxide	0.33	Mn^{2+}	0.19	$Mn(OH)_2$	0.27	MnO	0.21	65%

***NMC= $LiNi_{0.33}Mn_{0.33}Co_{0.33}O_2$, DES= Deep eutectic solvent, EC= Electrolysis, SCF= Supercritical fluid**

1

2 4.3.1 Life cycle assessment of standard scenario

3 Mass transfers, efficiencies (Table 3.2), and inventory collection (annexure 2, Section S1) were
4 employed for the life-cycle comparison of the different conceptual routes established. The analysis
5 used the recovery of 1 kg of cathode active material from NMC 111 LiBs as its functional unit.
6 Table 3.6 shows the impacts generated by each CRM extraction route for different impact
7 categories.

8

9

Table 3.6 Impacts made by each route under different impact categories*.

Impact category	Unit	Route 1	Route 2	Route 3	Route 4	Route 5	Route 6	Route 7
Global warming	kg CO_2 eq	5.26×10^{2}	1.53×10^{2}	2.56×10^{2}	2.09×10^{2}	1.28×10^{2}	1.74×10^{2}	2.82×10^{2}
Stratospheric ozone depletion	kg CFC11 eq	2.13×10^{-4}	5.38×10^{-4}	1.50×10^{-4}	1.24×10^{-4}	4.28×10^{-4}	5.63×10^{-4}	1.59×10^{-4}
Ionizing radiation	kBq Co-60 eq	5.42×10^{1}	1.71×10^{1}	1.99×10^{1}	1.63×10^{1}	1.41×10^{1}	1.96×10^{1}	2.25×10^{1}
Ozone formation, Human health	kg NO_x eq	1.09×10^{0}	3.29×10^{-1}	5.88×10^{-1}	4.77×10^{-1}	2.74×10^{-1}	3.71×10^{-1}	6.41×10^{-1}
Fine particulate matter formation	kg PM2.5 eq	1.07×10^{0}	3.43×10^{-1}	4.75×10^{-1}	3.76×10^{-1}	2.73×10^{-1}	3.75×10^{-1}	5.13×10^{-1}
Ozone formation, Terrestrial ecosystems	kg NO_x eq	1.11×10^{0}	3.32×10^{-1}	6.42×10^{-1}	5.20×10^{-1}	2.77×10^{-1}	3.75×10^{-1}	6.98×10^{-1}
Terrestrial acidification	kg SO_2 eq	1.78×10^{0}	5.80×10^{-1}	9.27×10^{-1}	7.17×10^{-1}	4.45×10^{-1}	6.10×10^{-1}	9.71×10^{-1}
Freshwater eutrophication	kg P eq	2.37×10^{-1}	7.41×10^{-2}	1.02×10^{-1}	8.31×10^{-2}	6.11×10^{-2}	8.38×10^{-2}	1.13×10^{-1}
Marine eutrophication	kg N eq	1.89×10^{-2}	6.00×10^{-3}	7.61×10^{-3}	6.14×10^{-3}	4.89×10^{-3}	6.37×10^{-3}	8.04×10^{-3}
Terrestrial ecotoxicity	kg 1,4-DCB	9.02×10^{2}	2.99×10^{2}	5.96×10^{2}	4.95×10^{2}	2.62×10^{2}	3.04×10^{2}	6.14×10^{2}
Freshwater ecotoxicity	kg 1,4-DCB	3.01×10^{1}	9.87×10^{0}	1.42×10^{1}	1.13×10^{1}	7.93×10^{0}	1.07×10^{1}	1.52×10^{1}
Marine ecotoxicity	kg 1,4-DCB	3.81×10^{1}	1.25×10^{1}	1.82×10^{1}	1.46×10^{1}	1.01×10^{1}	1.36×10^{1}	1.96×10^{1}

Human carcinogenic toxicity	kg 1,4-DCB	1.99×10^{1}	6.81×10^{0}	1.19×10^{1}	9.49×10^{0}	5.53×10^{0}	7.57×10^{0}	1.28×10^{1}
Human non-carcinogenic toxicity	kg 1,4-DCB	4.58×10^{2}	1.48×10^{2}	2.29×10^{2}	1.88×10^{2}	1.24×10^{2}	1.65×10^{2}	2.50×10^{2}
Land use	m^2a crop eq	7.16×10^{0}	2.27×10^{0}	3.96×10^{0}	3.23×10^{0}	1.91×10^{0}	2.49×10^{0}	4.25×10^{0}
Mineral resource scarcity	kg Cu eq	6.77×10^{-1}	7.18×10^{-1}	1.09×10^{0}	5.45×10^{-1}	2.52×10^{-1}	3.22×10^{-1}	7.12×10^{-1}
Fossil resource scarcity	kg oil eq	1.53×10^{2}	3.84×10^{1}	1.00×10^{2}	8.05×10^{1}	3.21×10^{1}	4.40×10^{1}	1.08×10^{2}
Water consumption	m^3	4.35×10^{0}	1.26×10^{0}	2.38×10^{0}	2.09×10^{0}	1.21×10^{0}	1.49×10^{0}	2.66×10^{0}

***Impacts made per 1kg of cathode active material treatment**

1

Table 3.6 shows that route 1 has the most significant effect on all types of impacts, such as DES-based leaching, oxalate-based purification, and metal-oxalate calcination. The high impact stemmed from the high electricity consumption of the leaching and calcination sections (around 2000 MJ). The percentage contributions of the two processes to the PEE were 53.3% and 38.6%, respectively. Moreover, the percentage contribution of Ni-oxalate calcination (13.7%) was higher than that of Mn and Co, where Co-oxalate calcination had the lowest (11.8%). However, route 1 has a lower impact on stratospheric ozone depletion and mineral resource scarcity. This is because of the use of organic solvents and the low mineral intensity of the materials used for the treatment process.

Route 7, which involved conventional leaching, solvent extraction, and calcination of metal hydroxide, had the second-highest impact. This is because the solvent extraction-based purification method significantly impacts the total emissions - 45.6%. Furthermore, the calcination of metal hydroxides accounted for approximately 46.6% of the impact in the same category. Among the calcination processes, Ni-hydroxide was the highest contributor (16.6%), followed by cobalt-hydroxide (16%) and Mn-hydroxide (14.2%). Compared with these, the contribution of the leaching step was negligible (7.5%). Nevertheless, route 7 showed less stratospheric ozone depletion impact because of the organic solvent-based purification process. The total energy requirement for route 7 is 721 MJ and major part of this is used by the calcination process.

Routes 3 and 4 provide the third- and fourth-highest contributions, respectively. Both methods use solvent-based extraction for purification, followed by hydroxide-based calcination. Further analysis of the two routes revealed that these two steps, not the leaching method used, were responsible for the highest contribution (48% contribution for route 3 and 46.2% for route 4) for the PEE. Nevertheless, route 3 had the greatest impact on mineral resource scarcity due to electrolyte materials' high contribution to EC leaching (50.5%) and the hydrochloric and organic solvents used in purification (38%). Organic extractants from petroleum-based raw materials (such as Cyanex 272) can contribute significantly to mineral resource scarcity. The energy requirement for route 3 was 607 MJ and for route 4 was 476 MJ.

Routes 5, 2, and 6, ranked from lowest to highest, had the lowest impacts. Although the reported routes had a lower impact in many categories, they had the highest impact on stratospheric ozone depletion. This is because the adsorbent material-based purification system utilizes ion-exchange

resins. Given that all three routes share the same calcination process, we can conclude that route 5 experienced the least impact owing to the SCF-based leaching process. However, it should be noted that SCF has lower material recovery efficiency (~58%). This characteristic of SCF leaching provides a lower mass of material to the next steps lowering the overall material consumption of the treatment mechanism which can ultimately lower the environmental impact of the route. This was followed by hydroxide-based calcination, which had the least environmental impact under calcination methods. Moreover, EC-based leaching lowers the impact compared with conventional leaching method which shows supremacy of the route even with high material recovery. Routes 2, 5 and 6 consumed 639, 501, and 754 MJ respectively. We normalized the impact categories by converting all impacts into a single unit to identify those that contributed more significantly than the others. Figures 3.6-a and b show the selected impact categories for each treatment route before and after normalization. Categories that give a broader outlook were manually selected over the 18 impact categories to keep the clarity of the figure.

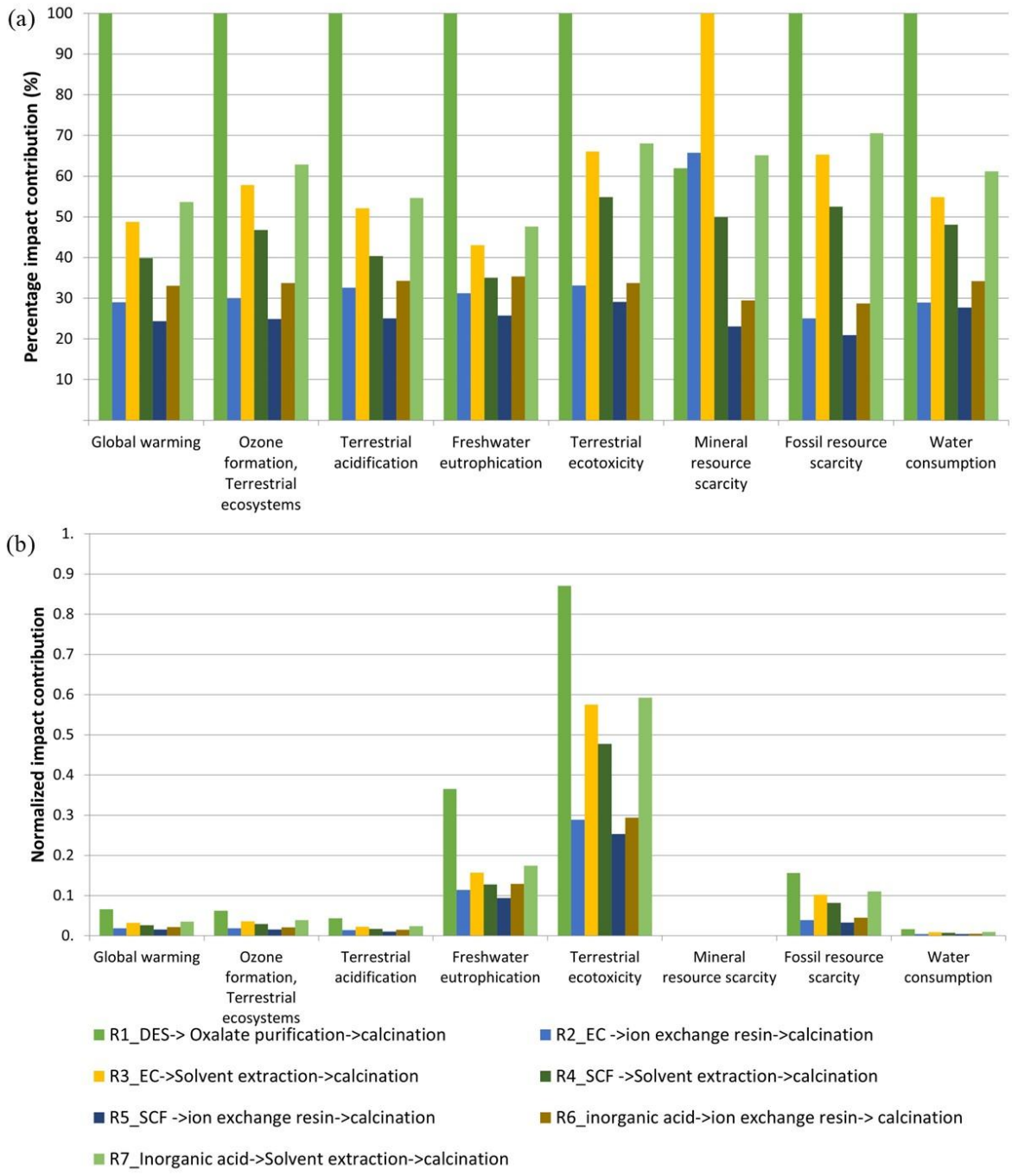

Figure 3.6 Comparison of a) percentage impacts made by each route under various impact categories; b) normalized impacts made under different impact categories by route (*DES= Deep eutectic solvent, EC= Electrolysis, SCF= Supercritical fluid).

The results in Figure 3.6 indicate that terrestrial ecotoxicity, freshwater eutrophication, and fossil resource scarcity have the highest significance among all impact categories. Hence, the identified

treatment procedures have a significantly higher impact on these categories. However, the order of the routes according to the highest-to-lowest impact generation remains unchanged, suggesting that Route 1 has the highest environmental impact while Route 5 has the lowest.

As the final part of the standard scenario analysis, a Monte Carlo analysis was performed with 1,000 iterations, considering routes 1 and 5. This was performed to evaluate the sensitivity of the model. Annexure 1, Figure S3.4, presents the results of the analysis. Accordingly, Route 5 is certainly better under many impact categories than Route 1, with 1000 adjustments of values within the standard deviation. Under the water consumption impact category, it is unclear whether Route 5 is always better than route 1. However, under stratospheric ozone depletion, Route 5 has an exceptionally low probability of lowering the impact.

4.4 Life cycle assessment for the improved scenario

For the improved version, industrial-level recycling rates, material usage, and waste material handling were used as specified in Section 3.2.6. Annexure 2, section S2 presents the comprehensive assessment of inventory. Table 3.7 shows the impacts produced by each improved route version under different impact categories.

Table 3.7 Impacts made by each improved route under different impact categories*

Impact category	Unit	Route 1	Route 2	Route 3	Route 4	Route 5	Route 6	Route 7
Global warming	kg CO_2 eq	1.07×10^{2}	3.43×10^{1}	9.95×10^{1}	7.85×10^{1}	2.74×10^{1}	3.38×10^{1}	1.02×10^{2}
Stratospheric ozone depletion	kg CFC11 eq	9.77×10^{-5}	4.11×10^{-4}	7.85×10^{-5}	6.23×10^{-5}	3.23×10^{-4}	4.27×10^{-4}	8.10×10^{-5}
Ionizing radiation	kBq Co-60 eq	1.11×10^{2}	3.58×10^{1}	3.63×10^{1}	3.09×10^{1}	3.05×10^{1}	4.16×10^{1}	4.22×10^{1}
Ozone formation, Human health	kg NO_x eq	2.08×10^{-1}	7.02×10^{-2}	2.08×10^{-1}	1.62×10^{-1}	5.41×10^{-2}	6.69×10^{-2}	2.11×10^{-1}
Fine particulate matter formation	kg PM2.5 eq	1.73×10^{-1}	6.45×10^{-2}	1.52×10^{-1}	1.16×10^{-1}	4.70×10^{-2}	5.92×10^{-2}	1.50×10^{-1}
Ozone formation, Terrestrial ecosystems	kg NO_x eq	2.14×10^{-1}	7.15×10^{-2}	2.30×10^{-1}	1.80×10^{-1}	5.51×10^{-2}	6.82×10^{-2}	2.33×10^{-1}
Terrestrial acidification	kg SO_2 eq	4.30×10^{-1}	1.58×10^{-1}	3.65×10^{-1}	2.78×10^{-1}	1.16×10^{-1}	1.52×10^{-1}	3.67×10^{-1}
Freshwater eutrophication	kg P eq	7.26×10^{-2}	2.49×10^{-2}	4.61×10^{-2}	3.66×10^{-2}	2.00×10^{-2}	2.59×10^{-2}	4.81×10^{-2}
Marine eutrophication	kg N eq	7.34×10^{-3}	2.97×10^{-3}	4.09×10^{-3}	3.05×10^{-3}	2.17×10^{-3}	2.78×10^{-3}	3.94×10^{-3}
Terrestrial ecotoxicity	kg 1,4-DCB	6.05×10^{2}	2.17×10^{2}	3.88×10^{2}	3.10×10^{2}	1.76×10^{2}	2.26×10^{2}	4.05×10^{2}
Freshwater ecotoxicity	kg 1,4-DCB	1.12×10^{1}	3.97×10^{0}	6.83×10^{0}	5.42×10^{0}	3.17×10^{0}	4.17×10^{0}	7.15×10^{0}
Marine ecotoxicity	kg 1,4-DCB	1.44×10^{1}	5.11×10^{0}	8.88×10^{0}	7.05×10^{0}	4.09×10^{0}	5.37×10^{0}	9.30×10^{0}
Human carcinogenic toxicity	kg 1,4-DCB	6.88×10^{0}	2.79×10^{0}	6.84×10^{0}	5.41×10^{0}	2.23×10^{0}	2.90×10^{0}	7.13×10^{0}
Human non-carcinogenic toxicity	kg 1,4-DCB	2.02×10^{2}	7.22×10^{1}	1.27×10^{2}	1.02×10^{2}	5.94×10^{1}	7.80×10^{1}	1.35×10^{2}
Land use	m^2a crop eq	7.32×10^{0}	2.45×10^{0}	3.42×10^{0}	2.79×10^{0}	2.03×10^{0}	2.71×10^{0}	3.73×10^{0}
Mineral resource scarcity	kg Cu eq	5.21×10^{-1}	6.12×10^{-1}	8.57×10^{-1}	4.03×10^{-1}	2.12×10^{-1}	3.03×10^{-1}	5.58×10^{-1}
Fossil resource scarcity	kg oil eq	3.88×10^{1}	8.94×10^{0}	3.66×10^{1}	2.89×10^{1}	7.22×10^{0}	9.09×10^{0}	3.79×10^{1}
Water consumption	m^3	6.19×10^{0}	2.02×10^{0}	2.75×10^{0}	2.32×10^{0}	1.75×10^{0}	2.34×10^{0}	3.09×10^{0}

***Impacts made per 1 kg of cathode active material treatment under an improved scenario**

1

According to the findings, all the routes reduced their impact under the improved scenario. Nevertheless, the order of the emissions from the highest to the lowest route remains unchanged, with the highest impact from route 1 and the lowest from route 5. Furthermore, Route 2 had a similar impact as Route 6, but considering only the total emissions. The emissions decreased almost five-fold on Route 1 with the improved scenario. Considering Route 1, impacts were significantly reduced in many categories, such as stratospheric ozone depletion, ozone formation and fine particulate matter. However, with the improved version, the ionizing radiation, land use, and water consumption impact categories had a higher impact on Route 1. All three categories have increased the impact because of adapting solar energy for electricity generation under improved scenario. Thin films used in solar photovoltaic (PV) cells, which may contain cadmium- or gallium-like radioactive elements, can elevate ionizing radiation. Furthermore, it employs copper or silicon which can emit radiation during refinement. Solar farms use more land than other energy sources, which can affect natural habitats and ecosystems. Producing PV cells requires cooling sources for thermal power plants which can also lead to increased water consumption. In addition, refining minerals such as silicon requires more water during many steps [61], [62].

Route 2 reduced its emissions by almost 78% compared to the standard scenario. Three impact categories—ionizing radiation, land use, and water consumption—have increased their impacts due to the usage of solar energy-based electricity. In contrast, Route 3 reduced the total impact on the emissions approximately by 62% with the improved scenario, while the ionizing radiation and water consumption categories exhibited increased impacts. The land-use impact category still demonstrated a decreased impact under the improved scenario. The increase in ionizing radiation and water consumption was due to solar-based energy utilization. However, reduced use of organic solvents and higher recycling rates led to a decrease in the impact of land use. Higher organic solvent usage significantly increased the impact of land use in the standard scenario. This is because of the extraction and production facilities required for the process of crude oil [63]. With the improved version, these impacts significantly decreased, such that the increased impacts due to solar energy use is negligible. Route 4, which also employed solvent extraction-based purification, exhibited a similar pattern for all three impact categories. However, this route also showed a significant 60% decrease in its emissions.

The improved processes of routes 5 and 6 follow the same pattern as routes 1 and 2, which did not use solvent extraction-based purification. However, route 7 again follows the pattern of routes 3 and 4, with increasing impacts only under ionizing radiation and water consumption. Moreover, routes 5, 6, and 7 decreased the emission impacts by 78%, 80%, and 63%, respectively. Therefore, routes 1 and 6 report the highest decrease in PEE, whereas route 3 reports the lowest decrease. This explains that using solar-based electricity and recycling DES up to 80% in route 1 can significantly reduce the impact. In addition, solar-based electricity, along with a reduced amount of reducing agents, can significantly lower the impact of Route 6. Moreover, 80% of the recycling of organic solvents may not reduce the related impacts of Route 3. However, the reduced impacts of Route 1 were still higher than those of the other treatment processes.

As Routes 1 and 6 reported the highest reduction in impact under the improved scenarios, a Montecarlo-sensitivity analysis was performed for these two routes with 1,000 iterations. Annexure 1, Figure S3.5 displays the results of the analysis. Accordingly, Route 6 was certainly better than Route 1, even after considerably reducing impacts in many categories. However, in the stratospheric ozone depletion category, route 1 was superior to route 6 for each value within the standard deviation. Moreover, in the water consumption category, both routes have a similar tendency to perform better.

4.5 Life cycle costing analysis

The LCC analysis was carried out considering the improved version of each route. This is primarily because of the high environmental impact observed in laboratory studies. An improved version can denote the industrial or at least pilot-scale emissions, which is much more reliable for analyzing the economic impact. Moreover, for the costing analysis only direct costs related to the treatment of 1 kg of cathode active materials were considered. Other operational costs (laborer costs or transportation costs) were assumed to be the same for all the treatment routes and hence not considered a major factor. Table 3.8 represents the main results of LCC assessment with mean prices and standard deviation. Further, annexure 2, section S3 provides a comprehensive list of mean costs for each chemical with the standard deviation of prices, treatment costs, income from byproduct and the quantities of the same required to treat 1 kg of the active cathode material.

Table 3.8 Cost of treatment for each route studied with standard deviation.

Treatment Route	Cost of treatment ($/kg of cathode material)	Standard deviation (±$)
Route 1: DES leaching-->Oxalate precipitate purification-->Oxalate calcination	191.16	1.90
Route 2: EC leaching-->adsorbent based purification-->Hydroxide calcination	103.94	24.38
Route 3: EC leaching-->Solvent extraction-based purification-->Hydroxide calcination	364.37	24.42
Route 4: SCF leaching-->Solvent extraction-based purification-->Hydroxide calcination	303.35	3.60
Route 5: SCF leaching-->adsorbent based purification-->Hydroxide calcination	99.10	3.33
Route 6: Conventional leaching-->Adsorbent material-based purification-->hydroxide calcination	118.50	0.71
Route 7: Conventional leaching-->Solvent extraction-based purification-->hydroxide calcination	389.76	1.53

As per the results, the highest cost was shown by route 3 and the lowest reported by route 5. Routes 2 and 3 have the highest deviations. Annexure 1, Figure S3.6 (a), (b) and (c) show the total treatment cost, average recovery efficiency and process emission effect per 1 kg of cathode active material under each route respectively.

Figure 3.7 generated to make a comparison between the costs, environmental impacts and efficiency of the routes. Hence, the figure shows the relative costs, the relative recovery efficiency and environmental impact (in terms of process emission effect) per 1 kg of cathode active material recovery. Moreover, Figure 3.7 was generated based on the percentage effect of each three parameters to enhance clarity and ease of comparison. Though the environmental impacts were analyzed through various categories, only emissions effect derived through global warming potential (GWP) was selected to include in Figure 3.7. The main reason for this decision is that ReCipe 2016 calculation method brings GWP as a holistic comprehensive indicator over the other parameters.

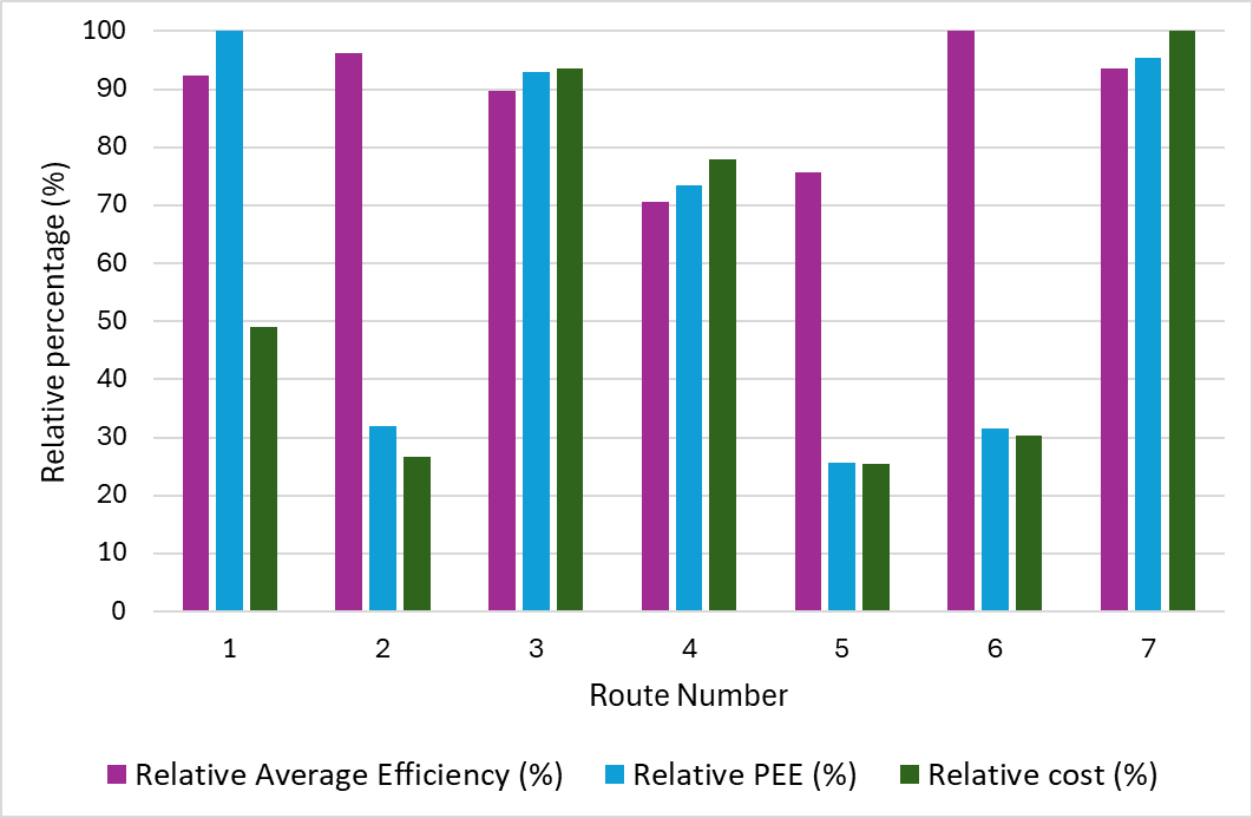

Figure 3.7 Comparison of each treatment route in terms of treatment cost efficiency, PEE, and recovery efficiency (PEE=process emission effect).

As per Figure 3.7 and Figure S3.6 (annexure 1) the treatment costs vary from ~$ 100 – 400 per 1 kg of cathode treatment under different routes considered. The highest costs were obtained when the solvent extraction technology is involved in the treatment sequence (Route number 3, 4 and 7). This is mainly due to the high unit cost of organic solvents (~$5.5/kg) and the quantity of materials required. Most of these costs can be recovered through obtaining used organic solvents which can be recycled or reused effectively. However, it seems that 80% of recycling is not sufficient for the reduction of overall costs resulted in using the organic solvents. The highest cost was reported by route 7 ($ 390), due to the high quantity of organic solvent required for the extraction of higher amount of metal ions leached through inorganic acid leaching. Hence, PEE of the route is also elevated (at 102 kg CO_2) according to Figure S3.6(b) (annexure 1). However, the average efficiency (73%) of the route is also reported to be high compared to other technologies. Route 4 has the lowest cost ($ 303) among the routes that use organic solvents for purification. However,

average efficiency (55%) and the PEE (27.4 kg CO_2) is also reduced as per the reduced quantity of organic solvents used.

Route number 1 has a slightly higher cost (~$190) than route 6 (~$120) considering 1kg of cathode material treatment. Though the material requirement and unit cost of materials is higher for DES manufacturing, most of these costs are covered through recycling possibility of DES. Moreover, using DES has other advantages like not having to add oxalic acid separately. Hence the purification can be done at a lower cost as the DES itself is made using ChCl and Oxalic acid. However, when different DES is used, the purification technology should be determined accordingly. Nevertheless, these advantages have reduced the overall cost of the treatment. On the other hand, the major cost determinant factor for route 6 is the electricity and the usage of ion-exchange resins. It was identified that around $ 88 cost needs to be spent for the ion-exchange resins considering the treatment of 1 kg of cathodic materials while for electricity $ 98. Moreover, it should be identified that the usage of inorganic acid-based leaching in technology has increased the quantity of leached metals in the solution which demands more ion-exchange materials for the purification step. This can be further identified by the higher average efficiency (78%) of the route. In contrary route 1 showed an average efficiency of 72%. Comparing the PEE of the two methods (Figure 3.7) suggest that route 6 is far more efficient than route 1 which reports a lower scale PEE (33.8 kg CO_2) than the route 1 (107 kg CO_2) thanks to the lower impacts generated by inorganic acid-based leaching and ion-exchange based purification technologies.

The lowest costs were reported by route 2 and 5, being route 5 the most cost-effective treatment sequence. The main reason for the lowest cost received is due to the lower usage of material quantities due to the effective leaching resulted by EC and SCF based leaching mechanisms. Both the leaching techniques produce lower quantities of leaching solutions compared to DES or inorganic acid based leaching solutions which demand lower quantity of materials for purification steps. Moreover, route 5 has the lowest cost due to the lower average recovery efficiency reported (59%) while route 2 shows 75% overall average recovery efficiency. Both the routes can be identified as greener methods with lower PEE at around 34.3 kg CO_2 for route 2 and 27.4 kg CO_2 for route 5. A comparative values of recovery rate, PEE and cost of treatment were given under Figure S3.6 for better understanding.

As the study provides information on the costs of the treatment for each route studied, it is possible to assume that lower the cost can increase the profitability of the treatment route in long term. However, the profitability of each route highly depends on the capital investment to establish the industrial treatment plants. For instance, supercritical fluid extraction or electrolysis-based extraction need a higher investment as the plants need specific instrument for the treatment. Moreover, frequent maintenance and work-related hazards can also play a major role in determining the overall profitability of the route, which needs to be extensively researched in future.

4.6 Benchmark analysis

Benchmarking is performed by comparing the results obtained in this study with those of other studies conducted to recycle and recover cathode active materials from EoL LiBs. This task is difficult, especially because of the lack of studies that have focused explicitly on cathode active materials. Moreover, differences in assumptions, functional units, and calculation methods made the analysis more problematic. Despite the limitations of available literature in the field, the results of the study were compared to the highest possible standard.

Castro et al. (2022) implemented a method to recover materials from EoL LiBs, justified by an LCA. This study revealed the impact of a 2.3-5.9 kg CO_2 eq. for the total emissions per cell (~ 500 g). According to the same study, the cathode material content was responsible for 28% of the battery, along with the aluminum current collector. Based on the study, cathode active material treatment may cause an overall emission of approximately 3.5 to 9.1 kg CO_2 eq. per 1 kg. The cathode mass in the cell is approximately 180 g. This study utilized organic acid-based leaching, and the LCA inventory included the avoided products. Given the use of avoided products, the impact may be very low compared to the current study. Interestingly, the authors reported that a higher citric acid recycling rate is required to make the process environmentally and economically sustainable, which is in line with the findings of the current study. Furthermore, a study reported a material recovery of approximately 44% through hydrometallurgical steps [16]. Wu et al. (2022) did another study that reports recycling of 1 kg of LCO-type cathode material released about 33–118 kg CO_2 eq. when only hydrometallurgical treatment was used. The values obtained by Wu et al. matched the results of the current study for various treatment mechanisms. Moreover, this study confirms that acid leaching has a comparably lower impact under different impact categories and

that metal separation impacts the environment more, further justifying the findings of the current study [17].

Fahimi et al. (2022) conducted a similar study, which revealed that 1 kg of cobalt recovery from LCO-type LiBs results in GHG emissions of approximately 5.1 kg CO_2 equivalent under hydrometallurgical-based treatment. This study used several articles to calculate the average GHG emissions using the ESCAPE method. However, this does not include carbon emissions related to energy utilization, thus lowering the overall emissions. Moreover, it is not possible to compare these values with those of the current study because of the different calculation methods and functional units used. However, the authors reported that organic acid-based treatment tends to increase the total GHG emissions owing to the higher quantities used. Moreover, treating organic acids requires higher recycling rates to reduce total emissions [15]. This finding further confirmed the results of this study. Different authors have reported different recovery rates for recycling procedures, with each hydrometallurgy step affecting the total recycling rate. A single process can significantly affect the final recovery rate. The amount of material transferred to the next step also significantly affects the environmental impact, making it a major uncertainty parameter affecting a recycling route's total sustainability [64], [65].

5. Conclusions

Considering the various hydrometallurgical treatment steps, energy use has emerged as a hotspot. Second, there are concerns about the high material consumption for organic chemicals. Study found that SCF based leaching gives less efficiency in terms of recovery of materials though it gives better environmental performance when used in a route. However, other leaching methods, EC based, conventional and DES based leaching provide better efficiency in recovery of metals. Nevertheless, DES-based leaching can significantly increase the environmental impact, thereby limiting the use of this technology. It was identified that material recycling rates higher than 80% are necessary to achieve better environmental and economic performance for DES based leaching. Consequently, conventional and EC-based leaching are better technologies for reducing the environmental impact while increasing the overall leaching of metals.

Adsorbent (ion-exchange)-based purification demonstrated better environmental performance when used in the route with a higher recovery rate (> 70%) than other purification technologies. Solvent-based extraction significantly increases the emissions when incorporated in the route.

Over 80% recycling of materials is likely to reduce the impacts involved with solvent extraction-based purification. Regarding the calcination method, hydroxide-based calcination provides better performance compared to oxalate calcination in terms of emissions.

The best overall performance is shown by inorganic acid based leaching mechanisms followed by adsorbent-based purification with hydroxide calcination (route 6) in terms of recovery efficiency (78%), environmental impact in terms of emissions (33.8 kg CO_2 eq.) and economic performance ($ 119) per 1 kg of cathode active material recovery. Under the other significant environmental impact categories identified, route 6 showed: terrestrial ecotoxicity; 176 kg 1,4-DCB, freshwater eutrophication; 0.02 kg P eq. and fossil resource scarcity; 7.22 kg oil eq. which only seconds to route 5 (SCF based leaching, adsorbent extraction and hydroxide calcination). Route that follows, DES-based leaching, oxalate precipitation and calcination (route 1) reported as the most polluting technology with high recovery rate (72.3 %) while route 3 (EC-based leaching, solvent based extraction and hydroxide calcination) reported as the worst treatment mechanisms considering both poor environmental and economic performances. This is mainly due to the use of an extraction-based purification method. Accordingly, technologies such as DES-based leaching and solvent extraction-based purification, should undergo further experimentation in the long run under laboratory conditions. Specifically, the recycling mechanisms of organic solvents require extensive studies to enhance their sustainability. Moreover, SCF-based leaching is more environmentally sustainable across various impact categories and mildly economical. Hence, further studies on optimization and 100% CO_2 recirculation can increase the industrial applicability of this technology.

Finally, the limitations such as pricing variations, and limitations in study-oriented data can deviate the results from the accurate values. Moreover, using different data sources and databases can change the findings of the study significantly as well.

References

[1] Statista, “Leading countries based on electronic waste generation worldwide in 2022 (in 1,000 metric tons),” 2024. Accessed: Oct. 29, 2024. [Online]. Available: https://www.statista.com/statistics/499952/ewaste-generation-worldwide-by-major-country/

[2] IEA, “Global EV Outlook 2023,” Paris, 2023. Accessed: May 03, 2024. [Online]. Available: https://www.iea.org/reports/global-ev-outlook-2023

[3] U. Akasapu and P. Hehenberger, “A design process model for battery systems based on existing life cycle assessment results,” *J Clean Prod*, vol. 407, p. 137149, Jun. 2023, doi: 10.1016/j.jclepro.2023.137149.

[4] Statista Research Department, “Distribution of lithium-ion battery plants 2023, by global region,” Mar. 2024. Accessed: Jun. 11, 2024. [Online]. Available: https://www.statista.com/statistics/1456534/lithium-ion-battery-plants-by-region-worldwide/

[5] Statista Research Department, “World leaders in projected lithium-ion battery manufacturing capacity 2022-2030,” Oct. 2023. Accessed: Jun. 11, 2024. [Online]. Available: https://www.statista.com/statistics/1420153/lithium-ion-battery-manufacturing-capacity-by-world-region-forecast/

[6] Madhumitha Jaganmohan, “Global projected growth in metal demand for battery production 2028,” Apr. 2024. Accessed: Jun. 11, 2024. [Online]. Available: https://www.statista.com/statistics/665038/projected-growth-in-metal-demand-for-battery-production-worldwide/

[7] R. H. de Castro, D. C. Romano Espinosa, L. A. Gobo, E. A. Kumoto, A. B. Botelho Junior, and J. A. S. Tenorio, “Design of Recycling Processes for NCA-Type Li-Ion Batteries from Electric Vehicles toward the Circular Economy,” *Energy & Fuels*, vol. 38, no. 6, pp. 5545–5557, Mar. 2024, doi: 10.1021/acs.energyfuels.3c04904.

[8] L. S. Martins, S. Rovani, A. B. Botelho Junior, and D. C. Romano Espinosa, “Sustainable Approach for Critical Metals Recovery through Hydrometallurgical Processing of Spent Batteries Using Organic Acids,” *Ind Eng Chem Res*, vol. 62, no. 44, pp. 18672–18682, Nov. 2023, doi: 10.1021/acs.iecr.3c03048.

[9] N. Vieceli, P. Benjamasutin, R. Promphan, P. Hellström, M. Paulsson, and M. Petranikova, “Recycling of Lithium-Ion Batteries: Effect of Hydrogen Peroxide and a Dosing Method on the Leaching of LCO, NMC Oxides, and Industrial Black Mass,” *ACS Sustain Chem Eng*, vol. 11, no. 26, pp. 9662–9673, Jul. 2023, doi: 10.1021/acssuschemeng.3c01238.

[10] E. Kallitsis, J. J. Lindsay, M. Chordia, B. Wu, G. J. Offer, and J. S. Edge, “Think global act local: The dependency of global lithium-ion battery emissions on production location and material sources,” *J Clean Prod*, vol. 449, p. 141725, Apr. 2024, doi: 10.1016/j.jclepro.2024.141725.

[11] Mathilde Carlier, “Different types of EV batteries’ market share worldwide 2020-2050,” Oct. 2023. Accessed: Jun. 11, 2024. [Online]. Available: https://www.statista.com/statistics/1248519/distribution-of-different-electric-vehicle-batteries-on-the-global-market/

[12] B. He *et al.*, “A Comprehensive Review of Lithium-Ion Battery (LiB) Recycling Technologies and Industrial Market Trend Insights,” *Recycling*, vol. 9, no. 1, p. 9, Jan. 2024, doi: 10.3390/recycling9010009.

[13] E. Kallitsis, A. Korre, and G. H. Kelsall, “Life cycle assessment of recycling options for automotive Li-ion battery packs,” *J Clean Prod*, vol. 371, p. 133636, Oct. 2022, doi: 10.1016/j.jclepro.2022.133636.

[14] T. G. Ambaye, M. Vaccari, F. D. Castro, S. Prasad, and S. Rtimi, “Emerging technologies for the recovery of rare earth elements (REEs) from the end-of-life electronic wastes: a review on progress, challenges, and perspectives,” *Environmental Science and Pollution Research*, vol. 27, no. 29, pp. 36052–36074, Oct. 2020, doi: 10.1007/s11356-020-09630-2.

[15] A. Fahimi *et al.*, “Evaluation of the sustainability of technologies to recycle spent lithium-ion batteries, based on embodied energy and carbon footprint,” *J Clean Prod*, vol. 338, p. 130493, Mar. 2022, doi: 10.1016/j.jclepro.2022.130493.

[16] F. Duarte Castro, E. Mehner, L. Cutaia, and M. Vaccari, “Life cycle assessment of an innovative lithium-ion battery recycling route: A feasibility study,” *J Clean Prod*, vol. 368, p. 133130, Sep. 2022, doi: 10.1016/j.jclepro.2022.133130.

[17] F. Wu *et al.*, “Environmental hotspots and greenhouse gas reduction potential for different lithium-ion battery recovery strategies,” *J Clean Prod*, vol. 339, p. 130697, Mar. 2022, doi: 10.1016/j.jclepro.2022.130697.

[18] M. Rinne, H. Elomaa, A. Porvali, and M. Lundström, “Simulation-based life cycle assessment for hydrometallurgical recycling of mixed LIB and NiMH waste,” *Resour Conserv Recycl*, vol. 170, p. 105586, Jul. 2021, doi: 10.1016/j.resconrec.2021.105586.

[19] S. Du, F. Gao, Z. Nie, Y. Liu, B. Sun, and X. Gong, “Life cycle assessment of recycled NiCoMn ternary cathode materials prepared by hydrometallurgical technology for power batteries in China,” *J Clean Prod*, vol. 340, p. 130798, Mar. 2022, doi: 10.1016/j.jclepro.2022.130798.

[20] Z. Zhou, Y. Lai, Q. Peng, and J. Li, “Comparative Life Cycle Assessment of Merging Recycling Methods for Spent Lithium Ion Batteries,” *Energies (Basel)*, vol. 14, no. 19, p. 6263, Oct. 2021, doi: 10.3390/en14196263.

[21] D. S. Premathilake, A. B. Botelho Junior, J. A. S. Tenório, D. C. R. Espinosa, and M. Vaccari, “Designing of a Decentralized Pretreatment Line for EOL-LIBs Based on Recent Literature of LIB Recycling for Black Mass,” *Metals (Basel)*, vol. 13, no. 2, p. 374, Feb. 2023, doi: 10.3390/met13020374.

[22] E. Vahidi and F. Zhao, “Environmental life cycle assessment on the separation of rare earth oxides through solvent extraction,” *J Environ Manage*, vol. 203, pp. 255–263, Dec. 2017, doi: 10.1016/j.jenvman.2017.07.076.

[23] Q. Zaib, M. J. Eckelman, Y. Yang, and D. Kyung, “Are deep eutectic solvents really green?: A life-cycle perspective,” *Green Chemistry*, vol. 24, no. 20, pp. 7924–7930, 2022, doi: 10.1039/D2GC01752K.

[24] L. A. Diaz, M. L. Strauss, B. Adhikari, J. R. Klaehn, J. S. McNally, and T. E. Lister, "Electrochemical-assisted leaching of active materials from lithium ion batteries," *Resour Conserv Recycl*, vol. 161, p. 104900, Oct. 2020, doi: 10.1016/j.resconrec.2020.104900.

[25] M. L. Strauss, L. A. Diaz, J. McNally, J. Klaehn, and T. E. Lister, "Separation of cobalt, nickel, and manganese in leach solutions of waste lithium-ion batteries using Dowex M4195 ion exchange resin," *Hydrometallurgy*, vol. 206, p. 105757, Dec. 2021, doi: 10.1016/j.hydromet.2021.105757.

[26] X. Chang *et al.*, "Selective Extraction of Transition Metals from Spent LiNixCoyMnx1−−yO2 Cathode via Regulation of Coordination Environment," *Angewandte Chemie - International Edition*, vol. 61, no. 24, Jun. 2022, doi: 10.1002/anie.202202558.

[27] Kelly Leitch, Gavin Hartigan, and Robert D'OrazioLivermore, "CO2, RECOVERY PROCESS FOR SUPERCRITICAL EXTRACTION," 2005. Accessed: Apr. 24, 2024. [Online]. Available: https://patentimages.storage.googleapis.com/da/b3/f2/3ecf3d498429f7/US6960242.pdf

[28] L. F. Guimarães, A. B. Botelho Junior, and D. C. R. Espinosa, "Sulfuric acid leaching of metals from waste Li-ion batteries without using reducing agent," *Miner Eng*, vol. 183, p. 107597, Jun. 2022, doi: 10.1016/J.MINENG.2022.107597.

[29] Dow chemical company, "Lenntech resin." Accessed: Mar. 01, 2024. [Online]. Available: https://www.lenntech.com/Data-sheets/Dowex-M-4195-L.pdf

[30] M. Villares, A. Işıldar, C. van der Giesen, and J. Guinée, "Does ex ante application enhance the usefulness of LCA? A case study on an emerging technology for metal recovery from e-waste," *Int J Life Cycle Assess*, vol. 22, no. 10, pp. 1618–1633, Oct. 2017, doi: 10.1007/s11367-017-1270-6.

[31] Intratec, "Monitor Hydrochloric Acid Prices Worldwide," 2024, Accessed: Jun. 14, 2024. [Online]. Available: https://www.intratec.us/chemical-markets/hydrochloric-acid-price

[32] ChemWorld trading, "Chemicals and Equipment Distributing." Accessed: Jun. 14, 2024. [Online]. Available: https://www.chemworld.com/

[33] Alibaba trading, "Alibaba." Accessed: Jun. 14, 2024. [Online]. Available: https://www.alibaba.com/

[34] Thunder Said Energy, "Global electricity prices vs. CO2 intensities," 2024, Accessed: Jun. 14, 2024. [Online]. Available: https://thundersaidenergy.com/downloads/global-electricity-prices-vs-co2-intensities/

[35] C. Boulder County, "Hazardous Waste Disposal Costs for Businesses." Accessed: May 03, 2024. [Online]. Available: https://bouldercounty.gov/environment/hazardous-waste/disposal-costs-for-businesses/

[36] A. Coskun and W. P. Oosterhuis, “Statistical distributions commonly used in measurement uncertainty in laboratory medicine,” *Biochem Med (Zagreb)*, vol. 30, no. 1, pp. 5–17, Feb. 2020, doi: 10.11613/BM.2020.010101.

[37] M. K. Tran, M. T. F. Rodrigues, K. Kato, G. Babu, and P. M. Ajayan, “Deep eutectic solvents for cathode recycling of Li-ion batteries,” *Nat Energy*, vol. 4, no. 4, pp. 339–345, Apr. 2019, doi: 10.1038/s41560-019-0368-4.

[38] D. A. Bertuol, C. M. Machado, M. L. Silva, C. O. Calgaro, G. L. Dotto, and E. H. Tanabe, “Recovery of cobalt from spent lithium-ion batteries using supercritical carbon dioxide extraction,” *Waste Management*, vol. 51, pp. 245–251, May 2016, doi: 10.1016/j.wasman.2016.03.009.

[39] C. O. Calgaro, D. F. Schlemmer, M. D. C. R. da Silva, E. V. Maziero, E. H. Tanabe, and D. A. Bertuol, “Fast copper extraction from printed circuit boards using supercritical carbon dioxide,” *Waste Management*, vol. 45, pp. 289–297, Nov. 2015, doi: 10.1016/j.wasman.2015.05.017.

[40] A. Preetam, P. R. Jadhao, S. N. Naik, K. K. Pant, and V. Kumar, “Supercritical fluid technology - an eco-friendly approach for resource recovery from e-waste and plastic waste: A review,” *Sep Purif Technol*, vol. 304, Jan. 2023, doi: 10.1016/j.seppur.2022.122314.

[41] S. Tang, M. Zhang, and M. Guo, “A Novel Deep-Eutectic Solvent with Strong Coordination Ability and Low Viscosity for Efficient Extraction of Valuable Metals from Spent Lithium-Ion Batteries,” *ACS Sustain Chem Eng*, vol. 10, no. 2, pp. 975–985, Jan. 2022, doi: 10.1021/acssuschemeng.1c06902.

[42] S. Virolainen, T. Wesselborg, A. Kaukinen, and T. Sainio, “Removal of iron, aluminium, manganese and copper from leach solutions of lithium-ion battery waste using ion exchange,” *Hydrometallurgy*, vol. 202, p. 105602, Jun. 2021, doi: 10.1016/j.hydromet.2021.105602.

[43] K. Omelchuk, P. Szczepański, A. Shrotre, M. Haddad, and A. Chagnes, “Effects of structural changes of new organophosphorus cationic exchangers on a solvent extraction of cobalt, nickel and manganese from acidic chloride media,” *RSC Adv*, vol. 7, no. 10, pp. 5660–5668, 2017, doi: 10.1039/C6RA21695A.

[44] W. Xuan, A. de Souza Braga, and A. Chagnes, “Development of a Novel Solvent Extraction Process to Recover Cobalt, Nickel, Manganese, and Lithium from Cathodic Materials of Spent Lithium-Ion Batteries,” *ACS Sustain Chem Eng*, vol. 10, no. 1, pp. 582–593, Jan. 2022, doi: 10.1021/acssuschemeng.1c07109.

[45] N. Zhang *et al.*, “Structural, Electrochemical, and Thermal Properties of Nickel-Rich $LiNi_xMn_yCo_zO_2$ Materials,” *Chemistry of Materials*, vol. 30, no. 24, pp. 8852–8860, Dec. 2018, doi: 10.1021/acs.chemmater.8b03827.

[46] J. Zhu, J. Yan, and L. Zhang, “High specific capacity Mg-doping LiNi $_{1/3}$ Mn $_{1/3}$ Co $_{1/3}$ O $_{2}$ cathode materials synthesised by a simple stepwise co-precipitation method,” *Micro Nano Lett*, vol. 14, no. 2, pp. 129–132, Feb. 2019, doi: 10.1049/mnl.2018.5011.

[47] N. Vieceli, P. Benjamasutin, R. Promphan, P. Hellström, M. Paulsson, and M. Petranikova, “Recycling of Lithium-Ion Batteries: Effect of Hydrogen Peroxide and a Dosing Method on the Leaching of LCO, NMC Oxides, and Industrial Black Mass,” *ACS Sustain Chem Eng*, vol. 11, no. 26, pp. 9662–9673, Jul. 2023, doi: 10.1021/acssuschemeng.3c01238.

[48] W.-S. Chen and H.-J. Ho, “Recovery of Valuable Metals from Lithium-Ion Batteries NMC Cathode Waste Materials by Hydrometallurgical Methods,” *Metals (Basel)*, vol. 8, no. 5, p. 321, May 2018, doi: 10.3390/met8050321.

[49] X. He, Y. Wen, X. Wang, Y. Cui, L. Li, and H. Ma, “Leaching NCM cathode materials of spent lithium-ion batteries with phosphate acid-based deep eutectic solvent,” *Waste Management*, vol. 157, pp. 8–16, Feb. 2023, doi: 10.1016/j.wasman.2022.11.044.

[50] S. Wang, Z. Zhang, Z. Lu, and Z. Xu, “A novel method for screening deep eutectic solvent to recycle the cathode of Li-ion batteries,” *Green Chemistry*, vol. 22, no. 14, pp. 4473–4482, Jul. 2020, doi: 10.1039/d0gc00701c.

[51] J. Zhang and G. Azimi, “Recycling of lithium, cobalt, nickel, and manganese from end-of-life lithium-ion battery of an electric vehicle using supercritical carbon dioxide,” *Resour Conserv Recycl*, vol. 187, p. 106628, Dec. 2022, doi: 10.1016/j.resconrec.2022.106628.

[52] X. Zhang, Z. Liu, and D. Qu, “Proof-of-Concept study of ion-exchange method for the recycling of LiFePO4 cathode,” *Waste Management*, vol. 157, pp. 1–7, Feb. 2023, doi: 10.1016/j.wasman.2022.12.003.

[53] W.-Y. Wang, H.-C. Yang, and R.-B. Xu, “High-Performance Recovery of Cobalt and Nickel from the Cathode Materials of NMC Type Li-Ion Battery by Complexation-Assisted Solvent Extraction,” *Minerals*, vol. 10, no. 8, p. 662, Jul. 2020, doi: 10.3390/min10080662.

[54] Z. Yang *et al.*, “Stepwise co-precipitation to synthesize LiNi1/3Co1/3Mn1/3O2 one-dimensional hierarchical structure for lithium ion batteries,” *J Power Sources*, vol. 272, pp. 144–151, Dec. 2014, doi: 10.1016/j.jpowsour.2014.08.052.

[55] X. Yao *et al.*, “Oxalate co-precipitation synthesis of LiNi0.6Co0.2Mn0.2O2 for low-cost and high-energy lithium-ion batteries,” *Mater Today Commun*, vol. 19, pp. 262–270, Jun. 2019, doi: 10.1016/j.mtcomm.2019.02.001.

[56] C.-Y. Wu, Q. Bao, Y.-T. Tsai, and J.-G. Duh, “Tuning (003) interplanar space by boric acid co-sintering to enhance Li+ storage and transfer in Li(Ni0.8Co0.1Mn0.1)O2 cathode,” *J Alloys Compd*, vol. 865, p. 158806, Jun. 2021, doi: 10.1016/j.jallcom.2021.158806.

[57] J. Li, H. Li, W. Stone, R. Weber, S. Hy, and J. R. Dahn, “Synthesis of Single Crystal LiNi $_{0.5}$ Mn $_{0.3}$ Co $_{0.2}$ O $_{2}$ for Lithium Ion Batteries,” *J Electrochem Soc*, vol. 164, no. 14, pp. A3529–A3537, Nov. 2017, doi: 10.1149/2.0401714jes.

[58] L. Xu, F. Zhou, J. Kong, Z. Chen, and K. Chen, “Synthesis of Li(Ni0.6Co0.2Mn0.2)O2 with sodium DL-lactate as an eco-friendly chelating agent and its electrochemical performances for lithium-ion batteries,” *Ionics (Kiel)*, vol. 24, no. 8, pp. 2261–2273, Aug. 2018, doi: 10.1007/s11581-017-2363-8.

[59] M. Eilers-Rethwisch, M. Winter, and F. M. Schappacher, “Synthesis, electrochemical investigation and structural analysis of doped Li[Ni0.6Mn0.2Co0.2-M]O2 (x = 0, 0.05; M = Al, Fe, Sn) cathode materials,” *J Power Sources*, vol. 387, pp. 101–107, May 2018, doi: 10.1016/j.jpowsour.2018.02.080.

[60] K. Binnemans and P. T. Jones, “Ionic Liquids and Deep-Eutectic Solvents in Extractive Metallurgy: Mismatch Between Academic Research and Industrial Applicability,” *Journal of Sustainable Metallurgy*, vol. 9, no. 2, pp. 423–438, Jun. 2023, doi: 10.1007/s40831-023-00681-6.

[61] G. Luderer *et al.*, “Environmental co-benefits and adverse side-effects of alternative power sector decarbonization strategies,” *Nat Commun*, vol. 10, no. 1, p. 5229, Nov. 2019, doi: 10.1038/s41467-019-13067-8.

[62] R. Zahedi, S. F. Moosavian, and A. Aslani, “Environmental and damage assessment of transparent solar cells compared with first and second generations using the LCA approach,” *Energy Sci Eng*, vol. 10, no. 12, pp. 4640–4661, Dec. 2022, doi: 10.1002/ese3.1294.

[63] Hugo Valin *et al.*, “The land use change impact of biofuels consumed in the EU,” Netharlands, Aug. 2015. Accessed: May 24, 2024. [Online]. Available: https://energy.ec.europa.eu/system/files/2016-03/Final%2520Report_GLOBIOM_publication_0.pdf

[64] F. Wu, Z. Zhou, S. Temizel-Sekeryan, R. Ghamkhar, and A. L. Hicks, “Assessing the environmental impact and payback of carbon nanotube supported CO2 capture technologies using LCA methodology,” *J Clean Prod*, vol. 270, p. 122465, Oct. 2020, doi: 10.1016/j.jclepro.2020.122465.

[65] L. Oliveira, M. Messagie, S. Rangaraju, J. Sanfelix, M. Hernandez Rivas, and J. Van Mierlo, “Key issues of lithium-ion batteries – from resource depletion to environmental performance indicators,” *J Clean Prod*, vol. 108, pp. 354–362, Dec. 2015, doi: 10.1016/j.jclepro.2015.06.021.

[66] Statista, “Average monthly electricity wholesale price in Italy from January 2019 to August 2024,” 2024. Accessed: Oct. 10, 2024. [Online]. Available: https://www.statista.com/statistics/1267548/italy-monthly-wholesale-electricity-price/

[67] Sigma Aldrich, “Merck, Italy.” Accessed: Sep. 10, 2024. [Online]. Available: https://www.sigmaaldrich.com/IT/en

[68] Reliable Recycling Center, “Pricing for Scrap Metal.” Accessed: Sep. 10, 2024. [Online]. Available: https://www.reliablerecyclingcenter.com/pricing/

[69] Alibaba express, “High quality 25kg Quick Lime Calcium Oxide Powder CaO Water Treatment.” Accessed: Sep. 10, 2024. [Online]. Available: https://www.alibaba.com/product-detail/High-Quality-25kg-Quick-Lime-Calcium_1601158793942.html?spm=a2700.galleryofferlist.p_offer.d_title.15fa36f2cDuc6K&s=p

[70] Marco Antelmi, “Valutazione Economica per il raggiungimento del Buono Stato Ecologico nel Bacino Lambro-Seveso-Olona,” POLITECNICO DI MILANO, Milano, 2016. Accessed: Sep. 10, 2024. [Online]. Available: https://www.aqualabfondazione.it/files/112_0000188_file_1.pdf

[71] Sally Zhang, “High copper concentrate costs, supply deficit to hurt copper smelters from 2025: LME Asia Week 2024,” 2024. Accessed: Sep. 10, 2024. [Online]. Available: https://www.fastmarkets.com/insights/high-copper-concentrate-costs-supply-deficit-to-hurt-copper-smelters-from-2025-lme-asia-week-2024/

[72] T. Liu *et al.*, “Adsorption of methylene blue from aqueous solution by graphene,” *Colloids Surf B Biointerfaces*, vol. 90, pp. 197–203, Feb. 2012, doi: 10.1016/j.colsurfb.2011.10.019.

[73] Y. Li *et al.*, “Comparative study of methylene blue dye adsorption onto activated carbon, graphene oxide, and carbon nanotubes,” *Chemical Engineering Research and Design*, vol. 91, no. 2, pp. 361–368, Feb. 2013, doi: 10.1016/j.cherd.2012.07.007.

[74] Y. Li *et al.*, “Methylene blue adsorption on graphene oxide/calcium alginate composites,” *Carbohydr Polym*, vol. 95, no. 1, pp. 501–507, Jun. 2013, doi: 10.1016/j.carbpol.2013.01.094.

[75] S. Natarajan and H. C. Bajaj, “Recovered materials from spent lithium-ion batteries (LIBs) as adsorbents for dye removal: Equilibrium, kinetics and mechanism,” *J Environ Chem Eng*, vol. 4, no. 4, pp. 4631–4643, Dec. 2016, doi: 10.1016/j.jece.2016.10.024.

[76] L. Das, S. Sengupta, P. Das, A. Bhowal, and C. Bhattacharjee, “Experimental and Numerical modeling on dye adsorption using pyrolyzed mesoporous biochar in Batch and fixed-bed column reactor: Isotherm, Thermodynamics, Mass transfer, Kinetic analysis,” *Surfaces and Interfaces*, vol. 23, p. 100985, Apr. 2021, doi: 10.1016/j.surfin.2021.100985.

[77] X. Cuong Nguyen *et al.*, “Sustainable carbonaceous biochar adsorbents derived from agro-wastes and invasive plants for cation dye adsorption from water,” *Chemosphere*, vol. 282, p. 131009, Nov. 2021, doi: 10.1016/j.chemosphere.2021.131009.

[78] L. Saikam, P. Arthi, N. D. Jayram, and N. Sykam, “Rapid removal of organic dyes from aqueous solutions using mesoporous exfoliated graphite,” *Diam Relat Mater*, vol. 130, p. 109480, 2022, doi: https://doi.org/10.1016/j.diamond.2022.109480.

[79] A. Rahmani-Sani *et al.*, “Use of chicken feather and eggshell to synthesize a novel magnetized activated carbon for sorption of heavy metal ions,” *Bioresour Technol*, vol. 297, p. 122452, Feb. 2020, doi: 10.1016/j.biortech.2019.122452.

[80] E. Ghasemi, A. Heydari, and M. Sillanpää, “Ultrasonic assisted adsorptive removal of toxic heavy metals from environmental samples using functionalized silica-coated magnetic multiwall carbon nanotubes (MagMWCNTs@SiO2),” *Engineering in Agriculture, Environment and Food*, vol. 12, no. 4, pp. 435–442, Oct. 2019, doi: 10.1016/j.eaef.2019.07.002.

[81] H. Chen *et al.*, “Graphene oxide modified waste newspaper for removal of heavy metal ions and its application in industrial wastewater,” *Mater Chem Phys*, vol. 244, p. 122692, Apr. 2020, doi: 10.1016/j.matchemphys.2020.122692.

[82] L. Chaabane, E. Beyou, A. El Ghali, and M. H. V. Baouab, “Comparative studies on the adsorption of metal ions from aqueous solutions using various functionalized graphene oxide sheets as supported adsorbents,” *J Hazard Mater*, vol. 389, p. 121839, May 2020, doi: 10.1016/j.jhazmat.2019.121839.

[83] Q.-U.- Ain, M. U. Farooq, and M. I. Jalees, “Application of Magnetic Graphene Oxide for Water Purification: Heavy Metals Removal and Disinfection,” *Journal of Water Process Engineering*, vol. 33, p. 101044, Feb. 2020, doi: 10.1016/j.jwpe.2019.101044.

Chapter Four-Anode Material Recovery

Comparative Analysis of Facile and Novel Graphite Recovery Methods from Spent Li-Ion Batteries: Environmental and Economic Implications

This paper is an adapted version of the manuscript published in *ACS Sustainable Chemistry & Engineering* (https://doi.org/10.1021/acssuschemeng.4c09084). The author contributed to writing the original draft, editing and reviewing, conceptualization, methodology, experiments, software, and formal analysis.

1. Introduction

Research on Li-ion battery (LiB) recycling has grown exponentially due to the availability of various critical and strategic raw materials. Several pilot and industrial processes were also established for first generation LiB recycling, particularly for $LiCoO_2$ (LCO) type cathode [1], [2]. However, given the advancements in the cathode materials variety in the market, investigations on recycling techniques are required for uprising new generation LiBs, particularly focused on Ni-Mn-Co (NMC) (NMC-111, NMC 532, NMC-622 and NMC-811) type cathodes. Having a higher material contribution and metal content compared to early versions of LiBs (LCO or Li-Fe-PO_4 (LFP) type cathodes) is the major reason behind this requirement [3]. Recovery of metals from cathode material has been focused due to the high economic and supply chain importance (such as cobalt and lithium) [4], [5]. However, recent developments can be seen for the recycling and value addition for anodic part (graphite) of the LiBs [6] as natural graphite is also categorized as a critical raw material and can be subjected into supply interruptions in future [7]. Up to the date, 77% of world graphite requirements are supplied by China. Mozambique and Madagascar also provide for around 12% of graphite from the world market. Battery-grade graphite production is 100% controlled by Chinese companies [8].

As the current battery technology largely depends on graphite as anode material and considering the growing demand of LiBs for green energy transition including new battery technologies (hard carbon for Na-ion batteries, for instance) [9], the development of recycling aiming at graphite recovery is required. Throughout the lifetime of the battery, graphite is subjected to continuous charge and discharge cycles which deteriorate structure of the same and make it contaminated with electrolytes, organic binders and lithium. These contaminations prevent the graphite being discarded into the environment without a proper treatment [10]. Moreover, due to the contaminated

and deteriorated nature of graphite resulted by the continuous charge and discharge cycles, the use of recovered graphite in new battery material needs prior treatment. Instead, authors often argue that reusing of graphite in lower quality and profit applications, such as adsorbents and reductant, would be alternatives [11], [12].

Current material recycling methods from LiBs can be categorized into three sections, 1) Hydrometallurgy, 2) Pyrometallurgy and 3) Mechanical extraction. Hydrometallurgy often results in high quality graphite but not battery grade; however, high temperatures for pretreatment (~400°C), longer leaching time (>1 hour) and corrosive acids (as H_2SO_4 and HCl) were often incorporated. Though leaching aims to dissolve the Polyvinylidene fluoride (PVDF) binders, it often remained with copper foils and lower quality purified graphite with slightly higher costs. However, if the leaching aims at dissolving copper to recover higher quality graphite, the process often requires oxidants such as H_2O_2 for effective dissolving of copper. These criteria elevate the environmental impact and the cost of the treatment significantly [13], [14]. Pyrometallurgy incorporates above 500°C reactions with longer oxidation time and higher energy requirements which results in high environmental impact and losses most of graphite as CO_2. Nevertheless, mechanical extraction through grinding (applying friction) to decompose binders, and sieving to liberate active materials is convenient over the other methods. The method performs better environmentally and economically but composed of some disadvantages as the recovered graphite contaminated with fine particles of copper and other organic and electrolyte materials [12]. Nevertheless, authors often argue that pretreatment/separation techniques used to recover graphite from the LiBs affect the overall quality of the materials [15]. Accordingly, sustainable graphite separation techniques need to be introduced to graphite recycling from LiBs.

Price of 1 kg of battery grade graphite varies from $ 0.83-2.45 depending on the region [16], [17]. Compared to lower prices of natural graphite, complex recycling mechanisms tend to increase the prices of secondary graphite preventing their usage in similar productions. Another reason for the price deviation is that the recycled graphite quality is lower than the virgin graphite [12], [18]. Moreover, priorities were given to technological and quality improvements of the material rather than overall sustainability of the technology. Evaluation of environmental performance or economical feasibilities for graphite recycling from LiBs were not previously reported. To reduce the gaps in the research area, this study evaluates production, optimization and product

characterization of three simple graphite separation methods from LiB anode followed by an environmental and economic analysis. The methods were developed based on the three current practices and here are identified as cold process (based on physical/mechanical recycling), wet process (based on hydrometallurgy) and hot process (based on pyrometallurgy). Further, parameters were evaluated in the modified processes to avoid extensive heat and longer leaching hours to enhance the sustainability of the processes. Characterization revealed the quality of the separated materials. Finally, environmental and economic performance evaluations were done using life cycle assessment (LCA) and life cycle costing (LCC) assessment aiming at identifying low-cost and environmentally friendly graphite separation methods from LiB-anode with reasonable quality for secondary applications or for further purifications.

2. Methodology

2.1 Experimental procedure

A spent LiB battery pack was received from RMB Spa (metal recycling company), Brescia, Italy for the study (Samsung, 2019 -NMC-111 and was used in Fiat-Panda Hybrid-EV). The spent battery pack was first dismantled manually using heavy tools to obtain the four battery modules inside. The modules were dipped in 10 wt.% NaOH solution for 24 hours to discharge for safety reasons (Premathilake, Botelho Junior, et al., 2023). After, each battery module was cut open using wrenches and hacksaw blades under the fume hood to let electrolytes evaporate. The opened modules contained two cells inside, each coiling up to make layers of cathode and anode. The cells were then untangled to separate anode, cathode, and separator materials. Finally, the anode part (copper current collector and the active material) was dried under 40°C for 24 hours to get rid of all the available electrolytes and organic solvents.

To determine the available graphite content in the anode material, a sample of 10 g was mixed with 50 ml (excess) of concentrated (70%) nitric acid at 50°C. The solution was stirred (300 rpm) for 1 hour. After, the solution was filtered, and the residual was washed with de-ionized (DI) water. Finally, the carbon content was analyzed through Carbon-Hydrogen-Nitrogen (CHN) analyzer. The result suggested that the carbon content is 96.6% in the residual which is in line with previous findings [11].

2.1.1 Graphite recovery from anode material

The graphite was extracted from the anode part by three different methods. Firstly, solely physical method (cold process) was used where; crushing, grinding, and sieving treatments were incorporated. The method was designed to release graphite from the current collector as fine material due to the friction (supposed to decompose polyvinylidene fluoride (PVDF) binder material effectively). The copper foil is malleable and did not break into fine particles. Grinding time and sieving size were optimized before characterizing the graphite recovered. A sample of 100 g of anode material was utilized for the optimization steps. Firstly, the size of the sieve was optimized by varying the sieve size aperture from 125 μm to 1 mm. For the grinding, a laboratory grade cutter grinder (SM-450, mrc made) was used. Optimization of grinding time was done through varying the grinding time from 1-5 minutes.

As the second process, a chemical method (wet process) was utilized where copper in the anode was removed by acid leaching (dissolving). Higher sieve size and grinding time were utilized to increase the graphite availability (500 μm with 5 minutes grinding). The leaching was done at room temperature to reduce the energy dependency of the process. Hence, corrosive acid needed to be used. Use of concentrated nitric acid which can actively dissolve copper is avoided as the environmental impact is very high according eco-invent 3.10 database of life cycle assessment (LCA) [20]. Also, if sulfuric acid is used here, using an oxidant (like H_2O_2) and heat is mandatory which also elevates the environmental impact of the whole process [21]. Hence, the next viable option of aqua regia (royal solution) was used to dissolve the copper current collector in the anode part. Prior to the characterization of the recovered graphite, an optimization step was carried out for the concentration of the acid, reaction time and the solid/liquid ratio. Firstly, optimizing leaching time was carried out using a diluted aqua regia solution. The concentrated aqua regia was prepared by mixing concentrated HCl and HNO_3 in a 3:1 molar ratio, as is standard practice. This stock solution was then diluted with deionized water to achieve an effective H^+ concentration of 1 mol/L for the experiments. The leaching conditions were set with an S/L ratio of 1:10 and a stirring speed of 300 rpm.

For the optimization of the S/L ratio, the leaching time was fixed at 60 minutes, the effective H^+ concentration at 1 mol/L, and the stirring speed at 300 rpm, while varying the S/L ratio from ½ to 1/20. Finally, for the optimization of the H^+ concentration, the conditions were set as a leaching

time of 60 minutes, stirring speed of 300 rpm, and S/L ratio of 1:10, with the H^+ concentration varied from 0.2 mol/L to 0.9 mol/L by diluting the stock aqua regia solution.

The hot process was utilized as the third method using CaO instead of direct heating to decompose PVDF which is not used before for graphite recovery reducing environmental impact in two ways, 1) Generation of HF will be avoided as PVDF reacts with CaO forming CaF_2 and 2) the heating temperature can be reduced drastically from above 500°C to below 300°C [22]. Liberation of graphite is expected to elevate effectively upon the decomposition of PVDF binders. Following this step, the anode material had to be washed with excess distilled water to remove excess CaO and CaF_2 [15]. Then, the materials were grinded to remove the copper through friction. Here, the mixing ratio of CaO:anode material was optimized varying the values from 1:1 to 5:1, heating temperature from 200 °C to 300 °C and heating time from 15 minutes to 45 minutes with the availability of atmospheric air.

2.1.2 Characterization

Characterization of recovered graphite under three different methods were done through: Carbon-hydrogen-nitrogen (CHN) analyzer (Thermo Scientific Flash Smart, United States), Raman spectroscopy (automated and integrated confocal micro-Raman spectrometer, XploRA Plus HORIBA Scientific, equipped with an Olympus microscope BX43), X-ray diffraction spectroscopy (XRD, Bruker D2 diffractometer on a zero-background sample holder in the 2-θ range 5°-50°, CuKα radiation, step scan 0.02°, and a counting time of 2 s/step at 40KV and 40 mA), X-ray Fluorescent spectroscopy (XRF), and Scanning Electron Microscopy (SEM). CHN analyzer detect carbon content in the sample. Raman spectra was utilized to understand the structure of the recovered graphite through each method at room temperature XRD results provided information on the crystal phases, structure and the amorphous material content in the samples. For the XRF analysis, (Bruker made, SN1893 with 40 kV voltage and 100 μA) it determined the elemental composition of the powdered samples. Finally, the SEM was utilized to determine the morphological structure of the raw and recovered samples (Zeiss EVO MA10, CarlZeiss, Oberkochen, Germany, equipped with an energy dispersive detector for EDS analysis, on gold-sputtered samples at 20 kV, secondary electrons images, working distance of 8.5 mm).

2.2 Life Cycle Study: object and scope

An attributional LCA study was conducted to understand the environmental impact of the three processes of recovering graphite. Stages that are common for all three processes such as used phase, collection of spent batteries, dismantling of batteries, and discharging, are not taken into consideration. The LCA study was carried out using hotspot analysis, identifying processes, that contribute to most of the impacts under each process. Later, a comparison was done to identify the pros and cons of each method. The study will provide better insight for recyclers or researchers to improve existing systems to be more environmentally friendly and cost effective.

2.2.1 Functional unit of the life cycle assessment

The functional unit of the study is considered as the extraction of 1 kg of pure graphite from anode material. Since each recovery method resulted with different active material recovery efficiency, we unified the metrics of the recovered active material to obtain pure graphite recovery potential (Equations 1-3).

$$Graphite\ recovery\ potential = \frac{mass\ of\ graphite\ in\ g}{Mass\ of\ anode\ used\ in\ Kg} \text{ ----------(1)}$$

$$Carbon\ content\ \% = \frac{mass\ of\ carbon}{Mass\ of\ recovered\ graphite} \times 100\% \text{ ----------(2)}$$

$$Pure\ graphite\ recovery\ potential = Graphite\ recovery\ potential\ \times Carbon\ content\% \text{ ----------(3)}$$

2.2.2 System boundary

Direct steps involved in recovering graphite from the anode materials were incorporated in the system boundary. Figure 4.1 shows the processes involved in each recovering mechanisms labeled according to the route. As the objective of the LCA study is to compare the recovering routes,

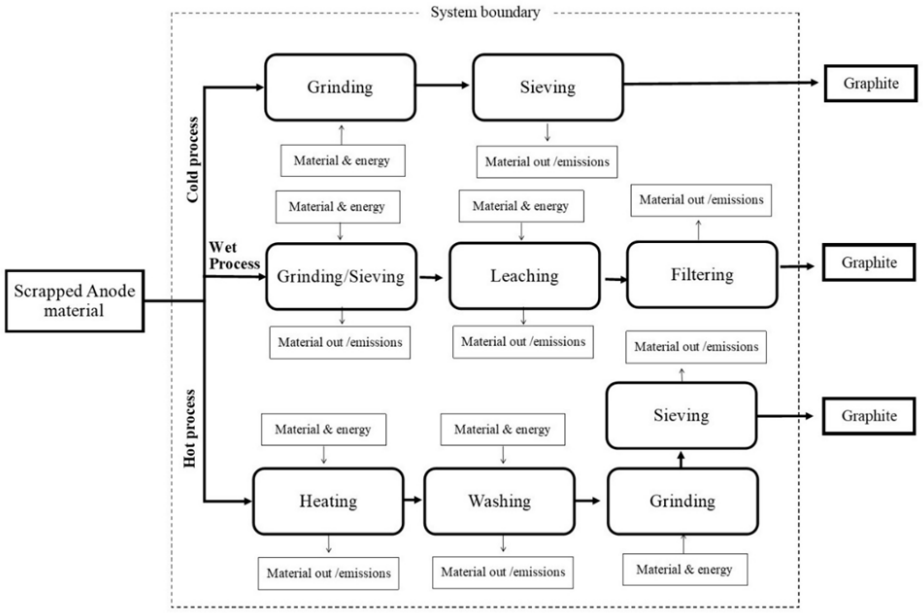

Figure 4.1 System boundary for the LCA study

impacts of scrapped anode material or impacts of use of recovered graphite were not included in the system boundary.

2.2.3 Inventory analysis and modelling

Inventory was calculated using the primary data for each method utilized for graphite recovery. Experiments were carried out using 100 g of anode materials for each process. For energy usage, power consumption of the instruments and time were measured. Since the electrical instruments were not used at their maximum capacity, 30% working potential was assumed throughout the time span. To calculate the emissions in each step, possible reactions depending on the availability of materials in the anode part were used. Solid and liquid emissions were detected through measurements. However, stoichiometric calculations were used to determine gas emissions [19]. In addition, replications were used to calculate the standard deviations which were also used to identify the sensitivity of the LCA model through Monte-Carlo analysis. Finally, the measured and calculated values were adjusted for 1 g of graphite recovery to feed in the LCA software (SimaPro 9.6.0.1).

The inventory values were modelled using Eco-Invent 3.10 V database (allocation cut-off, unit) in the Sima-Pro 9.6 (PhD version) software. The Italian average values were used to model the data as the experiments were carried out in the Italian territory. Further, dummy variables were used to connect two steps in one single recovery process. A complete inventory of the graphite recycling methods under different steps was given in Table 4.1.

Table 4.1. Inventory of the three graphite recovery methods utilized per 1 Kg of graphite recovery.

	Materials (1 g of graphite recovery)	Amount (Kg)	Amount (Kwh)	SD (±Kg)	Data source	Remarks	LCA process
				Cold Process			
Input	Anode materials	1.858		0.015	Measured		Eco-invent
	Energy		0.062		Calculated	100 W, 2-minute grinding	Eco-invent
Output	pure graphite	1.000			Measured		Dummy
	Scrap metal (Cu)	0.858		0.011	Measured		Eco-invent
				Hot Process			
input	Anode material	1.243		0.021	Measured		Eco-invent
	Lime	3.729		0.001	Measured		Eco-invent
	DI water	9.943		0.022	Measured		Eco-invent
	Energy		5.966		Calculated	Heating 250 °C for 20 min (1.8 Kwh)	Eco-invent
	Energy		0.041		Calculated	100 W, 2-minute grinding	Eco-invent
Output	Pure graphite	1.000					Dummy
	Ca and F compounds (75% CaF_2 and 25% Ca compounds)	3.729		0.024	Measured		Eco-invent
	Scrap metals (Cu)	0.243		0.002	Measured		Eco-invent
	Chemically polluted water	9.943		0.031	Measured		Eco-invent
				Wet Process			
Input	Anode material	1.193		0.009	Measured		Eco-invent
	Nitric acid	0.282		0.001	Measured		Eco-invent
	Hydrochloric acid	0.492		0.000	Measured		Eco-invent
	DI water	9.542		0.019	Measured		Eco-invent
	Energy		0.398		Calculated	Stirring 300 rpm for 20 min (100 W)	Eco-invent
Output	Pure graphite	1.000			Measured		Dummy
	Spent solution	0.711		0.011	Measured		Eco-invent

	Waste water (metal ions)	9.542	0.016	Measured		Eco-invent
	NO	0.237		Calculated	Used royal solution reaction with Cu, to produce NO	Eco-invent
	HF	0.019		Calculated	Assumed 5% of PVDF	Eco-invent
	Leach residue	0.193	0.002	Mass balance		Eco-invent

2.2.4 Comparison of environmental impacts of recovery methods

The three methodologies utilized to recover graphite from anode materials were analyzed individually to identify the hotspots. Then, three methods were compared with each other under various impact categories given under the calculation method: Environmental Footprint 3.1 (adapted) V1.01 / EF 3.1 normalization and weighting set. Finally, sensitivity analysis was carried out using Monte-Carlo simulation to evaluate the validity of the model.

Following impact categories given under the calculation method were used for the discussion: Acidification, Climate change, Ecotoxicity (freshwater), Particulate matter, Eutrophication (marine), Eutrophication (terrestrial), Human toxicity (cancer), Human toxicity (non-cancer), Photochemical ozone formation, Resource use (fossils), Resource use (mineral and metals), and water use.

2.3 Comparison of economic performance of recovery methods

Economic evaluation of the three methods utilized was carried out through Life Cycle Costing (LCC) approach taking the functional unit of 1 kg of graphite recovery from the anode material. Laboratory level consumption of chemicals and electricity was obtained from the process contribution in Sima Pro 9.6. Material and energy contribution with their unit prices and standard deviation were given in Table 4.2. Standard deviation (SD) of the costs was calculated based on equation 4 assuming that the costs are uniformly distributed [21].

$$Standard\ deviation = \frac{(Maximum\ price - Minimum\ price)}{\sqrt{12}} \text{----------(4)}$$

The main reason to use equation 4 to obtain the SD's is that there is no availability of multiple cost data for the materials considered. Instead, the range of values had to be utilized to calculate the SD of costs using the equation based on uniform distribution of prices. The price of the graphite extracted was considered for each graphite sample through multiplying the price of the pure graphite by the purity of the sample (Equation 5) to have a quality-based pricing.

$$Purity\ of\ graphite\ (\%) = \frac{Pure\ graphite\ recovery\ potential\ of\ the\ process}{Total\ recoverable\ pure\ graphite\ available} \times 100\% \text{-------(5)}$$

Moreover, these prices were given as negative values to show a possible income from selling. All the other prices were denoted as positives (potential cost). For the spent copper derived from each process was given the cost of recycling as it should undergo on secondary recycling. For the emitted gas treatment, the cost was determined by assuming that the gas purification utilizes carbon filters.

Table 4.2 Inventory of the cost of each treatment with price source.

Materials (1 g of graphite recovery)	Kg	MJ	Highest unit price ($/Kg) or ($/MJ)	Lowest unit price ($/Kg) or ($/MJ)	Highest total costs ($)	Lowest total costs ($)	Average Cost per 1kg treatment ($)	Standard deviation of the cost (±$)	Ref
				Cold process					
Anode materials	1.860		13.420	7.46	24.961	13.876	19.418	3.200	[35]
Energy		0.223	0.032	0.026	0.007	0.006	0.006	0.000	[66]
Graphite	1.000		-22.811	-105.448	-22.811	-105.448	-64.130	23.855	[67]
Scrap metal (Cu)	0.858		7.726	3.200	6.627	2.745	4.686	1.121	[68]
				Hot process					
Anode material	1.240		13.420	7.46	16.641	9.250	12.946	2.133	[35]
Lime	3.730		2.000	1.000	7.460	3.730	5.595	1.077	[69]
DI water	9.940		28.600	9.730	284.284	96.716	190.500	54.146	
Energy		21.600	0.032	0.026	0.691	0.562	0.626	0.037	[66]
Graphite	1.000		-32.521	-150.332	-32.521	-150.332	-91.426	34.009	[67]
Ca and F compounds (75% CaF_2 and 25% Ca compounds)	3.729		13.500	7.500	50.336	27.964	39.150	6.458	[35]
Scrap metals (Cu)	0.243		7.726	3.200	1.876	0.777	1.327	0.317	[68]
Chemically polluted water	9.943		0.001	0.000	0.005	0.004	0.005	0.001	[70]
				Wet process					
Anode material	1.193		13.420	7.46	16.007	8.898	12.452	2.052	[35]
Nitric acid	0.282		370.000	63.830	104.278	17.989	61.133	24.909	[67]
Hydrochloric acid	0.492		619.000	427.000	304.830	210.279	257.554	27.295	[67]
DI water	9.542		28.600	9.730	272.901	92.844	182.872	51.978	[67]
Energy		1.430	0.032	0.026	0.046	0.037	0.041	0.002	[66]
Graphite	1.000		-35.362	-163.464	-35.362	-163.464	-99.413	36.980	[67]
Spent acids	0.711		4.670	2.604	3.320	1.851	2.586	0.424	[35]
Waste water (metal ions)	9.542		0.001	0.000	0.005	0.004	0.004	0.000	[70]
Emitted gas treatment	0.256		10.660	5.938	2.730	1.521	2.125	0.349	[35]
Leach residue	0.193		0.080	0.023	0.015	0.004	0.010	0.003	[71]

3. Results and Discussion

3.1 Optimization of parameters

The maximum recoverable graphite content was required to evaluate the recovery efficiency of each extraction route. Section 2.1 describes the method utilized to determine the maximum recoverable graphite content. Equation 6 describes the reaction takes place between the copper available in the anode material and concentrated nitric acid.

$$3Cu + 8HNO_3 \rightarrow 3Cu(NO_3)_2 + 4H_2O + 2NO \text{----------(6)}$$

Accordingly, the dry mass of the residual material resulted from the leaching was 3.8 g with a carbon content of 96.6%. Which calculated to be 3.67 g of pure graphite in 10 g of anode materials (367 g/kg).

3.1.1 Cold process optimization

A grinding step followed by a sieving step was used for the liberation and the separation of graphite. Full potential (using 130 W) grinding was unable to be used effectively as the powdered graphite escaped in the form of dust over the cover causing graphite losses. The least potential (using 60 W) grinding was not very convenient due to poor friction produced. Hence, the grinding of medium potential (100 W) was utilized. Optimization of pore diameter and grinding time was done through varying the pore diameter from 125 µm to 1 mm and grinding time from 1-5 minutes at medium grinding stage (Figure 4.2).

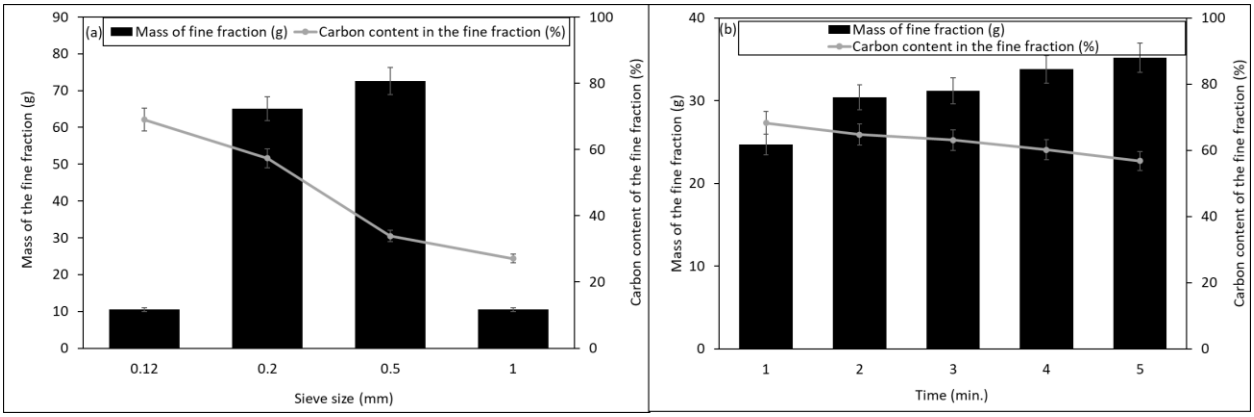

Figure 4.2 Optimization results (a) sieve size (b) grinding time of cold process of graphite recycling.

As optimized (Figure 4.2 (a)), mass of fine fractions that pass through the sieve increases proportional to the sieve size which is in accordance to the expected. Interestingly, the carbon content of the passing fraction is getting reduced as the size of pore diameter increases, suggesting

that increase of copper particles passing through the sieve which reduces the carbon concentration. Carbon content is highest (69%) when 0.12 mm sieve was used. However, this pore size was rejected as per the lower mass of graphite recovered through fine fraction (10.5 g out from 100 g of anode material used). A good compromise between the recovery mass (65.1 g) and the carbon content (57.4%) is shown by 0.2 mm. The identified pore diameter has been verified by previous findings as well [11], [15].

It can be noted that mass of fine fraction increases as the grinding time increases (Figure 4.2(b)) due to the prolonged friction applied to the anode materials increasing copper content in the fine fraction. As expected, the carbon percentage is decreasing with the increasing grinding periods (68.3% for 1 minute and 56.8% for 5 minutes). However, the mass of the passing content was increasing (24.7 g for 1 minute and 35.2 g for 5 minutes). Considering both the passing mass and the carbon content of the recovered materials, 2 minutes grinding was identified as the best grinding period. The selected grinding period brings 30.4 g of fine fraction with 64.8 % of carbon where other grinding periods lower either mass of the fine fraction or the carbon content.

It is possible to recover graphite rich fine fraction of 305.0 g per 1 kg of anode material with the carbon content of 64.8% through the cold method (physical processing) resulting in pure graphite recovery of 197.6 g/kg of anode material. This can be identified as 53.8 % recovery of total available pure graphite from the anode material.

3.1.2 Wet process optimization

The wet process was designed to recover graphite through acid leaching. To increase the graphite availability in the sample, sieve size 0.5 mm was used through cold process after 5 minutes of grinding. Royal solution (aqua regia) was used as the acidic solution to avoid problems arose with nitric acid or sulfuric acid-based leaching as described under section 2.1.1.

Figure 4.3 shows the parameter optimization graphs for the wet process utilized. As Figure 4.3 (a) leaching time optimization, the carbon content increased rapidly during the first 45 minutes (up to 72%) and gradually came to a fixed value during the next 75 minutes (from 60-120 minutes, carbon content varied 86-92%). Hence, 60 minutes were selected as the leaching time. Figure 4.3 (b) shows the optimization of S/L ratio for the leaching process. The conditions were set to; leaching time 60 minutes, H+ concentration 1 mol/L, and stirring speed 300 rpm while varying the S/L ratio

from ½ to 1/20. It can be noticed that increasing the liquid fraction has a positive effect on the recovery of carbon. However, carbon content remained constant after 1/10 S/L ratio (82-87%). The optimization of H^+ concentration was carried out while keeping; leaching time at 60 minutes, stirring speed at 300 rpm, and S/L ratio at 1/10 and varying H^+ concentration from 0.2 mol/L to 0.9 mol/L (Figure 4.3(c)). The results showed that increasing H^+ concentration increases the carbon content. Nevertheless, increasing the H^+ concentration above 0.5 mol/L does not significantly affect the carbon content, and 0.5 mol/L was selected as the optimized H^+ concentration.

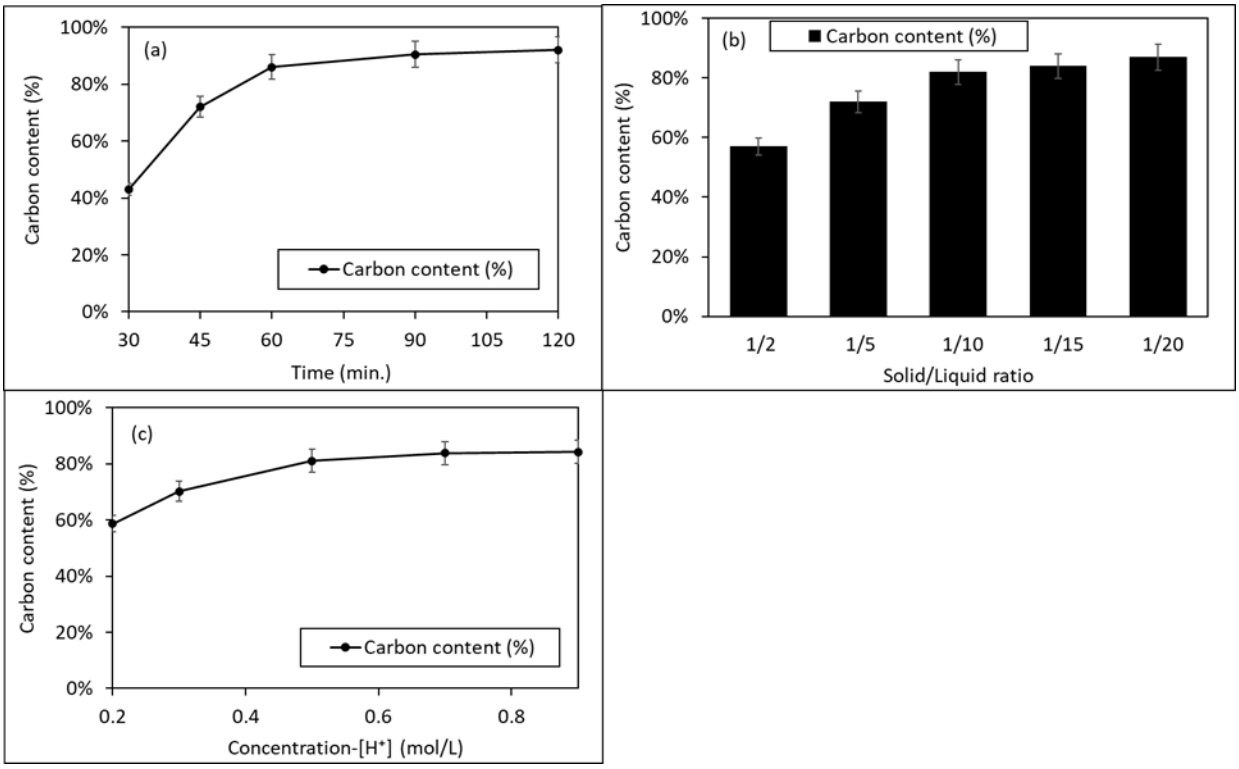

Figure 4.3 Optimization of wet process parameters (a) leaching time (conditions: S/L=1:20, Concentration= 1M) (b) S/L ratio (conditions: time= 60 minutes, Concentration=1 M) and (c) H^+ concentration (conditions: time= 60 minutes, S/L=1:10).

Utilizing the optimized values, 380.0 g of residual material was recovered from 1 kg of anode materials with carbon content 81% (307.8 g/kg of anode material). Compared to the recoverable graphite in the anode this is 83.8% recovery.

3.1.3 Hot process optimization

The hot process was designed to liberate graphite effectively from the anode current collectors by decomposing PVDF binders (Figure 4.4). PVDF decomposes at high temperatures (over 500 °C);

however, Wang et al (2019) reported that CaO can be used to decompose PVDF binders at lower temperatures (~300°C) as C-H bonds in the PVDF binders react with oxygen in the CaO decomposing PVDF. In addition, HF will not produce during the decomposition as fluorine forms CaF2 [22]. However, the method was optimized only for cathode current collectors, hence optimizations were carried out to apply the technology into anode current collectors. Optimizing of anode material to CaO ratio (Figure 4.4(a)) showed that increasing CaO content elevates the carbon content in the recovered graphite up to the ratio of 3:1 (58%). For higher ratios (4:1 and 5:1 of CaO:anode) the liberation of graphite (based on the carbon content) remained the same at maximum of 60%. Later, the optimization of temperature was carried out by keeping CaO: anode material ratio at 3:1 for 30 minutes of heating. The highest carbon content was received when the heating temperature is at 250 °C (69%, Figure 4.4(b)). At higher temperatures (>250 °C) the carbon content of the recovered materials gets lower (51% at 275 °C and 38% at 300 °C). Moreover, higher copper percentage (40-60%) is observed in these recovered samples suggesting that roasting of copper foils at higher temperatures makes the metal fragile. The fragile copper metals were shown to be less malleable hence easily tear off into fragments hindering the separation of graphite and copper metals through sieving. Moreover, at lower temperatures (<250 °C), carbon content of the recovered materials gets lower (43% at 225 °C and 33% at 200 °C) due to the poor decomposing of PVDF binders. Similar observations were received when optimizing the heating time which can be seen in Figure 4.4 (c). The maximum carbon content was observed when the heating time was at 20 minutes (at 71% of carbon content). When the heating time was set to 15 minutes, the carbon content of the recovered material was at 65%, suggesting a poor decomposition of PVDF. At higher heating time periods (>20 minutes) the carbon content of the recovered materials declined at an increasing rate (70% at 30 minutes, 65% at 40 minutes and 59% at 45 minutes). The reason for lowering the carbon content was identified as roasting of copper at prolonged heat exposure making the metal roasted and fragile. The effect of prolonged heating time (>20 minutes) and elevated heating temperatures (>250 °C) can be seen from Figure 4.4(d).

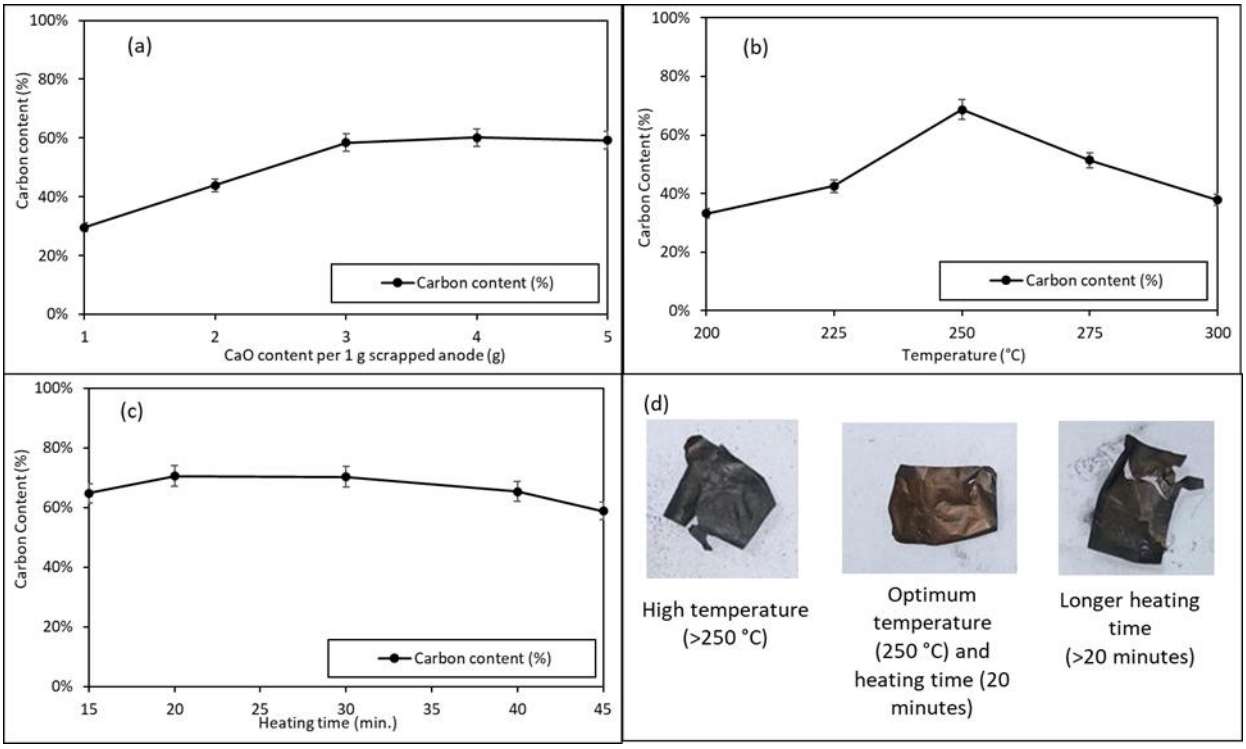

Figure 4.4 Optimization of hot process (a) CaO: anode material ratio (conditions: temperature= 275°C, time =30 minutes), (b) heating temperature (conditions: time =30 minutes, anode: Cao=1:3), and (c) heating time (conditions: temperature=250°C, anode: Cao=1:3) (d) images showing the effect of temperature and heating time (conditions: anode: Cao=1:3).

Grinding and sieving of recovered material through the CaO treatment resulted in 402.2 g of fine fraction per 1 kg of anode materials (1 minute grinding at medium speed-100W). Compared to the cold process fine fraction, the mass received in hot process confirms a significantly higher liberation of graphite from the current collector. The carbon content of the fine fraction was 70% (at optimum conditions) which is still higher than cold process (281.5 g/kg of anode materials). Compared to the available graphite in the anode this was a 76.7% recovery.

3.2 Characterization of recovered graphite

Pure graphite recovery is slightly higher through the wet process (83.8%) than hot process (76.6%). The cold process has the lowest pure graphite recovery at 53.8%. Peaks related to impurities like copper can be seen in both cold and hot processes derived from graphite (Figure 4.5(a)), and highly observed in cold process graphite (CG). Graphite recovered through wet process (WG) shows less impurity related peaks. Graphite peak (diffraction peak) of (002) is visible in all three recovered

samples within the range of 24.5°-27° in the XRD patterns. The highest graphite peak of each XRD analysis was utilized to calculate the interlayer spacings of corresponding recovered graphite sample using the Brag's equation (eq. 7) [30].

$$\lambda = 2dsin\theta \text{----------(7)}$$

Where, λ; X-ray wavelength, d; interlayer spacing and θ; the angle between incident and diffraction planes. Considering the lamellar spacings of graphite structure in samples, it appeared to be in the order of WG (0.356 nm, peak at 25.62°) > HG (0.354 nm, peak at 25.77°) ≥CG (0.354 nm, peak at 25.80°). The slightly higher interlayer spacings reported for the WG could be due to the slight oxidation of graphite that can take place because of acids used during the process. HG and CG showed the lowest interlayer spacing possibly due to the heat generated due to the friction in grinding stages. It is identified that the annealing effect of thermal treatment can cause shrinking of graphite layers showing lower interlayer spacings. Also, removing intercalated species in between the layers as the reaction progress between CaO and PVDF can also cause this shrinking [31]. More importantly, interlayer spacings of all the recovered graphite samples were slightly higher than fresh cell graphite interlayer spacings (0.334 nm) or acid leached graphite interlayer spacings (0.336 nm) as per the previous findings [11]. It is possible to have higher interlayer spacings in used cell graphite than fresh cell graphite due to continuous charging and discharging cycles. On the other hand, under normal acid leaching of graphite, heating for longer time periods can cause the annealing effect that can shrink the graphite layers. Since the current study utilizes acidic media without heat (at room temperature = ~25°C) it is possible to obtain slightly enhanced interlayer spacings. However, this fact is hard to confirm through the literature values as the room temperature leaching of graphite has not been done previously. Nevertheless, it is possible to understand that interlayer spacings of graphite can take a range of values due to identical separation techniques [18], [32], [33].

The impurities detected in the XRD spectra was identified through XRF analysis. The major impurity that could be found in CG and HG graphite samples is copper (around 34.50% in CG and 28.8% in HG). In HG, a minor amount of Calcium was detected that derived through CaO added during the treatment. However, the unreacted copper percentage in WG is around 16.34% and minor amount of nickel (1.90%) and iron (0.53%) was detected. The source of copper is the current collector. The sources of Ni and Fe are unknown as they cannot be derived from the casing

materials as they were removed at the beginning. It is possible that minor parts from the connector tabs of the current anode collector to the circuit contaminate here in minor amounts as these materials often contain a thinly plated layer of Ni-Fe to make it corrosion resistant [34]. Compared to the graphite that recovered through hydrometallurgical means using sulfuric with heating and oxidants [11], the amounts of impurities are higher in recovered graphite samples here. Moreover, in those many of the impurities were derived from cathode active materials (cathodic metal ions) rather than copper.

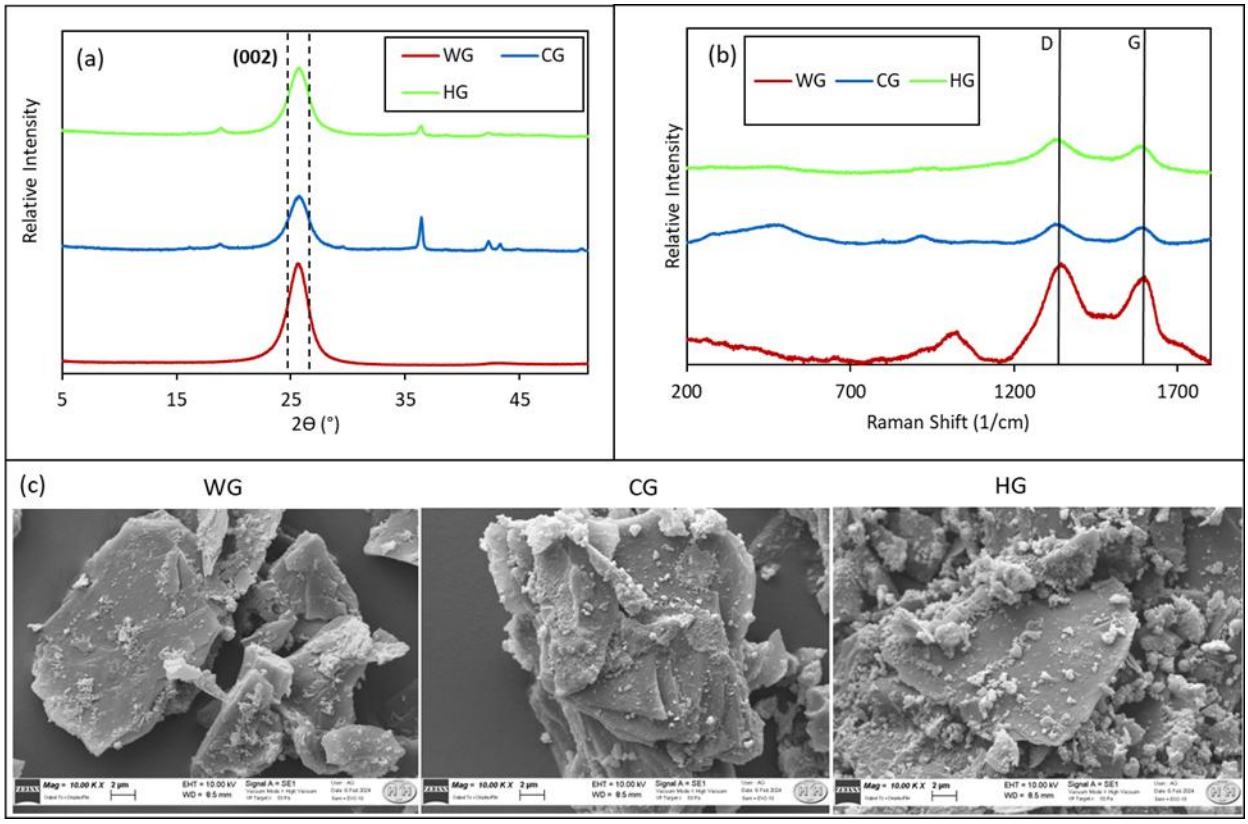

Figure 4.5 Characterization of recovered graphite (a) XRD graphs (b) Raman spectra (c) SEM images through wet process (WG), cold process (CG) and hot process (HG).

Figure 4.5-b shows the Raman spectra received for each recovered graphite sample. In graphite Raman spectra D (1344.6 cm-1) and G (1572.56 cm-1) peaks provide information about the structural quality of the sample. D-peak corresponds to structural deformities caused by disordered or vacant carbon atoms available in the structure while G-peak corresponds to the availability of the graphitic order. In high quality graphite (e.g. battery grade), intensity ratio between D peak to G peak is considerably lower (I(D):I(G) < 0.38) [11]. In the current study, D and G peaks are

clearly visible in WG samples. This is attributed to the less impurities available in the sample. In contrast, CG and HG show less intensities as the graphite content of the samples are relatively lower than that of the WG. I(D):I(G) ratios were received as 1.2595, 1.0222, 1.0331 for WG, CG and HG, respectively. Intensity ratios received are all above 1. This suggests that the methods utilized make more vacant and disordered carbon atoms in the structure. In recent literature, the intensity ratio reported is much lower. For instance, Lai et al (2023) reported intensity ratios below 0.52 for graphite samples that recovered through several methods. However, all the methods use high heat (450 - 800 °C) for longer periods (12 hours) and further, impurity removal mechanism was done through deep eutectic solvent (DES)-based leaching [35]. It is possible to understand that well preserved graphitic structure is attributed to the higher heat applied; nevertheless, this can be done later depending on the application of the secondary graphite recovered. The major drawback in the method utilized by Lai et al. (2023) is that utilizing DES leaching which can add more environmental pressure to the heat utilization as per the recent findings [21].

Lowest I(D):I(G) ratio received by CG suggesting that graphitic layers are relatively better preserved in cold process graphite than WG and HG. Highest I(D):I(G) ratio received by WG suggests that poor structural quality of recovered graphite. It seems that the corrosive acid used in the recovery process has oxidized the graphite up to some extent and given the Raman spectra more like in graphene oxide [11], [36]. This better explains even the high intensity D-peak received. CG and HG, on the other hand, have lower D-peak intensity. In HG, this can be due to the heat applied during the reaction between CaO and PVDF. For CG, this can be due to the heat generation that occurred on grinding friction. Nevertheless, D-peak in HG is relatively higher than CG which might be due to the use of CaO. As the grinding takes place in the hot process after the reaction, remaining CaO can cause structural deformities for the graphite structure due to the additional friction.

SEM-EDS analysis was also used to characterize the graphite recovered through the three procedures (Figure 4.5(c)). Surface of the WG is much cleaner and without impurities compared to CG and HG. HG shows the highest amount of surface impurities. EDS analysis showed that WG contains 95wt% of carbon and 3.02wt% of oxygen and minor amounts of chlorine. In CG, 68% carbon, 11% copper, 6.42% fluorine and minor amounts of chlorine were detected. Finally in HG, 70% carbon followed by 9% copper, 12 % oxygen, 5% iron, 1 % calcium and minor amounts

of phosphorus, sulfur, and chlorine were reported. The elemental analysis suggests that solid-electrolyte-interface (SEI) (Li-salts, polyolefins and semi carbonates) is present in both CG and HG samples [37]. Nevertheless, these impurities can be also derived from electrolyte or organic solvents. However, in WG, SEI layer is not to be found as the acid can effectively leach these elements out from the matrix. Graphite structures by cold and hot processes match with spent graphite structures by other authors as well [35]. Moreover, the structure and composition of the WG demonstrate similar acid leached graphite by the authors. However, it is important to note that the studies carried out by Lai et al (2023), involved higher temperatures than in this study.

3.3 Life cycle assessment

The LCA study of the graphite extracting routes evaluates the environmental impacts of each route focusing on key energy and material saving spots in the recycling route.

3.3.1 Hotspot analysis of cold process

Damage assessment of cold process reports negative values under all categories considered, mainly due to the high amount of spent metallic copper resulted (Figure 4.6). This is due to the copper metal recycling activities from electronic waste (battery waste). This activity generates a higher environmental benefit than the impact generates through electricity usage for the process. Process hotspots were identified as electricity usage and spent copper recovery. It is important to note that no avoid products were used in this study. Impacts made by each component were given under annexure 3. Table S4.1.

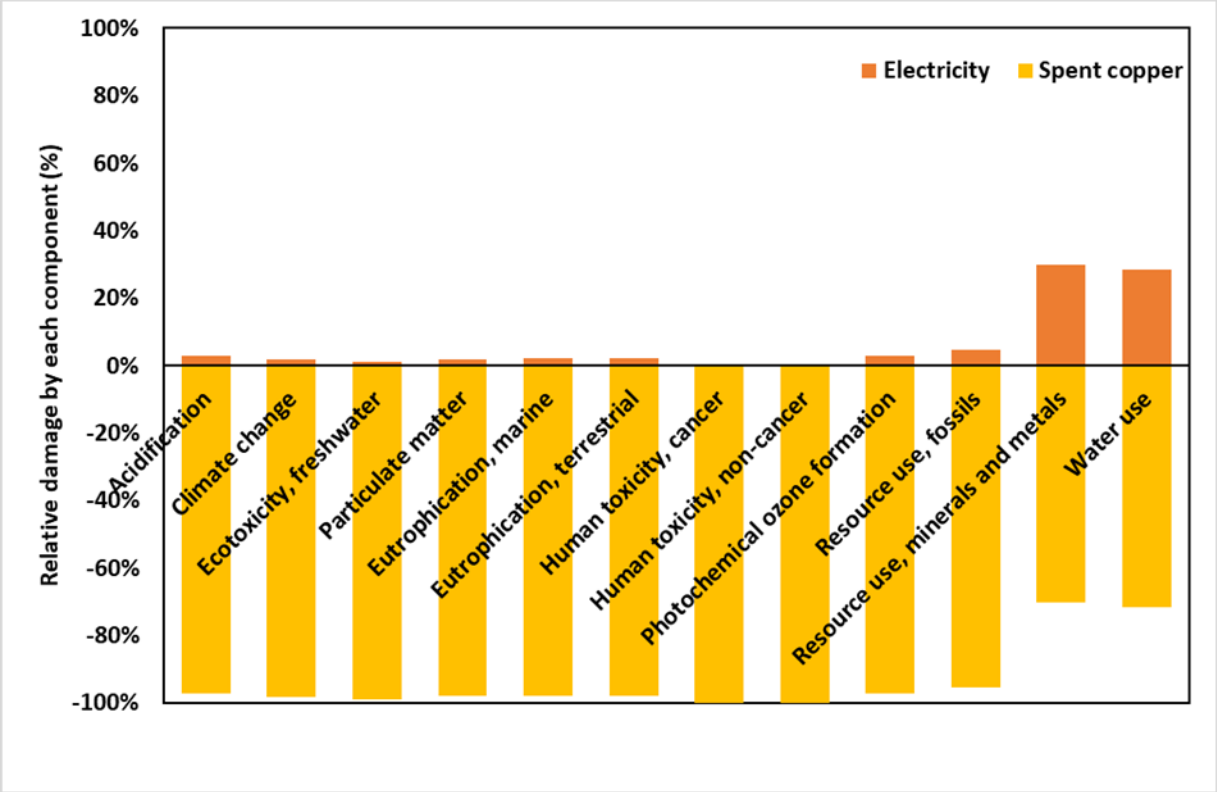

Figure 4.6 Relative percentage contribution for the damage assessment of cold process by each component.

Spent copper accumulation as a byproduct of the process gives benefits under all categories. Resource use (minerals and metals) (~30%) and water use (~29%) show a higher relative percentage of damage than the rest compared to the benefits received through copper recovery. Lowest relative damages were reported at <0.5% by Human toxicity categories. Damages occur through these categories under electricity usage can be due to infrastructure building and water use for cooling of generators. However, the highest actual damages were made under resource use (fossils) (3.52×10^{-01} MJ) and ecotoxicity (6.83×10^{-02} CTUe) impact categories which affected by electricity generation (Table S4.1). Moreover, the highest benefits ($-7.08\times10^{+00}$ MJ, $-5.50\times10^{+00}$ CTUe) were also received through the same categories due to the reductions of hazardous waste that could contaminate water sources by metal mining that would otherwise occur. Recycling of spent copper emits lower volumes of toxic gases and reduces water pollution compared to traditional mining methods [38]. However, the most affected impact categories are resource use, water use, and climate change in descending order. The high environmental benefit generation

under these categories was due to the large number of toxic gas and water born substances being avoided by copper recycling.

3.3.2 Hotspot analysis of hot process

The highest impacts were given by high electricity usage for the heating as per Figure 4.7. Benefits were made through the spent copper recovery. However, these benefits are not sufficient to overcome the damage made by other impact contributors such as CaO, water and direct emissions. Annexure, Table S4.2, shows the actual damage made under each category for various components in the hot process.

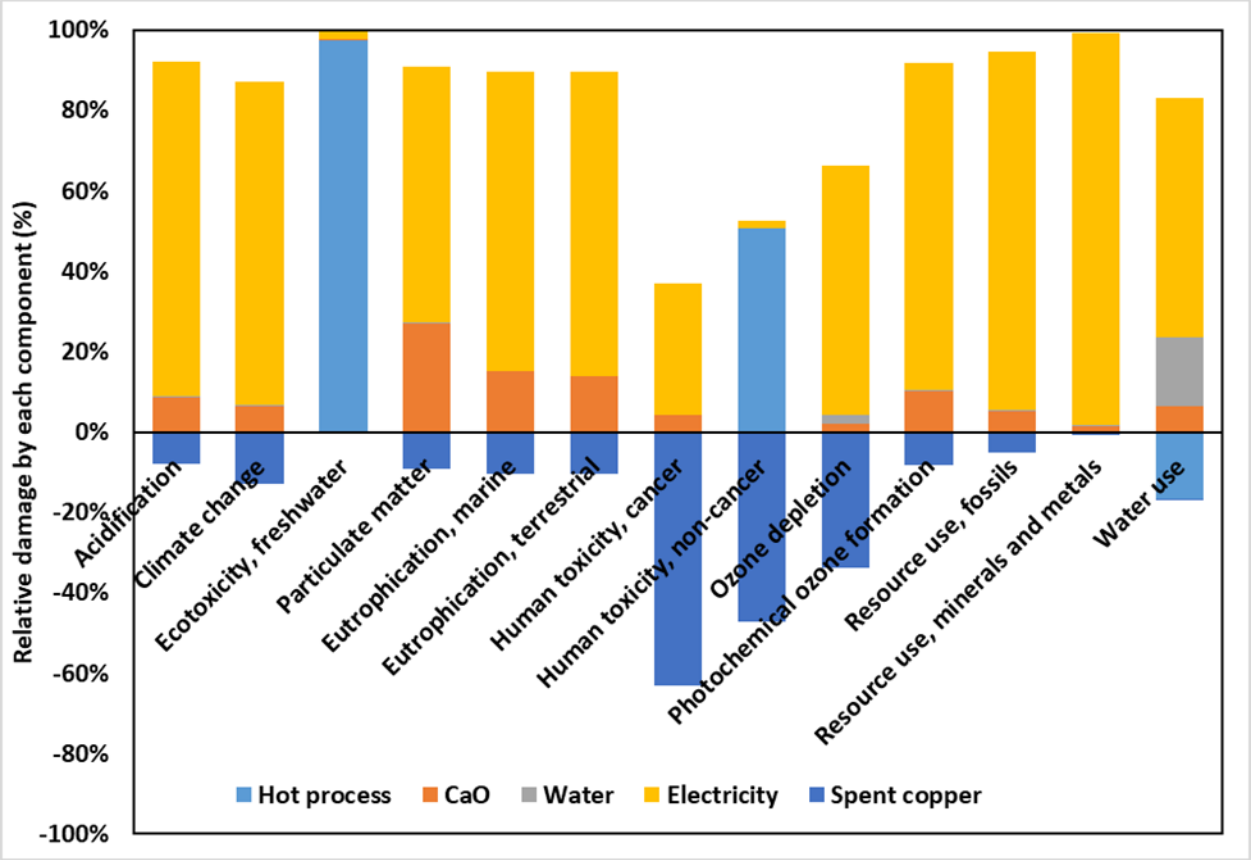

Figure 4.7 Relative percentage contribution for the damage assessment of hot process by each component.

Major damage (over 50%) under many impact categories except eco-toxicity (fresh water) and human toxicity categories were given by electricity usage. Mainly, these two impact categories were affected by the direct emission of Ca compounds to fresh water. Under Ecotoxicity (fresh water), this damage responsible for over 95% of the total damage by the category. For Human

toxicity, it is around 50%. CaO usage also shows damage under many impact categories, maximum being ~25% under particulate matter. This could be due to the CaO crushing to make powder form. Other than that, upon releasing remaining CaO to freshwater, it can increase the alkalinity favoring the dissolving of nutrients in water promoting algal blooming [39].

Recovering copper from the anode has benefits under all the considered impact categories. However, benefits under ecotoxicity (freshwater), mineral resource use and water use reported the lowest values, and the highest are human toxicity (Cancer) at 65% and non-cancer at 50%. Other categories also show benefits under 15%. These benefits are due to the avoidance of primary copper mining. Under water use category, water usage damages (~20%). However, discharging of water (as a direct emission), recharge surface waters adding benefits to the process at 17%.

The hotspot of impact is derived from electricity usage under climate change and resource use impact categories. Moreover, the direct impact of the process under ecotoxicity and human toxicity is also significant.

3.3.3 Hotspot analysis of wet process

Almost all the impact categories demonstrated only damages except under “water use” category. The “water use” category shows around 30% benefits as the water discharges through the process enriching surface waters. However, the damage involved with water use in the process is 32% (Figure 4.8). Numerical values of each damage under different categories of wet process were given in annexure, Table S4.3.

The top contributors to the environmental damage under wet process are the extraction process itself (use of royal solution and disposal of acidic wastewater). Direct extraction process of wet route seems to be impacting the environment under acidification (~70%), particulate matter (~90%), eutrophication (~95-98%), human toxicity (cancer) (~70%) and photochemical degradation (almost 99%) damage categories the most. The impacts are mainly due to the high amount of toxic (HF) and greenhouse gases (NO_2) emissions by the process. Moreover, the high amount of wastewater discharge (9.5 kg for the extraction of 1 kg of graphite) is also contributing to elevating damage. HCl gives slightly higher damages than HNO_3 under several impact categories as the quantity of HCl is higher in the royal solution (HNO_3:HCl molar ratio =1:3). Mainly, human toxicity (non-cancer) (over 70%), ozone depletion (~90%) and resource use (both

fossil and mineral) (~70% and ~80% respectively) categories denote damage from acid use. Climate change at ~58% and ecotoxicity at ~55%, report the highest damage through the spent acidic mixture disposal due to the acidic nature and availability of metals and leach residue in it.

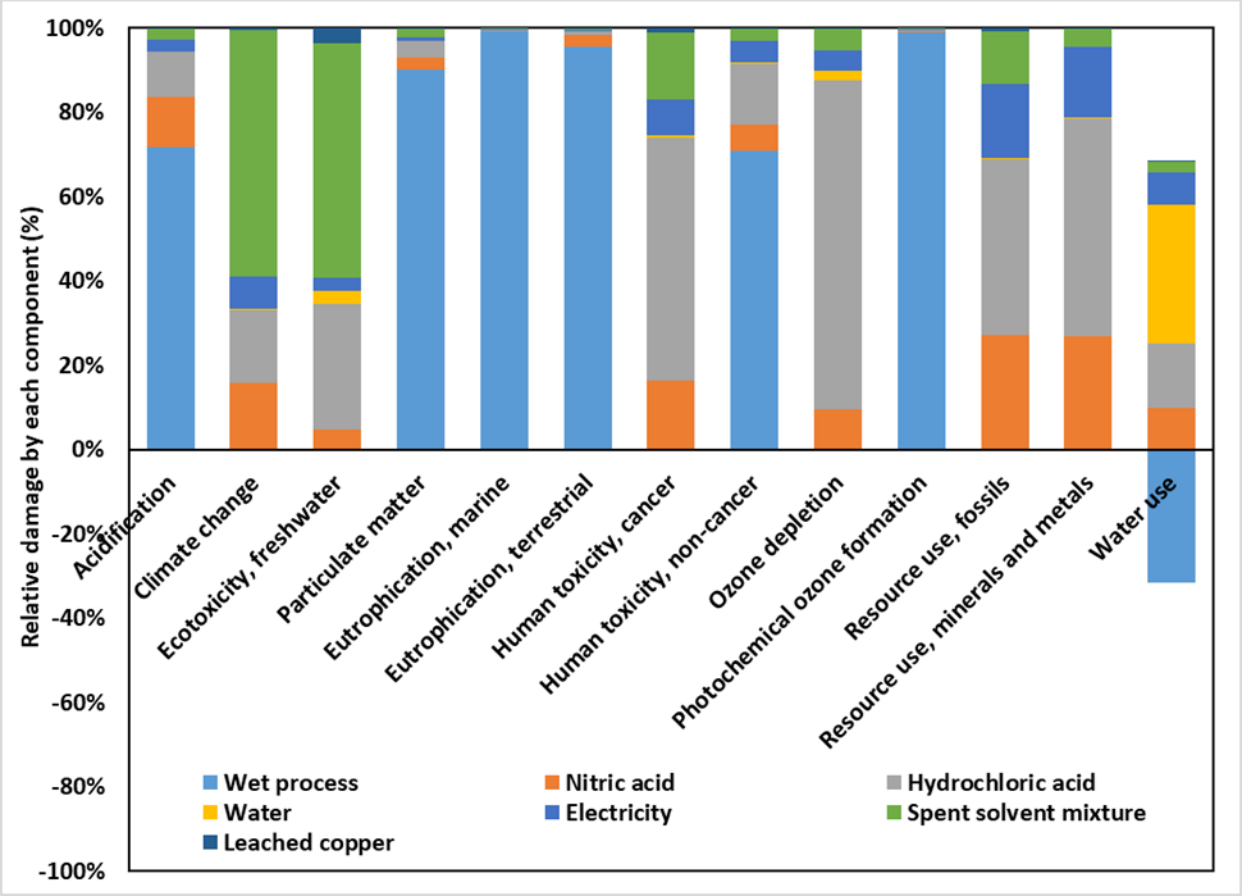

Figure 4.8 Relative percentage contribution for the damage assessment of wet process by each component.

Most significant impact categories under the wet process were identified as the photochemical ozone depletion, Eutrophication (marine and terrestrial) and particulate matter impact categories due to the high damages reported under these categories (Table S4.3). Further, the hots spot of the route can be identified as the process itself (direct emissions). Electricity usage has a very low effect on overall damage.

3.3.4 Comparison of extraction routes

The comparison of the extraction routes was done by assessing the damage done under each impact category of the three extraction routes (Table 4.3). The functional unit of the three extraction routes were kept as the recovery 1 kg of pure graphite from the anode materials.

Table 4.3 Comparison of damage generated by the three graphite extraction methods under different damage categories.

Damage category	Unit	Cold process Graphite	Hot process Graphite	Wet process Graphite
Acidification	mol H^+ eq	-2.90×10^{-03}	9.06×10^{-03}	2.15×10^{-02}
Climate change	kg CO_2 eq	$-1.17\times10^{+00}$	$1.97\times10^{+00}$	$1.84\times10^{+00}$
Ecotoxicity, freshwater	CTUe	$-5.43\times10^{+00}$	$3.61\times10^{+02}$	$1.48\times10^{+01}$
Particulate matter	disease inc.	-2.18×10^{-08}	5.69×10^{-08}	4.22×10^{-07}
Eutrophication, marine	kg N eq	-6.41×10^{-04}	1.42×10^{-03}	9.32×10^{-02}
Eutrophication, terrestrial	mol N eq	-7.01×10^{-03}	1.52×10^{-02}	3.68×10^{-01}
Human toxicity, cancer	CTUh	-3.75×10^{-08}	-4.42×10^{-09}	4.40×10^{-09}
Human toxicity, non-cancer	CTUh	-2.30×10^{-06}	7.40×10^{-08}	3.33×10^{-08}
Ionising radiation	kBq U-235 eq	-4.65×10^{-02}	2.69×10^{-01}	9.50×10^{-02}
Photochemical ozone formation	kg NMVOC eq	-2.20×10^{-03}	6.40×10^{-03}	2.40×10^{-01}
Resource use, fossils	MJ	$-6.73\times10^{+00}$	$3.42\times10^{+01}$	$1.30\times10^{+01}$
Resource use, minerals and metals	kg Sb eq	-3.72×10^{-07}	2.69×10^{-05}	1.07×10^{-05}
Water use	m^3 depriv.	-2.40×10^{-02}	$1.71\times10^{+00}$	4.76×10^{-01}

Lowest → **Highest**

The assessment shows benefits under all the damage categories of the cold process compared to the other two processes due to the extraction of copper as the second product in the metal form. Hence, cold process can be identified as the best method to recover graphite from the anode materials from an environmental perspective. Hot process and wet process, on the other hand, show higher environmental damage than cold process under almost all categories except for human

toxicity (cancer) where hot process shows the lowest at -4.42×10^{-09} CTUh. Moreover, climate change ($1.97\times10^{+00}$ $kgCO_2eq$), ecotoxicity-freshwater ($3.61\times10^{+02}$CTUe), resource use-fossils ($3.42\times10^{+01}$MJ) and water use ($1.71\times10^{+00}$ m^3 depriv.) categories show higher damage under the hot process. However, wet process also shows higher damage under these categories ($1.84\times10^{+00}$ $kgCO_2eq$., $1.48\times10^{+01}$ CTUe, $1.30\times10^{+01}$ MJ, 4.76×10^{-01} m^3 depriv. in respective order). Further, wet process also shows high environmental damage in eutrophication (marine and terrestial): 9.32×10^{-02} kg N eq., and 3.68×10^{-01} mol N eq, as well as photochemical ozone formation: 2.40×10^{-01} kg NMVOC eq. In contrast, only the damage under ionizing radiation category of hot process (2.69×10^{-01} kBq U-235 eq) significantly exceeds the damage from the wet process (9.50×10^{-02} kBq U-235 eq). This proves that the damage done by the wet process is crucial and paramount compared to the other two processes. To confirm this idea, normalization and weighting of the damage from the three extraction routes were evaluated (Figure 4.9(b)).

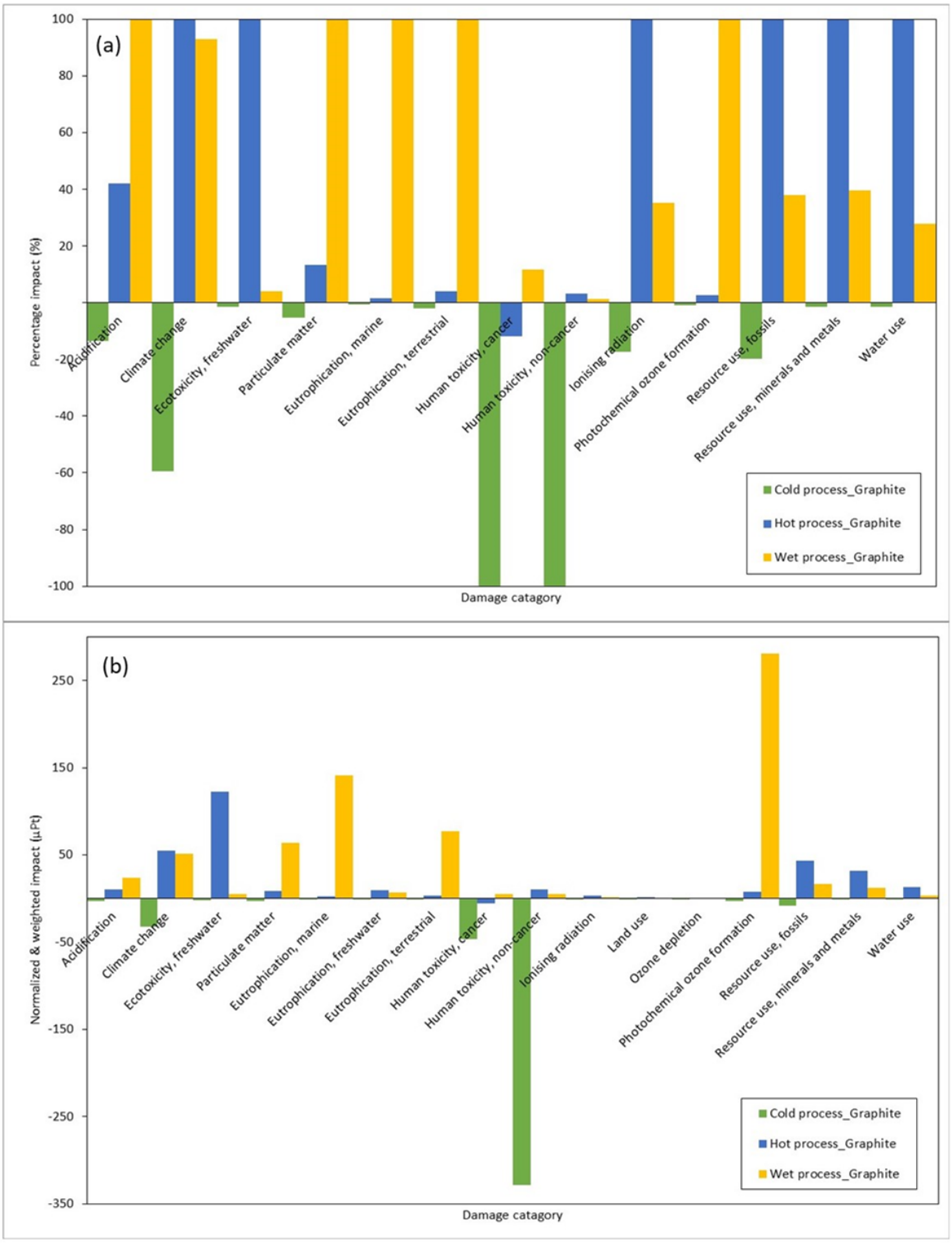

Figure 4.9 relative environmental damage under different impact categories (a) characterization (b) normalized and weighted.

Cold process brings environmental benefits through all the considered impact categories (highest under human toxicity-cancer (-46 µpt) and non-cancer (-328 µpt)). Significant damages occur under climate change, ecotoxicity (freshwater), particulate matter, eutrophication (marine), eutrophication (terrestrial), human toxicity, and photochemical ozone formation impact categories only. From those, climate change (54 µpt) and ecotoxicity (freshwater) (122 µpt) dominated by the hot process. However, in the wet process the values are: 51 µpt and 5 µpt respectively. Particulate matter (63 µpt), eutrophication (marine) (41 µpt), eutrophication (terrestrial) (77 µpt), and photochemical ozone formation (281 µpt) impact categories dominant by the wet process and the differences are crucially higher than hot process. This further confirms that the wet process brings more environmental degradation than the hot process. Using different acid reagents or oxidants can affect the wet process differently, maybe lowering the overall environmental impacts. To test this idea, partial LCA was done to compare the impacts of different acid reagents with oxidants that can be used for the treatment of graphite. In the case of HNO_3, oxidants are not required, however, for HCl or for H_2SO_4 using of H_2O_2 as an oxidant (usually 10 wt.%) is a must to avoid passivation of metals and enhance dissolution. Moreover, the usage of heat is also required for H_2SO_4 [40], [41]. Figure S4.1, in annexure 3 brings the comparison of different acid reagents that can be utilized in graphite recovery from anode materials dissolving copper. As Figure S4.1, it is confirmed that utilizing oxidants or heat can elevate the environmental damage than utilizing the royal solution at room temperature. This further confirms that the use of acid reagents in recovery of graphite from end-of-life LiBs is not the ideal setting.

To evaluate the consistency of the model developed and to understand the probability of having significantly higher damage under the wet process than the hot process given different emission values within the standard deviation, the Montecarlo analysis was performed with 1000 iterations. The results were given under Figure 4.10.

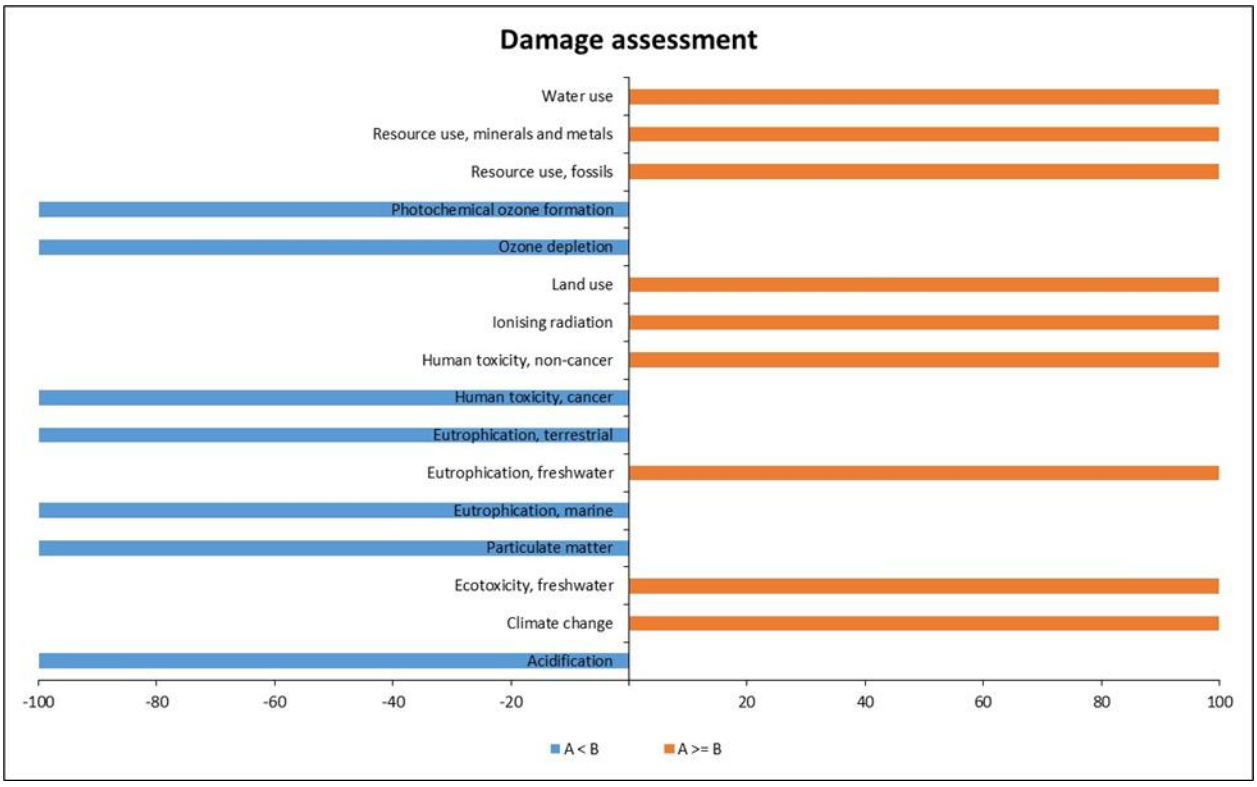

Figure 4.10: Montecarlo Uncertainty analysis of 1 kg 'Hot process' (A) minus 1 kg 'Wet process' (B). Method: Environmental Footprint 3.1 (adapted) V1.01 / EF 3.1 normalization and weighting set, confidence interval: 95 %.

As per the analysis, water use, resource use, land use, ionizing radiation, human toxicity (non-cancer), eutrophication (freshwater), ecotoxicity (freshwater) and climate change impact categories certainly bring the highest environmental damage through the wet process within the standard deviation under 95% confidence intervals. On the other hand, the hot process certainly brings damage to the environment under photochemical ozone formation, ozone depletion, human toxicity (cancer), eutrophication (terrestrial and marine), particulate matter and the acidification with 95% confidence interval. Accordingly, the study concludes that hot process is environmentally beneficial than the wet process. However, cold process is the best method given the lowest environmental damage.

3.4 Life cycle costing study

Costing analyses were done based on the material requirement for each of the graphite extraction processes studied (Figure 4.11). The price of recovered graphite was provided as a negative price

to denote potential selling of a product. Moreover, as the qualities of the products that derived from each method are different, the prices were multiplied by the carbon content available in the extracted carbon for standardization. Metals derived from each process were considered as sent to further refinement depending on their qualities.

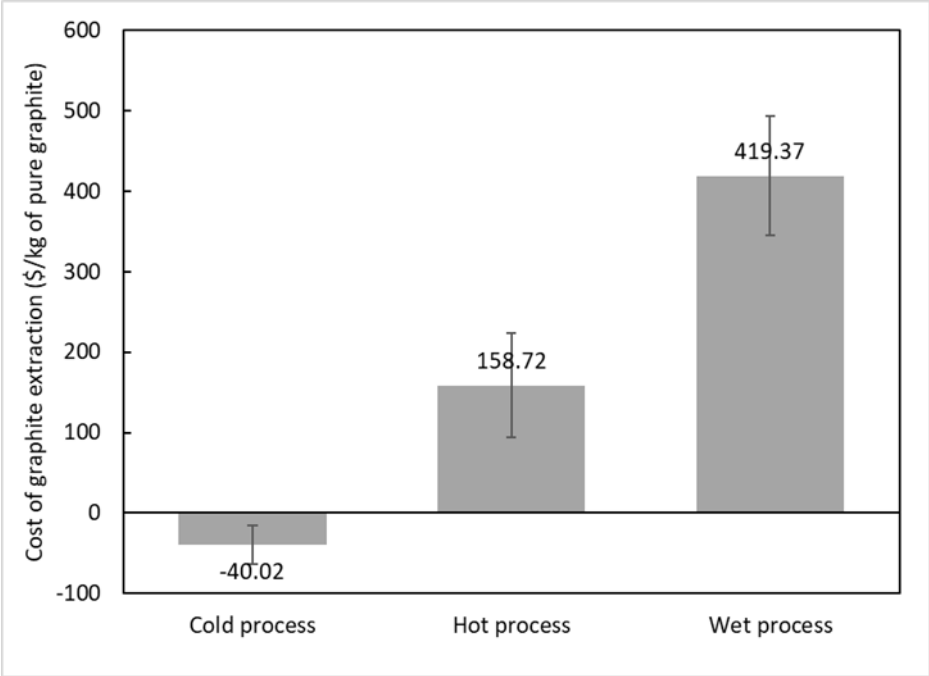

Figure 4.11 Cost of 1 kg of pure graphite extraction from each process studied.

The extraction of graphite through the cold process resulted in a negative cost (a profit) (~ $ -40/kg of graphite extraction) though the quality of the graphite was lower than the other two processes. The main feature that governs the negative cost of the process is the lower cost of expenditures on energy and material acquisition. As identified in the previous section, cold process energy requirement is very low (0.062 KWh/kg of graphite) and the yield of copper in the metallic form lower the cost for further treatment ($ 4.68/kg of graphite). However, low efficiency at 54% of the cold process requires a higher amount of anode materials (1.8 kg/kg of graphite) to use which contributes to increase the overall cost of the process. However, the error (± $ 24) in the cost is considerably higher compared to the total cost due to the uncertainty about the graphite prices. However, even the maximum error considered the cost of the treatment in the cold process provides a negative value. On the other hand, the cost of the hot process resulted in $ 158.72 per kg of graphite recycling. The main contributor for the significantly high cost compared to the cold process is the use of DI water. The total cost of DI water for 1 kg of graphite extraction is around

$ 190/kg of graphite. Secondly, purification of higher wastewater amount which contaminated with Ca compounds also generates significantly higher cost ($ 39/kg of graphite). However, handling of spent metals seemingly lower in cost, given the higher quality of the metal resulted. Also, income from the recycled graphite is higher in hot process ($ -91.43/kg of graphite) than cold process ($ -64.13/kg of graphite) because of higher quality of the recovered graphite (caron content at 64% and 70%, respectively). Considering the error of the hot process cost, the value received was higher than the cold process. However, given the cost of the hot process treatment, the error is reasonable. The deviations occurred due to the uncertainty in the costs of recovered graphite and DI water.

In the wet process, the cost is critically higher ($ 419.37/kg of graphite) than both other methods utilized though the quality of the graphite is higher (carbon content at 81%). The main cost contributor is the use of acid solutions ($ 318/kg of graphite) and DI water ($ 183/kg of graphite). The treatment of spent acid solution and wastewater seemingly cost effective at $ 2.5 and $ 0.004 per 1 kg of graphite. Moreover, the income from the recovered graphite is also higher (at $ -99.41) than other processes given the high quality of the extracted material. Compared to the costs resulted, error in costs is comparably lower at ± $73.75.

To understand the best practice for the recovery of graphite from spent LiBs, quality of recovered graphite, environmental impact and the costs needed to be considered at the same time (Figure 4.12). As the quality of the extracted materials, recovery efficiency was used, for the environmental performance, single score impact assessment was utilized and for economic performance cost of the treatment was used.

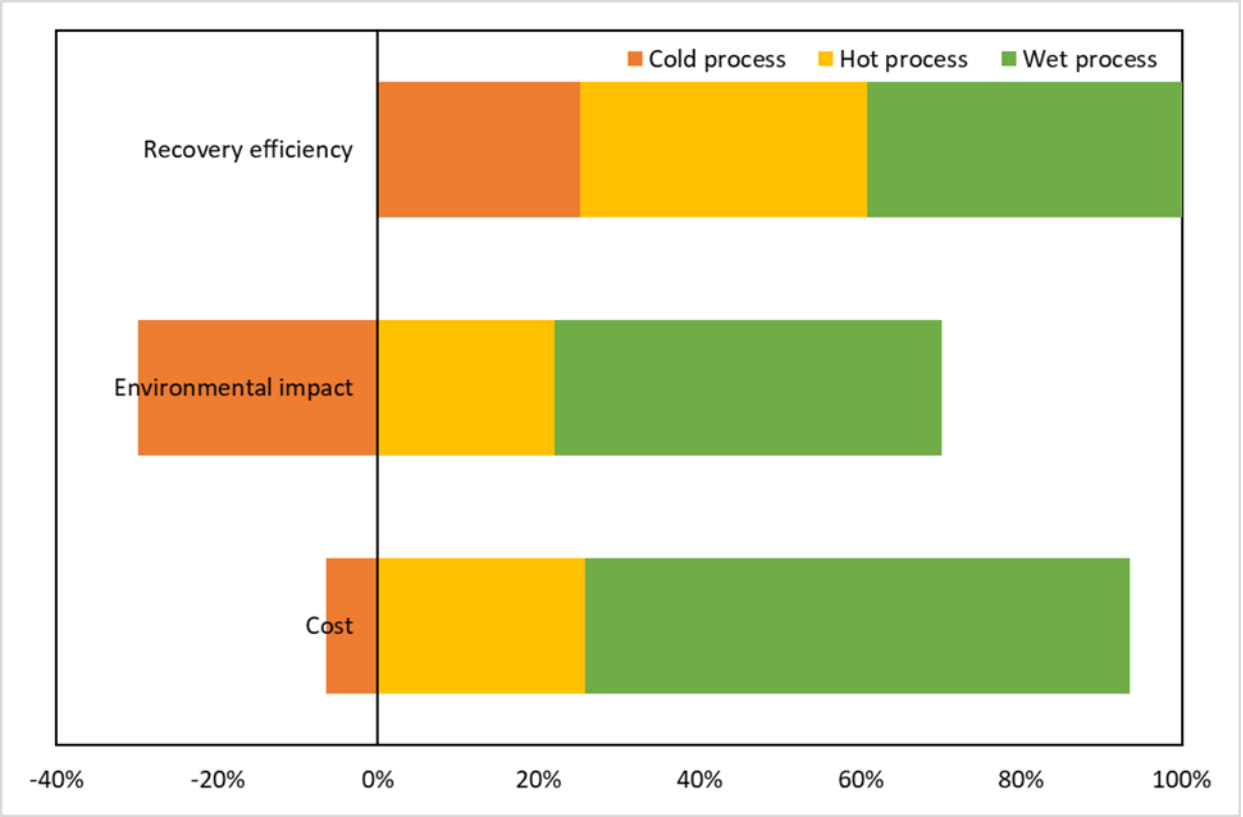

Figure 4.12 Comparison of cold, hot and wet processes for graphite recycling regarding recovery efficiency, environmental impact and cost.

It is visible that the cold process has lower quality graphite (54%), but better in environmental (-30%) and economic (-7%) performances. However, the hot and wet process shows slightly similar performance in the quality of recovered materials (~77% and 84% respectively). However, the hot process has comparably better performance under the environmental impact at 22% damage than wet process (48% damage). The cost of the extraction in hot process is also comparably lower than the wet process (~25% and ~67% respectively). It is possible to deduce that for lower quality application of graphite, cold process or sole physically based methods provide the best recovery. However, for higher quality applications of graphite, physical and heat treatment will result in the best quality. Nevertheless, chemical extraction is better when ultra high-quality graphite is needed to be extracted from the anode materials. However, since the current virgin graphite prices are lower in the market ($ 0.83-2.45/kg of graphite), using recycled graphite for high quality application would lead to drawbacks economically, environmentally and technically. Considering

factors like low environmental impacts and treatment cost, with comparably better quality of graphite, the best approach among cold, hot and wet process is the hot process. However, future studies aiming at improvements may focus on further lowering environmental impacts and elevating the quality of recycled graphite. Moreover, combining different methods of recycling with other battery materials in one recycling line could also lower the overall environmental and economic effects. Authors of this study recommend these approaches as future study paths.

4. Conclusions

The study focused on simplifying the graphite separation from LiB anode material while enhancing the overall sustainability of the products. Parameter optimization was carried out to lower the heat and material consumptions for each process studied. Moreover, characterization of recovered materials showed the quality of the products. Based on the analysis carried out through recovery efficiency, LCA and LCC, hot process seems to be the best mechanism to separate graphite from spent LiB anodes.

From the three modified novel methods utilized to recover graphite from the anode materials, the wet process seems to result in a higher graphite recovery (307.8 g/kg of anode) while the hot process resulted slightly similar value (281.5 g/kg of anode). The cold process resulted in the lowest recovery at 197.6 g/kg of anode. Quality analysis of the samples done by various techniques revealed that using heat-based treatment can elevate the structural quality of the graphite. Accordingly, the hot process resulted graphite showed lower interlayer spacing (0.345 nm) due to annealing effect. Moreover, utilizing CaO to decompose the PVDF binders lower the heat utilization drastically enhancing the overall sustainability of the process. Nevertheless, one advantage of the acid leaching is that effective removal of the SEI layer. As per the findings of the LCA study, sustainability of the graphite separation is highly dependent on the amount of copper that can be recycled in the form of metals. So, copper recycling should be focused when process is designed for graphite recovery. Accordingly, the cold process showed the best performance under the environmental performance with a single impact score of -432 μpt. Hot process resulted the single score impact of 317 μpt given the second highest copper recycling possibility. Electricity usage is a major drive (>50% of impacts arise from energy use) to elevate the environmental impacts on the hot process followed by the usage of CaO (maximum of 30% under particulate matter). The wet process showed the least performance in the LCA with a single score impact of

695 µpt. Direct emissions of HF and NO (up to 99% under eutrophication) and using corrosive acids (up to 88% under ozone depletion) significantly contribute to elevated impacts.

LCC evaluation suggested that the cold process has the least cost (mostly an income) at $ -40. For hot and wet processes, the cost of treatment resulted is higher at ~ $ 158 and ~ $ 419 per kg of graphite recovery. However, given the efficiency and quality (70% carbon content) of the recovered graphite, the hot process seems to be a better option with comparably lower cost and environmental degradation.

Recommendations on further purification of recovered graphite is suggested to enhance the quality of the graphite for high tech use. Finally, it is important to note that using different databases for LCA study can change the outcome of the analysis.

References

[1] Umicore, "Umicore Our Recycling Process." Accessed: Dec. 14, 2023. [Online]. Available: https://csm.umicore.com/en/battery-recycling/our-recycling-process/

[2] J. Xie and Y. Wang, "Recent Development of CO 2 Electrochemistry from Li–CO 2 Batteries to Zn–CO 2 Batteries," Acc Chem Res, vol. 52, no. 6, pp. 1721–1729, Jun. 2019, doi: 10.1021/acs.accounts.9b00179.

[3] E. Kallitsis, J. J. Lindsay, M. Chordia, B. Wu, G. J. Offer, and J. S. Edge, "Think global act local: The dependency of global lithium-ion battery emissions on production location and material sources," J Clean Prod, vol. 449, p. 141725, Apr. 2024, doi: 10.1016/j.jclepro.2024.141725.

[4] E. Pakostova, J. Graves, E. Latvyte, G. Maddalena, and L. Horsfall, "A novel closed-loop biotechnology for recovery of cobalt from a lithium-ion battery active cathode material," Microbiology (N Y), vol. 170, no. 7, Jul. 2024, doi: 10.1099/mic.0.001475.

[5] H. Yu, S. Wang, Y. Li, Q. Qiao, K. Wang, and X. Li, "Recovery of cobalt from spent lithium-ion battery cathode materials by using choline chloride-based deep eutectic solvent," Green Processing and Synthesis, vol. 11, no. 1, pp. 868–874, Sep. 2022, doi: 10.1515/gps-2022-0073.

[6] S. Natarajan and V. Aravindan, “An Urgent Call to Spent LIB Recycling: Whys and Wherefores for Graphite Recovery,” Adv Energy Mater, vol. 10, no. 37, Oct. 2020, doi: 10.1002/aenm.202002238.

[7] European Commission, “RMIS – Raw Materials Information System,” 2024. Accessed: Sep. 10, 2024. [Online]. Available: https://rmis.jrc.ec.europa.eu/

[8] Madhumitha Jaganmohan, “Global projected growth in metal demand for battery production 2028,” Apr. 2024. Accessed: Jun. 11, 2024. [Online]. Available: https://www.statista.com/statistics/665038/projected-growth-in-metal-demand-for-battery-production-worldwide/

[9] E. Irisarri, A. Ponrouch, and M. R. Palacin, “Review—Hard Carbon Negative Electrode Materials for Sodium-Ion Batteries,” J Electrochem Soc, vol. 162, no. 14, pp. A2476–A2482, 2015, doi: 10.1149/2.0091514jes.

[10] Q. Cheng, B. Marchetti, X. Chen, S. Xu, and X.-D. Zhou, “Separation, purification, regeneration and utilization of graphite recovered from spent lithium-ion batteries - A review,” J Environ Chem Eng, vol. 10, no. 2, p. 107312, Apr. 2022, doi: 10.1016/j.jece.2022.107312.

[11] D. S. Premathilake, F. Colombi, A. B. Botelho Junior, J. A. Soares Tenório, D. C. Romano Espinosa, and M. Vaccari, “Recycling lithium-ion battery graphite: Synthesis of adsorbent materials for highly efficient removal of dye and metal ions from wastewater,” Results in Engineering, vol. 22, p. 102232, Jun. 2024, doi: 10.1016/j.rineng.2024.102232.

[12] J. Liu et al., “Critical strategies for recycling process of graphite from spent lithium-ion batteries: A review,” Science of The Total Environment, vol. 816, p. 151621, Apr. 2022, doi: 10.1016/j.scitotenv.2021.151621.

[13] Y. He et al., “A critical review of current technologies for the liberation of electrode materials from foils in the recycling process of spent lithium-ion batteries,” Science of The Total Environment, vol. 766, p. 142382, Apr. 2021, doi: 10.1016/j.scitotenv.2020.142382.

[14] Y. Yang et al., “A process for combination of recycling lithium and regenerating graphite from spent lithium-ion battery,” Waste Management, vol. 85, pp. 529–537, Feb. 2019, doi: 10.1016/j.wasman.2019.01.008.

[15] D. S. Premathilake, A. B. Botelho Junior, J. A. S. Tenório, D. C. R. Espinosa, and M. Vaccari, “Designing of a Decentralized Pretreatment Line for EOL-LIBs Based on Recent Literature of LIB Recycling for Black Mass,” Metals (Basel), vol. 13, no. 2, p. 374, Feb. 2023, doi: 10.3390/met13020374.

[16] Business analytiq, “Natural graphite price index,” Aug. 2024, Accessed: Sep. 10, 2024. [Online]. Available: https://businessanalytiq.com/procurementanalytics/index/graphite-price-index/

[17] Z. Shi et al., “Establishment of green graphite industry: Graphite from biomass and its various applications,” SusMat, vol. 3, no. 3, pp. 402–415, Jun. 2023, doi: 10.1002/sus2.139.

[18] H. Tian, M. Graczyk-Zajac, A. Kessler, A. Weidenkaff, and R. Riedel, “Recycling and Reusing of Graphite from Retired Lithium-ion Batteries: A Review,” Advanced Materials, vol. 36, no. 13, Mar. 2024, doi: 10.1002/adma.202308494.

[19] F. Duarte Castro, E. Mehner, L. Cutaia, and M. Vaccari, “Life cycle assessment of an innovative lithium-ion battery recycling route: A feasibility study,” J Clean Prod, vol. 368, p. 133130, Sep. 2022, doi: 10.1016/j.jclepro.2022.133130.

[20] ecoinvent, “Ecoinvent version 3.10,” 2023. Accessed: Jul. 08, 2024. [Online]. Available: https://support.ecoinvent.org/ecoinvent-version-3.10

[21] D. S. Premathilake, T. G. Ambaye, A. B. Botelho Junior, A. T. M. Lima, D. C. R. Espinosa, and M. Vaccari, “Comparative environmental and economic assessment of emerging hydrometallurgical recycling technologies for Li-ion battery cathodes,” Sustain Prod Consum, vol. 51, pp. 327–344, Nov. 2024, doi: 10.1016/j.spc.2024.09.015.

[22] M. Wang, Q. Tan, L. Liu, and J. Li, “A Facile, Environmentally Friendly, and Low-Temperature Approach for Decomposition of Polyvinylidene Fluoride from the Cathode Electrode of Spent Lithium-ion Batteries,” ACS Sustain Chem Eng, vol. 7, no. 15, pp. 12799–12806, Aug. 2019, doi: 10.1021/acssuschemeng.9b01546.

[23] C. Boulder County, “Hazardous Waste Disposal Costs for Businesses.” Accessed: May 03, 2024. [Online]. Available: https://bouldercounty.gov/environment/hazardous-waste/disposal-costs-for-businesses/

[24] Statista, “Average monthly electricity wholesale price in Italy from January 2019 to August 2024,” 2024. Accessed: Oct. 10, 2024. [Online]. Available: https://www.statista.com/statistics/1267548/italy-monthly-wholesale-electricity-price/

[25] Sigma Aldrich, “Merck, Italy.” Accessed: Sep. 10, 2024. [Online]. Available: https://www.sigmaaldrich.com/IT/en

[26] Reliable Recycling Center, “Pricing for Scrap Metal.” Accessed: Sep. 10, 2024. [Online]. Available: https://www.reliablerecyclingcenter.com/pricing/

[27] Alibaba express, “High quality 25kg Quick Lime Calcium Oxide Powder CaO Water Treatment.” Accessed: Sep. 10, 2024. [Online]. Available: https://www.alibaba.com/product-detail/High-Quality-25kg-Quick-Lime-Calcium_1601158793942.html?spm=a2700.galleryofferlist.p_offer.d_title.15fa36f2cDuc6K&s=p

[28] Marco Antelmi, “Valutazione Economica per il raggiungimento del Buono Stato Ecologico nel Bacino Lambro-Seveso-Olona,” POLITECNICO DI MILANO, Milano, 2016. Accessed: Sep. 10, 2024. [Online]. Available: https://www.aqualabfondazione.it/files/112_0000188_file_1.pdf

[29] Sally Zhang, “High copper concentrate costs, supply deficit to hurt copper smelters from 2025: LME Asia Week 2024,” 2024. Accessed: Sep. 10, 2024. [Online]. Available: https://www.fastmarkets.com/insights/high-copper-concentrate-costs-supply-deficit-to-hurt-copper-smelters-from-2025-lme-asia-week-2024/

[30] X. Wang et al., “Mildly expanded graphite with exceptional performance from waste lithium ion batteries by space-confined intercalation of deep eutectic solvent,” Sep Purif Technol, vol. 354, p. 129329, Feb. 2025, doi: 10.1016/j.seppur.2024.129329.

[31] A. Lähde et al., “Effect of high temperature thermal treatment on the electrochemical performance of natural flake graphite,” J Mater Res, vol. 39, no. 6, pp. 944–954, Mar. 2024, doi: 10.1557/s43578-024-01282-z.

[32] R. Praats, A. Chernyaev, J. Sainio, M. Lundström, I. Kruusenberg, and K. Liivand, “Supporting critical raw material circularity – upcycling graphite from waste LIBs to Zn–air batteries,” Green Chemistry, vol. 26, no. 5, pp. 2874–2883, 2024, doi: 10.1039/D3GC04315K.

[33] L. Zhao, X. Liu, C. Wan, X. Ye, and F. Wu, “Soluble Graphene Nanosheets from Recycled Graphite of Spent Lithium Ion Batteries,” J Mater Eng Perform, vol. 27, no. 2, pp. 875–880, Feb. 2018, doi: 10.1007/s11665-018-3156-6.

[34] D. Claus and J. O. Besenhard, Handbook of Battery Materials. Wiley, 2011. doi: 10.1002/9783527637188.

[35] Y. Lai et al., “Recovery and regeneration of anode graphite from spent lithium-ion batteries through deep eutectic solvent treatment: Structural characteristics, electrochemical performance and regeneration mechanism,” Chemical Engineering Journal, vol. 457, p. 141196, Feb. 2023, doi: 10.1016/j.cej.2022.141196.

[36] D. S. Premathilake, M. Vaccari, A. B. Botelho Junior, J. A. S. Tenório, D. C. R. Espinosa, and F. Colombi, “Valorization of waste graphite deriving from ‘End Of Life Lithium-Ion Battery recycling’ for a second use in wastewater treatment.,” in 18th International Conference on Environmental Science and Technology, Athens, 2023. doi: 10.30955/gnc2023.00266.

[37] H. Adenusi, G. A. Chass, S. Passerini, K. V. Tian, and G. Chen, “Lithium Batteries and the Solid Electrolyte Interphase (SEI)—Progress and Outlook,” Adv Energy Mater, vol. 13, no. 10, Mar. 2023, doi: 10.1002/aenm.202203307.

[38] S. Manikandan, D. Inbakandan, C. Valli Nachiyar, and S. Karthick Raja Namasivayam, “Towards sustainable metal recovery from e-waste: A mini review,” Sustainable Chemistry for the Environment, vol. 2, p. 100001, Aug. 2023, doi: 10.1016/j.scenv.2023.100001.

[39] K. Suresh et al., “Recent advancement in water quality indicators for eutrophication in global freshwater lakes,” Environmental Research Letters, vol. 18, no. 6, p. 063004, Jun. 2023, doi: 10.1088/1748-9326/acd071.

[40] Y. Gao et al., “Graphite Recycling from the Spent Lithium-Ion Batteries by Sulfuric Acid Curing–Leaching Combined with High-Temperature Calcination,” ACS Sustain Chem Eng, vol. 8, no. 25, pp. 9447–9455, Jun. 2020, doi: 10.1021/acssuschemeng.0c02321.

[41] R. Li et al., “A facile approach for regeneration of graphite anodes from spent lithium-ion battery,” J Alloys Compd, vol. 993, p. 174691, Jul. 2024, doi: 10.1016/j.jallcom.2024.174691.

Chapter Five-Anode Material Reuse for Wastewater Treatment

Recycling Lithium-Ion Battery Graphite: Synthesis of Adsorbent Materials for Highly Efficient Removal of Dye and Metal Ions from Wastewater.

This paper has been published in the journal *Results in Engineering* (https://doi.org/10.1016/j.rineng.2024.102232) and the author contributed in writing the original draft, editing and reviewing, conceptualization, methodology, experiments and formal analysis.

1. Introduction

Since the first application in portable devices in early 90's, the demand of lithium-ion batteries (LIBs) grew rapidly. LIBs are now commonly used in various devices like electric vehicles, light machinery, mobile electronic devices, medical devices, recreational devices, due to their cycling efficacy, energy density and optimal capability. LIBs world market value was USD 29.86 billion in 2017 and is predicted to reach USD 139.36 billion by 2029 [1], [2]. However, the increasing demand for LIBs also brings challenges, particularly in managing spent batteries. Disposing of spent LIBs irresponsibly could harm the environment and human health as they contain toxic organic solvents, metals, and flammable plastics. Moreover, these batteries are composed of critical raw materials that have risk of supply interruption in the short and medium-term. Therefore, it is crucial to recycle spent LIBs to achieve the circular economy [3].

Recycling of LIBs is currently an attractive topic in industrial environments, national research institutes and among academic professionals. The elements obtained from recycled LIBs range from poor to high quality materials based on the extracting methods. There are three categories of recycling processes based on the final recovered materials: pyrometallurgical, hydrometallurgical, and direct physical recycling. Direct recycling, recovering materials mainly through physical methods, as an example; Shi et al. developed a non-invasive method to reconstruct $LiCoO_2$ using combination of brief heat treatments [4]. Though the authors reported promising results with recovery of graphite, in overall direct recycling was not yet succeeded in restoring the full potential of the cathode material [5]. Pyrometallurgical process involves smelting battery components at temperatures above 1000°C to obtain alloys such as Co, Ni, and Cu. Nevertheless, materials like graphite and organic electrolytes will be burnt in this process limiting their recovery, while Li is present in slag phase. Lee and the collaborators also identified a joint process (hydrometallurgy and calcination) to recycle $LiCoO_2$ type batteries followed by shredding and separation procedures.

The method produced $LiCoO_2$ powder from the used cathode materials that can be used as a new cathode. Though the cathode materials produced show better performance in charge and discharge cycles, materials including graphite and electrolytes were lost during the smelting steps and was not recovered [6].

Hydrometallurgical methods involve chemical processes in aqueous media that may include extraction through solvents, purification/precipitation steps, redox reactions, or reaction with acid-alkali solutions. Compared to pyrometallurgy, hydrometallurgy is a highly effective method that can recover nearly all materials present in LIBs, including cathodes, anodes, separators, and electrolytes. Also, Lithium may recover as a high-pure product. Most hydrometallurgical-based recycling methods follow a similar process with slight adjustments, such as using different synthesizing methods, reactants, and recycling channels [7], [8], [9], [10].

Cathode recovery was the spotlight in current LIBs recycling scenarios due to the economic importance, and low attention is given to graphite recovery. Currently, graphite, which is responsible for 10-15% of the total economic worth of the battery, ranges from minimum of 8 USD to maximum of 13 USD per kilogram of anode material. Furthermore, spent LIBs contain approximately 12-21 wt% graphite [11], [12]. With the high utilization of LIBs, the quantity of disposed graphite accumulates rapidly and soon the total would become an intolerable amount for easy disposal [13]. Hence, it is imperative and essential to incorporate recycled graphite anodes in a closed-loop or open-loop system.

During the use of graphite in LIBs, its structure is subjected to various deformities. For example, changes in crystalline structure, changes in interlayer distances and defects due to repeated cycles of charging and discharging [2]. It is widely reported that novel methods for graphite recovery need to be developed to reuse the graphite in new battery cells [14]. Though extraction or separation of graphite from active materials is challenging, enhancing the graphite properties to be reused in new battery materials is even more problematic. This is mainly due to the high cost of treatment methods identified such as leaching, surface modification, and pyrolysis [2]. Hence, closed loop recycling of graphite is still to be fully developed to make it economical. However, separating defective graphite from the cathode active material by physical means is experimented. Kepper and the collaborators reported that filtration-based separation of graphite from mixture of carbon coated LFP ($LiFePO_4$) and graphite resulted in a low separation efficiency around 1-15%

[15]. Moreover, an attempt made by Mennik et al (2023) to separate metals from spent LIBs through flotation and magnetic separation resulted in graphite ending up with the critical metals available in the cathodic part [16]. These findings suggest that hydrometallurgical methods are much more convincing in extracting the graphite available in the active materials. However, impurities accumulated throughout the hydrometallurgical methods along with structural deformities of graphite prevent recycled graphite from being used in new LIB applications. Instead, recovered graphite can be used in secondary applications such as reducing agents, negative electrodes, synthesis of graphene or derivatives, graphite-based materials, or functional materials [2]. Among those options, synthesis of graphene or derivatives is likely to be more convenient as it can be used as adsorbents for wastewater treatments.

On the other hand, wastewater treatment chemicals and processes that are used for treatment of dye wastewater or metallic ions contaminated water are at high cost [17]. However, most of these materials act as adsorbent materials with higher adsorption capacities. For an instant, scholars assessed the adsorption of malachite green using activated carbon, manufactured through gasification of waste. It is assessed that the material has an adsorbent capacity of 226.06 mg/g against malachite green [18]. Xu et al, presented methylene blue removal from distillers' grains hydro-char with an adsorption capacity of 340.3 mg/g [19]. Nevertheless, Cd^{2+} and Ni^{2+} removal was studied by a group of scientists using cherry kernels biochar. It was identified that adsorption capacities of these adsorptions to be 92.42 and 66.22 mg/g respectively [20]. Also, rice straw biochar was used to remove Zn^{2+} by Sakhiya et al. It was identified that the adsorption capacity for this to be 35.71 mg/g [21]. All these materials have considerably high adsorption capacity hence a higher cost is expected. Ighalo et al (2022) demonstrated that the costs of the adsorption treatment are highly dependent upon the adsorption capacity and the use of virgin raw materials. They also concluded that the cost of adsorption treatments can vary from USD 1 -200 per mol [22]. On the positive side, it is evident that most of these adsorbent materials listed above are made from carbon-based materials which resulted in comparably higher adsorption capacities. However, bio-based carbon products such as bio char needs to be treated at very high temperatures (300 ~ 1000 °C) prior to wastewater treatment application, utilizing higher energy for production [23]. This can lower the overall sustainability of such materials. Accordingly, the high cost of production and less sustainable synthesizing methods can be the main drawbacks of existing adsorbent materials. Hence a competitive adsorbent material would be made from recycled, carbon-based

material through less energy intensive synthesis. Hence the idea of using recycled graphite-based derivatives to replace existing adsorbents was generated.

Examining these challenges, the objective of the study is set; to assess the reusability of waste graphite derived from end-of-life (EoL) LIBs in effective pollutant removal from wastewaters. In achieving so, this manuscript describes a potential utilization of residual graphite that resulted as a waste from a real-life hydrometallurgical metal extraction route. The fate of this waste product is not yet explored in existing literature. Moreover, modification of residual graphite was carried out to synthesis Graphene oxide (GrO) and graphite oxide (GO). Enhanced properties of graphite derivatives (GO and GrO) such as higher surface area, increased pore spaces and higher adsorption capacities were expected to address the objectives of the study. We examined and identified the performances, capacities, and adsorption mechanisms of the produced graphite derivatives (adsorbent materials) through various analysis and calculations.

As organic pollutants Methylene blue (MB) and Malachite green (MG) were used. As per the metallic pollutants Cd^{2+}, Ni^{2+} and Zn^{2+} were used. MB and MG dyes are being used extensively in paper, leather, and textile industries. Moreover, these two dye types are extensively studied in literature, which makes it easier for comparative studies to understand the adsorption capacities of the newly made adsorbents. In the case of metallic adsorbates, they also have a wide range of applications and subjects to accumulate in the wastewaters. Hence, these adsorbates also studied well in laboratory studies making it easier for the comparison studies.

2. Methodology

2.1 Graphite recovery

Twenty cylindrical batteries of NMC 811 were discharged completely using Ni-Cr wire (4Ω). Subsequently, the discharged modules were milled and sieved to gain particle fraction <9 mm. Following this, another sieving step (> 5 mm) was utilized to remove the non-metallic fraction from the mixture. The coarser fraction here contained separator materials and plastics. Later, the finer fraction was left under the fume hood for 1 day at ambient temperature to evaporate organic solvents and electrolytics. After, the dried material is subjected to another milling and sieving step >2 mm. This step removed most of the copper and aluminum in the mixture leaving only active materials for the leaching steps. 1M H_2SO_4 was used for the leaching step of the active materials.

Conditions were set to 90 °C, at atmospheric pressure for 90 minutes of leaching with the condenser. The residue material, known as waste graphite (WG), was filtered, washed with deionized water, and dried for 24 h at 60°C [24]. The leach residue derived from this step was then dried at 60 °C for 1 day and taken for the next steps of the experiment.

2.2 Characterization of WG

WG recovered from hydrometallurgical leaching was analyzed using X-ray diffraction (Miniflex instrument, Rigaku), Raman spectroscopy (InVia R.M. instrument Renishaw), X-ray fluorescence-energy dispersive spectroscopy (XRF-EDX, EDX-7000 Shimadzu), particle size analysis (Mastersizer 2000 instrument Malvern), scanning electron microscopy (SEM-EDS, Phenom ProX instrument Thermo Fisher), and carbon content analysis (Elementrac CS instrument ELTRA GmbH).

2.3 Adsorption material synthesis

Chemical oxidization (Hummer's method) was utilized to prepare the graphite derivatives; GrO and GO [25]. This method was incorporated as it is the most widely accepted oxidization method to produce graphite-based derivatives industrially as the process it-self is safer and convenient compared to other existing methods [26]. To prepare GO, 230 ml of concentrated (98%) H_2SO_4 was mixed with WG in an ice bath (5 °C) in 1:23 (g/ml) ratio. The materials were kept in suspension using a mechanical stirrer (180 rpm) for 1 hour. Sudden temperature elevation was avoided while adding $KMnO_4$ (99%) slowly in the ratio of 3:1 ($KMnO_4$: WG) to the mixture. Ice baths were further used to keep the temperature less than 40°C during the addition of $KMnO_4$. Stirring continued for another 3 hours with the mentioned conditions. The dropping funnel method was used to add DI water dropwise in the ratio of 1:2 (H_2SO_4: DI water). This step elevated the temperature up to 90 °C and taken around 3 hours to complete. After another 30 minutes, more DI water was added to dilute the slurry (1:1 ratio of H_2SO_4: DI water) using the same method. Finally, the oxidation reaction was stopped by adding 30% of H_2O_2 in the ratio of 1:1 with graphite added (1 ml/g of graphite). The mixture was kept in suspension with stirring for another 15 minutes and then the slurry was filtered to be taken into further steps.

Excess of diluted (10%) HCl was used to wash the residue derived from the filtration of the above mixture. After further washing of the residue was carried out first by excess of 99% ethanol and second by DI water until the pH of the effluent water becomes 5.5. The remaining material was

dried at 50°C for 24 h, and then ground with a pestle and mortar. The resulting material was 13 g of GO.

Ultrasonication was utilized to prepare GrO through the exfoliation of a portion of GO that had been prepared [27]. Specifically, produced GO and DI water was inserted to a polypropylene tube with solid to liquid ratio of 2 g/L. The charged material underwent sonication (using an Ultrasonic Bath made of solid steel and 100W) for a period of 30 min. The 30 minutes sonication has been done using 6 cycles, where each cycle included 5 minutes sonication followed by 5 minutes centrifugation. The centrifugation was carried out at 3000 rpm. After the last centrifugation step, the sediment was recovered and was then dried for 24 hours at 50°C in a furnace before being ground using a pestle and mortar. Using 2 g of GO in total, the resulting sample was 1.4 g of GrO [24].

Chemical analysis for the adsorption materials prepared was carried out by using Raman spectroscopy, XRD, and SEM. Other than that, active functional groups of the prepared materials were evaluated through Fourier-transform infrared spectroscopy (FTIR) with a diamond plate and Smart iTR technology (Nicolet, Madison, WI, USA) before and after the adsorption processes.

2.5 Batch adsorption tests for spiked dye wastewater

A magnetic stirrer at 300 rpm was used to carry out the dye adsorption experiments. Initially, concentrations of dye solutions were set in the range 30-100 ppm with 50 mL of volume each. Typical dye concentration in textile effluents can vary from 50-2500 ppm. However, many authors used the effective concentration range of 30-100 ppm (as an average) for synthetic dye waste in laboratory studies [28]. Adsorption dosage was determined to be 10 mg for dye adsorption experiments. This was determined by analyzing the dye removal percentages at different GO and GrO dosages varied from 2 -25 mg with 50 ppm initial dye concentration. The adsorption experiments were carried out for 10 min, and samples were taken for UV-vis spectroscopy (Shimadzu AA-7000, Japan) analysis. These steps were carried out at room temperature (25 °C) and at pH of 5.5. Previous workings that have been done for similar materials (graphite derivatives) with MB and MG dye types showed the best effective temperature range for the maximum adsorption to be 20-29°C and the pH at around 5-6 [29], [30], [31]. Hence, the temperature and the pH values for the adsorption processes were pre-decided to be 25°C and pH to be 5.5 respectively. Moreover, decided values are closer to ambient temperature and pH of the waters,

confirming that the process can be carried out without adjusting the values prior to the adsorption, confirming the lowest cost of treatment.

The adsorption percentage and the equilibrium capacity of adsorption (qe,cal) (mg/g) were evaluated using Equations 1 and 2, respectively. C_0 and C_e denote the starting concentration and the concentration at equilibrium in mg/L respectively. The volume of the effluent is given by 'v' and the 'm' stands for the adsorbent mass added in g.

$$adsorption\ \% = \frac{c_0 - c_e}{c_0} \times 100\% \text{ ---------- (1)}$$

$$q_{e,cal} = (c_0 - c_e) \times \frac{v}{m} \text{ ----------(2)}$$

2.6 Batch adsorption tests for spiked metal ion contaminated wastewater

Stock solutions in the range 30 - 150 ppm from each metallic ion were prepared. Metal ion concentrations in industrial wastewater are dependent on various applications. For an instant, in plating industry wastewater, metal ion concentration can be up to 200 ppm for Nickel [32]. However, in the textile industry this can be lower as 60 ppm [28]. In order to cover up a higher range of concentrations this study utilizes the metal ion concentration of 30-150 ppm. Moreover, initial dosage optimization (2-25 mg with 50 ppm initial metal ion concentration) confirmed that 20 mg of adsorbent material dosage will be a good compromise between the removal percentage and the cost of treatment. Hence, 20 mg from each adsorbent materials were mixed with 20 mL of solution at room temperature (25 °C) under magnetic stirring. Experiments were performed within 24h and at each 2h intervals samples were taken out. Extracted solution samples were subjected for centrifugation for 5 min at 3000 rpm before analyzing in the Inductively Coupled Plasma (ICP-OES) spectroscopy. At the end of the 24 h, metallic ions concentrations were also determined using AAS.

The adsorption percentage and the adsorption capacity (qe,cal) (mg/g) of metallic ions in each of the adsorbents were identified using the equations 1 and 2 respectively.

3. Results

3.1 Characterization

The initial characterization of the WG was done to determine the particle size distribution, specific surface area and carbon content. The particle size analysis showed that the WG has a uniformity

index of 0.546, which suggests that the particles vary from d(0.1) at 7.727 μm to d(0.9) at 32.705 μm with the mean at 16.348 μm. Moreover, the specific surface area of the particles is at 0.461 m^2/g. Additionally, carbon content of the sample was 96.6 %.

To determine the impurities, present in the WG, chemical and physical characterizations were also done. Accordingly, XRD, XRF and SEM analysis were carried out. The sample contains graphite from anode and cathode materials mostly, other than that minor amount of aluminum oxide (where Al - 0.38%), undissolved cathode active materials (Ni-1.05%, Co-0.38%, Mn-0.32%), case (Fe-0.05%) and electrolyte (where Cl-1.98%) were present. The source of Al_2O_3 should be from cathode and anode or the Al_2O_3 coated separators. Though these materials along with other metals are supposed to leach and dissolved completely during the leaching steps, due to the inertness of Al2O3 and the incomplete reactions between the leaching solution and the metals, some of these materials can be present at the end of the leaching process. These results agree with the previous results obtained by Ma et al (2019)[33].

XRD results presented in Fig. 1-a suggest that the crystalline structure of the WG is well preserved as the (002) peak is the strongest. Further, the interlayer spacing of the recovered graphite is identified to be 0.336 nm through the attributed peak at 2-theta = 26.50. This is slightly higher than the standard graphite materials or fresh cell graphite materials reported (0.334 nm) by Maher and Yazami (2014) [34]. This suggests that the recovering technique used in the study is somewhat better in preserving the crystal structure of graphite for future applications. Also, structural deformities of WG reported [2] were not found in the graphite recovered.

After the oxidation (preparation of GO) of WG, the XRD pattern changed. Accordingly, 26.50° peak is no longer to be seen, instead a peak appeared at 2-theta = 10.90° resulting an interlayer spacing of 0.81 nm. When producing graphite oxide, interlayer spacing would be enhanced due to the introduction of functional groups (hydroxyl and epoxy groups) between the layers and due to their repulsive forces. This confirms better oxidation of graphite according to the literature [35], [36].

In the case of GrO prepared through ultra-sonication of GO, 2-theta peak shifted to 11.20 giving an interlayer spacing of 0.78 nm. This reduction shows separation or exfoliation of layers in GO hence reducing the interlayer spacing. This can be due to the GO layers that experience localized forces created by ultrasonication which cause their separation or exfoliation. The weak van der

Waals forces that hold these layers together are disrupted by the shear forces and turbulence generated through ultrasonic cavitation. This leads to a reduction in the interlayer spacing. Moreover, ultrasonication has the potential to induce dispersion and fragmentation of the graphite oxide sheets into smaller sizes. The mechanical energy that ultrasonic waves impart promotes the breakup of larger graphite oxide flakes or aggregates into smaller particles. In addition, the mechanical energy caused by ultrasonication can break some of the functional groups that are already bonded to GrO layers, making the repulsive forces between layers lower. This, in turn, can contribute further to the decrease in the interlayer spacing while increasing the total surface area [37]. In both GO and GrO, XRD patterns peaks corresponding to cathodic metals are completely disappearing confirming a complete reaction between the metals and the acids used in preparing the materials [38]

According to the Raman spectra of graphite, D-band and the G-band appeared at 1344.6 cm^{-1} and 1572.56 cm^{-1} respectively (Figure 5.1-b). G-band in graphite Raman Spectra corresponds to the vibrations of carbons atoms in a sp2 configuration and provide details about the graphitic order (stacking of layers) while the D-band corresponds to the vacant or disordered carbon atoms (activated by single phonon scattering process) and provide details about structural deformities of the material [34], [39]. Relative high intensity of G-band (I(D)/I(G) = 0.38) of recovered graphite confirms the presence of well structured graphitic order with well stacked graphite layers. Here, low intense D-band cannot be taken as a structural deformity as similar d-band was reported by Maher & Yazami (2014) in a fresh cell graphite structure as well [34]. Moreover, the presence of such characteristic (low intense D-band) does not contradict with the potential of augmented stacking arrangement of the layers of graphene during repetitive lithium intercalation and de-intercalation. Throughout this process, the layers of graphene slide against each other, ultimately forming AA stacking in LiC_6 after initially exhibiting ABAB and ABCABC stacking in hexagonal and rhombohedral graphite, respectively. During repetitive layer movement during cycling, the potential for the resolution of stacking defects in the initial graphite anode material arises, thus resulting in an improvement in crystallinity [38].

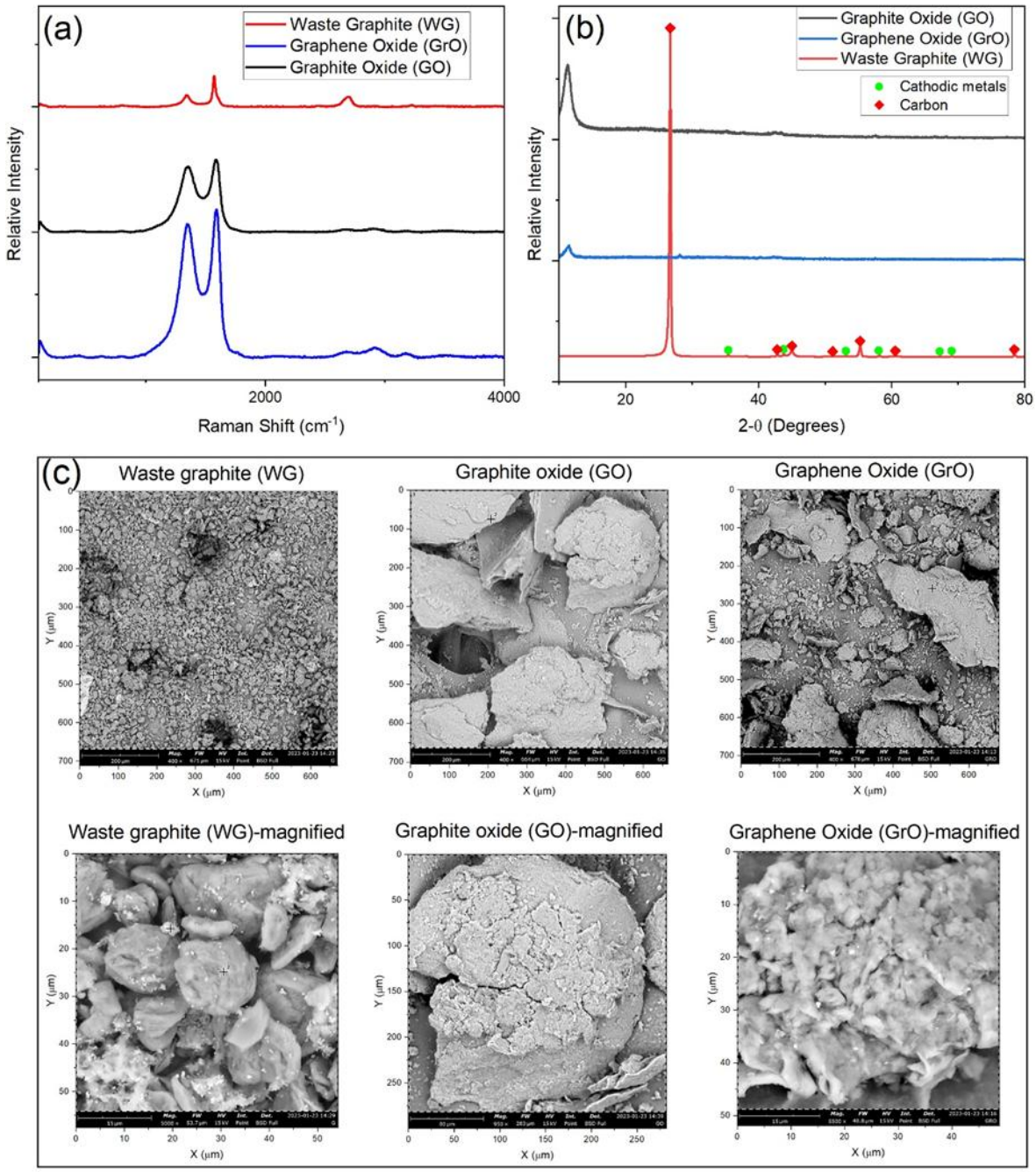

Figure 5.1 Characterization of waste graphite (WG), graphite oxide (GO) and graphene oxide (GrO) a) XRD results b) Raman spectra c) SEM images

In addition, the shoulder like structure appeared in G-band of the graphite Raman Spectra is known as the D'- band which is a result by a second order band activated by double phonon scattering effect [40]. Accordingly, D'-band also implies a possible deformity available in the graphite structure (I(D')/I(G) = 0.25). As the D'-band corresponds to sp^2 defects mostly, the reasons for this

deformity can be caused by the adsorption of foreign atoms or chemical functionalization occurred during the chemical reactions took place during the metal leaching [41], [42].

GO and GrO Raman Spectra (Figure 5.1-b) show a significant difference than WG as expected. Moreover, it is vital to discuss even 2D bands that appear in the Raman Spectra of these structures which corresponds to stacking of graphene layers. 2D region (entire region) can detect any modification in the graphitic layers. Basically, it would appear 2 peak profiles in 2D region in 2500 cm^{-1} to 3000 cm^{-1} range if it's a multilayer formation and only one peak profile very close to 2500 cm-1 if it's monolayer stacking [43]. In the Raman Spectra of GO, intense bands of D and G (I(D)/I(G) = 0.90) are observed with mostly flat part in 2D region. This suggests that during the oxidation of graphite, a higher number of functional groups have attached the graphene layers making the graphitic structures disturbed highly. This can be further convinced through comparing the 2D band region of graphite and GO. Relative intensity of the 2D region has considerably reduced in GO, which is highly sensitive to the number of layers available. As a matter of fact, it is possible to conclude that oxygen containing functional groups prevents stacking graphene layers in GO. In contrast, GrO shows further increase in the relative intensities of D and G bands (I(D)/I(G) = 0.88) while G band has slightly increased than D band than GO. Moreover, an identical 2 peak profile can also be seen in the GrO Raman Spectra in 2648 cm^{-1} and 2912 cm^{-1}. These details provide the information that exfoliation of GO causes partial healing of graphite basal plains by removing some of its functional groups attached previously. Broader D and G peaks of both GO and GrO are due to the availability of D'-bands as the graphitic structure is heavily disturbed. However, through the intensity enhancement of D and G bands of GrO, than the GO confirms that the exfoliation has occurred successfully. Similar results for Raman spectra of GO and GrO have been reported by [43], [44].

The effect of the recovery method used on the graphite was also examined by SEM-EDS presented in Figure 5.1-c some agglomerations and impurities can be seen on the surface of the graphite recovered. As suggested by EDS results, the agglomerations on the graphite surface are Al_2O_3 and small fraction of Cl. However, the morphology of the graphite did not show damage, giving credit to the recovery method used. Moreover, the SEI layer was not detected, which suggests that the recycling route removed it from the surface of the graphite. In contrast, GO shows a higher degree of oxidation giving that atomic ratio between C:O is at 3:2 confirming the availability of a high

number of functional groups attached. The morphology of the GO showed wrinkled and layered flakes with a rough appearance. This confirms the full oxidation of graphite layers available in its structure. A similar SEM image for GO was reported by [45], [46]. As reported by Yan et al (2014), GrO should show exfoliations of stacked layers of GO under sonication. Accordingly, the SEM image of GrO shows a degree of exfoliation under the magnification examined. The morphology of GrO appears to be rougher than GO with much smaller fragments under the same magnification. This is due to the shear stresses applied by the sonication. Also, under the higher magnification it shows expansion of layers making empty spaces appear. This further confirms the production of GrO [47]. Also, it is vital to note that in GrO, C:O ratio is slightly affected by the sonication. Accordingly, C:O ratio has reduced to 7:3. This could be due to the intense localized forces created by sonication making the functional groups detached or degrade during the processing.

3.2 Dye adsorption studies

The conditions were set for the initial dye solution at ambient temperature (25 °C) with pH of 5.5 for batch adsorption experiments. To ensure proper mixing and homogeneous sample, magnetic stirrer was utilized with 300 rpm stirring. Initial concentration was set to 30 mg/L of each dye solution with 50 mL of volume and 10 mg of adsorption materials. Dye removal capacities by each adsorbent was studied in 2 minutes interval for a 10 minute period of time. Figure 5.2-a,b shows time dependent dye removal efficiency by GrO and GO.

According to Figure 5.2-a,b, GrO absorbed relatively higher amount (94% for MB and 91% for MG) of dye waste than GO (90% for MB and 87.5% for MG) within 10 minutes time. However, in adsorbing MB, GO has a faster adsorption rate than GrO at the beginning. A possible reason for this observation could be the large number of functional groups in GO structure than GrO. So, it is possible to adsorb many pollutants at the beginning. As the time passes the surface-active groups cover and hence declining of the speed. In the case of GrO, though it has a lower number of functional groups than GO, the number of accessible functional groups is larger than GO given its exfoliated nature [48]. Figure 5.2-c,d shows dye removal percentage by each of the adsorbents at different initial dye concentrations.

According to Figure 5.2-c,d it is visible that GrO has a quite higher adsorption capacity than GO at different dye concentrations. However, it can be noted that increase of initial dye concentration reduces the dye removal percentage in both GO and GrO. Nevertheless, in GO this reduction is

lower than GrO. This could be a result of having more surface-active sites in GO. Specifically, at high concentration of dye pollutant particles are pressurized to access more functional groups that are difficult to access at lower dye concentrations in GO. However, overall GrO shows the highest adsorption efficiency. This is because GrO has oxygen-containing functional groups that offer stability, antifouling, and hydrophilicity, which can interact with pollutants through hydrogen bonding, van der Waals forces, and π-π stacking interactions easily than GO [48]. The probability of participating in these bonding mechanisms increased in GrO due to its high surface area compared to GO.

As per Figure 5.2-e, f, it is evident that increasing adsorbent material dosage increases the dye removal percentage as more adsorbent material provides more functional groups and void spaces that dye pollutants can be trapped. However, 10 mg of adsorbent dosage seems to be a good compromise between the removal percentage and the adsorbent mass used. Further increase of adsorbent materials does not cause a significant increase of dye removal percentage. It suggests that though more functional groups and void spaces are provided for the adsorption, the pollutant concentration is too low to pressure themselves into the available sites. Nevertheless, GrO shows higher adsorption (~93%, ~90%) of dye pollutants (MB and MG) than GO (~92%, ~89%) at different dosages due to its increased surface area and wide accessibility of functional groups.

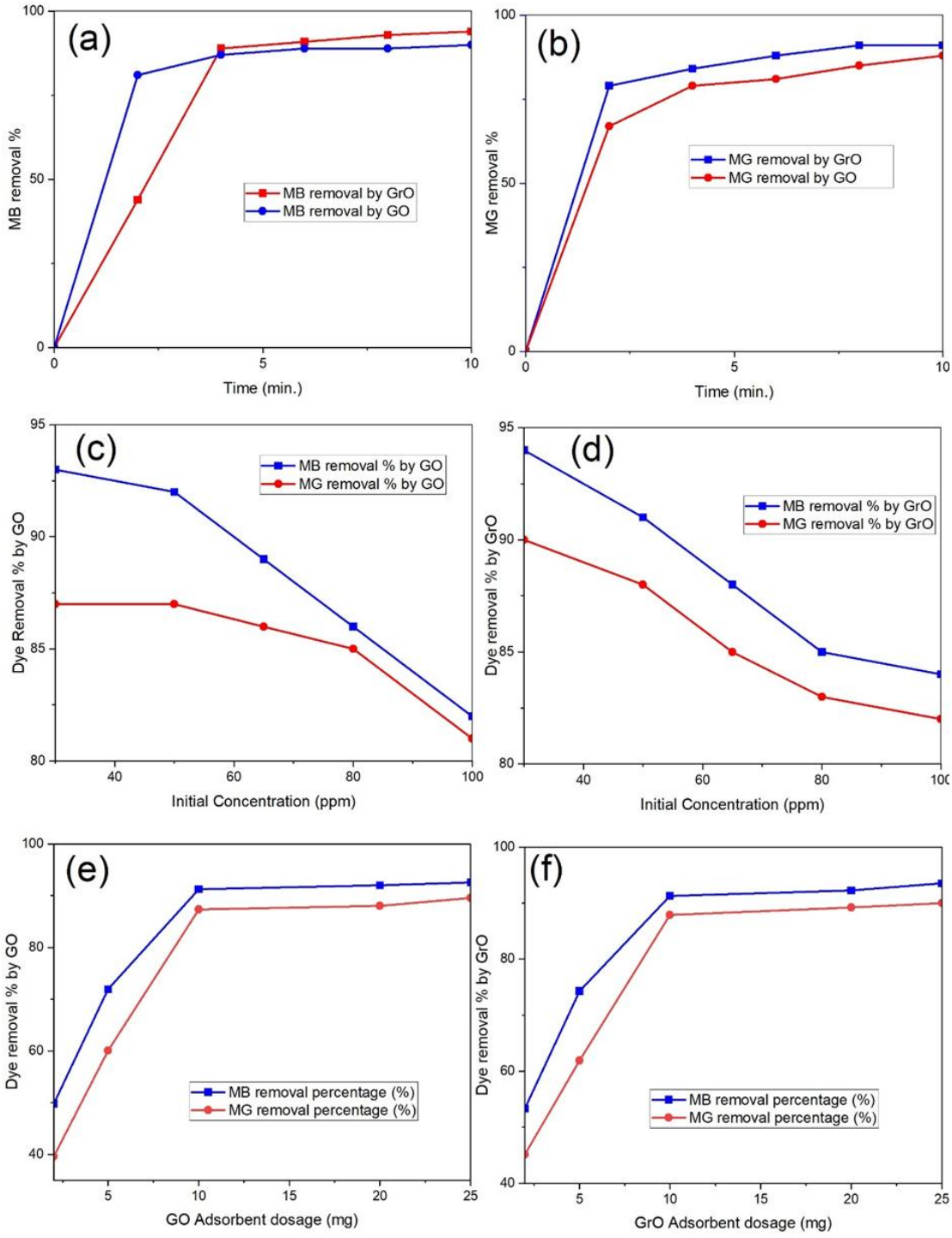

Figure 5.2 Dye adsorption experiment results a) Time dependent adsorption of MB dye to different adsorbents, b) Time dependent adsorption of MG dye to different adsorbents, c) Dye removal percentage by GO at different initial dye concentrations, d) Dye removal percentage by GrO at different initial dye

concentrations, e) Dye removal percentage at different dosages of GO and f) Dye removal percentage at different dosages of GrO.

Compared to literature values, these removal efficiencies are higher. For an instant, Liu et al. (2012) recorded <85% removal of MB under neutral pH levels using aqueous solution of graphene [49]. Also, around 85% removal efficiency of MB by graphene oxide/calcium alginate composites was reported by Li and others at neutral pH levels [50]. In the case of MG, 90% removal was reported by Sykam et al using exfoliated graphite [51]. Also, it is important to note that these materials are derived from virgin materials while materials produced in this study come from recovered graphite. In depth comparison of adsorption capacities is provided under adsorption capacity studies.

3.2.1 Dye adsorption kinetics

Time dependent adsorption of dye with different adsorbents was used to determine the adsorption kinetics. Liquid film diffusion (LFD), Elovich, Weber-Morris intra-particle diffusion (IPD) and frequently used Pseudo-first order (PFO) and second order (PSO) kinetic models were used to calculate the rate of the adsorption and adsorption mechanisms. The linear equations and parameter values obtained for each of the models studied were reported in Table 5.1 along with experimental conditions[1].

Table 5.1 Parameter values calculated for different adsorption kinetic models.

Model	Linear Function		Parameter (Units)	GrO+MB	GrO+MG	GO+MB	GO+MG
PFO	$\ln(q_e - q_t) = \ln q_{e,cal} - k_1 t$	(3)	$q_{e,cal}$ (mg/g)	147.70	143.91	70.34	88.99
			k_1 (g/mg.min)	0.62	0.73	0.59	0.39
			R^2	0.96	0.92	0.92	0.93
PSO	$\frac{t}{q_t} = \frac{1}{k_{obs} q_{e,cal}^2} + \frac{t}{q_{e,cal}}$	(4)	$q_{e,cal}$ (mg/g)	169.89	150.65	133.49	139.36
			k_2 (g/mg.min)	0.002	0.01	0.03	0.01
			R^2	0.94	1.00	1.00	1.00
Elovich	$q_t = \frac{1}{\beta}\ln(\alpha\beta) + \frac{1}{\beta}\ln t$	(5)	α (mg/g.min)	1.22×10^2	9.90×10^4	7.77×10^6	2.64×10^3
			β (g/mg)	0.024	0.078	0.123	0.056
			R^2	0.79	0.98	0.93	0.96
LFD	$\ln\left(1 - \frac{q_t}{q_e}\right) = -k_{fd} t$	(6)	k_{fd} (1/min)	0.62	0.73	0.59	0.39
			R^2	0.96	0.92	0.93	0.93
IPD	$q_t = k_{id} \times t^{0.5} + C$	(7)	K_{id} (mg/g.min$^{0.5}$)	44.32	44.36	39.87	40.25
			C (mg/g)	6.76	26.07	26.07	19.26
			R^2	0.91	0.82	0.79	0.87
			$q_{e,exp}$ (mg/g)	129.5	143.5	129.92	129.98

[1] Experimental condition: pH=5.5, Temperature= 25 °C, L/S = 5 L/g, Initial concentration of dye= 30 ppm

The PFO model (equation 3) developed based on the assumption that adsorption rate is proportional to the difference between initial and adsorbate surface concentration of the dye in an aqueous medium [52]. To evaluate the current study according to the PFO model, the linearized PFO model equation (3) was used.

The initial rate constant for adsorption, K_1, and the calculated equilibrium adsorption capacity, $q_{e,cal}$, were determined through the interception and slope of $\ln(q_e-q_t)$ vs. t graph. The plotted graphs were given in annexure 4. Figure S4.1-a while the parameter values were shown in Table 5.1. High R^2 values were obtained for all the adsorption processes ($R^2 > 0.92$), suggests that the processes could follow PFO model. Accordingly, K1 and qe,cal was calculated. Calculated q_e values for each adsorption is significantly different to the experimented qe values ($q_{e,exp}$ = 129.5 mg/g for MB with GrO, 143.5 mg/g for MG with GrO, 129.92 mg/g for MB with GO and 129.98 mg/g for MG with GO). Having inconsistencies with calculated and experimented q_e values limits the PFO model applicability to the current adsorption process.

The PSO model assumes that rate of the adsorption process depends on chemisorption [52]. To understand the applicability of the PSO model to the current study, equation 4 mentioned on the Table 5.1 under PSO model was used.

The second order rate constant for adsorption, K_{obs}, and the equilibrium adsorption capacity were obtained by analyzing the intercept and slope of the t/qt vs. t graph. The parameter values obtained were reported in Table 5.1 and the graphs were given in Figure S5.1-b. According to the higher coefficient of correlation obtained, it is safe to assume that the adsorption processes follow PSO model concluding that rate determining factor of the adsorption process is chemisorption of the heterogeneous mixture. Moreover, calculated $q_{e,cal}$ (169.89, 150.65, 133.49, 139.36 mg/g) are somewhat similar to the experimental $q_{e,exp}$ values (129.5, 143.5, 129.92 mg/g and 129.98 mg/g). However, slight discrepancy between the q_e values can be due to the other rate determining factors (such as decreasing dye concentration and decreasing number of unoccupied active sites) involved in the adsorption process.

Though Elovich model (equation 5) originally designed for the assessment of gas adsorption into solid adsorbents, it has been used frequently in assessing aqueous media adsorption mechanisms

[52]. The Elovich model also determines the second order kinetics based on the assumption that the surface of the adsorbent materials is heterogeneous and has non uniform adsorption energies. Moreover, it also provides information on the effect of pore sizes in the adsorption process. The equation 5 was adapted to evaluate the Elovich model for this study.

The preliminary adsorption rate; α and activation energy/ surface coverage coefficient; β were calculated using the interception and the slope of the graph between the qt vs. ln t. Figure S5.1-c shows the linear plot of the adsorption while Table 5.1 shows the important parameter data of the process. Higher correlation coefficients (above 0.9 except the case of GrO with MB) confirm that the adsorption processes may follow the Elovch model as well. Nevertheless, high values received for the adsorption rate constant (α) suggest that chemisorption occurred fast for MB adsorption to GO followed by MG into GrO. Also, the model suggests that there is a high surface coverage (β) by each adsorbate with higher adsorption rate (α). According to the model values, the slowest adsorption was shown by the MB with GrO. More importantly, considering the ending of the adsorption process, the process is much more likely to follow Elovich model with higher R2 values (0.95 for GrO+MB, 0.85 for GrO+MB. 0.98 for GO+MB and 1.00 for GO+MG). Further, this suggests that pore diffusion plays a significant role in the adsorption process [53].

LFD model (equation 6) uses the assumption that the adsorption rate depends on the rate that the adsorbate particles diffuse in the liquid film and the rate of the direct adsorption onto the adsorbent active sites [52]. Which means that the rate determining factor of the adsorption process is the spread of particles of the adsorbate within the liquid film surrounding the absorbent surface.

Liquid film diffusion rate factor K_{fd} was determined through the graph between $\ln\left(1-\frac{q_t}{q_t}\right)$ vs. t. The high R^2 value obtained suggests that the adsorption process can also follow the LFD model. However, as per Figure S5.1-d the graph does not go through the origin point of the graph (though it's very close to zero in most cases). This suggests that LFD model cannot describe the adsorption process alone and there is a contribution of other processes for the total rate of adsorption. This finding correlates with the suggestion received by Elovich and PSO models. Moreover, liquid film diffusion rate factor (K_{fd}) suggests that the highest diffusion rate received from MG adsorption to GrO (0.73 min^{-1}) followed by MB adsorption into GrO (0.62 min^{-1}). Adsorption of dye into GO is comparably slower as per the model diffusion rate values (0.59 min^{-1} for MB and 0.39 min^{-1} for MG).

Finally, IPD model (equation 7) assumes that the diffusion mechanism determines the total rate of the adsorption process [52]. To evaluate this hypothesis and the corresponding diffusion mechanism for the current study the linear equation of the model was used.

The k_{id}; the initial rate of intra-particle diffusion controlled adsorption was determined using the linear graph between q_t vs. $t^{0.5}$. The values obtained for k_{id} for each adsorption process are given in Table 5.1 and the corresponding figure is given in Figure S5.1-e. The relatively low coefficient of correlation values limits the use of IPD model to describe the adsorption process alone. However, intercept (C) values received for the IPD model provide information about the thickness of the boundary layer [53], [54]. As per the higher values received for C in IPD model suggests that effect of the boundary layer is higher in each adsorption process. Moreover, it can be concluded that the boundary layer in GrO is thinner than the GO as per the relatively lower C values received for the GrO systems. Which suggests that more mass transfer or more adsorptions can occur in GrO than GO.

From the evaluated kinetics models, to describe the rate determining factor of the adsorption process, PSO model matches perfectly well with significantly higher R^2 value. So, it is safe to say that chemisorption is the main rate determining factor of the adsorption process. However, in the order of highest coefficient of correlation except PSO, Elovich> LFD > PFO models also describe the adsorption mechanism with relatively higher R^2 values. Which can be interpreted as the rate of the adsorption mechanism also depends on the amount of adsorbate over time, variation of the maximum adsorption concentration of the adsorbents, and the rate of diffusion of adsorbate in the liquid film. However, the identification of Elovich model applicability with higher R^2 values for the ending part of the adsorption process suggests that the adsorption process turns to second order adsorption as the dye concentration in the aqueous solution reduces. In conclusion, the dye adsorption to the considered adsorbents initially controlled by multiple mechanisms such as the chemisorption, variation of dye concentrations in liquid phase and the adsorbent phase, and the diffusion of the adsorbate in the liquid film. Nevertheless, to the end, the adsorption process mainly controlled by chemisorption and liquid film diffusion rate (second order processes).

3.2.2 Dye adsorption isotherms

The Langmuir (LI), Freundlich (FI), Temkin (TI), Halsey (HI) and Harkins-Jura (HJI) isotherms were employed to investigate the interactions of the adsorbent particles on the adsorbent surface once the adsorption process reached equilibrium. Consequently, the adsorption experiments were carried out at pH of 5.5, with stirring speed of 300 rpm in the ambient temperature, using a liquid-to-solid ratio of 5. The initial concentrations of the dye waste were changed from 30 ppm to 100 ppm to attain the maximum adsorption capacity at each initial dye concentration. The linear equations and parameter values obtained for each of the models studied were reported in Table 5.2.

Table 5.2 Different isotherm models used for the evaluation along with main parameters, units and calculated values.

Model	Linear Function		Parameter (Units)	GrO+MB	GrO+MG	GO+MB	GO+MG
LI	$\frac{c_e}{q_e} = \frac{1}{K_L q_{max}} + \frac{c_e}{q_{max}}$	(8)	q_{max} (mg/g)	546.77	640.68	527.87	813.14
			K_L (L/mg)	0.17	0.09	0.19	0.06
			R^2	0.97	0.98	1.00	0.96
			R_L	0.16	0.27	0.15	0.37
FI	$\ln q_e = \ln K_F + \frac{1}{n} \ln C_e$	(10)	K_F (mg/L)	112.44	76.32	111.89	56.56
			1/n	0.47	0.58	0.47	0.70
			R^2	1.00	0.99	0.97	0.97
			q_{max} (mg/g)	557.59	554.50	558.49	616.99
TI	$q_e = B_T ln k_T + B_T ln C_e$	(11)	B_T (J/mol)	118.06	142.92	119.72	172.58
			K_T (L/mg)	1.78	0.85	1.71	0.57
			R^2	0.96	0.98	1.00	1.00
HI	$\ln q_e = \frac{1}{n_H} \ln k_H - \frac{1}{n_H} ln C_e$	(13)	n_H	-2.12	-1.72	-2.12	-1.42
			K_H	2.27×10^4	1.69×10^3	2.16×10^4	3.12×10^2
			R^2	1.00	0.99	0.97	0.97
HJI	$\frac{1}{q_e^2} = \frac{B_{HJ}}{A_{HJ}} - \left(\frac{1}{A_{HJ}}\right) \log C_e$	(14)	A_{HJ}	2.25×10^4	1.72×10^4	2.28×10^4	1.40×10^4
			B_{HJ}	1.22	1.26	1.23	1.23
			R^2	0.92	0.88	0.82	0.81
			$q_{e,exp}$ (mg/g)	421.50	410.55	410.15	406.10

[2] Experimental conditions: pH=5.5, Temperature= 25 °C, L/S = 5 L/g, Initial concentration of dye= 30-100 ppm

The Langmuir isotherm model (equation 8) was established assuming that binding sites are homogeneous, and the adsorption energies of the binding sites are identical. Furthermore, it assumes that there are no intermolecular interactions between adsorbents [52]. The linearized model of the Langmuir isotherm was used for the calculation of parameters and plotting of the graph.

Theoretical maximum adsorption capacity q_{max}, and Langmuir constant K_L determine the maximum adsorption capacity of the adsorbent and the affinity of the sites that bind respectively. These parameters were calculated through the graph C_e/q_e vs. C_e. Here, C_e; dye concentration in the solution at equilibrium, C_0; initial dye concentration in the solution, q_e; adsorption capacity at equilibrium. The values obtained were depicted in Table 5.2 and the corresponding graph can be found in Figure S5.2-a. Moreover, the unitless separation factor, R_L provides the validity of the Langmuir isotherm, which can be calculated through equation 9.

$$R_L = \frac{1}{1+K_L C_0} \quad \text{----------(9)}$$

When $R_L > 1$, the adsorption becomes adverse, if $R_L<1$, it shows a desirable adsorption. For $R_L=0$, it shows an irrevocable adsorption and for $R_L=1$, means a linear adsorption [52]. As per the results obtained, it can be deduced that both adsorbent materials interactions with two different dyes follow a linear pattern at different initial concentrations. This can be confirmed by the high R2 values obtained (0.96-1.00). Moreover, the q_{max} values obtained for GrO/MB, GrO/MG, GO/MB and GO/MG are 546.7, 640.68, 527.87, 813.14 mg/g respectively. These values obtained are somewhat like the evaluated experimented values except for the GO/MG adsorption (421.5, 410.55, 410.15, 406.2 mg/g). Nevertheless, the separation factor (R_L) values obtained also suggests a favorable adsorption, being all the values less than 1 (0.16, 0.27, 0.15, 0.37). Also, it is observed that, R_L value for the adsorption of MB is less than MG with both GO and GrO, indicating that, there is a higher inclination towards adsorbing MB dye by the adsorbent materials produced.

Freundlich model (equation 10) describes that energy distribution in surface sites are not uniform and hence, multilayer adsorption can be taken place [52]. To understand the applicability of multilayer adsorption, the linear form of Freundlich isotherm model was considered (equation 10).

The graph ln q_e vs. C_e was utilized to determine Freundlich rate constant, K_F and unit less heterogeneity factor ,1/n. Freundlich rate constant indicates the adsorbents maximum adsorption capacity and heterogeneity factor describes the desirability of the adsorption process. Also, heterogeneity factor can predict the heterogeneity of the surface of the adsorbent materials. For an instant, if the value of 1/n becomes zero or very close to zero, it indicates that the adsorption is much desirable [52]. On the other hand, “n” closer to 1 shows a more homogeneous structure and deviations to the higher than 1 indicates more heterogeneous structure [55]. Hence, the logarithmic

graph of q_e vs. C_e was used to determine K_F and 1/n parameters. The important parameters of the adsorption indicated in Table 5.2, and the graphs can be found in Figure S5.2-b. Higher correlation coefficients (R^2 = 0.97 to 1.00) suggest that adsorption processes adhered to Freundlich isotherm as well. Moreover, heterogeneity factors (1/n) for each adsorption, are closer to zero (varies 0.4 to 0.7) indicating that a better adsorption and heterogeneous structure of the GO and GrO surfaces. The highest Freundlich rate constants were shown by GrO with MB (112.44 mg/L) followed by GO with MB (111.90 mg/L). Rate constant for the adsorption of MG by each adsorbent material is lower than MB (GrO showed 76.33 mg/L, GO showed 56.56 mg/L with MG). Accordingly, it is possible to understand that MB has a higher inclination for the adsorption process than MG. Focusing on the R^2 at higher concentrations (mostly ≈1.00) (depicted on the graph) illustrates that 2nd order isotherms are much adhered to the adsorption process at higher concentrations better than considering the whole range of concentrations.

The Temkin isotherm model (equation 11) is developed taking "heat of adsorption produced by the indirect interaction between absorbent and adsorbate" into consideration. It is assumed that the heat of adsorption of the adsorption sites declines linearly as the coverage increases. The linear model of Temkin isotherm (equation 11) was used to determine the applicability of the model.

A graph was plotted between q_e and ln C_e to determine the important parameters of the model. Accordingly, the graph can be seen in Figure S5.2-c and the parameters calculated are shown in Table 5.2. B_T in the model is the Temkin constant and it provides information about the heat of adsorption. K_T is the equilibrium binding constant [52]. Further, B_T is related to b_T, Temkin isotherm exponent through.

$$B_T = \frac{RT}{b_T} \text{----------(12)}$$

Here, R stands for the universal gas constant (8.314 J/K.mol), and T the temperature in Kelvin (298 K). b_T, the Temkin isotherm exponent provides details about the favorability of the adsorption being close to 1. Significant lower values of b_T, indicates negative cooperativity in binding [56]. As for the high coefficient of correlation, it is possible to consider that the adsorption follows the Temkin model as well. However, values obtained for b_T exceed 1 in all cases. Higher values of b_T imply that the rate of linear reduction of the heat of adsorption is much lower than the standard Temkin model rate, limiting the applicability of the model to the adsorption system. However, this

suggests the surface of the adsorbates are more heterogeneous as higher b_T can reduce the B_T (heat of adsorption) significantly [53], [57]. Nevertheless, comparably lower values of BT for MB adsorption (118.06 and 119.72 J/mol) suggest that adsorption requires lower energy, hence favorable adsorption than MG into the adsorbent materials [56].

The Halsey isotherm model (Equation 13) assumes a multilayer adsorption with heterogeneous sites available in the adsorbent which is like the assumptions made in Freundlich model. However, there are distinguishable differences between the two empirical models. Moreover, Halsey focuses specifically on the heterogeneity of the adsorbent surface while the Freundlich considers heterogeneous adsorption energy distribution on the surface and affinities.

Parameters such as k_H, and n_H; were obtained through the graph between ln q_e vs. ln C_e. Parameter values obtained were shown in Table 5.2 and the plotted graphs are shown in Figure S5.2-d. Halsey isotherm constant (k_H) provides information about the adsorption capacity and Halsey equilibrium exponent (n_H) provides an insight of the heterogeneity of the surface and related to the energy distribution of the adsorption sites available. Higher values of n_H indicate a greater heterogeneity [56]. R^2 values obtained for each of the adsorption mechanisms suggest that the adsorption process follows the Halsey model as well. Accordingly, very high adsorption capacities can be identified for GrO with MB (2.24×10^4) and GO with MB (2.16×10^4). For GrO with MG and GO with MG, the adsorption values are still high (1.69×10^3 and 3.12×10^2 respectively) but lower than that of MB. In contrast, n_H values obtained for each adsorption are negative, which indicates that the model does not correctly explain the adsorption reaction alone [56], [58].

Harkins-Jura isotherm model (Equation 14) can predict both monolayer and multilayer adsorption between the adsorbent and the adsorbate. It was built on the assumption of availability of varied pore sizes in the adsorbent materials which implies the heterogeneity of the surface [52], [56]. The linear equation of the model was used to evaluate the model applicability.

A linear graph was plotted between $\frac{1}{q_e^2}$ vs. log C_e to obtain the parameter values for B_{HJ} and A_{HJ}, Harkins-Jura isotherm parameter and constant respectively. Table 5.2 denotes the values calculated for the model parameters whereas the graph can be found in Figure S5.2-e. Goodness of fit of the obtain values to the model shows a strong negative relationship which suggests that the adsorption processes follow the Harkins-Jura's model. Higher Harkins-Jura heterogeneity constant (A_{HJ})

received for adsorbents with MB (2.25×10^4, 2.28×10^4) shows higher surface area and heterogeneity than with MG (1.72×10^4, 1.40×10^4). This further confirms the high affinity of MB dye to the adsorption materials studied. Further, monolayer heat of adsorption constants (1.22, 1.26, 1.23 and 1.23 for MB and MG with GrO and MB, MG with GO respectively) values are slightly higher in GrO than GO in average. This indicates that physisorption can be involved in the adsorption process of GrO more than GO. The reason for this could be the availability of pore spaces in GrO than GO.

The coefficient of correlation (R^2) values for each isotherm models can be listed as follows from the highest to lowest, Freundlich>Halsey>Temkin>Langmuir>Harkins-Jura. Taking this order and the analysis done above into consideration we can conclude that the adsorbent materials follow Freundlich Isotherm (2nd order isotherm) with cationic dyes studied at higher concentrations with acceptable parameter values. Also, it's possible to deduce that adsorption can follow 1st order adsorptions at lower concentrations. It is reasonable to think that at higher concentrations, interactions between pores, functional groups and adsorbates are much more complex and hence can be fit into different isotherms as studied. Though Halsey and Temkin also have very high coefficient of correlation, it is not ideal to use these isotherms due to unacceptable parameter values obtained as discussed above. Hence, maximum adsorption capacities (q_{max}) of GrO and GO for corresponding dye waste were calculated according to the Freundlich isotherm parameters using equation 15 for the comparison with recent studies [59].

$$q_{max} = K_F C_0^{1/n} \text{----------(15)}$$

Where K_F represents the Freundlich constant and C_0 is the initial concentration of adsorbate used. Calculated q_{max} values are present in Table 5.2 and a comparison of q_{max} with recent study values was listed in Table S5.1 in the annexure 4. Accordingly, high maximum adsorption capacities can be observed for the material synthesized in this study (GO = 558.49 mg/g with MB, 616.99 mg/g with MG and GrO = 557.59 mg/g with MB & 554.5 mg/g with MG for a dose of 0.2 g/L). It is proven that the adsorption capacity is influenced by various factors such as available functional groups, pore space structure and surface area. These factors are mainly governed by the material modification method and the degree of oxidization of the graphite material [60]. Hence, we can deduce that extracted graphite from LIBs can be easily oxidized to a higher degree with mild oxidization like Hummer's method. The reason behind this easy oxidization can be the slightly

enhanced interlayer spacings of the spent graphite occurred due to repetitive charging and discharging cycles of the LIBs as discussed in section 3.1. This can be further justified by the higher maximum adsorption capacity obtained by Nataraja et al (2016) (to be around 1000 mg/g with 5 g/L dosage). Nataraja and the collaborators also utilized graphite derived from spent LIBs for their study [36]. However, different modification and recovery methods resulted in a higher maximum adsorption capacity for the current study compared to the used adsorbent dosage.

3.3 Metallic ions adsorption experiments

Adsorption experiments of metallic ions were carried separately for each metal ion type at room temperature (25 °C) with the pH of 5.5. 30 mg/L Initial metal ion concentration was used for each stock solution with 20 mL of volume. After 20 mg of adsorption materials were added into each solution. Metallic ions removal capacities by each adsorbent were studied in 4 hours intervals for 24 hours. Figure 5.3-a,b shows the time dependent metallic ion removal efficiency by GO and GrO for each ion studied respectively. GrO has the highest removal efficiency compared to GO. This is mainly due to the availability of more accessible sites in GrO. GO, on the other hand, has more surface sites, but accessbility is limited due to the compacted nature. Further, it can be identified that, Ni^{2+} has the highest kinetics in adsorbing into each adsorbent material studied. Zn^{2+} showed the slowest kinetics among all the metal ions studied.

Figure 5.3-b and 3-c presents the removal efficiency of considered adsorbates at different initial concentrations using the two adsorbent materials. The observation received for the final concentrations were non-monotonic, hence the mean value used to calculate the percentage removal also shows a fluctuating nature. Hence, trending line of the observations were considered to make the comparison between the adsorbent materials. Generally, all metal adsorption capacities decrease along with the increasing of initial metal concentrations in the aqueous media. Moreover, It is clear that GrO performance is better at different metallic ion concentrations for Cd^{2+}, Ni^{2+} and Zn^{2+}. Moreover, Ni^{2+} has the highest removal efficiency (95% with GrO, 92% with GO with 30 ppm initial concentration) with both the adsorbents and Zn^{2+} is the least adsorbed metal ion (86% removal with GrO and 80% removal with GO). Cd^{2+} adsorption was at 90% with GO at 30 ppm of initial Cd^{2+} concentration and GrO showed 94% adsorption at the same initial metal concentration.

Metal ion removal percentages were studied with varying adsorbent dosages (2-25 mg) at 50 ppm initial metal ion concentrations. Figure 5.3-e,f shows the results obtained through experimental studies. Accordingly, increase of adsorbent material dosage of both GO and GrO increase the metal ion removal percentage. As explained before, this is mainly due to the availability of more functional groups and void spaces. Nevertheless, adsorption of metal ions is higher in GrO at different dosages than GO. This can be explained by the availability of more accessible sites in GrO than GO as per the exfoliated nature of GrO. Moreover, it can be predicted that metal ion may be trapped in between the layers of GrO enhancing its total adsorption capacity. In addition, the affinity of Ni^{2+} seems to be higher towards both of the adsorbent materials than Cd^{2+} and Zn^{2+}. Zn^{2+} reported the lowest adsorption efficiency compared to the rest.

Guo et al in 2018 reported similar results for the dye removal efficiency using carbon-based adsorption materials. According to the study, adsorption material longan hull, could remove 92% of Ni^{2+} and 87% of Cd^{2+} available in the wastewater with an absorbent dosage of 1.2 g and 1.5 g respectively [64]. In another recent study done by, Dhaouadi et al (2021), it also reported that among the metal ion studied, Ni^{2+} has the highest adsorption followed by Cd^{2+} and Zn^{2+}. Authors used pyrolyzed carbon-based materials for the adsorption of these metals at 30°C and pH of 5 [65]. A detailed comparison of adsorption capacities is provided under adsorption capacity studies.

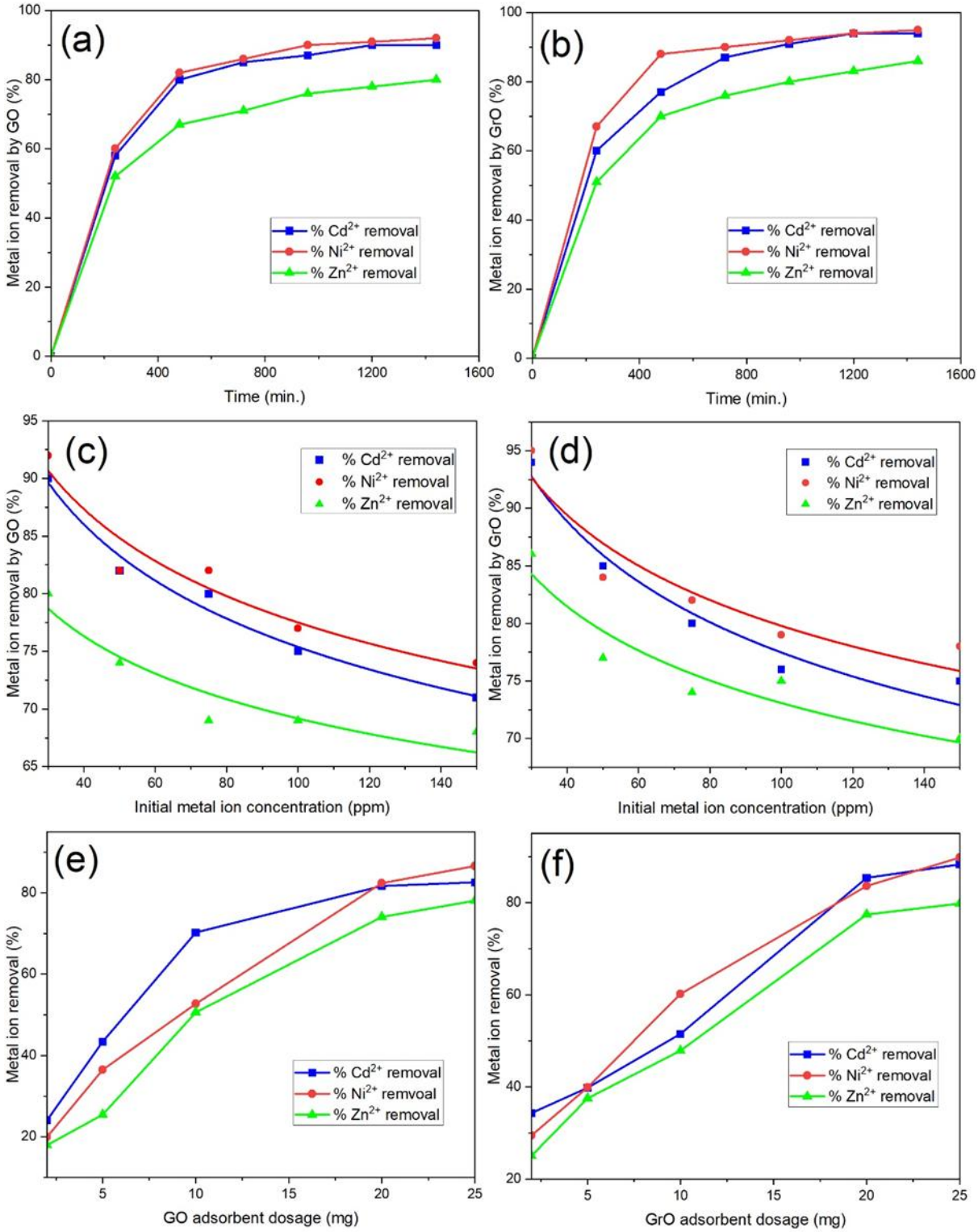

Figure 5.3 Metal ion adsorption experiment results a) Time dependent adsorption of metal ions to GO, b) Time dependent adsorption of metal ions to GrO, c) Metal ion removal percentage by GO at different initial dye concentrations, d) Metal ion removal percentage by GrO at different initial

dye concentrations, e) Metal ion removal percentage by GO at different dosages, f) Metal ion removal percentages by GrO at different dosages.

3.3.1 Metal ion adsorption kinetics

To analyze the adsorption kinetics and mechanisms, PFO, PSO, Elovich, LFD, and IPD kinetic models were employed. The linear equations and parameter values obtained for each of the models studied were reported in Table 5.3 along with the experimental conditions2.

Table 5.3 Linearized kinetic models, parameter values and units calculated for different adsorption kinetic models.

Model	Linear Function	Parameter (Units)	GO			GrO		
			Cd^{2+}	Ni^{2+}	Zn^{2+}	Cd^{2+}	Ni^{2+}	Zn^{2+}
PFO	$\ln(q_e - q_t) = \ln q_{e,cal} - k_1 t$	$q_{e,cal}$ (mg/g)	27.56	23.18	19.47	31.84	18.72	21.68
		k_1 (g/mg.min)	4.20×10^{-3}	3.71×10^{-3}	2.94×10^{-3}	4.13×10^{-3}	3.34×10^{-3}	2.66×10^{-3}
		R^2	0.98	0.99	0.99	0.98	0.94	0.99
PSO	$\frac{t}{q_t} = \frac{1}{k_{obs} q_{e,cal}^2} + \frac{t}{q_{e,cal}}$	$q_{e,cal}$ (mg/g)	30.08	30.32	26.72	32.03	30.56	29.68
		k_2 (g/mg.min)	2.27×10^{-4}	2.44×10^{-4}	2.23×10^{-4}	1.76×10^{-4}	3.24×10^{-4}	1.55×10^{-4}
		R^2	1.00	1.00	1.00	1.00	1.00	1.00
Elovich	$q_t = \frac{1}{\beta}\ln(\alpha\beta) + \frac{1}{\beta}\ln t$	α (mg/g.min)	0.75	0.97	0.65	0.59	2.48	0.38
		β (g/mg)	0.19	0.20	0.22	0.17	0.23	0.17
		R^2	0.90	0.90	0.98	0.96	0.85	0.97
LFD	$\ln\left(1 - \frac{q_t}{q_e}\right) = -k_{fd} t$	k_{fd} (1/min)	4.23×10^{-3}	3.50×10^{-3}	2.68×10^{-3}	4.28×10^{-3}	2.81×10^{-3}	2.44×10^{-3}
		R^2	0.96	0.99	0.99	0.97	0.93	0.99
IPD	$q_t = k_{id} \times t^{0.5} + C$	K_{id} (mg/g.$min^{0.5}$)	0.40	0.38	0.35	0.45	0.33	0.45
		C (mg/g)	13.29	14.27	11.29	12.49	17.13	9.82
		R^2	0.81	0.81	0.93	0.90	0.75	0.92
		$Q_{e,exp}$ (mg/g)	27.00	27.50	23.97	28.20	28.50	25.90

[3] Experimental conditions: pH=5.5, Temperature= 25 °C, L/S = 1 L/g, Initial concentration of metal ions= 30 ppm

As shown under section 3.2.1, equation 3 explains the PFO model's linear equation along with the assumptions used in the model and the important parameters. Accordingly, a graph was plotted between $\ln(q_e\text{-}q_t)$ vs. t to understand the applicability of the corresponding model to the adsorption process experimented with metal ions. The graph received is shown under Figure S5.3-a and the corresponding parameter values have been demonstrated in Table 5.3. Coefficient of correlation for each adsorption process are very high ranging from 0.94 to 0.99 suggesting that, adsorption rate may be proportional to the variation of the dye concentration in the solution. Moreover, adsorption capacity at equilibrium (q_e) calculated using the PFO model (27.56, 19.47, 31.84 mg/g) close to the experimented values in the case of GO with Cd^{2+}, Zn^{2+}, and GrO with Cd^{2+}(27.00, 23.97, 28.20 mg/g) respectively. However, the rest of the values are not consistent with experimented q_e values. This inconsistency reduces the applicability of PFO model to the adsorption process entirely. In addition, it is worth noting that, coefficient of correlation is much

higher (>0.99) for the PFO model during the initial part of the adsorption process suggesting that the initial rate determining factor could be the concentration variation of the metal ions in the liquid and the adsorbent phase (physisorption).

The PSO model assumes that adsorbent consist of heterogeneous functional groups is responsible for the adsorption while chemisorption being the rate determining factor. This was previously explained under equation 3. To understand the applicability of the model to the current study of metal ion adsorption, a graph was plotted between t/q_t and t. The parameter values calculated are shown in Table 5.3 and the graphs are in Figure S5.3-b. Coefficient of correlation received the highest value of 1.00 to the nearest two decimal places suggesting that chemisorption is the rate determining factor. Moreover, calculated q_e values using the model (30.08, 30.32, 26.72, 32.03, 30.56, 29.68 mg/g) have much consistency with the experimented values (27, 27.5, 23.97, 28.2, 28.5, 25.9 mg/g) for each adsorption process. Having higher consistency with experimented and calculated q_e values in PSO model, supports the idea that the PSO model can explain the rate determining step better than PFO model. However, the discrepancy between the values could be due to the other rate determining factors such as variation of dye concentration and unoccupied active site availability that involved with the process as suggested by Mosaffa and collaborators [52].

The Elovich model developed assuming that functional groups in the adsorbent surface are heterogeneous and contain different adsorption energies. Moreover, diffusion of pore spaces and their effect on the adsorption can be understood using the Elovich model. The model explained above under equation 5, and it determines the second order kinetics. As per the results obtained through the graph qt vs. ln t (given in Fig. S3-c), Elovich model also suggests that the adsorptions follow second order kinetics with higher R^2 values (above 0.9 except GrO adsorption with Ni^{2+}). On the other hand, adsorption rate constant (α) determined through the Elovich model explains the rate of the adsorption process (parameters given in Table 5.3). It is possible to observe that Ni^{2+} adsorption into GrO is quite faster (2.48 mg/g.min. while the rest is < 1.00 mg/g.min.) than the rest of the adsorption. This fast adsorption could be a reason for the less coefficient of correlation received for the adsorption process with Elovich model. However, considering the ending part of the adsorption process, the coefficient of the correlation is above 0.93 in all the cases (even reached 1.00 in the case of GrO with Ni^{2+} and Zn^{2+}). This suggests that the rate can be due to the second

order adsorption during the later part of the adsorption process. This suggests that physisorption may start the adsorption process due to the pore spaces at the starting and later, when adsorbates attract to active sites turns the process into the second order adsorption (chemisorption).

Equation 6 in section 3.2.1 explains the LFD model. As per the model, it is assumed that the rate of the adsorption determined by both by the speed of liquid film diffusion around the solid adsorbent and the adsorption of the adsorbates onto the active groups of the adsorptive material. To understand the applicability of the model, the graph was drawn between $\ln\left(1-\frac{q_t}{q_e}\right)$vs. t. Table 5.3 contains the parameter values received for the model while the Fig. S3-d shows the graph plotted. High R^2 values (>0.93) received for the model suggest that the interaction between the liquid film and the adsorbent can also determine the rate of the adsorption. Moreover, Liquid diffusion rate for Cd^{2+} is higher with both GO and GrO (4.23×10^{-3} min^{-1} and 4.28×10^{-3} min^{-1} respectively) suggesting that higher adsorption rate of Cd2+ into the adsorbents. The second highest diffusion rate reported by Ni^{2+} and the Zn^{2+} (3.50×10^{-3} min^{-1}, 2.68×10^{-3} min^{-1} respectively with GO and 2.81×10^{-3} min^{-1} and 2.44×10^{-3} min^{-1} respectively with GrO). This suggests that Cd^{2+} has a higher affinity towards the adsorbents studied followed by Ni^{2+} and Zn^{2+}.

Finally, equation 7 explained above deals with IPD model, which suggests the diffusion mechanism can determine the rate limiting factor. A linear graph was drawn (q_t vs. $t^{0.5}$) to determine the compatibility of the process with the IPD model. Table 5.3 consists with the important parameters worked out for the model while the graph is given in Figure S5.3-e. The low R^2 values received for the graphs compared to the initially studied models suggest that the incompatibility of the IPD model to the adsorption process studied. Nevertheless, close monitoring of the last part of the adsorption process suggest that the R^2 value enhanced. This suggests that intra particle diffusion can be a part of the rate determination of the process at the ending part of the adsorption mechanism. Moreover, higher intercept values received for the model values suggests that comparably lower thickness of the layers in GrO increasing the mass transfer of the same than the GO [54].

Referring to the graph demonstrated in Figure S5.3, it is possible to see that initially adsorption processes are much more likely to follow the PFO model and later it's much adhered to second order graphs like PSO and Elovich models. This suggests that the rate of the adsorption process initially controlled by saturation of dye particles in the liquid and the adsorbate. However, when

the time passes the rate will be controlled by several other factors like chemisorption and liquid film diffusion rather than the concentration of the metal ions. In physical meaning, initially, as the concentration of the metal ion particles are higher and there is more availability of unoccupied active sites, the concentration variation can undertake a fast adsorption which adhered with the first order adsorption. Nevertheless, as the unoccupied sites and concentration of metal ions are diminishing over time, adsorption rate will be determined by the diffusion of the adsorbate in the liquid film surrounded the functional groups and bonds that involve interactions between molecules [53], [54]. This explains the findings of the adsorption kinetic evaluation.

3.3.2 Metal ion adsorption isotherms

Five different isotherms; Langmuir (LI), Freundlich (FI), Temkin (TI), Halsey (HI) and Harkins-Jura (HJI) were employed to investigate the interface correlation between the metal ions; Cd^{2+}, Ni^{2+} and Zn^{2+} with the two adsorbents (GO and GrO) under equilibrium conditions. Consequently, experimental conditions were set to pH of 5.5, liquid-to-solid ratio of 1 (L/g), stirring speed of 300 rpm at ambient temperature of 25 °C. Initial metal ion concentrations were changed from 30 -150 ppm to evaluate the highest adsorption capacities as a function of changing initial concentrations. Table 5.4 reports the linear equations and parameter values obtained for each of the models studied along with the experimental conditions used [4].

Table 5.4 Different isotherm models used to evaluate along with main parameters, units and calculated parameter values of metal ion adsorption.

Model	Linear Function	Parameter (Units)	GO			GrO		
			Cd^{2+}	Ni^{2+}	Zn^{2+}	Cd^{2+}	Ni^{2+}	Zn^{2+}
LI	$\frac{c_e}{q_e} = \frac{1}{K_L q_{max}} + \frac{c_e}{q_{max}}$	q_{max} (mg/g)	146.41	154.54	204.80	138.54	152.32	171.86
		K_L (L/mg)	0.05	0.05	0.02	0.07	0.06	0.03
		R^2	0.91	0.87	0.77	0.83	0.77	0.84
		R_L	0.40	0.39	0.65	0.32	0.34	0.52
FI	$\ln q_e = \ln K_F + \frac{1}{n} \ln C_e$	K_F (mg/L)	14.48	15.85	6.60	19.90	21.07	10.34
		1/n	0.52	0.51	0.69	0.44	0.44	0.60
		R^2	0.98	0.97	0.99	0.95	0.91	0.97
		q_{max} (mg/g)	83.99	89.85	68.30	88.03	93.19	78.29
TI	$q_e = B_T ln k_T + B_T ln C_e$	B_T (J/mol)	28.92	29.17	35.51	25.03	25.42	32.33
		K_T (L/mg)	0.63	0.72	0.26	1.14	1.28	0.40
		R^2	0.91	0.88	0.89	0.82	0.78	0.89
HI	$\ln q_e = \frac{1}{n_H} \ln k_H - \frac{1}{n_H} ln C_e$	n_H	-1.93	-1.96	-1.46	-2.29	-2.29	-1.68
		K_H	175.96	225.19	15.59	934.94	1068.08	50.61
		R^2	0.98	0.97	0.99	0.95	0.91	0.97
HJI	$\frac{1}{q_e^2} = \frac{B_{HJ}}{A_{HJ}} - \left(\frac{1}{A_{HJ}}\right) \log C_e$	A_{HJ}	883.78	924.62	547.03	1097.85	1114.35	711.98
		B_{HJ}	1.57	1.54	1.63	1.56	1.52	1.59
		R^2	0.92	0.94	0.92	0.97	0.98	0.94
		$q_{e,max}$ (mg/g)	106.77	111.02	101.91	113.15	116.63	104.66

[4] Experimental conditions: pH=5.5, Temperature= 25 °C, L/S = 1 L/g, Initial concentration of metal ions= 30-150 ppm

The Langmuir isotherm was built based on monolayer adsorption with sites that have uniform adsorption energies as explained under equation 8. Moreover, it rejects the idea of having intermolecular interactions. To evaluate the applicability of the model to the current metal ion adsorption process, equation 8 was utilized. Accordingly, a graph was drawn using the ratio between equilibrium concentration and adsorption capacity vs. equilibrium concentration. The obtained graph was reported in Figure S5.4-a and the parameter values obtained were reported in Table 5.4. The R^2 values recorded for the adsorption processes are comparably lower for most of the processes. The maximum coefficient of correlation was given by GO with Cd^{2+} (0.91) and the minimum coefficient of correlation was reported by GO with Zn^{2+} and GrO with Ni^{2+} (0.77). However, it is worth understanding that, at lower metal ion concentrations, the adsorption follows the Langmuir model better with higher coefficient of correlation (>0.90 in all cases). For instance, GO with Zn^{2+}, the R^2 was 0.98, and GrO with Cd^{2+} the coefficient of correlation was 0.97. Hence, it is possible to assume that the adsorption processes follow the Langmuir model at lower concentrations. Moreover, Considering the separation factor R_L, it is possible deduce that, the adsorption is much favorable for Cd^{2+} and Ni^{2+} with both the adsorbents ($R_L \approx 0.39$ with GO and o.33 with GrO). However, Zn^{2+} adsorption R_L is much closer to 1 (0.65 with GO and 0.52 with GrO) showing less favorability than the other two metal ions considered. Nevertheless, Zn^{2+} adsorption is more favorable with GrO than GO given the slightly less R_L value received. Maximum adsorption capacities (146.41, 154.54, 204.80, 138.54, 152.32, and 171.86 mg/g) modeled by the Langmuir isotherm is not similar to the experimented adsorption capacities (106.77, 111.02, 101.91, 113.15, 116.63, and 104.66 mg/g), limiting the further application of the model fully to the current metal ion adsorption process. Though Langmuir model assumes monolayer adsorption with uniform adsorption energies, real application could be much more complex than that. Specifically, heterogeneity of the adsorbent sites, variations in the adsorption energies, interactions between adsorbates can influence the experimental maximum adsorption capacities to deviate from the model values. Moreover, ideal conditions assumed by the model do not exist in real life applications influencing experimental values to deviate from the expected model values. Further, this suggests that other adsorption mechanisms can be incorporated into the studied sorption process.

Freundlich Isotherm on the other hand hypothesis multilayer adsorption with non-uniform adsorption sites as described under equation 10. The applicability of Freundlich model was also

tested with the current adsorption using the graph depicted in Figure S5.4-b. The graph resulting from ln q_e vs. ln C_e was used to work out the important parameters that are given under Table 5.4. Freundlich isotherm model fitted well with the processes with higher R^2 values. For an instant, R^2 values are 0.98, 0.97, 0.99, 0.95, 0.91, and 0.97 for Cd^{2+}, Ni^{2+}, Zn^{2+} with GO and Cd^{2+}, Ni^{2+}, Zn^{2+} respectively. Moreover, it is possible to observe that the R^2 is much higher if only higher concentrations were considered (0.98, 0.99, 1.00, 0.98, 0.98, and 0.96). This suggests that multilayer adsorption is much preferable for medium to higher concentrations mostly. Heterogeneity factor 1/n, shows that, the adsorption is favorable for all the metal ions considered given the value of 1/n less than 1. Moreover, it is possible to assume that the affinity decreases in the order of Ni^{2+}>Cd^{2+}>Zn^{2+} (1/n = 0.52, 0.51, and 0.69 with GO and 0.44, 0.44, and 0.60 with GrO respectively). Also, the affinity of metal ions towards the GrO is higher than GO as the 1/n values received are comparably lower for GrO with metal ions. This further confirms by the Freundlich rate constant received for each metal ion adsorption with the adsorbents. Further, analysis of the value of "n" can provide information about the heterogeneity of the surface [55]. The higher values (n>1) received for the heterogeneity factor "n" suggests that the functional groups available in the adsorbent surfaces are heterogeneous and contains different adsorption energies.

Temkin's model is described under equation 11, section 3.2.2. According to Temkin's model, indirect coordination of the adsorbate and the adsorbent produce the heat of adsorption which linearly decreases as the coverage of the adsorption sites increases. Figure S5.4-c was developed based on the linear equation of the Temkin's model taking q_e on the y-axis and ln C_e on the x-axis. The parameters calculated for Temkin's model were depicted under Table 5.4. Though R^2 values received for the model (varies from 0.78 to 0.91) are not very high like Freundlich model, it is possible to observe that for higher concentrations the R^2 value is comparably higher (varies from 0.94 to 0.99). This suggests that there is a possibility of linear decline of heat of energy of the adsorption process at higher concentrations, elevating the adsorption. Moreover, Lower values received for the B_T (heat of adsorption) suggest that the adsorption process is favorable. In fact, the favorability of the adsorption decreases in the order of, Cd^{2+}>Ni^{2+}>Zn^{2+} in both the cases of GO and GrO. Moreover, the favorability of metal adsorption towards the GrO is higher than that of GO according to the B_T values received. Though the model provides useful information about the adsorption process under many aspects, the values received for the b_T (Temkin isotherm

exponent) according to the equation 12 are higher than 1 in all cases. This limits the applicability of the model to the current metal ion adsorption.

The Halsey isotherm model, which is built upon the base of heterogeneous functional groups availability in the adsorbents as explained under section 3.2.2, equation 13 was also employed to assess the adsorption process in question. It further assumes that heterogeneity of functional groups supports multilayer adsorption of adsorbates on to the adsorbent surface. The graph ln q_e vs. ln C_e was used to determine the Halsey isotherm constant (k_H) and Halsey equilibrium exponent (n_H) as per Figure S5.4-d. Table 5.4 shows the parameters calculated for the model. High coefficient of correlations (>0.91 in all cases) received for each of the graphs confirms the applicability of the Halsey model to the metal adsorption mechanism confirming greater heterogeneity of adsorption sites. The Halsey Isotherm constant values received confirms that the affinity of Ni^{2+} is significantly higher towards GrO (k_H=1068.08) than the other metals. Zn^{2+} affinity to GO (k_H=15.59) is the lowest among. Comparing the two adsorbents, GrO (k_HCd=934.94, k_HNi=1068.96, k_HZn=50.61) seems to be more efficient in adsorbing metal ions than GO (k_HCd=175.96, k_HNi=225.19, k_HZn=15.59) with significantly high k_H values received. However, values calculated for n_H become negative as the slope of the graph shows a positive relationship which limits the applicability of the model to adsorption mechanism.

The application of Harkins-Jura's Isotherm model was also examined using the graph between $\frac{1}{q_e^2}$ and log C_e according to the equation 14. The model assumes a heterogeneous adsorption with different affinities towards multi sized pore spaces. Moreover, the model can predict both monolayer and multilayer adsorptions through its parameter. The parameter values received for the model were given in Table 5.4, while the graph is shown in Figure S5.4-e. High R^2 values (>0.92) received for the model confirms the applicability of the model to the current adsorption mechanism. Accordingly, parameter A_{HJ} gives an implication on the heterogeneity and the surface area of the adsorbent and B_{HJ} shows the affinity of the adsorption via monolayer heat of adsorption [56], [66]. GrO shows very high surface areas with the highest heterogeneity as per the high values received for the heterogeneity factor (for GrO with Cd^{2+}, Ni^{2+} and Zn^{2+} A_{HJ}= 1097.85, 114.35, 711.98 while for GO, A_{HJ}=883.78, 924.62, 547.03 respectively). Among the metal ions, higher adsorption can be seen from Ni^{2+} given the high A_{HJ} values received. On the other hand, low monolayer heat of adsorption values reported for the model indicate that monolayer adsorptions

are also possible. The monolayer heat of adsorption is lowest in GrO with different metal ions (For GrO B_{HJ}= 1.56, 1.52 and 1.59 for Cd^{2+}, Ni^{2+} and Zn^{2+} respectively, For GO B_{HJ}= 1.57, 1.54 and 1.63 for Cd^{2+}, Ni^{2+} and Zn^{2+} respectively). However, observed slight changes in B_{HJ} values indicate that the heat of monolayer adsorption is the same for both the adsorbent materials. Hence, considering both parameters it is safe to say that the adsorption is mainly governed by heterogeneity of the active sites and pore sizes which leads to multilayer adsorption of metal ions.

Considering the coefficient of correlation values obtained for the different isotherms studied, it is possible to order the models that best describe the adsorption of metal ions to the adsorbents. Accordingly, Freundlich> Halsey> Harkins-Jura> Temkin> Langmuir explains the adsorption in the decreasing order. Hence, authors are confident enough to conclude that the adsorption follows the Freundlich model (2nd order) isotherms the best. However, with the other findings and partial analysis of R^2 values indicate that it is possible for the metal ion adsorption to follow physisorption at lower concentrations.

Table 5.4 has given the maximum adsorption values for each metal ion with each adsorbent according to the Freundlich model calculated through equation 15. Further, Table S5.2 compares the maximum adsorption capacities of other similar carbon-based materials with the current study values. As per the results reported by other authors, the adsorption materials synthesized in this study show a competitive adsorption capacity (for GO = 88.03, 93.19, 78.29 mg/g while GrO = 83.99, 89.85, 68.30 mg/g with Cd^{2+}, Ni^{2+} and Zn^{2+} respectively). Maximum adsorption capacities for metal ion adsorption are comparably lower than dye waste adsorption values. This is due to the size of the ionic radii of the metal ions and their comparably high charge density [67]. Moreover, the affinity of functional groups for the dye waste can be higher than that of metal ions [68]. However, comparing metal ion adsorption of this study with existing studies, the reported values for the maximum adsorption capacities varies in a very high range. For instance, Murphy et al (2023) reported 76.3, 45.5, and 32.6 mg/g (Cd^{2+}, Ni^{2+} and Zn^{2+} respectively) maximum adsorption capacities for a dosage of 0.025 g/L which is 40 times lower than the dosage used in this study [66]. Moreover, Chen et al (2020) reported only 3.25 mg/g maximum adsorption capacity with Ni^{2+} for a dose of 0.25 g/L [69]. However, the maximum adsorption values we received in this study consist within the average values found in literature. Nevertheless, considering the maximum adsorption capacity with dye waste and metal ions in the current study, it is safe to say that the

modified materials have a higher affinity towards the dye waste rather than metal ion adsorption. Key findings of the kinetic and isotherm analysis for each adsorbent across pollutants were briefly given in the Table 5.5.

Table 5.5 Key findings of the adsorbent materials across pollutants.

Pollutant type	GrO	GO
Dye pollutants	• Initial rate determinants govern by multiple mechanisms (both physisorption and chemisorption) • Chemisorption and liquid film diffusion responsible for the rate determination at the ending • Multilayer adsorption is highly probable at higher concentrations as the surface of the adsorbent is heterogeneous. • Both functional groups and pore spaces distribution are responsible for the adsorption. • Lower layer thickness. • Very high adsorption. • Higher affinity towards MB.	• Rate determination mainly governs by second order kinetics throughout the process (Chemisorption and liquid film diffusion). • Fast adsorption than GrO in the first few minutes. • Multilayer adsorption is prominent, active sites have considerable differences and adsorption energies. • Availability of functional groups mainly responsible for the adsorption. • The thickness of the layer is higher than GrO. • Relatively lower adsorption than GrO. • Higher affinity towards MB
Metal ions	• Overall rate of adsorption is determined by Chemisorption. • Initially, physisorption can make the adsorption faster. • Multilayer adsorption is observed. • Both functional groups and pore spaces are responsible for the absorption. • Low adsorption than dye pollutants govern by the size of the atomic radii, changes in the charge and affinity.	• Initial fast adsorption due to multiple mechanisms, mainly physisorption and chemisorption. • As per the ending, the influence of chemisorption and liquid film diffusion is higher. • Multilayer adsorption. • Functional groups are responsible for the adsorption. • Low affinity towards the metal ion than dye pollutants.

	• Relatively higher affinity towards Ni^{2+}.	• Relatively higher affinity towards Ni^{2+}.

3.4 Evaluation of adsorption mechanism

The study was carried out using mono-elementary synthetic solutions to evaluate the performance and mechanisms of the adsorption process of the newly modified adsorbent materials. It is important to note that, if used multi-elementary solutions, it would be difficult to assess the mechanisms of the adsorption due to complexity arise according to the many elements contain in the solution.

According to the FTIR analysis (Figure 5.4) (4000–400 cm^{-1} range at 4 cm^{-1} resolutions) of the adsorbent materials, it is possible to understand that the availability of functional groups such like epoxide (C-O-C) at 1065-1226 cm^{-1}, hydroxyl (-OH) at 3254-3420 cm^{-1}, carbonyl (-C=O) at 1622-1739 cm^{-1} and carboxyl (-C-OH) at 951-1015 cm^{-1} which are readily disperse in aqueous solution and make the solution negatively charged. This finding is also in line with the latest publication by Fauziyah et al. (2023) [73]. Hence, cationic dyes and the cations which act as positively charged ions can easily absorb onto adsorbents through electrostatic bonding. Moreover, Pi-Pi bonding is another key factor that enhances the adsorption capacity of the graphite-based adsorbents considered. Aromatic rings of the dye and the adsorbent materials can interact with each other through Pi-Pi bonding. Nevertheless, Pi-Pi interactions can also occur between aromatic rings of the metal ions and the surface of the adsorbents. Also, all the adsorbents contain H containing hydroxyl groups on their surfaces which can induce H-bonding with the cationic dyes.

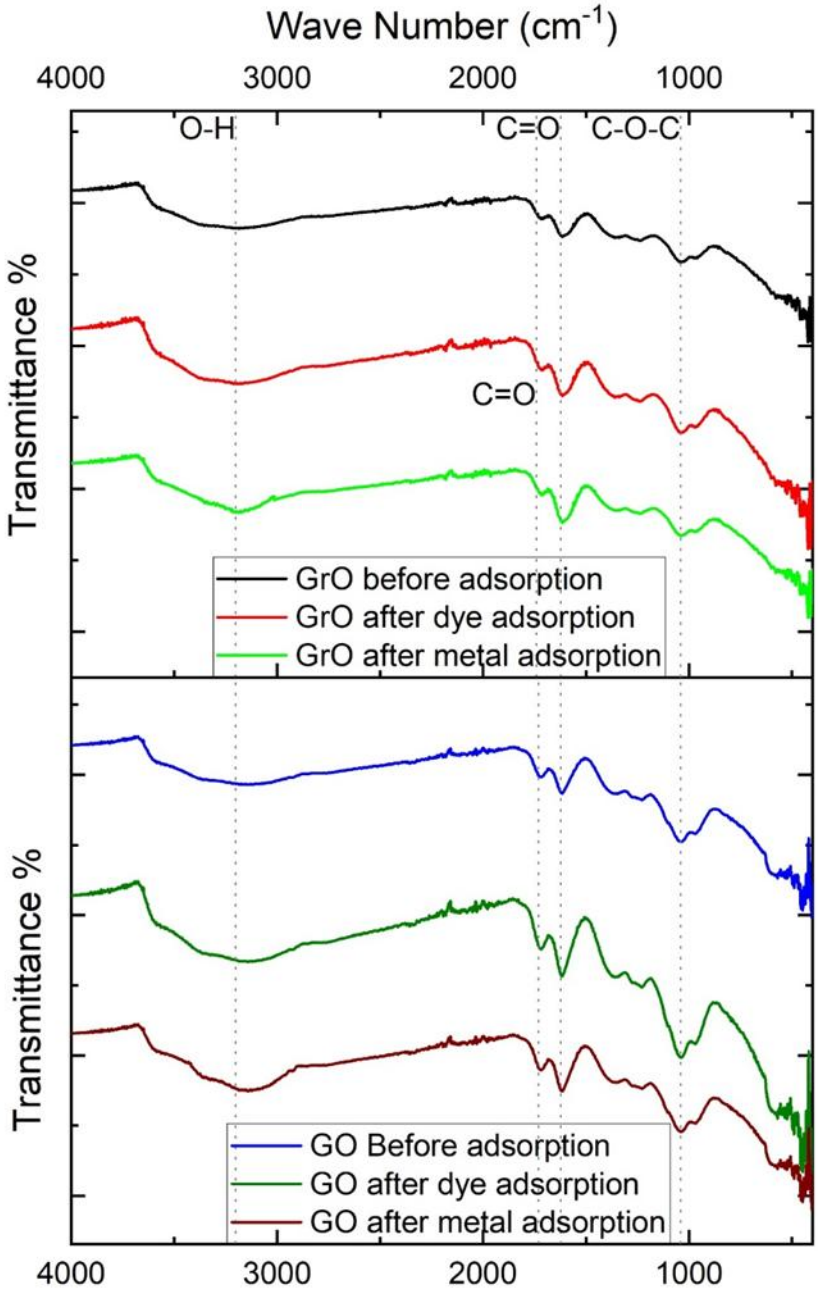

Figure 5.4 FTIR analysis of the two adsorbent materials GrO and GO before and after the adsorption of dye and metal ions.

Mostly, N and S atoms in MB and MG cationic dyes may act as H-bonding acceptors. Another main reason to have higher adsorption between metallic ions with adsorbents is coordination bonding. Since adsorbent surface contains more O containing functional groups, coordination bonding can occur through the donation of electron pairs from O atoms to the metal ions forming a stable complex. This is also visible through the differences between the intensities of each

functional group before and after the adsorption processes. In addition, given the structure of the graphite materials, interplanar Vander-walls forces can also interact with dye particles that can also affect absorbing the dye particles. Another important factor for the observed high adsorption of modified materials is the pore size distribution. The approximate size of dye particles is 1.2 – 1.8 nm and for metals it is even less. The pore size of meso-porous materials such as graphite derivatives vary between 2-50 nm [74]. Hence, dye particles and metal ions can trap inside the pores of adsorbents making the adsorption of the same very high. These mechanisms are also validated by previous studies [36], [51], [75], [76].

GrO has a slightly lower number of adsorption sites compared to GO as per the intensities of the FTIR analysis. However, GrO showed very high adsorption towards cationic dyes and metallic ions, even though it has a lower number of active sites than GO. The main reasons for this observation could be the larger surface area and high porosity of GrO. It has a relatively higher surface area giving a higher number of accessible sites for organic dye and metals owing to the exfoliated structure. This can be further convinced by the adsorption isotherm (Harkins-Jura isotherm findings) studies carried out previously. Also, expanded nature provides more pores that can trap pollutants inside enhancing the adsorption capacity. Moreover, it is studied that the reactivity of the GrO is higher than GO due to its high oxygen contain monolayer structure and can contribute to its high hydrophilic nature and excellent ion-exchange capacity [77].

Figure 5.5 depicts a possible adsorption mechanism that explains the arguments made above. In the figure D’ stands for cationic dye while M’ stands for the metallic ion and the red dot represents metal or dye pollutants.

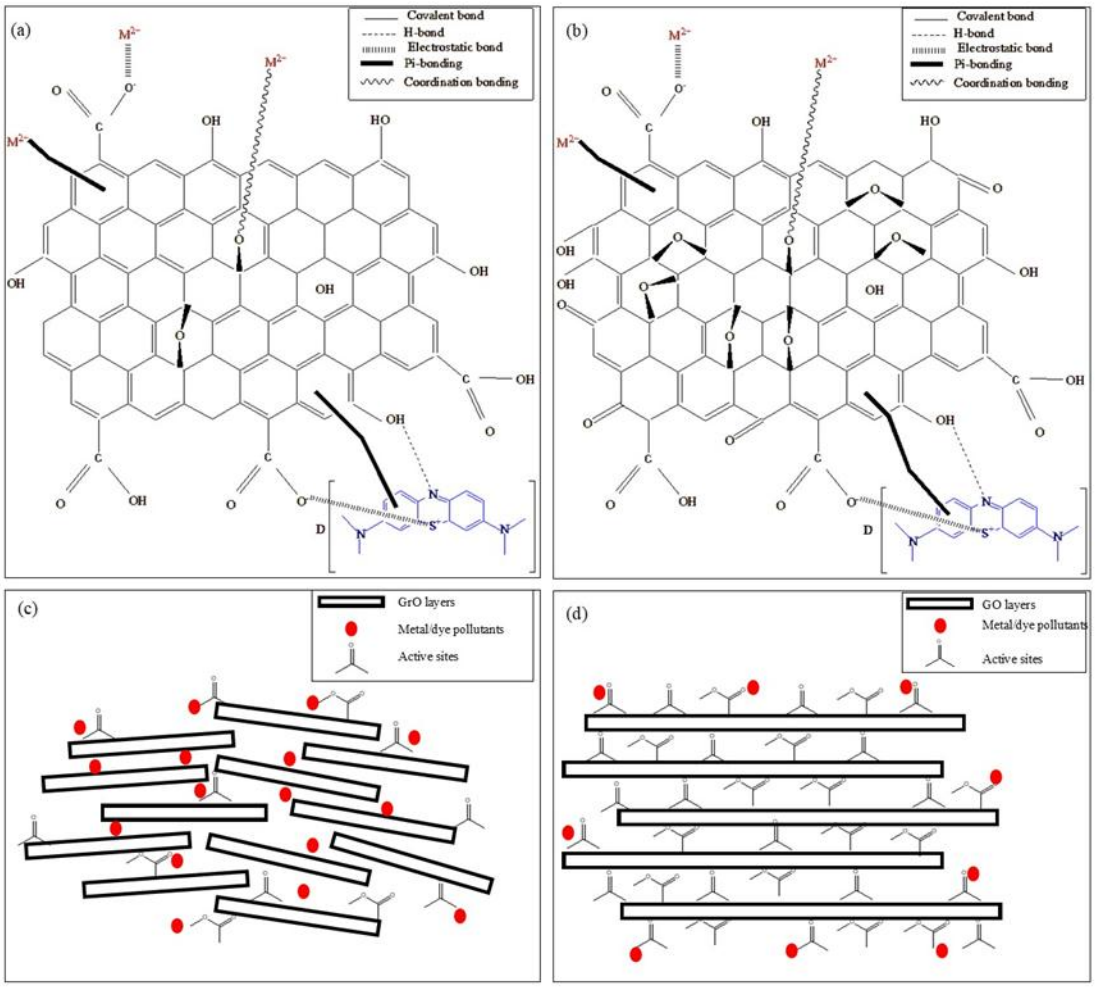

Figure 5.5 Possible adsorption mechanisms by (a) Graphene oxide surface active sites (b) Graphite oxide surface active sites with cationic dyes (as D) and metallic ions (as M^{2+}) (c) graphene oxide adsorption through cross section (d) graphite oxide adsorption through cross section.

The results and the discussion support the idea that the waste graphite recovered from spent LiBs are a better source to synthesize adsorption materials such as graphite oxide or graphene oxide. Also, better results can be expected from such prepared materials than the commercially available ones as the interlayer spacings have a slight expansion than natural graphite leading to easy oxidation. The adsorption material can be used for dye waste removal more efficiently than the metal ion removal due to the high maximum adsorption capacities received with dye pollutants. The adsorption will be mainly governed by chemisorption. However, the effect of physisorption also provides considerable support for the process.

4. **Conclusions**

The graphite recovered from spent LiBs through a real-life hydrometallurgical route. Graphite was modified using chemical oxidation, to produce value-added materials such as graphite oxide and graphene oxide. Characterization of the produced adsorbents showed synthesis of desired materials with higher quality than the commercially available substances. The main reason for better synthesis is identified to be the expanded nature of the used-up graphite as it was subjected to continuous charge and discharge cycles. Graphite oxide showed high oxidization and higher number of functional groups further identified through the FTIR analysis. Graphene oxide was shown to be having less functional groups but higher surface area with high porosity due to the ultrasonic vibration. The best adsorption was shown by GrO and in the case of dye waste, the adsorption rate was at around 95% with 30 ppm dye concentration, and for metallic ions around 94% at 30 ppm concentration. Kinetic analysis revealed, rate determinant factor of the overall process is chemisorption. However, initial, high concentration of dye or metal ion can lead to physisorption during the first few minutes. Dye adsorption of the adsorbents occurred in 10 minutes; nevertheless, metal ion adsorption took around 24 hours to complete. Isotherm analysis showed that, adsorbent contain heterogenous structure with different adsorption energies. Multilayer adsorption was shown by graphene oxide due to the availability of functional groups and pore spaces. Graphite oxide seems to have different functional groups that drive it to show multilayer adsorption. High affinity towards the dye adsorption was shown by the adsorbents with the best adsorption between methylene blue and graphene oxide. Ni^{2+} absorbed the best to graphene oxide than other metal ions. The highest adsorption capacity with dye waste was shown by GO at 616.99 mg/g for MG and 558.49 mg/g for MG. In the case of metallic ions, the highest adsorption capacities were shown by GrO with Cd^{2+}, Ni^{2+} and Zn^{2+}; 88.03, 93.19, 78.29 mg/g respectively. Compared to existing maximum adsorption materials, the synthesized material showed higher capacities, attributed to the possibility of preparing high quality adsorption material from spent graphite. This is mainly because waste graphite from spent LiBs shows slightly more exfoliated nature than natural graphite making it easier to generate value-added materials like graphite oxide and graphene oxide.

Reference:

[1] X. Meng et al., “Recycling of LiNi1/3Co1/3Mn1/3O2 cathode materials from spent lithium-ion batteries using mechanochemical activation and solid-state sintering,” Waste Management, vol. 84, pp. 54–63, Feb. 2019, doi: 10.1016/j.wasman.2018.11.034.

[2] Q. Cheng, B. Marchetti, X. Chen, S. Xu, and X.-D. Zhou, “Separation, purification, regeneration and utilization of graphite recovered from spent lithium-ion batteries - A review,” J Environ Chem Eng, vol. 10, no. 2, p. 107312, Apr. 2022, doi: 10.1016/j.jece.2022.107312.

[3] D. S. Premathilake, A. B. Botelho Junior, J. A. S. Tenório, D. C. R. Espinosa, and M. Vaccari, “Designing of a Decentralized Pretreatment Line for EOL-LIBs Based on Recent Literature of LIB Recycling for Black Mass,” Metals (Basel), vol. 13, no. 2, p. 374, Feb. 2023, doi: 10.3390/met13020374.

[4] Y. Shi, G. Chen, and Z. Chen, “Effective regeneration of LiCoO 2 from spent lithium-ion batteries: a direct approach towards high-performance active particles,” Green Chemistry, vol. 20, no. 4, pp. 851–862, 2018, doi: 10.1039/C7GC02831H.

[5] F. Larouche et al., “Progress and Status of Hydrometallurgical and Direct Recycling of Li-Ion Batteries and Beyond,” Materials, vol. 13, no. 3, p. 801, Feb. 2020, doi: 10.3390/ma13030801.

[6] C. K. Lee and K.-I. Rhee, “Preparation of LiCoO2 from spent lithium-ion batteries,” J Power Sources, vol. 109, no. 1, pp. 17–21, Jun. 2002, doi: 10.1016/S0378-7753(02)00037-X.

[7] A. Sobianowska-Turek, “Hydrometallurgical recovery of metals: Ce, La, Co, Fe, Mn, Ni and Zn from the stream of used Ni-MH cells,” Waste Management, vol. 77, pp. 213–219, Jul. 2018, doi: 10.1016/j.wasman.2018.03.046.

[8] T. Tawonezvi, M. Nomnqa, L. Petrik, and B. J. Bladergroen, “Recovery and Recycling of Valuable Metals from Spent Lithium-Ion Batteries: A Comprehensive Review and Analysis,” Energies (Basel), vol. 16, no. 3, p. 1365, Jan. 2023, doi: 10.3390/en16031365.

[9] W. Urbańska and M. Osial, “Investigation of the Physico-Chemical Properties of the Products Obtained after Mixed Organic-Inorganic Leaching of Spent Li-Ion Batteries,” Energies (Basel), vol. 13, no. 24, p. 6732, Dec. 2020, doi: 10.3390/en13246732.

[10] B. Makuza, D. Yu, Z. Huang, Q. Tian, and X. Guo, “Dry Grinding - Carbonated Ultrasound-Assisted Water Leaching of Carbothermally Reduced Lithium-Ion Battery Black Mass

Towards Enhanced Selective Extraction of Lithium and Recovery of High-Value Metals," Resour Conserv Recycl, vol. 174, p. 105784, Nov. 2021, doi: 10.1016/j.resconrec.2021.105784.

[11] A. Mayyas, D. Steward, and M. Mann, "The case for recycling: Overview and challenges in the material supply chain for automotive li-ion batteries," Sustainable Materials and Technologies, vol. 19, p. e00087, Apr. 2019, doi: 10.1016/j.susmat.2018.e00087.

[12] L. F. Guimarães, A. B. Botelho Junior, and D. C. R. Espinosa, "Sulfuric acid leaching of metals from waste Li-ion batteries without using reducing agent," Miner Eng, vol. 183, p. 107597, Jun. 2022, doi: 10.1016/J.MINENG.2022.107597.

[13] Y. Yang et al., "A process for combination of recycling lithium and regenerating graphite from spent lithium-ion battery," Waste Management, vol. 85, pp. 529–537, Feb. 2019, doi: 10.1016/j.wasman.2019.01.008.

[14] S. Natarajan and V. Aravindan, "An Urgent Call to Spent LIB Recycling: Whys and Wherefores for Graphite Recovery," Adv Energy Mater, vol. 10, no. 37, Oct. 2020, doi: 10.1002/aenm.202002238.

[15] M. Kepper, A. Rother, J. Thöming, and G. R. Pesch, "Polarisability-dependent separation of lithium iron phosphate (LFP) and graphite in dielectrophoretic filtration," Results in Engineering, vol. 21, p. 101854, Mar. 2024, doi: 10.1016/j.rineng.2024.101854.

[16] F. Mennik, N. İ. Dinç, and F. Burat, "Selective recovery of metals from spent mobile phone lithium-ion batteries through froth flotation followed by magnetic separation procedure," Results in Engineering, vol. 17, p. 100868, Mar. 2023, doi: 10.1016/j.rineng.2022.100868.

[17] M. C. Collivignarelli, S. Sorlini, C. Milanese, W. A. M. A. N. Illankoon, F. M. Caccamo, and S. Calatroni, "Rice Industry By-Products as Adsorbent Materials for Removing Fluoride and Arsenic from Drinking Water—A Review," Applied Sciences, vol. 12, no. 6, p. 3166, Mar. 2022, doi: 10.3390/app12063166.

[18] A. A. Ahmad, M. A. Ahmad, N. K. E. Yahaya, A. T. Mohd Din, and A. R. W. Yaakub, "Honeycomb-like porous-activated carbon derived from gasification waste for malachite green adsorption: equilibrium, kinetic, thermodynamic and fixed-bed column analysis," Desalination Water Treat, vol. 196, pp. 329–347, 2020, doi: 10.5004/dwt.2020.26067.

[19] Q. Xu et al., “Hydrothermal carbonization of distillers grains with clay minerals for enhanced adsorption of phosphate and methylene blue,” Bioresour Technol, vol. 340, p. 125725, Nov. 2021, doi: 10.1016/j.biortech.2021.125725.

[20] D. Vukelic et al., “Eco-design of a low-cost adsorbent produced from waste cherry kernels,” J Clean Prod, vol. 174, pp. 1620–1628, Feb. 2018, doi: 10.1016/j.jclepro.2017.11.098.

[21] A. K. Sakhiya, P. Baghel, A. Anand, V. K. Vijay, and P. Kaushal, “A comparative study of physical and chemical activation of rice straw derived biochar to enhance Zn+2 adsorption,” Bioresour Technol Rep, vol. 15, p. 100774, Sep. 2021, doi: 10.1016/j.biteb.2021.100774.

[22] J. O. Ighalo, F. O. Omoarukhe, V. E. Ojukwu, K. O. Iwuozor, and C. A. Igwegbe, “Cost of adsorbent preparation and usage in wastewater treatment: A review,” Cleaner Chemical Engineering, vol. 3, p. 100042, Sep. 2022, doi: 10.1016/j.clce.2022.100042.

[23] J. Mathew Tharayil and P. Chinnaiyan, “Sustainable waste valorisation: Novel Areca catechu L. husk biochar for anthraquinone dye adsorption - Characterization, modelling, kinetics, and isotherm studies,” Results in Engineering, vol. 20, p. 101624, Dec. 2023, doi: 10.1016/j.rineng.2023.101624.

[24] D. S. Premathilake, M. Vaccari, A. B. Botelho Junior, J. A. S. Tenório, D. C. R. Espinosa, and F. Colombi, “Valorization of waste graphite deriving from ‘End Of Life Lithium-Ion Battery recycling’ for a second use in wastewater treatment.,” in 18th International Conference on Environmental Science and Technology, Athens, 2023. doi: 10.30955/gnc2023.00266.

[25] W. S. Hummers Jr. and R. E. Offeman, “Preparation of Graphitic Oxide,” J Am Chem Soc, vol. 80, no. 6, pp. 1339–1339, May 2002, doi: 10.1021/ja01539a017.

[26] A. A. MOOSA and M. S. ABED, “Graphene preparation and graphite exfoliation,” Turk J Chem, vol. 45, no. 3, pp. 493–519, Jun. 2021, doi: 10.3906/kim-2101-19.

[27] I. Ogino, Y. Yokoyama, S. Iwamura, and S. R. Mukai, “Exfoliation of Graphite Oxide in Water without Sonication: Bridging Length Scales from Nanosheets to Macroscopic Materials,” Chemistry of Materials, vol. 26, no. 10, pp. 3334–3339, May 2014, doi: 10.1021/cm501305c.

[28] D. A. Yaseen and M. Scholz, “Textile dye wastewater characteristics and constituents of synthetic effluents: a critical review,” International Journal of Environmental Science and Technology, vol. 16, no. 2, pp. 1193–1226, Feb. 2019, doi: 10.1007/s13762-018-2130-z.

[29] P. Vassileva, V. Tumbalev, D. Kichukova, D. Voykova, D. Kovacheva, and I. Spassova, “Study on the Dye Removal from Aqueous Solutions by Graphene-Based Adsorbents,” Materials, vol. 16, no. 17, p. 5754, Aug. 2023, doi: 10.3390/ma16175754.

[30] M. ÇELEBİ and E. G. SÖĞÜT, “High-efficiency removal of cationic dye and heavy metal ions from aqueous solution using amino-functionalized graphene oxide, adsorption isotherms, kinetics studies, and mechanism,” Turk J Chem, vol. 46, no. 5, pp. 1577–1593, Jan. 2022, doi: 10.55730/1300-0527.3462.

[31] M. Yin, Y. Pan, and C. Pan, “Adsorption properties of graphite oxide for Rhodamine B,” Micro Nano Lett, vol. 14, no. 11, pp. 1192–1197, Sep. 2019, doi: 10.1049/mnl.2018.5820.

[32] X. Y. Qin, M. R. Chai, D. Y. Ju, and O. Hamamoto, “Investigation of plating wastewater treatment technology for chromium, nickel and copper,” IOP Conf Ser Earth Environ Sci, vol. 191, p. 012006, Nov. 2018, doi: 10.1088/1755-1315/191/1/012006.

[33] X. Ma, M. Chen, B. Chen, Z. Meng, and Y. Wang, “High-Performance Graphite Recovered from Spent Lithium-Ion Batteries,” ACS Sustain Chem Eng, vol. 7, no. 24, pp. 19732–19738, Dec. 2019, doi: 10.1021/acssuschemeng.9b05003.

[34] K. Maher and R. Yazami, “A study of lithium ion batteries cycle aging by thermodynamics techniques,” J Power Sources, vol. 247, pp. 527–533, Feb. 2014, doi: 10.1016/j.jpowsour.2013.08.053.

[35] J. Wu, X. Shen, L. Jiang, K. Wang, and K. Chen, “Solvothermal synthesis and characterization of sandwich-like graphene/ZnO nanocomposites,” Appl Surf Sci, vol. 256, no. 9, pp. 2826–2830, Feb. 2010, doi: 10.1016/j.apsusc.2009.11.034.

[36] S. Natarajan and H. C. Bajaj, “Recovered materials from spent lithium-ion batteries (LIBs) as adsorbents for dye removal: Equilibrium, kinetics and mechanism,” J Environ Chem Eng, vol. 4, no. 4, pp. 4631–4643, Dec. 2016, doi: 10.1016/j.jece.2016.10.024.

[37] S. Pan and I. A. Aksay, “Factors controlling the size of graphene oxide sheets produced via the graphite oxide route,” ACS Nano, vol. 5, no. 5, pp. 4073–4083, May 2011, doi: 10.1021/nn200666r.

[38] Y. Imai and A. Watanabe, “Energetic evaluation of possible stacking structures of Li-intercalation in graphite using a first-principle pseudopotential calculation,” J Alloys Compd, vol. 439, no. 1–2, pp. 258–267, Jul. 2007, doi: 10.1016/j.jallcom.2006.08.061.

[39] M. A. Pimenta, G. Dresselhaus, M. S. Dresselhaus, L. G. Cançado, A. Jorio, and R. Saito, “Studying disorder in graphite-based systems by Raman spectroscopy,” Phys. Chem. Chem. Phys., vol. 9, no. 11, pp. 1276–1290, 2007, doi: 10.1039/B613962K.

[40] A. Y. Lee et al., “Raman study of D* band in graphene oxide and its correlation with reduction,” Appl Surf Sci, vol. 536, p. 147990, Jan. 2021, doi: 10.1016/j.apsusc.2020.147990.

[41] M. D. Bhatt, H. Kim, and G. Kim, “Various defects in graphene: a review,” RSC Adv, vol. 12, no. 33, pp. 21520–21547, 2022, doi: 10.1039/D2RA01436J.

[42] W. Tian, W. Li, W. Yu, and X. Liu, “A Review on Lattice Defects in Graphene: Types, Generation, Effects and Regulation,” Micromachines (Basel), vol. 8, no. 5, p. 163, May 2017, doi: 10.3390/mi8050163.

[43] A. Kaniyoor and S. Ramaprabhu, “A Raman spectroscopic investigation of graphite oxide derived graphene,” AIP Adv, vol. 2, no. 3, p. 032183, Sep. 2012, doi: 10.1063/1.4756995.

[44] N. M. S. Hidayah et al., “Comparison on graphite, graphene oxide and reduced graphene oxide: Synthesis and characterization,” in AIP Conference Proceedings, American Institute of Physics Inc., Oct. 2017. doi: 10.1063/1.5005764.

[45] N. M. S. Hidayah et al., “Comparison on graphite, graphene oxide and reduced graphene oxide: Synthesis and characterization,” 2017, p. 150002. doi: 10.1063/1.5005764.

[46] E. Kusrini, A. A. Suhrowati, A. Usman, Dr. V. Degirmenci, and M. Khalil, “Synthesis and Characterization of Graphite Oxide, Graphene Oxide and Reduced Graphene Oxide from Graphite Waste using Modified Hummers’s Method and Zinc as Reducing Agent,” International Journal of Technology, vol. 10, no. 6, p. 1093, Nov. 2019, doi: 10.14716/ijtech.v10i6.3639.

[47] H. Yan et al., “Effects of the oxidation degree of graphene oxide on the adsorption of methylene blue,” J Hazard Mater, vol. 268, pp. 191–198, Mar. 2014, doi: 10.1016/j.jhazmat.2014.01.015.

[48] N. Morimoto, T. Kubo, and Y. Nishina, “Tailoring the Oxygen Content of Graphite and Reduced Graphene Oxide for Specific Applications,” Sci Rep, vol. 6, no. 1, p. 21715, Feb. 2016, doi: 10.1038/srep21715.

[49] T. Liu et al., “Adsorption of methylene blue from aqueous solution by graphene,” Colloids Surf B Biointerfaces, vol. 90, pp. 197–203, Feb. 2012, doi: 10.1016/j.colsurfb.2011.10.019.

[50] Y. Li et al., “Methylene blue adsorption on graphene oxide/calcium alginate composites,” Carbohydr Polym, vol. 95, no. 1, pp. 501–507, Jun. 2013, doi: 10.1016/j.carbpol.2013.01.094.

[51] L. Saikam, P. Arthi, N. D. Jayram, and N. Sykam, “Rapid removal of organic dyes from aqueous solutions using mesoporous exfoliated graphite,” Diam Relat Mater, vol. 130, p. 109480, 2022, doi: https://doi.org/10.1016/j.diamond.2022.109480.

[52] E. Mosaffa, A. Banerjee, and H. Ghafuri, “Sustainable high-efficiency removal of cationic and anionic dyes using new super adsorbent biochar: performance, isotherm, kinetic and thermodynamic evaluation,” Environ Sci (Camb), vol. 9, no. 10, pp. 2643–2663, Aug. 2023, doi: 10.1039/d3ew00464c.

[53] M. S.V., R. S. Baghel, and M. Kumar, “Performance evaluation of cement–carbon composite for adsorptive removal of acidic and basic dyes from single and multi-component systems,” Environ Technol Innov, vol. 16, p. 100478, Nov. 2019, doi: 10.1016/j.eti.2019.100478.

[54] S. V. Manjunath, R. Singh Baghel, and M. Kumar, “Antagonistic and synergistic analysis of antibiotic adsorption on Prosopis juliflora activated carbon in multicomponent systems,” Chemical Engineering Journal, vol. 381, p. 122713, Feb. 2020, doi: 10.1016/j.cej.2019.122713.

[55] R. Vitek and J. C. Masini, “Nonlinear regression for treating adsorption isotherm data to characterize new sorbents: Advantages over linearization demonstrated with simulated and experimental data,” Heliyon, vol. 9, no. 4, p. e15128, Apr. 2023, doi: 10.1016/j.heliyon.2023.e15128.

[56] R. Ramadoss, D. Gunasekaran, and D. Subramanian, “Removal of Divalent Nickel from Aqueous Solution Using Blue Green Marine Algae: Adsorption Modelling and Applicability of Various Isotherm Models,” in Progress in Microalgae Research - A Path for Shaping Sustainable Futures, IntechOpen, 2022. doi: 10.5772/intechopen.103940.

[57] S. Kalam, S. A. Abu-Khamsin, M. S. Kamal, and S. Patil, “Surfactant Adsorption Isotherms: A Review,” ACS Omega, vol. 6, no. 48, pp. 32342–32348, Dec. 2021, doi: 10.1021/acsomega.1c04661.

[58] A. O. Dada, F. A. Adekola, E. O. Odebunmi, A. S. Ogunlaja, and O. S. Bello, “Two–three parameters isotherm modeling, kinetics with statistical validity, desorption and thermodynamic studies of adsorption of Cu(II) ions onto zerovalent iron nanoparticles,” Sci Rep, vol. 11, no. 1, p. 16454, Aug. 2021, doi: 10.1038/s41598-021-95090-8.

[59] O. HAMDAOUI and E. NAFFRECHOUX, “Modeling of adsorption isotherms of phenol and chlorophenols onto granular activated carbonPart I. Two-parameter models and equations allowing determination of thermodynamic parameters,” J Hazard Mater, vol. 147, no. 1‑2, pp. 381–394, Aug. 2007, doi: 10.1016/j.jhazmat.2007.01.021.

[60] L. Chaabane, E. Beyou, A. El Ghali, and M. H. V. Baouab, “Comparative studies on the adsorption of metal ions from aqueous solutions using various functionalized graphene oxide sheets as supported adsorbents,” J Hazard Mater, vol. 389, p. 121839, May 2020, doi: 10.1016/j.jhazmat.2019.121839.

[61] Y. Li et al., “Comparative study of methylene blue dye adsorption onto activated carbon, graphene oxide, and carbon nanotubes,” Chemical Engineering Research and Design, vol. 91, no. 2, pp. 361–368, Feb. 2013, doi: 10.1016/j.cherd.2012.07.007.

[62] L. Das, S. Sengupta, P. Das, A. Bhowal, and C. Bhattacharjee, “Experimental and Numerical modeling on dye adsorption using pyrolyzed mesoporous biochar in Batch and fixed-bed column reactor: Isotherm, Thermodynamics, Mass transfer, Kinetic analysis,” Surfaces and Interfaces, vol. 23, p. 100985, Apr. 2021, doi: 10.1016/j.surfin.2021.100985.

[63] X. Cuong Nguyen et al., “Sustainable carbonaceous biochar adsorbents derived from agro-wastes and invasive plants for cation dye adsorption from water,” Chemosphere, vol. 282, p. 131009, Nov. 2021, doi: 10.1016/j.chemosphere.2021.131009.

[64] X. Guo, S. Tang, Y. Song, and J. Nan, “Adsorptive removal of Ni 2+ and Cd 2+ from wastewater using a green longan hull adsorbent,” Adsorption Science & Technology, vol. 36, no. 1–2, pp. 762–773, Feb. 2018, doi: 10.1177/0263617417722254.

[65] F. Dhaouadi et al., “Adsorption mechanism of Zn2+, Ni2+, Cd2+, and Cu2+ ions by carbon-based adsorbents: interpretation of the adsorption isotherms via physical modelling,” Environmental Science and Pollution Research, vol. 28, no. 24, pp. 30943–30954, Jun. 2021, doi: 10.1007/s11356-021-12832-x.

[66] O. P. Murphy, M. Vashishtha, P. Palanisamy, and K. V. Kumar, “A Review on the Adsorption Isotherms and Design Calculations for the Optimization of Adsorbent Mass and Contact Time,” ACS Omega, vol. 8, no. 20, pp. 17407–17430, May 2023, doi: 10.1021/acsomega.2c08155.

[67] A. Thanarasu, K. Periyasamy, P. Manickam Periyaraman, T. Devaraj, K. Velayutham, and S. Subramanian, “Comparative studies on adsorption of dye and heavy metal ions from effluents using eco-friendly adsorbent,” Mater Today Proc, vol. 36, pp. 775–781, 2021, doi: 10.1016/j.matpr.2020.07.001.

[68] R. Mallampati and S. Valiyaveettil, “Application of tomato peel as an efficient adsorbent for water purification—alternative biotechnology?,” RSC Adv, vol. 2, no. 26, p. 9914, 2012, doi: 10.1039/c2ra21108d.

[69] H. Chen et al., “Graphene oxide modified waste newspaper for removal of heavy metal ions and its application in industrial wastewater,” Mater Chem Phys, vol. 244, p. 122692, Apr. 2020, doi: 10.1016/j.matchemphys.2020.122692.

[70] A. Rahmani-Sani et al., “Use of chicken feather and eggshell to synthesize a novel magnetized activated carbon for sorption of heavy metal ions,” Bioresour Technol, vol. 297, p. 122452, Feb. 2020, doi: 10.1016/j.biortech.2019.122452.

[71] E. Ghasemi, A. Heydari, and M. Sillanpää, “Ultrasonic assisted adsorptive removal of toxic heavy metals from environmental samples using functionalized silica-coated magnetic multiwall carbon nanotubes (MagMWCNTs@SiO2),” Engineering in Agriculture, Environment and Food, vol. 12, no. 4, pp. 435–442, Oct. 2019, doi: 10.1016/j.eaef.2019.07.002.

[72] Q.-U.- Ain, M. U. Farooq, and M. I. Jalees, “Application of Magnetic Graphene Oxide for Water Purification: Heavy Metals Removal and Disinfection,” Journal of Water Process Engineering, vol. 33, p. 101044, Feb. 2020, doi: 10.1016/j.jwpe.2019.101044.

[73] N. A. Fauziyah, D. A. Kristanti, P. C. Kusumaningtyas, P. Cahya Wardhani, P. Sampe Tola, and T. A. Fadly, “Analysis of Carbon Functional Groups through FTIR Patterns in The Preparation of Reduced Graphene Oxide (RGO),” 2023. [Online]. Available: www.techniumscience.com

[74] S. Cheng et al., “Facile one-pot green synthesis of magnetic separation photocatalyst-adsorbent and its application,” Journal of Water Process Engineering, vol. 47, p. 102802, Jun. 2022, doi: 10.1016/j.jwpe.2022.102802.

[75] P. Bradder, S. K. Ling, S. Wang, and S. Liu, “Dye Adsorption on Layered Graphite Oxide,” J Chem Eng Data, vol. 56, no. 1, pp. 138–141, Jan. 2011, doi: 10.1021/je101049g.

[76] W. Zhang et al., “Fast and Considerable Adsorption of Methylene Blue Dye onto Graphene Oxide,” Bull Environ Contam Toxicol, vol. 87, no. 1, pp. 86–90, Jul. 2011, doi: 10.1007/s00128-011-0304-1.

[77] V. Gupta, N. Sharma, U. Singh, Mohd. Arif, and A. Singh, “Higher oxidation level in graphene oxide,” Optik (Stuttg), vol. 143, pp. 115–124, Aug. 2017, doi: 10.1016/j.ijleo.2017.05.100.

[78] M. S. Vallabha, P. C. Nagaraj, and A. K. K. Mallikarjunappa, “Competitive and cooperative adsorption analysis for dye removal from multicomponent system using Prosopis juliflora activated carbon,” Environmental Science and Pollution Research, vol. 30, no. 39, pp. 90362–90382, Dec. 2022, doi: 10.1007/s11356-022-24721-y.

[79] M. S. Vallabha, P. C. Nagraj, N. O. Sanjeev, M. Mahadev, R. Devadas, and V. Govindappa, “Valorization of Parthenium hysterophorus weed into biochar for adsorptive removal of industrial

dyes from multi-pollutant aqueous systems," Biomass Convers Biorefin, Apr. 2024, doi: 10.1007/s13399-024-05534-0.

Chapter Six-Conclusion

In response to the critical challenge of spent lithium-ion battery (LIB) disposal and the subsequent environmental impact, this thesis has explored sustainable methodologies for LIB recycling, focusing on recovering essential materials such as cathode metals, anode graphite, and potential value additions. Driven by the growing demand for LIBs, largely fueled by the electric vehicle (EV) market, the proper treatment of end-of-life (EOL) batteries becomes crucial to alleviating the stress on natural resources, reducing environmental harm, and meeting future circular economic requirements. The proposed recycling approach spans from a detailed pretreatment phase, which then prolonged to cathode and anode parts.

The findings are presented over four key chapters, each contributing unique insights into specific aspects of LIB recycling. Chapter two focused on pretreatment methodologies to separate and prepare LIB components, presenting a decentralized collection and pretreatment strategy. Chapter 3 assessed the efficacy, environmental impact and economic impact of various hydrometallurgical techniques for metal recovery. Chapter 4 introduced and optimized three novel methods—cold, hot, and wet processes—for graphite recovery from anodes, each evaluated through Life Cycle Assessment (LCA) and Life Cycle Costing (LCC). Chapter 5 explored value-added applications for recovered graphite, demonstrating successful transformation into adsorbents for dye and metal ion removal from aqueous solutions.

1. Key Findings

1.1 Chapter 2 - Pretreatment

Chapter 2 emphasized the importance of pretreatment in enhancing the overall efficiency of LIB recycling by providing a common processing line for diverse LIB types. The proposed approach overcomes collection and sorting challenges by leveraging decentralized pretreatment facilities, which improve material recovery quality while reducing environmental costs. The literature review provided guidance for dismantling LIBs safely, using innovative methods such as N_2 and water sprays for dismantling without discharging. A two-step mechanical separation using flotation-based techniques was shown to maximize recovery of plastics, separators, and current collectors like Cu and Al. Utilizing of CaO for the decompose of Polyvinylidene fluoride (PVDF) can reduce the pyrolyzing temperature to 300 °C. By implementing these steps, the pretreatment

line optimized in this chapter offers an efficiency exceeding 98% in the recovery of electrode and current collector materials.

1.2 Chapter 3 – Environmental and economical evaluation of emerging hydrometallurgical treatment for cathode.

Hydrometallurgical recovery processes were evaluated in Chapter 3, focusing on efficiency, economic viability, and environmental impact. While Supercritical Fluid (SCF)-based leaching offers improved environmental performance, its lower metal recovery rate limits its current feasibility. Conversely, electrochemical (EC)-based and conventional leaching methods achieved higher recovery rates, up to 78%, while balancing emissions and costs. Adsorbent-based purification was found superior to solvent-based extraction, which showed high emissions, especially when recovery exceeded 80%. Inorganic acid-based leaching, followed by ion-exchange resin-based purification with hydroxide calcination, achieved the best balance, demonstrating high recovery efficiency (78%), lower CO_2 emissions (33.8 kg CO_2 eq.), and favorable economic performance ($119/kg). This comprehensive route serves as a benchmark for future scaling of hydrometallurgical recycling processes for LIBs.

1.3 Chapter 4 - Graphite Recovery from Anodes

The graphite recovery methods developed in Chapter 4—cold, hot, and wet processes—demonstrate varied efficacy depending on environmental and economic priorities. The wet process achieved the highest graphite yield (307.8 g/kg anode), though it resulted in significant environmental impacts due to emissions and corrosive acid use. The hot process, with a slightly lower recovery (281.5 g/kg anode), yielded high-quality graphite (70% carbon content) and proved the most promising overall. The annealing effect of heat reduced interlayer spacing in graphite, enhancing structural integrity. CaO was utilized to decompose PVDF binders efficiently, decreasing both heat demand and costs. Meanwhile, the cold process achieved the lowest recovery rate (197.6 g/kg anode) but showed superior environmental performance with minimal emissions and a low net cost (-$40/kg of graphite). These findings highlight the need for selecting recovery processes that match the economic and environmental goals of future LIB recycling facilities.

1.4 Chapter 5 - Value-Added Applications for Recovered Graphite

Chapter 5 explored the transformation of recovered graphite into adsorbents, specifically graphite oxide (GrO) and graphene oxide (GO), which exhibited remarkable adsorption capacities for dye and metallic ions. The oxidized nature and expanded surface area of recovered graphite, attributed to prior charge-discharge cycles, enhanced its adsorption efficiency, with GrO achieving adsorption rates as high as 95% for dyes and 94% for metallic ions at 30 ppm initial dye concentrations. GrO showed multilayer adsorption, while GO demonstrated high affinity for methylene blue dye and Ni^{2+} ions due to increased pore space and functional group density. With adsorption capacities up to 616.99 mg/g for dyes and 93.19 mg/g for Ni^{2+}, these materials surpass existing commercial adsorbents, proving that waste graphite can indeed be transformed into high-quality, sustainable materials for wastewater treatment.

2. Overall Implications

This study provides significant advancements in the field of LIB recycling. It identifies efficient pretreatment, hydrometallurgical, and graphite recovery processes that not only maximize material recovery rates but also minimize environmental impacts. Furthermore, by transforming waste graphite into valuable adsorbents, this work highlights a sustainable pathway to utilize spent LIB components in water treatment, contributing to broader environmental and economic benefits.

The proposed pretreatment line and hydrometallurgical process establish a comprehensive recycling framework with high recovery efficiency and economic viability. The research demonstrates that optimizing process parameters can enhance material yield, quality, and economic feasibility, ultimately encouraging the adoption of LIB recycling. Future work should focus on scaling these methods, especially the promising applications of graphite-based adsorbents, to foster a more circular and sustainable approach to LIB end-of-life management.

Annexure 1

Comparative Environmental and Economic Assessment of Emerging Hydrometallurgical Recycling Technologies for Li-Ion Battery Cathodes.

This document contains a detailed flow diagrams designed by the authors for easy understanding of the different processes used in Chapter 3. Moreover, figures and tables generated by the SimaPro software for various analysis done were also given in this document. Specially, characteristic impacts of different technologies under each impact category and Monte-Carlo analysis done under standard and improved scenarios are given in this document.

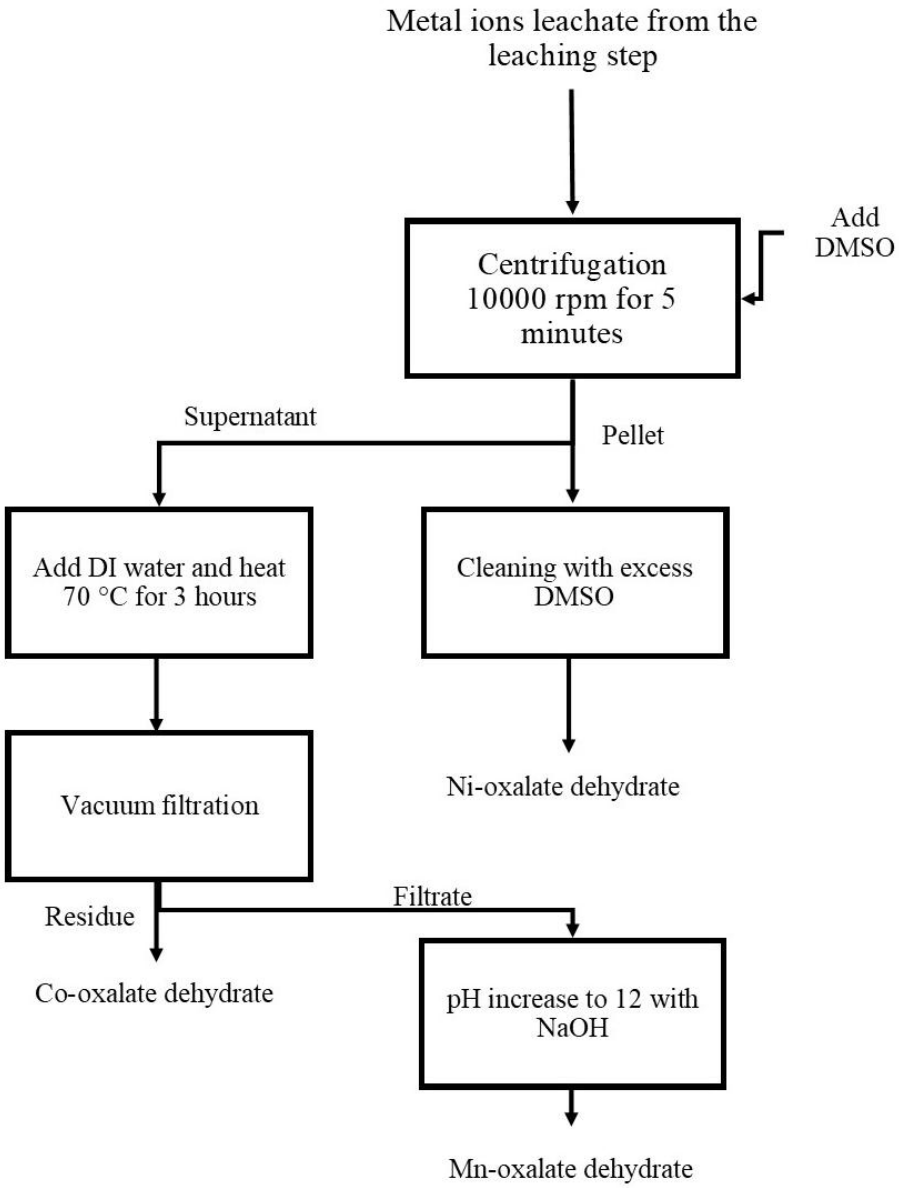

Figure S3.1 Purification process for oxalate-based purification

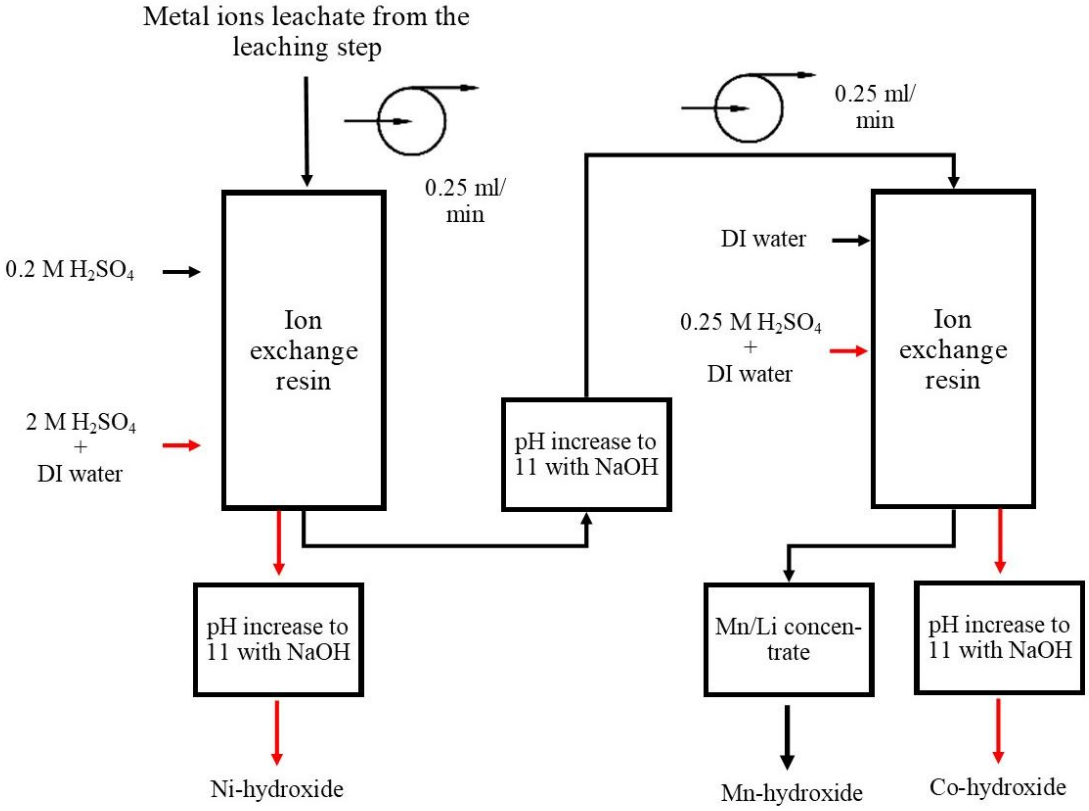

Figure S3.2 Purification process for ion exchanged (adsorption material) based purification

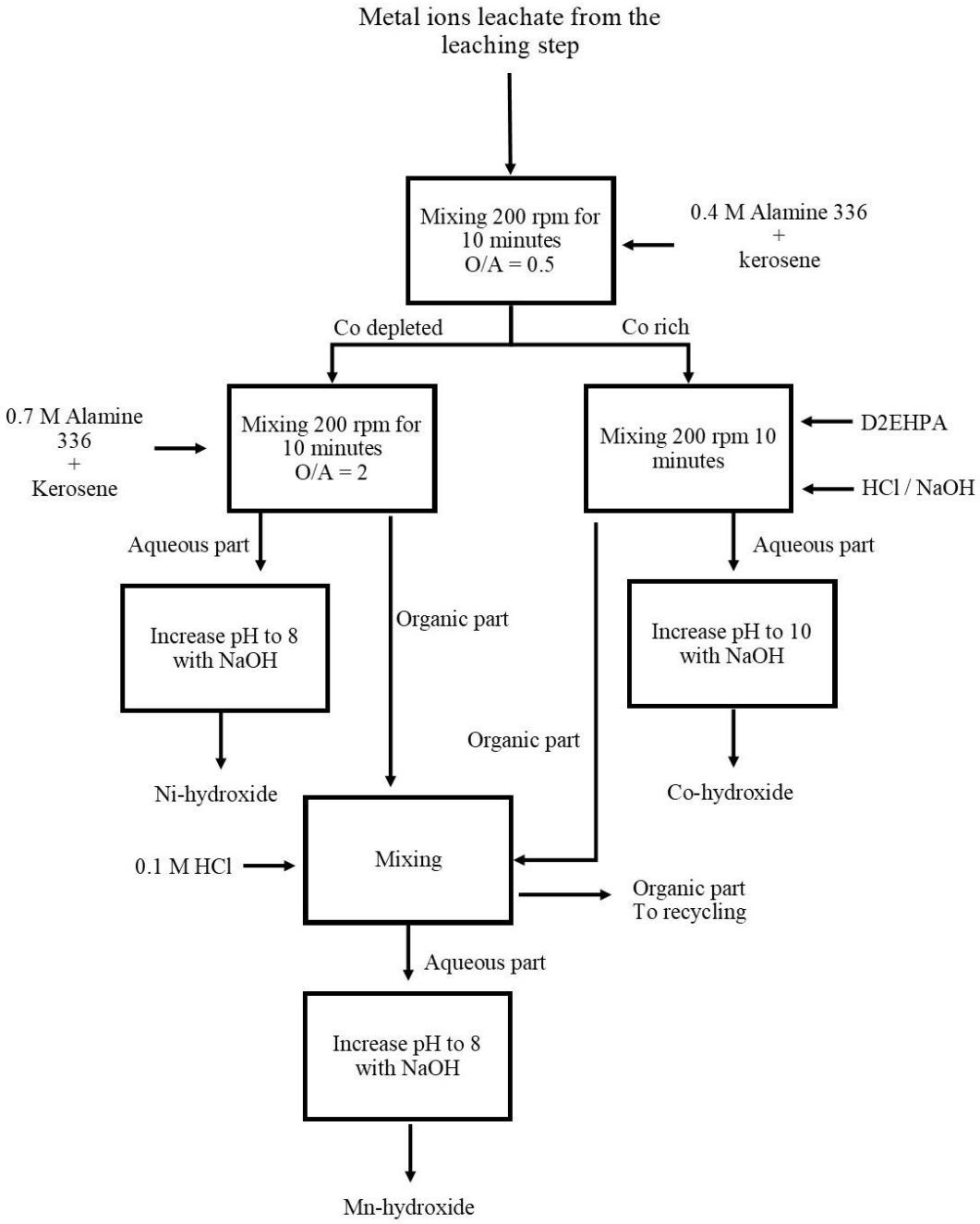

Figure S3.3 Purification process for Solvent extraction (organic solvent) based purification

Table S3.1 Impacts made by each leaching method studied under different impact categories.

Impact category	Unit	Inorganic acid leaching	DES leaching	EC based leaching	SCF based leaching
Global warming	kg CO_2 eq	2.14×10^{1}	2.80×10^{2}	6.39×10^{0}	1.34×10^{1}
Stratospheric ozone depletion	kg CFC11 eq	8.92×10^{-6}	1.12×10^{-4}	5.23×10^{-6}	1.06×10^{-5}
Ionizing radiation	kBq Co-60 eq	2.35×10^{0}	2.88×10^{1}	5.91×10^{-1}	1.12×10^{0}
Ozone formation, Human health	kg NO_x eq	4.90×10^{-2}	6.01×10^{-1}	1.94×10^{-2}	3.13×10^{-2}
Fine particulate matter formation	kg PM2.5 eq	5.22×10^{-2}	5.71×10^{-1}	3.25×10^{-2}	2.94×10^{-2}
Ozone formation, Terrestrial ecosystems	kg NO_x eq	4.95×10^{-2}	6.11×10^{-1}	1.97×10^{-2}	3.17×10^{-2}
Terrestrial acidification	kg SO_2 eq	9.58×10^{-2}	9.42×10^{-1}	8.65×10^{-2}	5.85×10^{-2}
Freshwater eutrophication	kg P eq	1.04×10^{-2}	1.26×10^{-1}	3.65×10^{-3}	5.86×10^{-3}
Marine eutrophication	kg N eq	7.95×10^{-4}	1.12×10^{-2}	6.54×10^{-4}	6.94×10^{-4}
Terrestrial ecotoxicity	kg 1,4-DCB	5.30×10^{1}	4.92×10^{2}	5.78×10^{1}	7.30×10^{1}
Freshwater ecotoxicity	kg 1,4-DCB	1.58×10^{0}	1.60×10^{1}	1.09×10^{0}	1.04×10^{0}
Marine ecotoxicity	kg 1,4-DCB	2.01×10^{0}	2.03×10^{1}	1.39×10^{0}	1.35×10^{0}
Human carcinogenic toxicity	kg 1,4-DCB	1.08×10^{0}	1.08×10^{1}	5.83×10^{-1}	6.47×10^{-1}
Human non-carcinogenic toxicity	kg 1,4-DCB	2.54×10^{1}	2.47×10^{2}	1.43×10^{1}	1.94×10^{1}
Land use	m^2a crop eq	3.30×10^{-1}	3.83×10^{0}	1.93×10^{-1}	2.81×10^{-1}
Mineral resource scarcity	kg Cu eq	1.49×10^{-1}	3.67×10^{-1}	5.52×10^{-1}	1.21×10^{-1}
Fossil resource scarcity	kg oil eq	5.63×10^{0}	8.78×10^{1}	1.60×10^{0}	3.21×10^{0}
Water consumption	m^3	3.17×10^{-1}	2.45×10^{0}	1.35×10^{-1}	3.26×10^{-1}

Table S3.2 Impacts made by each separation/purification method studied under different impact categories.

Impact category	Unit	Ion-exchange resin	Oxalate based	Solvent extraction
Global warming	kg CO_2 eq	1.99×10^{1}	7.50×10^{1}	2.18×10^{2}
Stratospheric ozone depletion	kg CFC11 eq	8.38×10^{-4}	2.60×10^{-5}	1.59×10^{-4}
Ionizing radiation	kBq Co-60 eq	4.67×10^{-1}	2.00×10^{0}	7.14×10^{0}
Ozone formation, Human health	kg NO_x eq	2.86×10^{-2}	9.53×10^{-2}	5.18×10^{-1}
Fine particulate matter formation	kg PM2.5 eq	2.05×10^{-2}	8.88×10^{-2}	2.87×10^{-1}
Ozone formation, Terrestrial ecosystems	kg NO_x eq	2.97×10^{-2}	9.89×10^{-2}	6.08×10^{-1}
Terrestrial acidification	kg SO_2 eq	4.74×10^{-2}	2.41×10^{-1}	7.10×10^{-1}
Freshwater eutrophication	kg P eq	4.40×10^{-3}	1.64×10^{-2}	6.12×10^{-2}
Marine eutrophication	kg N eq	1.34×10^{-3}	1.45×10^{-3}	4.66×10^{-3}
Terrestrial ecotoxicity	kg 1,4-DCB	4.63×10^{1}	1.55×10^{2}	5.93×10^{2}
Freshwater ecotoxicity	kg 1,4-DCB	7.20E-01	2.76×10^{0}	9.28×10^{0}
Marine ecotoxicity	kg 1,4-DCB	9.41E-01	3.57×10^{0}	1.22×10^{1}
Human carcinogenic toxicity	kg 1,4-DCB	1.12×10^{0}	1.33×10^{0}	1.06×10^{1}
Human non-carcinogenic toxicity	kg 1,4-DCB	1.62×10^{1}	4.46×10^{1}	1.74×10^{2}
Land use	m^2a crop eq	1.96×10^{-1}	6.96×10^{-1}	3.39×10^{0}
Mineral resource scarcity	kg Cu eq	5.81×10^{-2}	1.93×10^{-1}	7.33×10^{-1}
Fossil resource scarcity	kg oil eq	5.64×10^{0}	2.66×10^{1}	1.18×10^{2}
Water consumption	m^3	2.00×10^{-1}	6.75×10^{-1}	2.30×10^{0}

Table S3.3 Impacts made by two calcination methods studied under different impact categories for Cobalt.

Impact category	Unit	Metal oxide by oxalate calcination	Metal oxides by hydroxide calcination
Global warming	kg CO_2 eq	9.47×10^{1}	6.06×10^{1}
Stratospheric ozone depletion	kg CFC11 eq	4.00×10^{-5}	2.59×10^{-5}
Ionizing radiation	kBq Co-60 eq	1.13×10^{1}	7.30×10^{0}
Ozone formation, Human health	kg NO_x eq	2.04×10^{-1}	1.32×10^{-1}
Fine particulate matter formation	kg PM2.5 eq	2.07×10^{-1}	1.34×10^{-1}
Ozone formation, Terrestrial ecosystems	kg NO_x eq	2.05×10^{-1}	1.33×10^{-1}
Terrestrial acidification	kg SO_2 eq	3.24×10^{-1}	2.10×10^{-1}
Freshwater eutrophication	kg P eq	4.72×10^{-2}	3.05×10^{-2}
Marine eutrophication	kg N eq	3.19×10^{-3}	2.06×10^{-3}
Terrestrial ecotoxicity	kg 1,4-DCB	1.50×10^{2}	9.67×10^{1}
Freshwater ecotoxicity	kg 1,4-DCB	5.82×10^{0}	3.76×10^{0}
Marine ecotoxicity	kg 1,4-DCB	7.35×10^{0}	4.75×10^{0}
Human carcinogenic toxicity	kg 1,4-DCB	3.89×10^{0}	2.51×10^{0}
Human non-carcinogenic toxicity	kg 1,4-DCB	8.65×10^{1}	5.59×10^{1}
Land use	m^2a crop eq	1.36×10^{0}	8.82×10^{-1}
Mineral resource scarcity	kg Cu eq	9.27×10^{-2}	5.99×10^{-2}
Fossil resource scarcity	kg oil eq	2.34×10^{1}	1.51×10^{1}
Water consumption	m^3	7.01×10^{-1}	4.53×10^{-1}

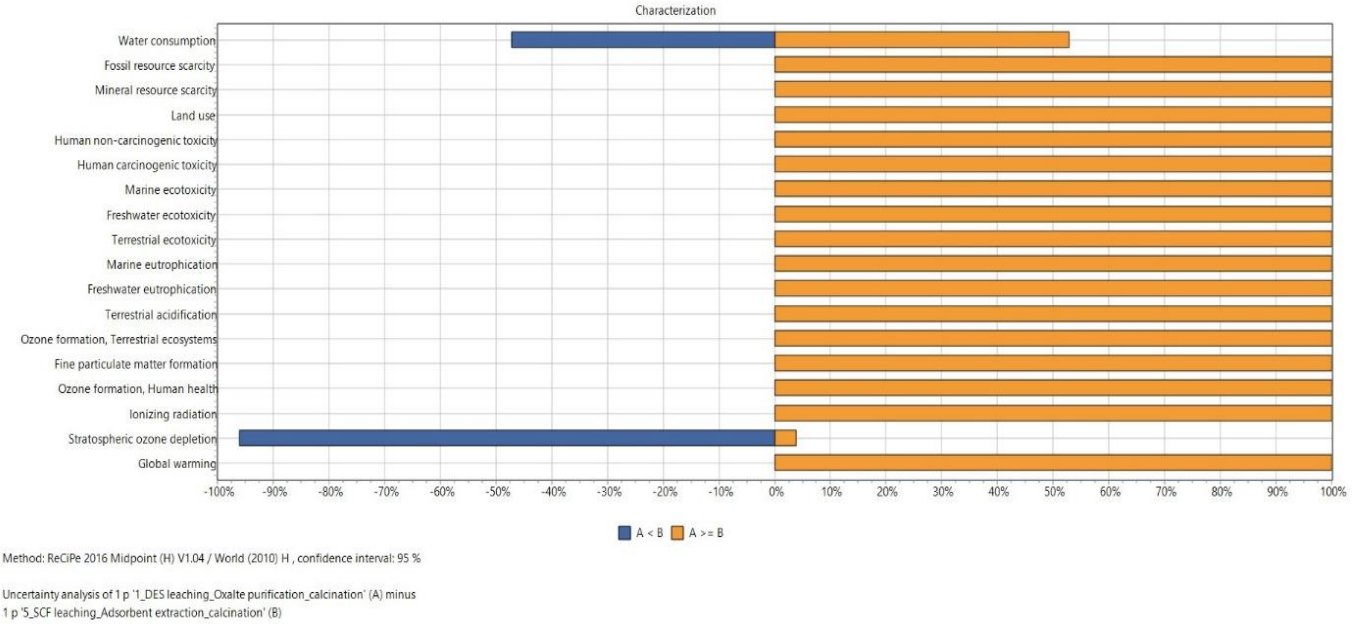

Figure S3.4 Montecarlo sensitivity analysis for the best (route 5-B) and the worst (route 1-A) routes.

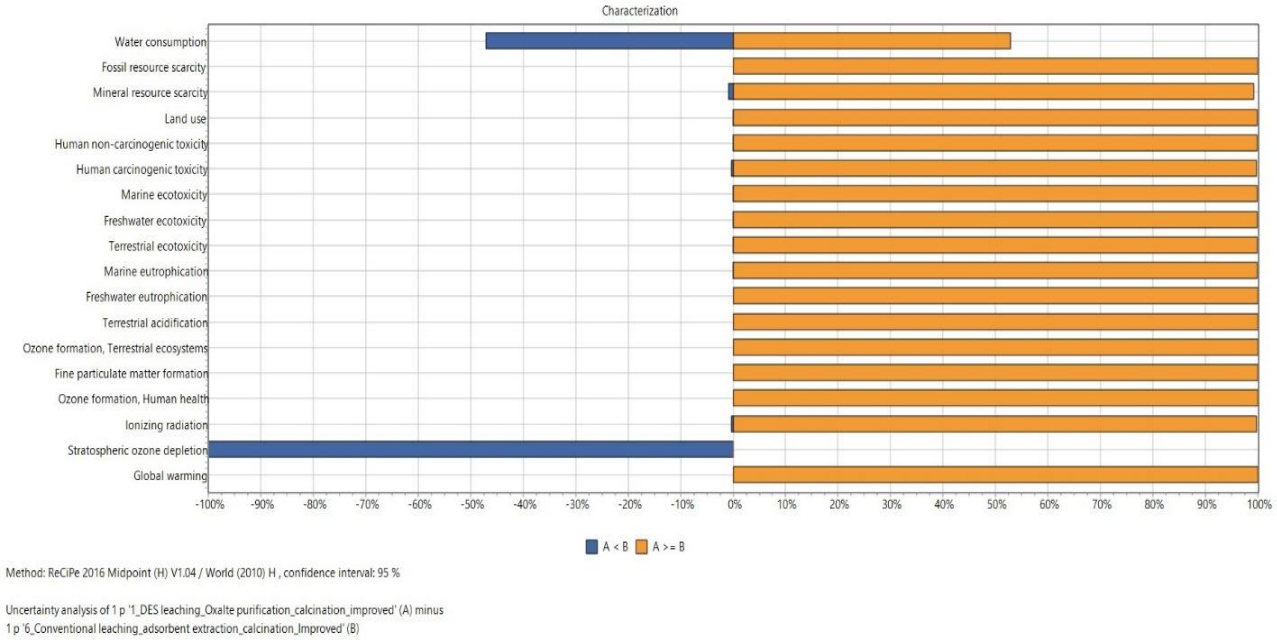

Figure S3.5 Montecarlo sensitivity analysis for the improved version of routes that showed the highest impact reduction (Route 1-A and Route 6-B)

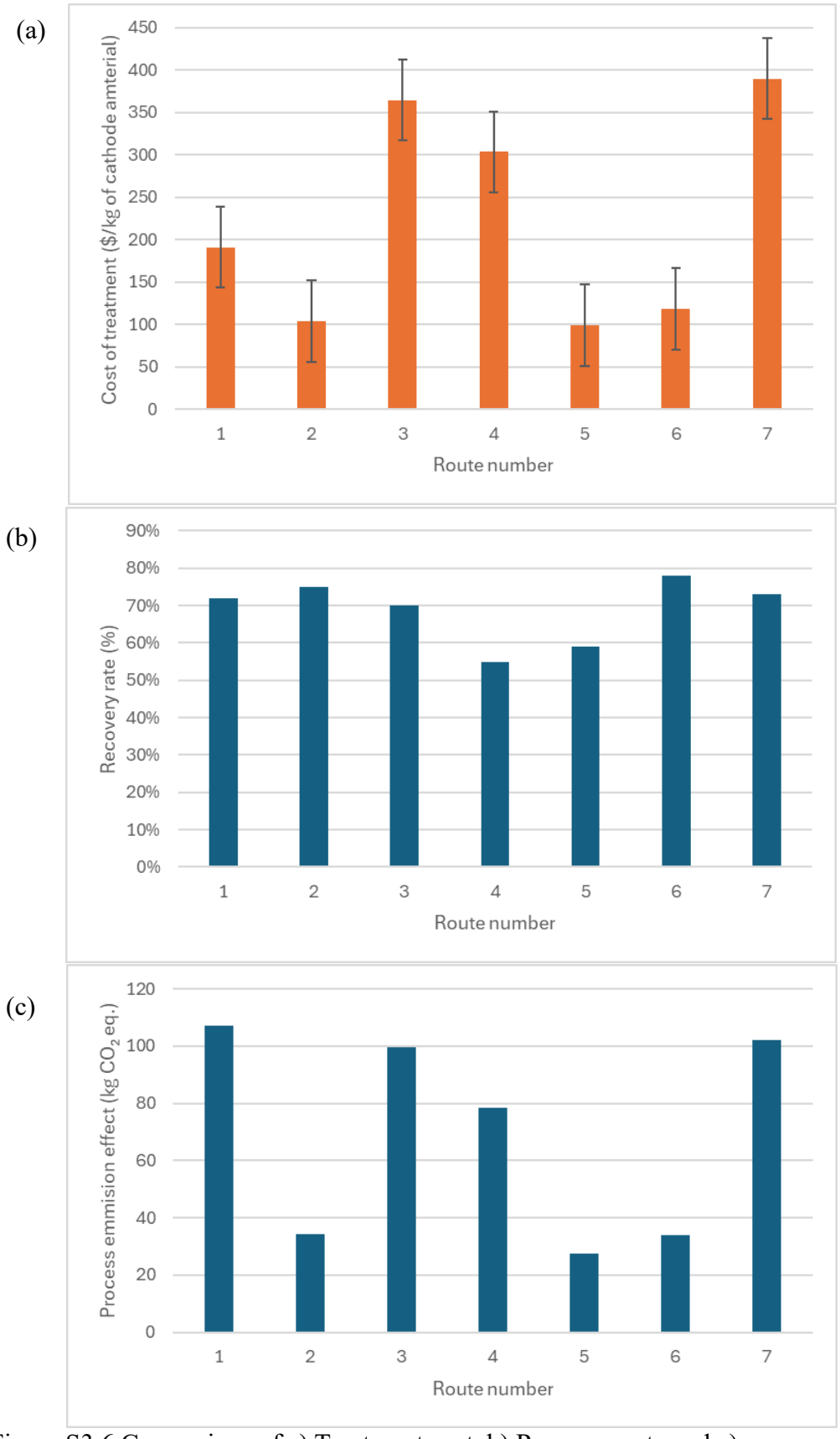

Figure S3.6 Comparison of a) Treatment cost, b) Recovery rate and c) process emission effect

under different routs

Annexure 2

Comparative Environmental and Economic Assessment of Emerging Hydrometallurgical Recycling Technologies for Li-Ion Battery Cathodes.

This document contains the inventories of standard scenario, improved scenario and the inventory of the economic analysis used in Chapter 3.

Section 1. Inventory of the standard scenario.

Simapro input/output	Material per 1 g of NMC cathode treatment	Energy per 1 g of NMC cathode treatment	Data source	Remarks	LCA process
Unit	g	Wh			
Conventional leaching					
Inputs from technosphere					
Sulfuric acid {RoW}| market for sulfuric acid | Cut-off, U	3.68±1.67		Guimareus (2022), Vieceli et al (2023), Chen et al (2018)		Eco-invent
Hydrogen peroxide, without water, in 50% solution state {RoW}| market for	1.43±1.91				Eco-invent
Electricity, low voltage {GLO}| market group for | Cut-off, U		24.5±0.01		1.4 KWh heating coil, 10 min preheat, 30% working capacity through out the reaction time (110 min.).	Eco-invent
Emmisions to air					
Oxygen	0.0024		Stoichiometry		Eco-invent
Outputs to technosphere					
Leached metal ions (Co2+, Ni2+, Mn2+)	0.59		Stoichiometry		Dummy variable
DES based leaching					
Inputs from technosphere					
Deep Eutectic Solvent (Oxalic acid & Choline Chloride)	15.5±4.58		Chang et al (2022), He et al (2022), Tang et al (2022), Naik et al (2023)	50% recycling assumed, authors reported 80%-100% recycling.	Zaib et al (2022), Vahidi & Zhao (2017)
Electricity, low voltage {GLO}| market group for | Cut-off, U		288.6±64.7		1.4 KWh heating coil, 10 min preheat, 30% working capacity through out the reaction time (110 min.).	Eco-invent
Outputs to technosphere					
Leached metal ions (Co2+, Ni2+, Mn2+)	0.57		Stoichiometry		Dummy variable
EC based leaching					
Inputs from technosphere					
Sulfuric acid {RoW}| market for sulfuric acid | Cut-off, U	0.767±0.01		Strauss et al (2021), Diaz et al (2020)		Eco-invent
Iron sulfate {RoW}| market for iron sulfate | Cut-off, U	0.00112±0.001				Eco-invent
Electrolyte, KOH, LiOH additive {GLO}| market for | Cut-off, U	2.5±0.01				Eco-invent
Steel, chromium steel 18/8 {GLO}| market for | Cut-off, U	0.118±0.01			Electrode use for 20 times is assumed	Eco-invent
Electrode, negative, Ni {GLO}| market for | Cut-off, U	0.0225±0.01			Electrode use for 20 times is assumed	Eco-invent
Electricity, low voltage {GLO}| market group for | Cut-off, U		0.00333±0.001			Eco-invent
Emmisions to water					
Potassium compounds, unspecified	2.5		mass balance		Eco-invent
Outputs to technosphere					
Scrap steel {GLO}| market for | Cut-off, U	0.14		mass balance	Electrode use for 20 times is assumed	Eco-invent
Leached metal ions (Co2+, Ni2+, Mn2+)	0.566		Stoichiometry		Dummy variable
SCF based leaching					
Inputs from technosphere					
Sulfuric acid {RoW}| market for sulfuric acid | Cut-off, U	2.085±2.60		Bertuol (2016), Zhang et al (2022)		Eco-invent
Hydrogen peroxide, without water, in 50% solution state {RoW}| market for	0.599±0.51				Eco-invent
Carbon dioxide, liquid {RoW}| market for | Cut-off, U	3.706±1.55				Eco-invent
Sodium hydroxide, without water, in 50% solution state {GLO}| market for |	6.488±2.50				Eco-invent
Water, deionised {RoW}| market for water, deionised | Cut-off, U	0.1622±0.06				Eco-invent
Electricity, low voltage {GLO}| market group for | Cut-off, U		0.0478±0.008		4.6 W ,CO2 dosing pump work for 5 min. & 1KW reactor for 10 min pre-heat and 30% working potential for 5 min.	Eco-invent
Emmisions to water					
Wastewater	0.163		Stoichiometry		Eco-invent
Sodium compounds, unspecified	8.595		Stoichiometry		Eco-invent
Outputs to technosphere					
Leached metal ions (Co2+, Ni2+, Mn2+)	0.445		Stoichiometry		Dummy variable

Precicpitation (Oxalate) based purification for DES leaching					
Inputs from technosphere					
Dimethyl sulfoxide {GLO}| market for | Cut-off, U	13.357±0.01		Chang et al (2022), He et al (2022), Tang et al (2022)		Eco-invent
Water, deionised {RoW}| market for water, deionised | Cut-off, U	7.285±0.01				Eco-invent
Sodium hydroxide, without water, in 50% solution state {GLO}| market for |	0.003±0.001				Eco-invent
Electricity, low voltage {GLO}| market group for | Cut-off, U		0.0128±0.01		150 W centrifuge machine for 5 min., 200 W filter pump for approx. 10 min filtration (2 times)	Eco-invent
Emmisions to air					
Oxygen	0.027		Stoichiometry		Eco-invent
Outputs to technosphere					
Spent solvent mixture {GLO}| market for | Cut-off, U	35.257		Stoichiometry	50% recycling assumed through the authors mentioned	Eco-invent
NiC2O4	0.493		Stoichiometry		Dummy variable
CoC2O4	0.4252		Stoichiometry		Dummy variable
MnC2O4	0.47		Stoichiometry		Dummy variable
Adsorbent material (ion-exchange resin) based purification					
Inputs from technosphere					
Anionic resin {RoW}| market for anionic resin | Cut-off, U	2.242±0.02		Strauss et al (2021), Zhang et al (2023)	Assumed 8 years shelf life. (https://www.lenntech.com/Data-sheets/Dowex-M-4195-L.pdf)	Eco-invent
Sulfuric acid {RoW}| market for sulfuric acid | Cut-off, U	0.276±0.07				Eco-invent
Water, deionised {RoW}| market for water, deionised | Cut-off, U	7.500±0.01				Eco-invent
Sodium hydroxide, without water, in 50% solution state {GLO}| market for |	0.00065±0.0001				Eco-invent
Ammonium hydroxide	0.075±0.03				Eco-invent
Ammonium acetate	0.075±0.01				Eco-invent
Electricity, low voltage {GLO}| market group for | Cut-off, U		0.0195±0.01		Circulating pumps, 65 W, working with minimum flow rate 0.25mL/min. 30% working power, time 12 hours	Eco-invent
Emmisions to water					
Waste water	7.926		Stoichiometry		Eco-invent
Outputs to technosphere					
Spent anion exchange resin from potable water production {RoW}| treatme	0.00922		mass balance	Assumed 8 years shelf life. (https://www.lenntech.com/Data-sheets/Dowex-M-4195-L.pdf)	Eco-invent
Hazardous waste, for incineration {RoW}| treatment of hazardous waste, h	1.006		mass balance		
Ni(OH)2	0.305		Stoichiometry		Dummy variable
Co(OH)2	0.305		Stoichiometry		Dummy variable
Mn(OH)2	0.292		Stoichiometry		Dummy variable
Solvent extraction based purification					
Inputs from technosphere					
Hydrochloric acid, without water, in 30% solution state {RoW}| market for	13.14±0.58		Xuan et al (2022), Wang et al (2020), Omelchuk et al (2017)		Eco-invent
Solvent, organic {GLO}| market for | Cut-off, U	46.479±11.54			50% recycling is used, though authors reported more than that	Eco-invent
Sodium hydroxide, without water, in 50% solution state {GLO}| market for |	1.800±0.01				Eco-invent
Water, deionised {RoW}| market for water, deionised | Cut-off, U	187.5±0.01				Eco-invent
Electricity, low voltage {GLO}| market group for | Cut-off, U		2.00±0.4			Eco-invent
Emmisions to water					
Waste water	189.665		Stoichiometry		Eco-invent
Outputs to technosphere					
Spent solvent mixture {GLO}| market for | Cut-off, U	46.479		mass balance	50% recycling is used, though authors reported more than that	Eco-invent
Hazardous waste, for incineration {RoW}| treatment of hazardous waste, h	12.78		mass balance		Eco-invent
Ni(OH)2	0.28		Stoichiometry		Dummy variable
Co(OH)2	0.274		Stoichiometry		Dummy variable
Mn(OH)2	0.257		Stoichiometry		Dummy variable

Metal hydroxide precicpitate calcination					
Inputs from technosphere					
Air	0.0574		Stoichiometry	Li et al (2017), Eilers-Rethwisch et al (2018), Zhang et al	Eco-invent
Electricity, low voltage {GLO}| market group for | Cut-off, U		0.591+0.42		Calcination of metal residue, pre-sintering at 490 C for 2 hours, sintering 870 C with 1.8 kW, 40 min pre heat, 30% working capacity for 30 hours. Li et al (2017), Eilers-Rethwisch et al (2018), Zhang et al (2018), Xu et al (2018)	Eco-invent
Emmisions to air					
Water	0.5903		Stoichiometry	Li et al (2017), Eilers-Rethwisch et al (2018), Zhang et al	Eco-invent
Outputs to technosphere					
CoO	0.864		Stoichiometry		Dummy variable
NiO	0.806		Stoichiometry		Dummy variable
MnO	0.797		Stoichiometry		Dummy variable
Metal oxalate precicpitate calcination					
Inputs from technosphere					
Air	0.112		Stoichiometry	Yang et al (2014), Zhu et al (2019), Yao et al (2019), Wu	Eco-invent
Electricity, low voltage {GLO}| market group for | Cut-off, U		0.573±0.05		Calcination of Co residue pre-sintering at 500 C for 2 hours and Sintering at 850 C for 29 hours with 1.8 kWh, 40 min pre heat, 30% working capacity	Eco-invent
Emmisions to air					
Carbon dioxide	1.515		Stoichiometry	Yang et al (2014), Zhu et al (2019), Yao et al (2019), Wu et al (2021)	Eco-invent
Carbon monoxide	0.191		Stoichiometry		Eco-invent
Water	0.202		Stoichiometry		Eco-invent
Outputs to technosphere					
CoO	0.546		Stoichiometry		Dummy variable
NiO	0.509		Stoichiometry		Dummy variable
MnO	0.496		Stoichiometry		Dummy variable

Section 2: Inventory of the improved scenario.

Simapro input/output	Material per 1 g of NMC cathode treatment	Energy per 1 g of NMC cathode treatment			
Unit	g	Wh			
Conventional leaching					
Inputs from technosphere					
Sulfuric acid {RoW}| market for sulfuric acid | Cut-off, U	3.68				
Hydrogen peroxide, without water, in 50% solution state {RoW}| market for	0.715		Decreased the reducing agent by 50%		
Electricity, low voltage {CH}| market for | Cut-off, S		24.5	Energy mix		
Emmisions to air					
Oxygen	0.0024				
Outputs to technosphere					
Leached metal ions (Co2+, Ni2+, Mn2+)	0.59				
DES based leaching					
Inputs from technosphere					
Deep Eutectic Solvent (Oxalic acid & Choline Chloride)	6.2		80% recycling		
Electricity, low voltage {CH}| market for | Cut-off, S		288.6	Energy mix		
Outputs to technosphere					
Leached metal ions (Co2+, Ni2+, Mn2+)	0.57				
EC based leaching					
Inputs from technosphere					
Sulfuric acid {RoW}| market for sulfuric acid | Cut-off, U	0.767				
Iron sulfate {RoW}| market for iron sulfate | Cut-off, U	0.00112				
Electrolyte, KOH, LiOH additive {GLO}| market for | Cut-off, U	2.5				
Steel, chromium steel 18/8 {GLO}| market for | Cut-off, U	0.0472		Electrode use for 50 times is assumed		
Electrode, negative, Ni {GLO}| market for | Cut-off, U	0.009		Electrode use for 50 times is assumed		
Electricity, low voltage {CH}| market for | Cut-off, S		0,00333	Energy mix		
Emmisions to water					
Potassium compounds, unspecified	2.5				
Outputs to technosphere					
Scrap steel {GLO}| market for | Cut-off, U	0.056		Electrode use for 50 times is assumed		
Leached metal ions (Co2+, Ni2+, Mn2+)	0.566				
SCF based leaching					
Inputs from technosphere					
Sulfuric acid {RoW}| market for sulfuric acid | Cut-off, U	2				
Hydrogen peroxide, without water, in 50% solution state {RoW}| market for	0.599				
Carbon dioxide, liquid {RoW}| market for | Cut-off, U	0.741		Recyling of 80% of CO2 assumed		
Sodium hydroxide, without water, in 50% solution state {GLO}| market for |	1.298		80% of reduction due to higher CO2 recirculation		
Water, deionised {RoW}| market for water, deionised | Cut-off, U	0.1622				
Electricity, low voltage {CH}| market for | Cut-off, S		0.0478	Energy mix		
Emmisions to water					
Wastewater	0.163				
Sodium compounds, unspecified	1.719		80% of reduction due to higher CO2 recirculation		
Outputs to technosphere					
Leached metal ions (Co2+, Ni2+, Mn2+)	0.445				
Precicpitation (Oxalate) based purification for DES leaching					
Inputs from technosphere					
Dimethyl sulfoxide {GLO}| market for | Cut-off, U	9.350		30% reduction of consumption		
Water, deionised {RoW}| market for water, deionised | Cut-off, U	7.285				
Sodium hydroxide, without water, in 50% solution state {GLO}| market for |	0.003				
Electricity, low voltage {CH}| market for | Cut-off, S		0.013	Energy mix		
Emmisions to air					
Oxygen	0.027				
Outputs to technosphere					
Spent solvent mixture {GLO}| market for | Cut-off, U	14.102		80% recycling		
NiC2O4	0.493				
CoC2O4	0.4252				
MnC2O4	0.47				

Adsorbent material (ion-exchange resin) based purification					
Inputs from technosphere					
Anionic resin {RoW}| market for anionic resin | Cut-off, U	1.794		Shelf life of 10 years assumed		
Sulfuric acid {RoW}| market for sulfuric acid | Cut-off, U	0.276				
Water, deionised {RoW}| market for water, deionised | Cut-off, U	7.5				
Sodium hydroxide, without water, in 50% solution state {GLO}| market for |	0.00065				
Ammonium hydroxide	0.075				
Ammonium acetate	0.075				
Electricity, low voltage {CH}| market for | Cut-off, S		0.0195	Energy mix		
Emmisions to water					
Waste water	7.926				
Outputs to technosphere					
Spent anion exchange resin from potable water production {RoW}| treatme	0.00738		Shelf life of 10 years assumed		
Hazardous waste, for incineration {RoW}| treatment of hazardous waste, h	0.905		10% reduction via treatment		
Ni(OH)2	0.305				
Co(OH)2	0.305				
Mn(OH)2	0.292				
Solvent extraction based purification					
Inputs from technosphere					
Hydrochloric acid, without water, in 30% solution state {RoW}| market for	13.14				
Solvent, organic {GLO}| market for | Cut-off, U	18.59		80% recycling		
Sodium hydroxide, without water, in 50% solution state {GLO}| market for |	1.8				
Water, deionised {RoW}| market for water, deionised | Cut-off, U	187.5				
Electricity, low voltage {CH}| market for | Cut-off, S		2	Energy mix		
Emmisions to water					
Waste water	189.665				
Outputs to technosphere					
Spent solvent mixture {GLO}| market for | Cut-off, U	18.59		80% recycling		
Hazardous waste, for incineration {RoW}| treatment of hazardous waste, h	11.502		10% reduction via treatment		
Ni(OH)2	0.28				
Co(OH)2	0.274				
Mn(OH)2	0.257				
Metal hydroxide precicpitate calcination					
Inputs from technosphere					
Air	0.0574				
Electricity, low voltage {CH}| market for | Cut-off, S		0.591	Energy mix		
Emmisions to air					
Water	0.5903				
Outputs to technosphere					
CoO	0.864				
NiO	0.806				
MnO	0.797				
Metal oxalate precicpitate calcination					
Inputs from technosphere					
Air	0.112				
Electricity, low voltage {CH}| market for | Cut-off, S		0.573	Energy mix		
Emmisions to air					
Carbon dioxide	1.515				
Carbon monoxide	0.191				
Water	0.202				
Outputs to technosphere					
CoO	0.546				
NiO	0.509				
MnO	0.496				

Section 3: Inventory of economic analysis.

Data source for Electricity prices (world average)	https://thundersaidenergy.com/downloads/global-electricity-prices-vs-co2-intensities/
Data source for chemical prices	https://www.alibaba.com/
Hazardous waste disposal prices	https://bouldercounty.gov/environment/hazardous-waste/disposal-costs-for-businesses/
DI water prices (industrial)	https://www.chemworld.com/Delonized-Water-s/2622.htm
Hydrochloric acid prices (industrial)	https://www.intratec.us/chemical-markets/hydrochloric-acid-price
Hydrogen peroxide (industrial)	https://www.chemworld.com/Food-Grade-Hydrogen-Peroxide-Tote-p/chemworld-54-310.htm
Sulfuric acid prices (industrial)	https://www.chemworld.com/Sulfuric-Acid-NSF-approved-p/66be-4200.htm
Scrap metal disposal/recycling prices	https://doi.org/10.1016/j.jclepro.2022.133130

Constituent	Quantity (kg or MJ)	Higest unit price ($/kg) or ($/MJ)	Lowest unit price ($/kg) or ($/MJ)	Highest total costs ($) per 1 kg of cathode treatment	Lowest total costs ($) per 1 kg of cathode treatment	Average Cost per 1kg treatment ($)	Standard deviation of the cost (±$)	Variance	Remarks
Route 1: DES leaching-->Oxalate precipitate purification-->Oxalate calcination									
Deep Eutectic Solvent (Oxalic acid & Choline Chloride)	6.20	12.38	10.63	76.73	65.88	71.30	3.13	9.81	10% increased to the price of ChCl to assume the price of DES
Dimethyl sulfoxide (GLO)| market for | Cut-off, S	9.35	46.25	43.75	432.44	409.06	420.75	6.75	45.53	
Electricity, low voltage {CH}| market for | Cut-off, S	1995.42	0.15	0.11	304.30	214.51	259.41	25.92	671.91	
Sodium hydroxide, without water, in 50% solution state {GLO}| market for | Cut-	0.00	1.08	0.90	0.00	0.00	0.00	0.00	0.00	
Spent solvent mixture {GLO}| market for | Cut-off, S	14.10	-39.38	-41.63	-555.27	-587.00	-571.13	9.16	83.90	Price of the DMSO was taken with 10% reduction
Water, deionised {RoW}| market for water, deionised | Cut-off, S	8.53	1.31	1.23	11.20	10.48	10.84	0.21	0.04	
						191.16	**28.48**		
Route 2: EC leaching-->adsorbent based purification-->Hydroxide calcination									
Ammonium acetate	0.08	48.13	46.88	3.61	3.52	3.56	0.03	0.00	
Ammonium hydroxide	0.08	0.25	0.25	0.02	0.02	0.02	0.00	0.00	
Anionic resin {RoW}| market for anionic resin | Cut-off, S	1.79	1.17	1.09	2.09	1.96	2.03	0.04	0.00	
Electricity, low voltage {CH}| market for | Cut-off, S	639.00	0.15	0.11	97.45	68.69	83.07	8.30	68.90	
Electrode, negative, Ni {GLO}| market for | Cut-off, S	0.01	51.88	33.13	0.47	0.30	0.38	0.05	0.00	
Electrolyte, KOH, LiOH additive {GLO}| market for | Cut-off, S	2.50	1.36	1.35	3.39	3.38	3.39	0.00	0.00	
Hazardous waste, for incineration {RoW}| treatment of hazardous waste, hazarc	0.91	1.77	1.53	1.60	1.39	1.49	0.06	0.00	
Iron sulfate {RoW}| market for iron sulfate | Cut-off, S	0.00	0.07	0.07	0.00	0.00	0.00	0.00	0.00	
Scrap steel {GLO}| market for | Cut-off, S	0.06	1.07	1.07	0.06	0.06	0.06	0.00	0.00	
Sodium hydroxide, without water, in 50% solution state {GLO}| market for | Cut-	0.00	1.08	0.90	0.00	0.00	0.00	0.00	0.00	
Spent anion exchange resin from potable water production {RoW}| treatment of,	0.01	4.03	3.49	0.03	0.03	0.03	0.00	0.00	
Steel, chromium steel 18/8 {GLO}| market for | Cut-off, S	0.05	24.20	-20.80	1.14	-0.98	0.08	0.61	0.38	
Sulfuric acid {RoW}| market for sulfuric acid | Cut-off, S	1.04	0.21	0.20	0.21	0.21	0.21	0.00	0.00	
Water, deionised {RoW}| market for water, deionised | Cut-off, S	7.58	1.31	1.23	9.94	9.30	9.62	0.18	0.03	
						103.94	**8.33**		
Route 3: EC leaching-->Solvent extraction based purification-->Hydroxide calcination									
Electricity, low voltage {CH}| market for | Cut-off, S	607.33	0.15	0.11	92.62	65.29	78.95	7.89	62.24	
Electrode, negative, Ni {GLO}| market for | Cut-off, S	0.01	51.88	33.13	0.47	0.30	0.38	0.05	0.00	
Electrolyte, KOH, LiOH additive {GLO}| market for | Cut-off, S	2.50	1.36	1.35	3.39	3.38	3.39	0.00	0.00	
Hazardous waste, for incineration {RoW}| treatment of hazardous waste, hazarc	11.98	1.77	1.53	21.18	18.36	19.77	0.81	0.66	
Hydrochloric acid, without water, in 30% solution state {RoW}| market for | Cut-	13.69	0.11	0.05	1.45	0.63	1.04	0.24	0.06	
Iron sulfate {RoW}| market for iron sulfate | Cut-off, S	0.00	0.07	0.07	0.00	0.00	0.00	0.00	0.00	
Scrap steel {GLO}| market for | Cut-off, S	0.06	1.07	1.07	0.06	0.06	0.06	0.00	0.00	
Sodium hydroxide, without water, in 50% solution state {GLO}| market for | Cut-	1.87	1.08	0.90	2.02	1.69	1.86	0.09	0.01	
Solvent, organic {GLO}| market for | Cut-off, S	19.36	6.63	4.38	128.28	84.72	106.50	12.58	158.18	D2EHPA price
Spent solvent mixture {GLO}| market for | Cut-off, S	19.36	-3.94	-5.96	-76.24	-115.46	-95.85	11.32	128.13	Price of D2EHPA with 10% reduction
Steel, chromium steel 18/8 {GLO}| market for | Cut-off, S	0.05	24.20	-20.80	1.14	-0.98	0.08	0.61	0.38	
Sulfuric acid {RoW}| market for sulfuric acid | Cut-off, S	0.77	0.21	0.20	0.16	0.16	0.16	0.00	0.00	
Water, deionised {RoW}| market for water, deionised | Cut-off, S	195.30	1.31	1.23	256.24	239.83	248.04	4.74	22.43	
						364.37	**19.29**		
Route 4: SCF leaching-->Solvent extraction based purification-->Hydroxide calcination									
Carbon dioxide, liquid {RoW}| market for | Cut-off, S	0.74	17.79	11.27	13.18	8.35	10.77	1.39	1.94	
Electricity, low voltage {CH}| market for | Cut-off, S	524.07	0.15	0.11	79.92	56.34	68.13	6.81	46.35	
Hazardous waste, for incineration {RoW}| treatment of hazardous waste, hazarc	9.40	1.77	1.53	16.61	14.40	15.51	0.64	0.41	
Hydrochloric acid, without water, in 30% solution state {RoW}| market for | Cut-	10.74	0.11	0.05	1.14	0.49	0.82	0.19	0.03	
Hydrogen peroxide, without water, in 50% solution state {RoW}| market for hydr	0.60	3.22	3.00	1.93	1.80	1.86	0.04	0.00	
Sodium hydroxide, without water, in 50% solution state {GLO}| market for | Cut-	2.77	1.08	0.90	2.98	2.50	2.74	0.14	0.02	
Solvent, organic {GLO}| market for | Cut-off, S	15.19	6.63	4.38	100.62	66.45	83.53	9.86	97.31	
Spent solvent mixture {GLO}| market for | Cut-off, S	15.19	-3.94	-5.96	-59.80	-90.56	-75.18	8.88	78.82	
Sulfuric acid {RoW}| market for sulfuric acid | Cut-off, S	2.09	0.21	0.20	0.43	0.42	0.42	0.00	0.00	
Water, deionised {RoW}| market for water, deionised | Cut-off, S	153.35	1.31	1.23	201.19	188.31	194.75	3.72	13.83	
						303.35	**15.45**		
Route 5: SCF leaching-->adsorbent based purification-->Hydroxide calcination									
Ammonium acetate	0.06	48.13	46.88	2.83	2.76	2.79	0.02	0.00	
Ammonium hydroxide	0.06	0.25	0.25	0.01	0.01	0.01	0.00	0.00	
Anionic resin {RoW}| market for anionic resin | Cut-off, S	1.41	1.17	1.09	1.64	1.54	1.59	0.03	0.00	
Carbon dioxide, liquid {RoW}| market for | Cut-off, S	0.74	17.79	11.27	13.18	8.35	10.77	1.39	1.94	
Electricity, low voltage {CH}| market for | Cut-off, S	549.00	0.15	0.11	83.72	59.02	71.37	7.13	50.86	
Hazardous waste, for incineration {RoW}| treatment of hazardous waste, hazarc	0.71	1.77	1.53	1.25	1.09	1.17	0.05	0.00	
Hydrogen peroxide, without water, in 50% solution state {RoW}| market for hydr	0.60	3.22	3.00	1.93	1.80	1.86	0.04	0.00	
Sodium hydroxide, without water, in 50% solution state {GLO}| market for | Cut-	1.30	1.08	0.90	1.40	1.17	1.29	0.07	0.00	
Spent anion exchange resin from potable water production {RoW}| treatment of,	0.01	4.03	3.49	0.02	0.02	0.02	0.00	0.00	
Sulfuric acid {RoW}| market for sulfuric acid | Cut-off, S	2.30	0.21	0.20	0.47	0.47	0.47	0.00	0.00	
Water, deionised {RoW}| market for water, deionised | Cut-off, S	6.10	1.31	1.23	8.01	7.50	7.75	0.15	0.02	
						99.10	**7.27**		
Route 6: Conventional leaching-->Adsorbent material based purification-->hydroxide calcination									
Water, deionised {RoW}| market for water, deionised | Cut-off, S	7.89	1.31	1.23	10.35	9.69	10.02	0.19	0.04	
Sulfuric acid {RoW}| market for sulfuric acid | Cut-off, S	3.97	0.21	0.20	0.82	0.80	0.81	0.00	0.00	
Anionic resin {RoW}| market for anionic resin | Cut-off, S	1.87	1.17	1.09	2.18	2.04	2.11	0.04	0.00	
Ammonium acetate	0.08	48.13	46.88	3.76	3.66	3.71	0.03	0.00	
Ammonium hydroxide	0.08	0.25	0.25	0.02	0.02	0.02	0.00	0.00	
Hydrogen peroxide, without water, in 50% solution state {RoW}| market for hydr	0.72	3.22	3.00	2.30	2.15	2.22	0.04	0.00	
Spent anion exchange resin from potable water production {RoW}| treatment of,	0.01	4.03	3.49	0.03	0.03	0.03	0.00	0.00	
Sodium hydroxide, without water, in 50% solution state {GLO}| market for | Cut-	0.00	1.08	0.90	0.00	0.00	0.00	0.00	0.00	
Hazardous waste, for incineration {RoW}| treatment of hazardous waste, hazarc	0.94	1.77	1.53	1.67	1.44	1.56	0.06	0.00	
Electricity, low voltage {CH}| market for | Cut-off, S	754.00	0.15	0.11	114.99	81.06	98.02	9.79	95.94	
						118.50	**9.80**		
Route 7: Conventional leaching-->Solvent extraction based purification-->hydroxide calcination									
Electricity, low voltage {CH}| market for | Cut-off, S	720.83	0.15	0.11	109.93	77.49	93.71	9.36	87.68	
Hazardous waste, for incineration {RoW}| treatment of hazardous waste, hazarc	12.48	1.77	1.53	22.06	19.13	20.59	0.85	0.72	
Hydrochloric acid, without water, in 30% solution state {RoW}| market for | Cut-	14.26	0.11	0.05	1.51	0.66	1.08	0.25	0.06	
Hydrogen peroxide, without water, in 50% solution state {RoW}| market for hydr	0.72	3.22	3.00	2.30	2.15	2.22	0.04	0.00	
Sodium hydroxide, without water, in 50% solution state {GLO}| market for | Cut-	1.95	1.08	0.90	2.10	1.76	1.93	0.10	0.01	
Solvent, organic {GLO}| market for | Cut-off, S	20.17	6.63	4.38	133.63	88.25	110.94	13.10	171.64	
Spent solvent mixture {GLO}| market for | Cut-off, S	20.17	-3.94	-5.96	-79.42	-120.27	-99.84	11.79	139.03	
Sulfuric acid {RoW}| market for sulfuric acid | Cut-off, S	3.68	0.21	0.20	0.76	0.74	0.75	0.00	0.00	
Water, deionised {RoW}| market for water, deionised | Cut-off, S	203.44	1.31	1.23	266.92	249.83	258.37	4.93	24.34	
						389.76	**20.58**		

Annexure 3

Comparative Analysis of Facile and Novel Graphite Recovery Methods from Spent Li-Ion Batteries: Environmental and Economic Implications.

This document contains figures and tables generated by the SimaPro software for various analysis done by the authors for easy understanding of the life cycle analysis of Chapter 4. Specifically, damages under the hotspot analysis are given here with actual values instead of the percentages shown in the original chapter. The percentage values are calculated based on these figures. Also, comparison between different leaching agents with corresponding conditions that can be utilized for the copper dissolving are shown here.

Table S4.1 Damage assessment of cold process by each component.

Damage category	Unit	Total	Electricity	Spent copper
Acidification	mol H^+ eq	-2.90×10^{-03}	9.23×10^{-05}	-2.99×10^{-03}
Climate change	kg CO_2 eq	$-1.17\times10^{+00}$	2.20×10^{-02}	$-1.19\times10^{+00}$
Ecotoxicity, freshwater	CTUe	$-5.43\times10^{+00}$	6.83×10^{-02}	$-5.50\times10^{+00}$
Particulate matter	disease inc.	-2.18×10^{-08}	4.55×10^{-10}	-2.23×10^{-08}
Eutrophication, marine	kg N eq	-6.41×10^{-04}	1.38×10^{-05}	-6.55×10^{-04}
Eutrophication, terrestrial	mol N eq	-7.01×10^{-03}	1.50×10^{-04}	-7.16×10^{-03}
Human toxicity, cancer	CTUh	-3.75×10^{-08}	5.65×10^{-11}	-3.75×10^{-08}
Human toxicity, non-cancer	CTUh	-2.30×10^{-06}	2.73×10^{-10}	-2.30×10^{-06}
Photochemical ozone formation	kg NMVOC eq	-2.20×10^{-03}	6.43×10^{-05}	-2.26×10^{-03}
Resource use, fossils	MJ	$-6.73\times10^{+00}$	3.52×10^{-01}	-7.08×10+00
Resource use, minerals and metals	kg Sb eq	-3.72×10^{-07}	2.74×10^{-07}	-6.46×10^{-07}
Water use	m^3 depriv.	-2.40×10^{-02}	1.59×10^{-02}	-3.99×10^{-02}

Table S4.2 Damage assessment of hot process by each component.

Damage category	Unit	Total	Hot process	CaO	Water, deionized	Electricity	Scrap copper
Acidification	mol H^+ eq	9.06×10^{-03}	$0.00\times10^{+00}$	9.10×10^{-04}	4.30×10^{-05}	8.95×10^{-03}	-8.46×10^{-04}
Climate change	kg CO_2 eq	$1.97\times10^{+00}$	$0.00\times10^{+00}$	1.74×10^{-01}	4.05×10^{-03}	$2.13\times10^{+00}$	$-3.38\times10^{-0}1$
Ecotoxicity, freshwater	CTUe	$3.61\times10^{+02}$	$3.55\times10^{+02}$	8.56×10^{-01}	5.10×10^{-01}	$6.63\times10^{+00}$	$-1.56\times10^{+00}$
Particulate matter	disease inc.	5.69×10^{-08}	$0.00\times10^{+00}$	1.87×10^{-08}	3.40×10^{-10}	4.41×10^{-08}	-6.31×10^{-09}
Eutrophication, marine	kg N eq	1.42×10^{-03}	$0.00\times10^{+00}$	2.70×10^{-04}	3.36×10^{-06}	1.34×10^{-03}	-1.85×10^{-04}
Eutrophication, terrestrial	mol N eq	1.52×10^{-02}	$0.00\times10^{+00}$	2.68×10^{-03}	3.35×10^{-05}	1.46×10^{-02}	-2.03×10^{-03}
Human toxicity, cancer	CTUh	-4.42×10^{-09}	$0.00\times10^{+00}$	6.98×10^{-10}	2.96×10^{-11}	5.48×10^{-09}	-1.06×10^{-08}
Human toxicity, non-cancer	CTUh	7.40×10^{-08}	6.97×10^{-07}	1.27×10^{-09}	5.91×10^{-11}	2.65×10^{-08}	-6.51×10^{-07}
Ozone depletion	kg CFC11 eq	2.56×10^{-08}	$0.00\times10^{+00}$	1.74×10^{-09}	1.52×10^{-09}	4.90×10^{-08}	-2.66×10^{-08}
Photochemical ozone formation	kg NMVOC eq	6.40×10^{-03}	$0.00\times10^{+00}$	7.90×10^{-04}	1.32×10^{-05}	6.24×10^{-03}	-6.40×10^{-04}
Resource use, fossils	MJ	$3.42\times10^{+01}$	$0.00\times10^{+00}$	$2.00\times10^{+00}$	5.25×10^{-02}	$3.41\times10^{+01}$	$-2.01\times10^{+00}$
Resource use, minerals and metals	kg Sb eq	2.69×10^{-05}	$0.00\times10^{+00}$	4.02×10^{-07}	5.43×10^{-08}	2.66×10^{-05}	-1.83×10^{-07}
Water use	m^3 depriv.	$1.71\times10^{+00}$	-4.27×10^{-01}	1.67×10^{-01}	4.42×10^{-01}	$1.54\times10^{+00}$	-1.13×10^{-02}

Table S4.3 Damage assessment of wet process by each component

Damage category	Unit	Total	Wet process	Nitric acid	Hydrochloric acid	Water, deionized	Electricity	Spent solution	Leached Copper
Acidification	mol H^+ eq	2.15×10^{-02}	1.54×10^{-02}	2.55×10^{-03}	2.29×10^{-03}	4.13×10^{-05}	5.92×10^{-04}	5.41×10^{-04}	5.04×10^{-05}
Climate change	kg CO_2 eq	$1.84\times10^{+00}$	$0.00\times10^{+00}$	2.92×10^{-01}	3.18×10^{-01}	3.89×10^{-03}	1.41×10^{-01}	$1.07\times10^{+00}$	7.46×10^{-03}
Ecotoxicity, freshwater	CTUe	$1.48\times10^{+01}$	6.48×10^{-03}	6.96×10^{-01}	$4.41\times10^{+00}$	4.89×10^{-01}	4.39×10^{-01}	$8.22\times10^{+00}$	5.36×10^{-01}
Particulate matter	disease inc.	4.22×10^{-07}	3.80×10^{-07}	1.28×10^{-08}	1.63×10^{-08}	3.26×10^{-10}	2.92×10^{-09}	8.70×10^{-09}	7.35×10^{-10}
Eutrophication, marine	kg N eq	9.32×10^{-02}	9.24×10^{-02}	2.05×10^{-04}	2.65×10^{-04}	3.22×10^{-06}	8.84×10^{-05}	2.23×10^{-04}	1.88×10^{-05}
Eutrophication, terrestrial	mol N eq	3.68×10^{-01}	3.51×10^{-01}	1.04×10^{-02}	2.63×10^{-03}	3.21×10^{-05}	9.64×10^{-04}	1.88×10^{-03}	1.94×10^{-04}
Human toxicity, cancer	CTUh	4.40×10^{-09}	$0.00\times10^{+00}$	7.27×10^{-10}	2.53×10^{-09}	2.84×10^{-11}	3.63×10^{-10}	7.03×10^{-10}	4.65×10^{-11}
Human toxicity, non-cancer	CTUh	3.33×10^{-08}	2.36×10^{-08}	2.04×10^{-09}	4.88×10^{-09}	5.67×10^{-11}	1.75×10^{-09}	8.88×10^{-10}	7.04×10^{-11}
Ozone depletion	kg CFC11 eq	6.43×10^{-08}	$0.00\times10^{+00}$	6.18×10^{-09}	5.01×10^{-08}	1.46×10^{-09}	$3.24\times^{10-09}$	3.22×10^{-09}	1.17×10^{-10}
Photochemical ozone formation	kg NMVOC eq	2.40×10^{-01}	2.37×10^{-01}	6.91×10^{-04}	9.83×10^{-04}	1.27×10^{-05}	$4.13\times^{10-04}$	$5.78\times^{10-04}$	$6.11\times^{10-05}$
Resource use, fossils	MJ	$1.30\times10^{+01}$	$0.00\times10^{+00}$	$3.54\times10^{+00}$	$5.39\times10^{+00}$	5.04×10^{-02}	$2.26\times10^{+00}$	$1.62\times10^{+00}$	1.03×10^{-01}
Resource use, minerals and metals	kg Sb eq	1.07×10^{-05}	$0.00\times10^{+00}$	2.86×10^{-06}	5.51×10^{-06}	5.21×10^{-08}	1.76×10^{-06}	4.60×10^{-07}	$2.12E^{-08}$
Water use	m^3 depriv.	4.76×10^{-01}	-4.10×10^{-01}	1.27×10^{-01}	2.00×10^{-01}	4.25×10^{-01}	1.02×10^{-01}	3.10×10^{-02}	5.66×10^{-04}

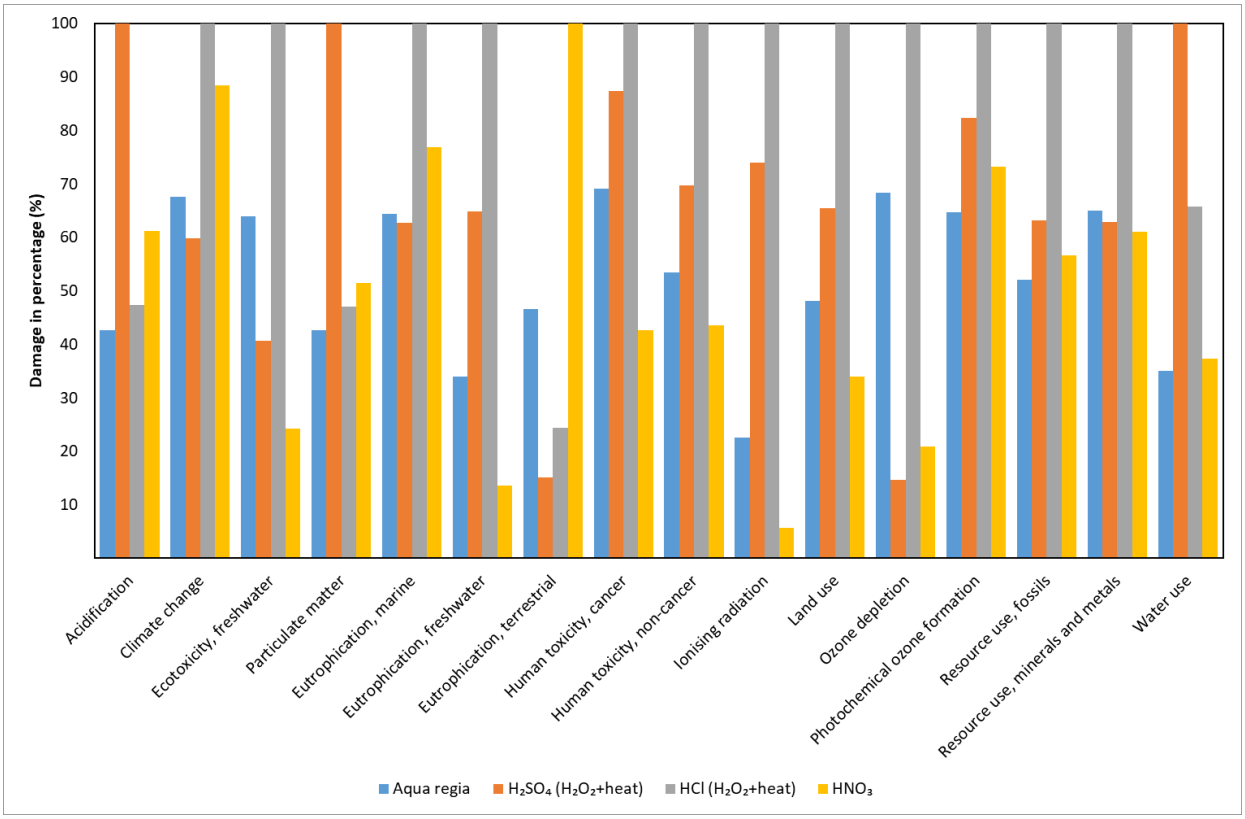

Figure S4.1 Comparison of different acid reagents with corresponding conditions for the utilization of graphite leaching.

Annexure 4

Recycling Lithium-Ion Battery Graphite: Synthesis of Adsorbent Materials for Highly Efficient Removal of Dye and Metal Ions from Wastewater.

This document presents the kinetic and isotherm graphs used for the investigation carried out in Chapter 5. We used Liquid film diffusion (LFD), Elovich, Weber-Morris intra-particle diffusion (IPD) and frequently used Pseudo-first order (PFO) and second order (PSO) kinetic models for the evaluation of the adsorption processes. Moreover, as the isotherm models, Langmuir (LI), Freundlich (FI), Temkin (TI), Halsey (HI) and Harkins-Jura (HJI) isotherms were utilized.

Other than that, comparison of maximum adsorption values received for the current study with existing literature values were carried out and demonstrated in this document.

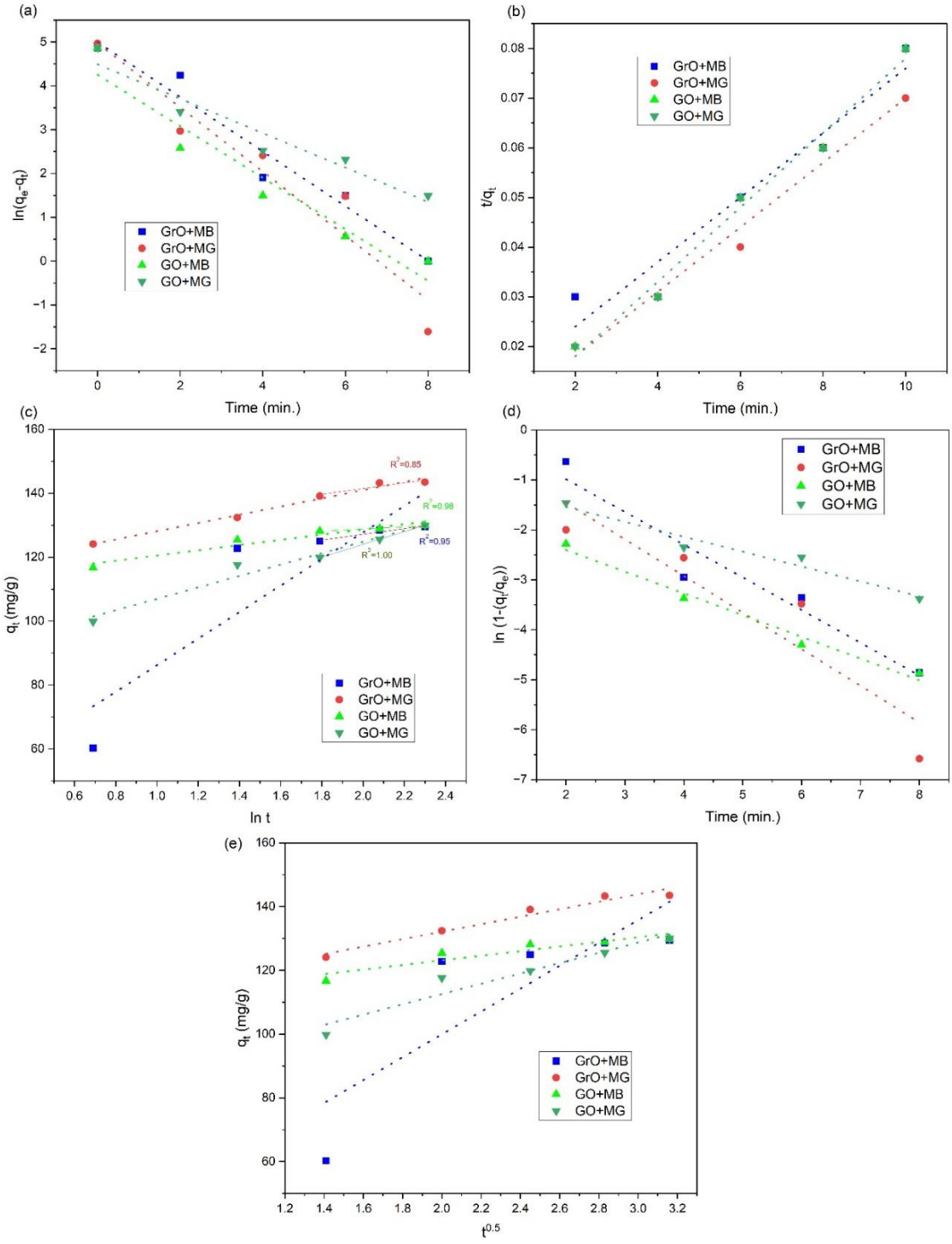

Figure S5.1 Adsorption kinetics plots for dye adsorptions (a) Pseudo First order model (b) Pseudo second order model (c) Elovich model (d)Liquid Film diffusion model (e) Weber-Morris intra-particle diffusion model.

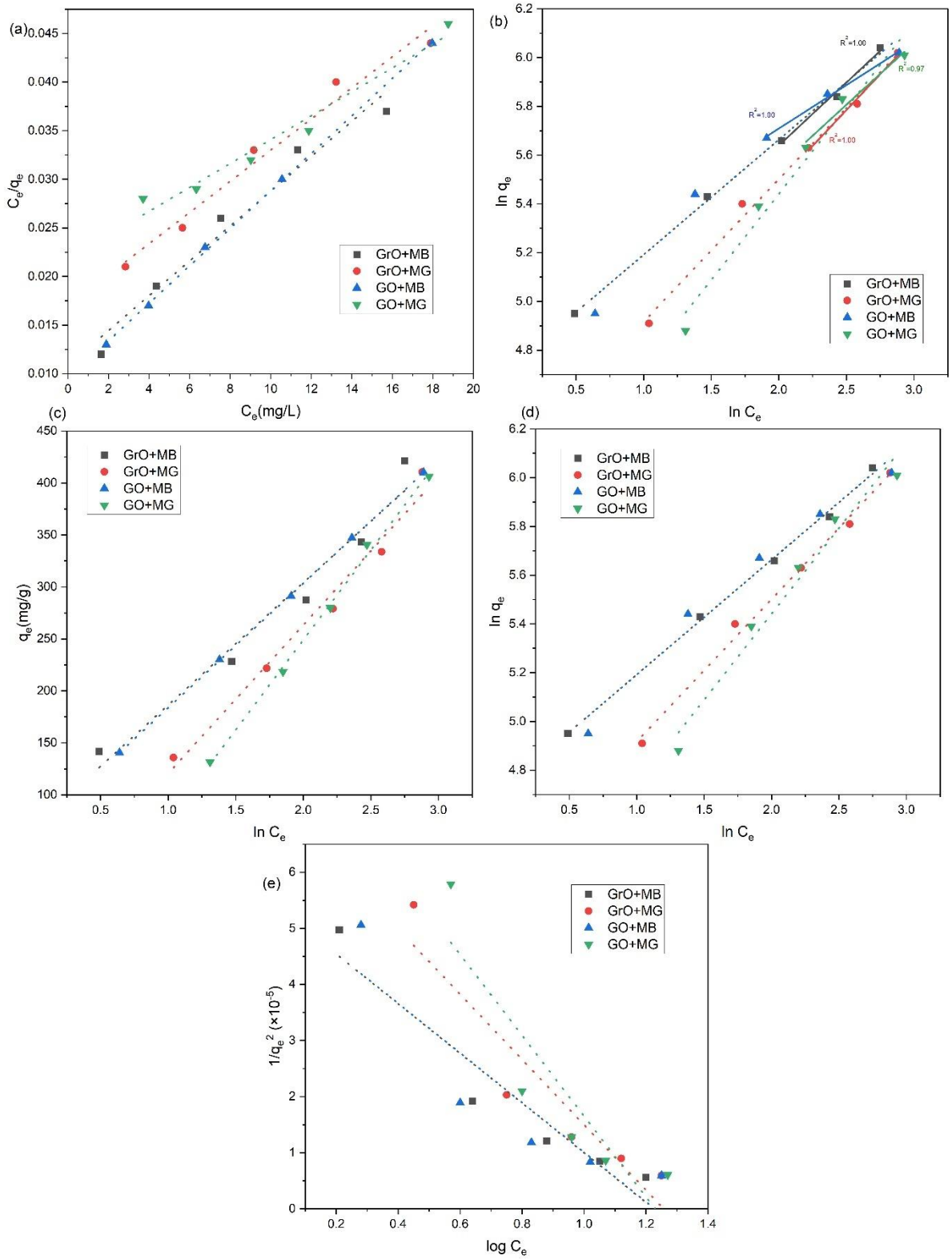

Figure S5.2 Adsorption isotherm plots for dye adsorptions (a) Langmuir model (b) Freundlich model (c) Temkin model (d) Halsey model (e) Harkins-Jura model

Table S5.1: Comparison of recent maximum adsorption values obtained for similar adsorbent materials with dye waste.

Adsorbent	Experimental condition	Maximum adsorption capacity (mg/g)	Dye	Ref.
Graphene (Commercial)	pH=5, T=19.85 °C, 0.5 g/L dose for 855 min.	153.85	MB	[72]
GrO (Commercial)	pH=5, T=25 °C, 0.5 g/L dose for 300 min.	243.90	MB	[73]
GO (Commercial)	pH=5.4, T=25 °C, 0.5 g/L dose for 420 min.	144.92	MB	[74]
GO from LIBs	pH= 10, T=30 °C, 5.0 g/L dose for 5 min.	Up to 1000	MB	[75]
GrO from LIBs	pH=5.5, T=25 °C, 0.2 g/L dose for 10 min.	557.59	MB	Current study
GO from LIBs	pH=5.5, T=25 °C, 0.2 g/L dose for 10 min.	558.49	MB	Current study
Reduced GrO	pH=6, T=30 °C, 1 g/L dose for 3 hrs.	279.85	MG	[76]
ZnCl2 treated pyrolyzed mesoporous biochar	pH & T unavailable, 5 g/L dose for 3 hrs.	90.1	MG	[77]
Exfoliated Graphite	pH= 6, T=26.85 °C, 1 g/L dose for 10 min.	192.3	MG	[78]
GrO from LIBs	pH=5.5, T=25 °C, 0.2 g/L dose for 10 min.	554.50	MG	Current study
GO from LIBs	pH=5.5, T=25 °C, 0.2 g/L dose for 10 min.	616.99	MG	Current study

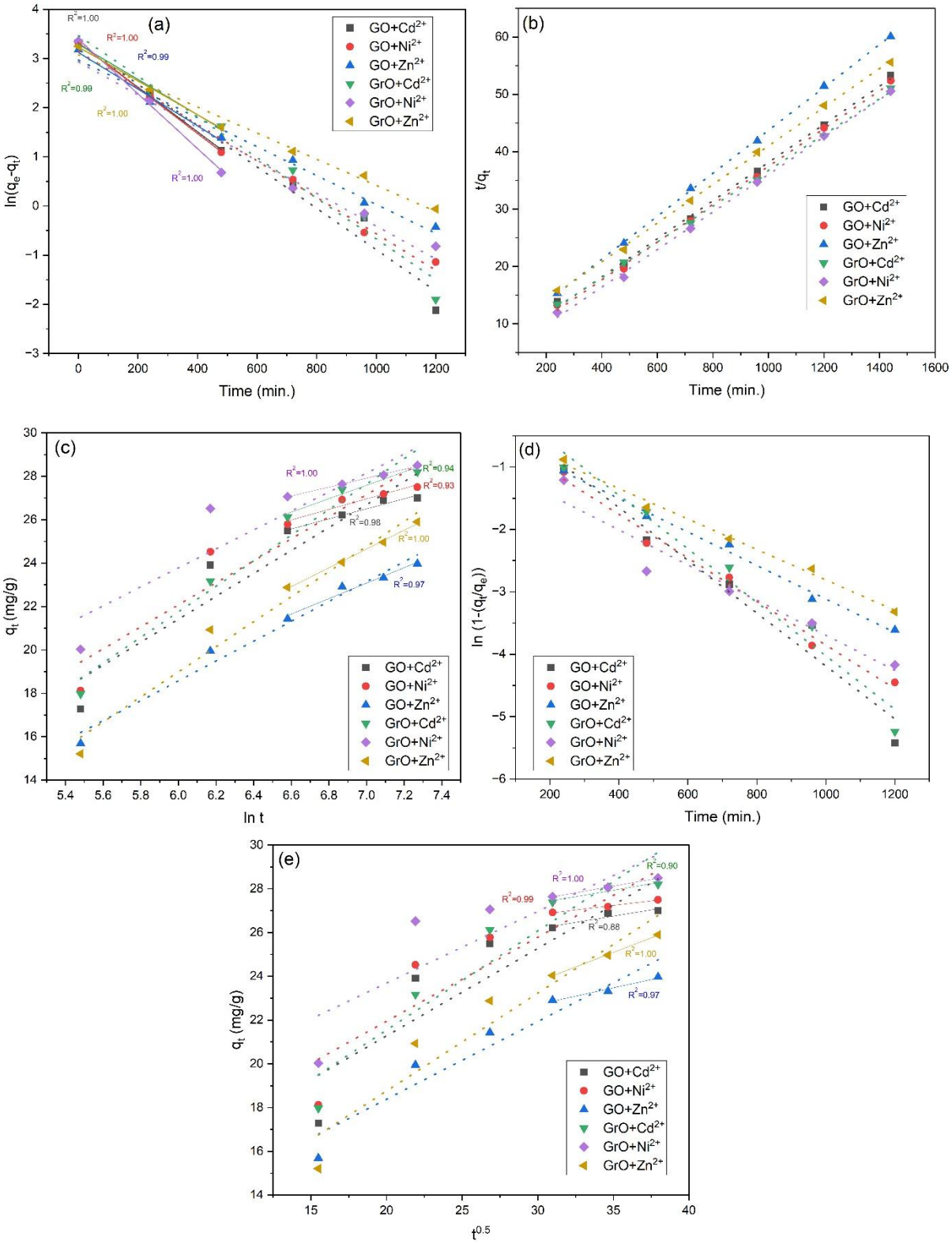

Figure S5.3 Adsorption kinetics plots for metal ion adsorptions (a) Pseudo First order model (b) Pseudo second order model (c) Elovich model (d)Liquid Film diffusion model (e) Weber-Morris intra-particle diffusion model

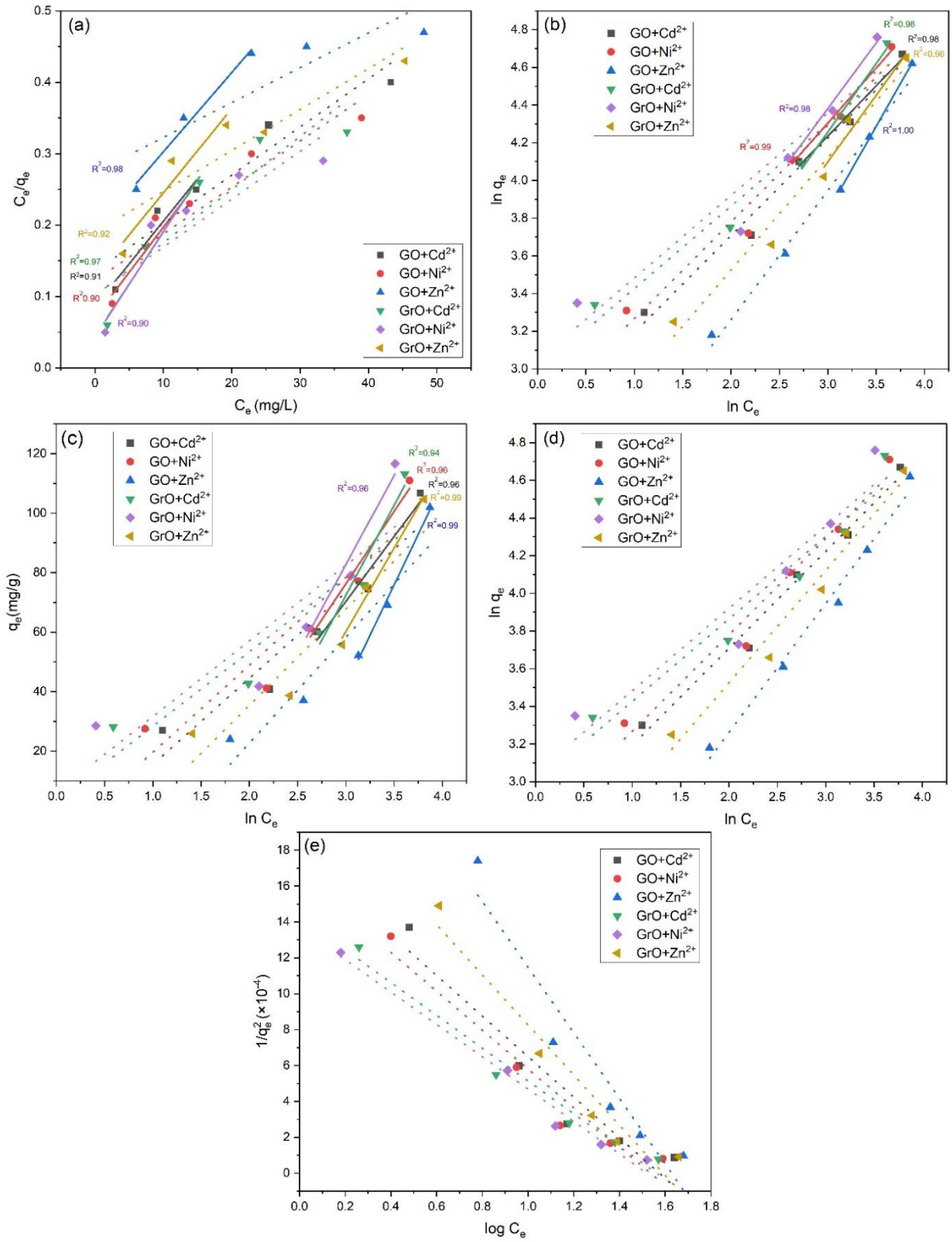

Figure S5.4 Adsorption isotherm plots for metal ion adsorptions (a) Langmuir model (b) Freundlich model (c) Temkin model (d) Halsey model (e) Harkins-Jura model

Table S5.2 Comparison of maximum adsorption values for considered metal ion adsorption process through Freundlich Isotherm reported in recent studies.

Adsorbent	Experimental condition	Maximum adsorption capacity (mg/g)	Metal ion	Ref.
Activated Carbon	pH=5.5, T= 25 °C, 0.025 g/L dose for 60 min.	76.3 45.5 32.6	Cd^{2+} Zn^{2+} Ni^{2+}	[79]
Carbon Nano Tubes	pH & T are Unavaialable, 0.01g/L dose for 6o min.	94.5	Cd^{2+}	[80]
Chemically modified GrO with waste news paper	pH=4, T=25 °C, 0.04 g/L dose for 12 hrs.	29.04 31.35	Ni^{2+} Cd^{2+}	[81]
BPED modified GrO	pH=7, T=20 °C, 0.25 g/L dose for 24 hrs.	3.25	Ni^{2+}	[82]
Magnetized GrO with iron particles	pH=7, T=25 °C, with 0.25 g/L dose for 25 min. pH=8, T=25 °C, 0.25 g/L dose for 25 min.	63.7 51.02	Zn^{2+} Ni^{2+}	[83]
GrO from LIBs	pH=5.5, T=25 °C, 1 g/L dose for 24 hrs.	83.99 89.85 68.30	Cd^{2+} Ni^{2+} Zn^{2+}	Current study
GO from LIBs	pH=5.5, T=25 °C, 1 g/L dose for 24 hrs.	88.03 93.19 78.29	Cd^{2+} Ni^{2+} Zn^{2+}	Current study